NUMERICAL ANALYSIS OF SEMICONDUCTOR DEVICES

by

John G. Shaw

A thesis
presented to the University of Manitoba
in partial fulfillment of the
requirements for the degree of
Doctor of Philosophy
in
Electrical Engineering

Winnipeg, Manitoba, 1983

NUMERICAL ANALYSIS OF SEMICONDUCTOR DEVICES

by

John Gary Shaw

A thesis submitted to the Faculty of Graduate Studies of
the University of Manitoba in partial fulfillment of the requirements
of the degree of

DOCTOR OF PHILOSOPHY

ABSTRACT

This thesis presents an accurate method of solving the transport equations associated with semiconductor devices using a novel finite-element algorithm.

An energy functional for a nonlinear Poisson-like equation is formed and subsequently minimized in terms of variational parameters of potential. The functional is shown to be valid under the Dirichlet, Neumann, and mixed boundary conditions. The medium and source are allowed to be arbitrary functions of position, time, and potential.

To fully describe all transport phenomena, as many as three, highly-nonlinear partial differential equations must be solved simultaneously. For each step of a Newton-Raphson sequence, a sparse set of linear equations is generated by applying finite-element discretization over the region of interest. The resulting system is solved using a direct, bifactorization technique.

Both quasi-linear and quadratic elements are implemented in one, two, and three spatial dimensions. Time-integration is handled through a simple backward-difference scheme. Several possible extensions are discussed and a number of relevant examples are presented.

ACKNOWLEDGMENTS

The author wishes to thank Professor Howard C. Card for his patient supervision and encouragement throughout the extent of this project.

The author is also indebted to numerous colleagues, especially those associated with the Materials and Devices Research Laboratory (MDRL) and the Numerical Applications Group (NAG) at the University of Manitoba for various discussions and suggestions.

Financial assistance from the Natural Sciences and Engineering Research Council of Canada is gratefully acknowledged.

CONTENTS

LIST OF FIGURES

LIST OF TABLES

LIST OF SYMBOLS

Symbol	Description	Units
$\underline{b}$	Source vector	
C	Capacitance	F
D	Diffusion coefficient	cm2 s-1
E	Electric field strength	V cm-2
E_i	Intrinsic energy level	eV
E_f	Fermi energy level	eV
E_t	Trap energy level	eV
F	Energy functional	
G	Generation rate	cm-3 s-1
h	Planck constant	J s
J	Current density	A cm-1
J	Jacobian matrix	
k	Boltzmann constant	J K-1
kT	Thermal energy	eV
L	Generic operator	
m_{de}	Effective mass of electrons	g
m_{dh}	Effective mass of holes	g
m*	Effective mass	g
n	Density of free electrons	cm-3
$\hat{n}$	Unit normal vector	
N_a	Acceptor impurity density	cm-3
N_d	Donor impurity density	cm-3

N_{dope}	Doping concentration	cm-3
n_i	Intrinsic carrier density	cm-3
p	Density of free holes	cm-3
q	Magnitude of electronic charge	C
Q	Charge	C
R	Recombination rate	cm-3 s-1
$\underline{R}$	Residual vector	
S	System matrix	
t	Time	s
T	Absolute temperature	K
V_{bi}	Built-in junction potential	V
v_n	Velocity of electrons	cm s-1
v_p	Velocity of holes	cm s-1
V_t	kT/q	V
X	Spatial coordinate	cm
$\underline{\alpha}$	Shape functions	
$\overline{\overline{\varepsilon}}$	Permittivity tensor	F cm-1
τ	Lifetime	s
μ_n	Electron mobility	cm2 v-1 s-1
μ_p	Hole mobility	cm2 v-1 s-1
ϕ_s	Intrinsic Fermi potential	V
ϕ_n	Quasi-Fermi potential for electrons	V
ϕ_p	Quasi-Fermi potential for holes	V
σ	Surface charge density	C cm-2
ρ	Volume charge density	C cm-3

Chapter I

INTRODUCTION

Until recently, the fabrication and characterization of semiconductor devices has been largely an experimental process. Analytic models, where they exist, are often crude and restricted in scope. With the rapid advance of digital computer technology, it seems natural that computer aided design (CAD) tools based on sound numerical techniques will become more prevalent as device complexity increases.

In order to efficiently simulate the transport processes associated with semiconductor materials, one requires a model which is both physically realistic and numerically stable. Previous researchers have successfully applied variations of the finite-difference [1, 2, 3] and finite-element [4, 5, 6] methods to a number of semiconductor problems. Unfortunately, many of the earlier techniques suffer from lack of generality (e.g. restricted forms of carrier transport) and limited accuracy of solutions.

Undoubtedly, solution of the generalized semiconductor transport equations is one of the most difficult tasks faced by device physicists of today. Device behavior is governed by a set of three highly-nonlinear, partial differential equations (PDE's) involving both spatial and time-dependence

of source and material properties. It is indeed fortunate that the particular operator associated with these equations is self-adjoint, thus solution by proven variational techniques becomes feasible.

The method presented here uses isoparametric finite elements together with a fully implicit Newton-Raphson algorithm to achieve accurate electrostatic and Fermi-potentials with acceptable computational effort. The operator in question is similar to the standard Laplacian when inhomogeneous, anisotropic media are involved. In this case, both the medium and source terms are allowed to be arbitrary functions of potential, position, and time.

Based on a variational approach, an energy functional is derived and from it, a large sparse system of linear equations is formed. The solution to that system represents an approximation, incorporating a polynomic interpolation scheme, to the actual field distribution within the device. Due to the nonlinearity of the problem, one such system is generated during each iteration of the Newton-Raphson algorithm.

A collection of related programs, grouped to form the MANIFEST[1] system, was written to implement these concepts and provide a general purpose CAD tool suitable for use by device physicists and integrated-circuit design engineers. The programs allow the solution of the general semiconductor

---

[1] Manitoba Finite-Element Semiconductor Tool.

transport problem in one, two, or three spatial dimensions. The treatment of quantum effects are not included at present; carrier transport is described by a macroscopic mobility which may however depend upon position. Transient simulations are implemented via a simple backward-difference scheme. Various pre- and post-processing programs provide support for data preparation and display. Additionally, users may select between quasi-linear and quadratic elements when optimizing program speed and accuracy.

Several novel extensions to the basic Newton-Raphson algorithm have been incorporated into MANIFEST. To improve stability, an automatic step-limiting feature calculates an optimum deacceleration matrix if the iterative procedure begins to diverge. When running two- or three-dimensional simulations, the user may choose to utilize the disk-swapping controller which avoids recalculation of the elementary system matrices.

Many of the proofs presented in this thesis were drawn (indirectly) from Mikhlin's book "Variational Methods in Mathematical Physics" [7], which describes in detail the principle of variational analysis as applied to energy functionals. The set of lecture notes "Finite Elements for Technologists" [8], was also instrumental in formulating the concepts presented here. In particular, several of the proofs in Chapter III (which also appear in Ref. [8]) can be attributed to A. Wexler. For an excellent introduction to

the topics covered by this thesis, readers are referred to Kurata's book, "Numerical Analysis for Semiconductor Devices" [9] which influenced much of Chapter II. Documentation on the MANIFEST system may be found in either of two companion volumes to this thesis. The "MANIFEST User's Guide" [10] (see Appendix A) details many of the program's inner workings and outlines its associated command language. The "MANIFEST Installation Guide" [11] provides source listings and aids the user when installing the system on his (or her) own computer. Portions of this thesis have been published or presented at conferences. They are listed in references [62-65].

In summary, this thesis presents a method of simulating semiconductor device transport using modern finite-element techniques. The method is based on minimizing an energy functional while simultaneously applying a Newton-Raphson iteration to handle medium and source nonlinearities. Although many improvements are still possible, the resulting CAD package (MANIFEST) incorporates many state-of-the-art features not found in other design tools.

Chapter II

SEMICONDUCTOR-DEVICE PHYSICS

Before attempting to solve the generalized semiconductor transport equations, a brief review of the associated device physics is in order. As the information in this chapter is presented in a rather cursory fashion, readers are encouraged to consult the references for a more detailed discussion. As a general comment, much of this chapter is adapted from Kurata [9, Chapter 2] (who in turn appears to have relied heavily on Smith, Sze, and Adler [12, 13, 14]).

2.1 CARRIER CONCENTRATIONS

A pure, crystalline semiconductor has an intrinsic carrier density given by:

$$n_i = \frac{4\pi(4m_{de}m_{dh})^{3/4}}{h^3} \int_{E_c}^{\infty} \frac{(E - E_c)^{1/2}\, dE}{\exp[(E - E_F)/kT] + 1} \qquad (2.1)$$

Assuming the validity of Boltzmann statistics and an equal effective mass for electrons and holes, (2.1) reduces to

$$n_i = 2\left(\frac{2\pi m^* kT}{h^2}\right)^{3/2} \exp\left(-\frac{E_g}{2kT}\right) \qquad (2.2)$$

for a bandgap energy of E_g. For each electron created in such a crystal, a corresponding hole must also appear since the only means of populating conduction-band states is by emptying valence-band states. Thus the intrinsic hole density must also equal n_i. For silicon, n_i evaluates to 1.5×10^{10} cm-3 at 300K.

The conductivity

$$\sigma = q\mu_n n + q\mu_p p \tag{2.3}$$

with $n=p=n_i$, electron mobility μ_n = 1500 cm2 sec-1 v-1, and hole mobility μ_p = 450 cm2 sec-1 v-1, is seen to be only 4.7×10^{-6} Ohm cm-1. This implies that pure (intrinsic) silicon has a very low conductivity at room temperature.

If a small quantity of appropriate impurities are introduced into the crystal, the energy-band structure is perturbed and an extrinsic conduction property may be observed. Dopants of valence five (such as As, P, or Sb) create energy levels close to the conduction band. Thus they are able to donate free electrons to the crystal structure and produce an n-type semiconductor. Conversely, dopants of valence three (such as Ga, B, or Al) accept valence electrons and give rise to p-type semiconductors. Near room temperature, $n=N_d$ for n-type materials and $p=N_a$ for p-type materials.

In thermal equilibrium, the product of electron and hole concentrations is independent of doping and equal to n_i^2:

$$pn = n_i^2 \tag{2.4}$$

For contemporary semiconductor devices, the donor and acceptor concentrations can be controlled over a range of 10^{13} to 10^{21} cm-3.

2.2 CARRIER MOBILITIES

Free electrons and holes are the important charge carriers whose transport determines the current through the semiconductor device. One of the basic quantities related to carrier transport is mobility. Assume, for the moment, that a constant potential is applied across a uniformly doped semiconductor which is also isotropic (e.g. silicon). If we average all microscopic scattering effects over sufficently long distances and periods of time, we observe a net carrier drift either with or against the applied electric field (depending on whether holes or electrons are being considered). That is

$$v_n = -\mu_n E \quad \text{and} \quad v_p = \mu_p E \tag{2.5}$$

where E is the electric field, μ_n and μ_p are the electron and hole mobilities, and v_n and v_p are their corresponding drift velocities. In general, carrier mobility is not constant; rather it depends upon the host material, its impurity concentration, and the field strength.

If the drift velocity depends upon the direction of the electric field, the medium is said to be anisotropic. This can happen if the crystal structure of the semiconductor un-

der study contains certain, inherent asymmetries (e.g. Wurtzite structures, which occur in AlN, GaN, and ZnSe) [15]. In this case, the scalar mobilities of (2.5) must be replaced by an appropriate second or third rank dyadic tensor. More will be said about anisotropic materials in Section 2.7.

In general, an increase in impurity concentration, as well as in field strength, enhances the scattering rate, decreasing mobilities in the following manner [9, p. 11]:

$$\mu = \left[\frac{\mu_{max} - \mu_{min}}{1 + \left(\frac{|N|}{N_{ref}} \right)^{\alpha} + f} + \mu_{min} \right] \cdot \frac{1}{\left[1 + \left(\frac{E}{E_c} \right)^{\beta} \right]^{1/\beta}} \qquad (2.6)$$

The constant values are tabulated in Appendix B and the factor f

$$f = \left[\frac{(pn)^{1/2}}{2.04\ N_{ref}} \right]^{\alpha} \qquad (2.7)$$

takes into account carrier-to-carrier scattering at high injection levels. Note that f should be set to zero under low to moderate injection levels.

2.3 CURRENT-TRANSPORT EQUATIONS

If the carrier density is spatially nonuniform, a diffusion current occurs of magnitude proportional to the density gradient; that is

$$\vec{J}_{n,diff} = qD_n \nabla n \quad \text{and} \quad \vec{J}_{p,diff} = -qD_p \nabla p \tag{2.8}$$

where D_n and D_p denote diffusion constants for electrons and holes. In addition, the drift current occurs such that its magnitude is proportional to the field and the respective carrier density:

$$\vec{J}_{n,drift} = q\mu_n n\vec{E} \quad \text{and} \quad \vec{J}_{p,drift} = q\mu_p p\vec{E} \text{ with } \vec{E} = -\nabla\phi_s \tag{2.9}$$

The total conduction current is given by the sum of the diffusion and drift components; thus:

$$\vec{J}_n = qD_n \nabla n - q\mu_n n \nabla\phi_s \tag{2.10}$$

$$\vec{J}_p = -qD_p \nabla p - q\mu_p \nabla\phi_s \tag{2.11}$$

Using the Einstein relationships

$$D_n = \frac{kT}{q}\mu_n \tag{2.12}$$

$$D_p = \frac{kT}{q}\mu_p \tag{2.13}$$

and defining the quasi-Fermi levels ϕ_n and ϕ_p such that

$$n = n_i \exp\left[\frac{q}{kT}(\phi_s - \phi_n)\right] \tag{2.14}$$

$$p = n_i \exp\left[\frac{q}{kT}(\phi_p - \phi_s)\right] \tag{2.15}$$

the conduction currents can be written as

$$\vec{J}_n = -q\mu_n n \nabla\phi_n \tag{2.16}$$

$$\vec{J}_p = -q\mu_p p \nabla\phi_p \tag{2.17}$$

2.4 CONTINUITY EQUATIONS

The continuity equations, which hold separately for electrons and holes, are a statement of the conservation of charge within a semiconductor. That is

$$\frac{\partial n}{\partial t} = \frac{1}{q} \nabla \cdot \vec{J}_n + G_n - R_n \tag{2.18}$$

$$\frac{\partial p}{\partial t} = -\frac{1}{q} \nabla \cdot \vec{J}_p + G_p - R_p \tag{2.19}$$

where G_n, G_p are the generation rates for electrons and holes; and R_n, R_p are their respective recombination rates.

Shockley-Read-Hall (SRH) statistics constitute the most common model of carrier recombination (through defects in semiconductors with indirect bandgaps, such as silicon) used for device modelling. Written for the case of single-ener-

gy-level recombination centers

$$R = R_n = R_p = \frac{pn - n_i^2}{\tau_n(n + n_1) + \tau_p(p + p_1)} \tag{2.20}$$

where

$$n_1 = n_i \exp\left(\frac{E_t - E_{Fi}}{kT}\right) \tag{2.21}$$

$$p_1 = n_i \exp\left(-\frac{E_t - E_{Fi}}{kT}\right) \tag{2.22}$$

The electron and hole minority-carrier lifetimes, τ_n and τ_p, can be written under low-injection conditions, as

$$\tau_p = \frac{1}{\sigma_p v_{th} N_t} \tag{2.23}$$

$$\tau_n = \frac{1}{\sigma_n v_{th} N_t} \tag{2.24}$$

where σ_n and σ_p are their respective capture cross-sections, v_{th} is the thermal velocity of free carriers, and N_t is the volume density of the trapping centers.

Under certain conditions, the excess carrier densities may be very large and Auger recombination becomes important. In this process, an electron-hole pair can vanish without the aid of a trapping center. The simplest expression de-

scribing this phenomenon is

$$R_{Aug} = r(n^2p + p^2n) \tag{2.25}$$

with $r=2x10^{-31}$ cm6 s-1 for silicon.

Aside from conditions of optical illumination, where one can set $G_n=G_p=G$, the most important carrier generation process is impact ionization. In high electric fields, carriers traveling through the semiconductor crystal gain sufficient energy to impact ionize the bonds, producing electron-hole pairs. Generation by impact ionization [9, p. 14] is given by

$$G = \frac{1}{q}\left(\alpha_n|\vec{J}_n| + \alpha_p|\vec{J}_p|\right) \tag{2.26}$$

with ionization rates α_n, α_p of

$$\alpha_n = A_n \exp\left[-\left(\frac{b_n}{|\vec{E}|}\right)\right] \tag{2.27}$$

$$\alpha_p = A_p \exp\left[-\left(\frac{b_p}{|\vec{E}|}\right)\right] \tag{2.28}$$

Appropriate constants for equations (2.27) and (2.28) are tabulated in Appendix B.

2.5 POISSON'S EQUATION

The relation between the space-charge density and the electrostatic potential is described by Poisson's equation:

$$\nabla \cdot (\bar{\bar{\varepsilon}} \nabla \phi_s) = -q(N_d - N_a + p - n) \tag{2.29}$$

Generally, the permittivity is an inhomogeneous, anisotropic tensor; but for most elemental semiconductors (e.g. Si, Ge) $\bar{\bar{\varepsilon}}$ is often taken to be a constant scalar. The spatial distributions of the impurity concentrations N_a and N_d are referred to as the doping profile:

$$N_{dope} = N_d - N_a \tag{2.30}$$

Ultimately, the fundamental behavior of any given device is determined explicitly by the doping profile and the appropriate boundary conditions.

2.6 BOUNDARY CONDITIONS

In order to fully define deterministic problems relating to Poisson's equation, the appropriate boundary conditions must be specified. These include the Dirichlet,

$$\phi\Big|_s = g(s) \tag{2.31}$$

Neumann,

$$\hat{n} \cdot \bar{\bar{\varepsilon}} \nabla \phi\Big|_s = h(s) \tag{2.32}$$

and mixed

$$\hat{n} \cdot \overline{\overline{\varepsilon}} \nabla\phi \Big|_s + \overline{\overline{\sigma}} \phi \Big|_s = h(s) \tag{2.33}$$

boundary conditions. Note that the Neumann boundary is just a special case of the mixed condition. In standard semiconductor problems, the mixed boundary seems to have little direct application.

Similar to the Neumann boundary, is the (interior) interface condition

$$\hat{n} \cdot (\overline{\overline{\varepsilon}}_1 \nabla\phi - \overline{\overline{\varepsilon}}_2 \nabla\phi) \Big|_i = Q(i) \tag{2.34}$$

which relates the change in normal flux across a disjoint interface to the surface charge on that interface. The primary motivation for including such a condition is to model semiconductor devices with interface-controlled transport mechanisms (e.g. Schottky barriers, MOS devices, or grain-boundary behaviour in polycrystalline materials).

2.7 ANISOTROPIC MATERIALS

It is well known that flux density[2] and potential gradients are related through a proportionality constant. Let $\overline{\overline{\varepsilon}}$ describe the material properties associated with the region of interest. It shall be represented as a dyadic tensor. If $\overline{\overline{\varepsilon}}$ can be reduced to a positive, diagonal matrix $\overline{\overline{\varepsilon}}'$, the

[2] In the case of Poisson's equation, the flux in question is the ELECTRIC FLUX associated with the electric displacement vector D. For the current continuity equations, the flux is the PARTIAL CARRIER CURRENTS J_n and J_p.

medium is said to be orthotropic. Physically, each component $\overline{\overline{\varepsilon}}'$ represents a quantity (such as conductivity or permittivity) relating field strength to flux density along the local principal axis of that medium. As the principal axis may change direction throughout the region of interest, (e.g. due to grain-reorientation in a polycrystalline semiconductor), a unitary matrix T can be defined which relates the local coordinate system to the physical coordinate system. The principal-axis transformation [16, p. 138]

$$\overline{\overline{\varepsilon}} = T^{-1}\,\overline{\overline{\varepsilon}}'\,T = \begin{bmatrix} \varepsilon_{xx} & \varepsilon_{xy} & \varepsilon_{xz} \\ \varepsilon_{yx} & \varepsilon_{yy} & \varepsilon_{yz} \\ \varepsilon_{zx} & \varepsilon_{zy} & \varepsilon_{zz} \end{bmatrix} \tag{2.35}$$

$$\begin{aligned} &\varepsilon_{xx}\,\hat{u}_x\hat{u}_x + \varepsilon_{xy}\,\hat{u}_x\hat{u}_y + \varepsilon_{xz}\,\hat{u}_x\hat{u}_z \\ = &+ \varepsilon_{yx}\,\hat{u}_y\hat{u}_x + \varepsilon_{yy}\,\hat{u}_y\hat{u}_y + \varepsilon_{yz}\,\hat{u}_y\hat{u}_z \\ &+ \varepsilon_{zx}\,\hat{u}_z\hat{u}_x + \varepsilon_{zy}\,\hat{u}_z\hat{u}_y + \varepsilon_{zz}\,\hat{u}_z\hat{u}_z \end{aligned}$$

then generates the symmetric tensor $\overline{\overline{\varepsilon}}$.

In general, the components of (2.35) are easily computed if one knows ε'_{xx}, ε'_{yy}, ε'_{zz} and the relation between the local and reference coordinate systems. For inhomogeneous media, the components of $\overline{\overline{\varepsilon}}$ will be functions of position. By simple expansion, one can verify

$$\vec{u} \cdot (\overline{\overline{\varepsilon}} \cdot \vec{u}) = (\vec{u} \cdot \overline{\overline{\varepsilon}}) \cdot \vec{u} = \vec{u} \cdot \overline{\overline{\varepsilon}} \cdot \vec{u} \tag{2.36}$$

for an arbitrary vector $\vec{u}$. Note that if the medium is isotropic, $\varepsilon_{xx} = \varepsilon_{yy} = \varepsilon_{zz}$ and $\overline{\overline{\varepsilon}}$ reduces to a scalar.

2.8 BASIC DEVICE MODELLING

Collecting the current-transport equations (2.16 and 2.17), the continuity equations (2.18 and 2.19), and Poisson's equation (2.29), leads to a system of three coupled nonlinear Poisson-like[3] equations which must be solved for the electrostatic potential ϕ_s and quasi-Fermi potentials ϕ_n, ϕ_p:

$$\nabla \cdot (\bar{\bar{\varepsilon}} \nabla \phi_s) = -q(p - n + N_{dope}) \tag{2.37}$$

$$\nabla \cdot (\bar{\bar{\mu}}_n n \nabla \phi_n) = \left(G_n - R_n - \frac{\partial n}{\partial t}\right) \tag{2.38}$$

$$\nabla \cdot (\bar{\bar{\mu}}_p p \nabla \phi_p) = -\left(G_p - R_p - \frac{\partial p}{\partial t}\right) \tag{2.39}$$

To ensure the development of a well-posed problem, an appropriate set of boundary/interface conditions must also be specified.

For any given problem, the doping profile $(N_d - N_a)$ specifies the device (e.g. diode, transistor, or thyristor) under investigation. Likewise, the boundaries model the operating conditions of that device. In the simplest sense, Dirichlet boundaries are akin to voltage sources while Neumann boundaries represent current sources. Note that a zero Neumann

[3] Although (2.37, 2.38, and 2.39) each appear to have the form of Poisson's equation, we must remember that the medium and source terms are nonlinear and may assume nearly any characteristic. Hence, for arbitrary mobility and recombination expressions, the associated operators may not be strictly Laplacian.

boundary is equivalent to zero flux crossing that interface. In effect, this is the same as encapsulating the device in a perfect insulator. This fact will be extremely useful to us when the variational method is developed in the next chapter.

2.9 GREEN'S IDENTITIES

Before proceeding with our discussion of variational methods, it will be useful to state Green's theorem in a form suitable for our use.

For arbitrary u and v note the relation:

$$\nabla \cdot u(\bar{\bar{\varepsilon}}\nabla v) = \nabla u \cdot (\bar{\bar{\varepsilon}}\nabla v) + u\nabla \cdot (\bar{\bar{\varepsilon}}\nabla v) \tag{2.40}$$

Integrating and applying the divergence theorem gives

$$\int u(\bar{\bar{\varepsilon}}\nabla v) \cdot \hat{n}\, ds = \int [\nabla u \cdot (\bar{\bar{\varepsilon}}\nabla v) + u\nabla \cdot (\bar{\bar{\varepsilon}}\nabla v)]\, d\Omega \tag{2.41}$$

for Green's first identity.

Now exchange the roles of u and v and subtract the result from (2.41):

$$\int [u(\bar{\bar{\varepsilon}}\nabla v) - v(\bar{\bar{\varepsilon}}\nabla u)] \cdot \hat{n}\, ds$$

$$= \int [\nabla u \cdot (\bar{\bar{\varepsilon}}\nabla v) + u\nabla \cdot (\bar{\bar{\varepsilon}}\nabla v) - \nabla v \cdot (\bar{\bar{\varepsilon}}\nabla u) - v\nabla \cdot (\bar{\bar{\varepsilon}}\nabla u)]\, d\Omega \tag{2.42}$$

In orthotropic media, $\bar{\bar{\varepsilon}} = \bar{\bar{\varepsilon}}^T$ so:

$$\nabla u \cdot (\bar{\bar{\varepsilon}}\nabla v) = \nabla v \cdot (\bar{\bar{\varepsilon}}\nabla u) \tag{2.43}$$

After substituting (2.43) into (2.42) we obtain

$$\int [u(\bar{\bar{\varepsilon}}\nabla v) - v(\bar{\bar{\varepsilon}}\nabla u)] \cdot \hat{n}\, ds$$

$$= \int [u\nabla \cdot (\bar{\bar{\varepsilon}}\nabla v) - v\nabla \cdot (\bar{\bar{\varepsilon}}\nabla u)]\, d\Omega \qquad (2.44)$$

for Green's second identity.

Chapter III

VARIATIONAL PRINCIPLES

The technique used to solve the equations of the preceding chapter involves forming a functional which assumes a minimum (or at least stationary) value when the solution to the problem is substituted. Although several such functionals can be written -- e.g. those based on a least squares approach -- the one chosen here is derived from the principle of minimum free energy.

Provided a given linear operator satisfies a number of conditions, most notably those of self-adjointness and positive-definiteness, one can guarantee stable convergence for the associated numerical processes [7, 8]. In practice, problems which do not fully satisfy these requirements may still work rather well. Experience, to a large degree, indicates what liberties one may take in order to obtain acceptable results.

Unfortunately, the operators associated with semiconductor physics are highly nonlinear. Hence, any guarantee of uniqueness will generally not apply. If, however, some moderate restrictions are placed on the form of the medium, the nonlinearity should not affect the energy minimization principle. The Newton-Raphson algorithm, which will be de-

scribed in the next chapter, solves a nonlinear problem by generating a sequence of simpler, linear problems. Thus, to ensure a legitimate solution to a nonlinear equation, it is sufficient to justify the variational basis of the finite-element algorithm for the linear case only. Those readers with interest in nonlinear magnetostatics should note that much of this chapter was written to follow a parallel development with Chapter III of Ref. [17].

3.1 PHYSICAL BASIS

The solution to many physical problems is often obtained when the system under consideration achieves its minimum potential energy. For example, the magnetostatic fields of common inductors and the electrostatic fields of capacitors are such that their stored energy is minimized. Although it is not always true that potential energy is strictly minimized, these ideas do provide an intuitive basis for the variational approach.

Most common operators associated with these physical problems possess two important properties: they are symmetrical, and they are positive-definite.

The first property is a direct result of the reciprocity between a field's cause and its effect. Often problems associated with truly anisotropic materials do not possess symmetrical operators. A symmetrical differential operator can be shown to be self-adjoint. Additionally, any corre-

sponding inverse operators -- as more than one may exist -- will also be symmetrical [7, p. 29].

The second property is related to the energy content of the field. A system governed by a semi-definite or indefinite operator may be able to change states without additional energy. On the other hand, a system described by a definite operator does require energy to effect such a change. However, this change may occur with an arbitrarily small amount of energy expended over a sufficiently long period of time. In practice, the stricter requirement of being positive-bounded-below (or alternatively negative-bounded-above) may occur. This implies that a minimum amount of energy must be expended in order to achieve a new state. Linear, definite operators -- which are also self-adjoint -- possess a unique inverse [7, pp. 74-75].

Self-Adjoint Operators

For a given operator L, the adjoint operator L_a is defined by

$$\langle Lu,v\rangle = \langle u,L_a v\rangle \tag{3.1}$$

If $L=L_a$, the operator is said to be self-adjoint. Consider the equation

$$Lu = -\nabla \cdot (\bar{\bar{\varepsilon}}\nabla u) \tag{3.2}$$

with the inner product defined as

$$\langle u,v\rangle = \langle v,u\rangle = \int uv \, d\Omega \tag{3.3}$$

Using the first form of Green's identity, one can see:

$$\langle Lu,v\rangle - \langle u,Lv\rangle = \int [u \cdot (\bar{\bar{\varepsilon}}\nabla u) - v \cdot (\bar{\bar{\varepsilon}}\nabla u)] \cdot \hat{n} \, ds \tag{3.4}$$

Clearly, L is self-adjoint provided the surface integral of (3.4) vanishes.

Now consider the following homogeneous boundary conditions for a given scalar field ϕ

$$\phi\Big|_S = 0 \tag{3.5}$$

$$\hat{n} \cdot (\bar{\bar{\varepsilon}}\nabla\phi)\Big|_S = 0 \tag{3.6}$$

$$\hat{n} \cdot (\bar{\bar{\varepsilon}}\nabla\phi)\Big|_S + \sigma\phi\Big|_S = 0 \tag{3.7}$$

which u and v also satisfy. Obviously conditions (3.5) and (3.6), together or individually, imply a vanishing surface integral. With regard to the mixed condition, note that

$$\hat{n} \cdot (\bar{\bar{\varepsilon}}\nabla u) = -\sigma u \tag{3.8}$$

and

$$\hat{n} \cdot (\bar{\bar{\varepsilon}}\nabla v) = -\sigma v \tag{3.9}$$

Substituting (3.8) and (3.9) into (3.4) produces

$$\int [v(\sigma u) - u(\sigma v)]\, ds \tag{3.10}$$

which is identically zero.

Positive-Definite Operators

A symmetric operator L is said to be positive-definite if, for any function u within its domain:

$$\langle Lu,u\rangle \begin{cases} > 0 & u \neq 0 \\ = 0 & u = 0 \end{cases} \tag{3.11}$$

To demonstrate that L is positive-definite, we shall use the second form of Green's identity with $u=\phi$:

$$\int \phi(\bar{\bar{\varepsilon}}\nabla\phi) \cdot \hat{n}\, ds = \int [\nabla\phi \cdot (\bar{\bar{\varepsilon}}\nabla\phi) + \phi\nabla \cdot (\bar{\bar{\varepsilon}}\nabla\phi)]\, d\Omega \tag{3.12}$$

The last term of (3.12) is simply

$$-\langle L\phi,\phi\rangle \tag{3.13}$$

and the left-hand side may be written as

$$\int \phi[\hat{n} \cdot (\bar{\bar{\varepsilon}}\nabla\phi)]\, ds \tag{3.14}$$

thus showing

$$\langle L\phi,\phi\rangle = \int \nabla\phi \cdot (\bar{\bar{\varepsilon}}\nabla\phi)\, d\Omega - \int \phi[\hat{n} \cdot (\bar{\bar{\varepsilon}}\nabla\phi)]\, ds \tag{3.15}$$

For the homogeneous Dirichlet (3.5) and Neumann (3.6) boundary conditions, the surface integral of (3.15) vanish-

es. Under the homogeneous mixed condition (3.7),

$$\hat{n} \cdot (\bar{\bar{\varepsilon}}\nabla\phi)\Big|_S = -\sigma\phi\Big|_S \tag{3.16}$$

and

$$\int \phi[\hat{n} \cdot (\bar{\bar{\varepsilon}}\nabla\phi)]\, ds = -\int \sigma\phi^2\, ds \tag{3.17}$$

thus leading to

$$\langle L\phi,\phi\rangle = \int \nabla\phi \cdot (\bar{\bar{\varepsilon}}\nabla\phi)\, d\Omega + \int \sigma\phi^2\, ds \tag{3.18}$$

which is zero provided ϕ is zero. Let:

$$\vec{E} = -\nabla\phi \tag{3.19}$$

Thus if

$$\vec{E} \cdot (\bar{\bar{\varepsilon}}\vec{E}) > 0 \tag{3.20}$$

and

$$\vec{E} \cdot (\bar{\bar{\varepsilon}}' \vec{E}) > 0 \tag{3.21}$$

both integrands of (3.18) are strictly positive and hence L is positive-definite.

The condition under which (3.20) is true may be discovered by considering when

$$\sigma\phi^2 > 0 \tag{3.22}$$

where $\bar{\bar{\varepsilon}}'$ represents the diagonalized form of $\bar{\bar{\varepsilon}}$. Writing $\vec{E}$ and $\bar{\bar{\varepsilon}}'$ in dyadic notation and performing the required expan-

sion leads to

$$\varepsilon'_{xx}E_x^2 + \varepsilon'_{yy}E_y^2 + \varepsilon'_{zz}E_z^2 > 0 \tag{3.23}$$

As E_x, E_y, and E_z are arbitrary; ε'_{xx}, ε'_{yy}, and ε'_{zz} must all be greater than zero for relation (3.22) to be true. This may be interpreted as a statement that $\overline{\overline{\varepsilon}}$ must have a positive-definite form (i.e. $\overline{\overline{\varepsilon}}'$ has real, positive eigenvalues).

From the above discussion, one can see that both terms of (3.18) are in fact nonnegative. If a suitable $\overline{\overline{\varepsilon}}$ exists, the complete inner product will be positive for any nonzero ϕ. Thus the operator is positive-definite under the stated boundary conditions.

Uniqueness of Solution

A linear, positive-definite operator can have no more than one solution. As proof [7], assume that two solutions (u_1 and u_2) exist and define

$$u = u_1 - u_2 \tag{3.24}$$

as the difference field. Since

$$L(u_1 - u_2) = Lu = 0 \tag{3.25}$$

then

$$< Lu, u > = 0 \tag{3.26}$$

Because L is positive-definite, $\langle Lu,u \rangle$ can vanish only when u is zero. Therefore u_1 must equal u_2 and the solution is proven unique. If L is semi-definite or nonlinear, multiple solutions must be anticipated.

3.2 THE EXTREMUM FORMULATION

As seen earlier, the variational method requires a suitable energy functional. Mikhlin [7, pp. 318-328] provides the required form as a theorem. For simplicity, a real vector space is assumed, but the extension to a generalized Hilbert space is not difficult.

Homogeneous Boundaries

For the deterministic problem,

$$Lu = f \tag{3.27}$$

the functional to be minimized is

$$F = \langle Lu, u \rangle - 2 \langle u, f \rangle \tag{3.28}$$

where f and u are assumed to be real functions (either scalar or vector) and L is a real operator. Let u_0 be the exact solution to (3.27) in which case (3.28) can be rewritten as

$$F = \langle Lu, u \rangle - 2 \langle u, Lu_0 \rangle \tag{3.29}$$

Adding and subtracting $< Lu_0, u_0 >$ from (3.29)

$$\begin{aligned} F &= < Lu, u > - 2 < u, Lu_0 > + < Lu_0, u_0 > - < Lu_0, u_0 > \\ &= < Lu, u > - 2 < Lu_0, u > + < Lu_0, u_0 > - < Lu_0, u_0 > \\ &= < L(u - u_0), u > + < Lu_0, (u_0 - u) > - < L u_0, u_0 > \end{aligned} \tag{3.30}$$

and as the operator is self-adjoint:

$$\begin{aligned} F &= < Lu, (u - u_0) > - < Lu_0, (u - u_0) > - < Lu_0, u_0 > \\ &= < L(u - u_0), (u - u_0) > - < Lu_0, u_0 > \end{aligned} \tag{3.31}$$

Furthermore, if L is also positive-definite, the last term of the functional is positive (provided a nonzero solution exists) and the first term is nonnegative. Thus when $u=u_0$, F assumes its minimum value.

Stationarity of the Functional

Once a functional has been given, we shall seek a stationary point through application of the Rayleigh-Ritz discretization procedure. If u_0 causes the functional to become stationary, we wish to show:

1. That u_0 is a solution to the original operator equation; and
2. The value of the functional is actually at a minimum.

Assume u_0 causes F to be stationary and let η represent an arbitrary function. Thus

$$u = u_0 + \alpha\eta \tag{3.32}$$

is also an arbitrary function for some real number α. Substituting (3.32) into (3.28) and expanding

$$F = \langle Lu_0, u_0 \rangle + \alpha \langle Lu_0, \eta \rangle + \alpha \langle L\eta, u_0 \rangle + \alpha^2 \langle L\eta, \eta \rangle - 2 \langle u_0, f \rangle - 2 \alpha \langle \eta, f \rangle \tag{3.33}$$

while differentiating with respect to α gives:

$$\frac{dF}{d\alpha} = \langle Lu_0, \eta \rangle + \langle L\eta, u_0 \rangle + 2 \alpha \langle L\eta, \eta \rangle - 2 \langle \eta, f \rangle \tag{3.34}$$

By hypothesis, the stationary point of (3.34) occurs when α equals zero so

$$\left.\frac{dF}{d\alpha}\right|_{\alpha = 0} = \langle Lu_0, \eta \rangle + \langle L\eta, u_0 \rangle - 2 \langle \eta, f \rangle = 0 \tag{3.35}$$

and if L is also self-adjoint:

$$\langle Lu_0 - f, \eta \rangle = 0 \tag{3.36}$$

As η is completely arbitrary, (3.36) is satisfied if and only if

$$Lu_0 = f \tag{3.37}$$

identically. In other words, the function u_0 that makes F stationary must be the solution to the original equation.

To show that this solution actually minimizes the functional, we differentiate (3.35) again yielding:

$$\frac{d^2F}{d\alpha^2} = 2 \langle L\eta, \eta \rangle \tag{3.38}$$

If L is positive-definite, equation (3.38) is always nonnegative. Thus the solution occurs at a minimum of F. Similarly, a negative-definite operator will maximize the functional. Note however that multiple solutions must be anticipated if semi-definite or indefinite operators are considered.

Inhomogeneous Boundaries

In order to include the case of inhomogeneous boundary conditions, we shall reformulate the problem to that of an equivalent homogeneous case with additional source terms.

We express the boundary condition as

$$Bu\Big|_s = b(s) \tag{3.39}$$

where B is a linear operator defined along the boundary. We now assume that a function w exists which satisfies (3.39) and define

$$v = u - w \tag{3.40}$$

Note that w is not assumed to be a solution to the differential equation, it need only satisfy the desired boundary conditions.

As B is a linear operator,

$$Bv = Bu - Bw = 0 \tag{3.41}$$

which is equivalent to a homogeneous boundary condition in v. Considering v as the unknown quantity and attempting to solve

$$Lv = f' \tag{3.42}$$

If u_0 is a solution, then

$$V_0 = x_0 - w \tag{3.43}$$

and so

$$Lv_0 = L(u_0 - w) = f - Lw \tag{3.44}$$

At this point, the equivalent source term

$$f' = f - Lw \tag{3.45}$$

is introduced.

Solving

$$Lv = f' \tag{3.46}$$

under homogeneous boundary conditions requires minimization of the functional

$$F = < Lv, v > - 2 < v, f' > \tag{3.47}$$

As v_0 and w are both known, u_0 may then be easily recovered. However, by eliminating v from (3.47) -- through substitution of (3.40) -- it becomes apparent that w need not be found at all.

Finally, substituting (3.40) into (3.47),

$$F = \langle L(u - w), (u - w) \rangle - 2 \langle (u - w), (f - Lw) \rangle$$
$$= \langle Lu, u \rangle - 2 \langle u, f \rangle + \langle u, Lw \rangle - \langle Lu, w \rangle \qquad (3.48)$$
$$+ 2 \langle w, f \rangle - \langle Lw, w \rangle$$

where both f and w are fixed. Although the last two terms of (3.48) influence the value of the functional, they do not affect which uo is needed to achieve minimization. Therefore, a new functional

$$F = \langle Lu, u \rangle - 2 \langle u, f \rangle + \langle u, Lw \rangle - \langle Lu, w \rangle \qquad (3.49)$$

may be defined, the last two terms (to be called F*) being due to the presence of the inhomogeneous boundary conditions.

3.3 BOUNDARY CONDITIONS

Now that the general form of the energy functional has been developed, we shall proceed to derive F explicitly under the boundary conditions of Section 2.6. In addition, it may be desirable to allow the presence of interior sheet charges. Although in theory such sources can exist only on the surface of perfect conductors, they may be useful when modelling various devices or active interfaces (e.g. grain boundaries).

Dirichlet Boundaries

To derive a functional which caters for inhomogeneous Dirichlet boundaries, let B from (3.39) be the identity operator such that

$$\phi\Big|_S = g(s) \tag{3.50}$$

Using the symmetrical form of Green's identity:

$$\langle\phi,L w\rangle - \langle L\phi,w\rangle = \int [w(\bar{\bar{\varepsilon}}\nabla\phi) - \phi(\bar{\bar{\varepsilon}}\nabla w)] \cdot \hat{n}\, ds \tag{3.51}$$

On the surface S, $\phi(s)=w(s)=g(s)$ thus:

$$\langle\phi,L w\rangle - \langle L\phi,w\rangle = \int [g(\bar{\bar{\varepsilon}}\nabla\phi) - g(\bar{\bar{\varepsilon}}\nabla w)] \cdot \hat{n}\, ds \tag{3.52}$$

As the second term on the RHS of (3.52) is not a function of ϕ, it may be dropped from the functional giving

$$F = \langle L\phi,\phi\rangle - 2\langle\phi,\rho\rangle + \int g(\bar{\bar{\varepsilon}}\nabla\phi) \cdot \hat{n}\, ds \tag{3.53}$$

By Green's first identity

$$\int g(\bar{\bar{\varepsilon}}\nabla\phi) \cdot \hat{n}\, ds = \int \nabla g \cdot (\bar{\bar{\varepsilon}}\nabla\phi)\, d\Omega - \langle g,L\phi\rangle \tag{3.54}$$

and substituting (3.54) into (3.53)

$$F = \langle L\phi,\phi\rangle - 2\langle\phi,\rho\rangle + \int \nabla g \cdot (\bar{\bar{\varepsilon}}\nabla\phi)\, d\Omega - \langle g,L\phi\rangle \tag{3.55}$$

Finally, using $\phi=g$ (and remembering that L is self-adjoint)

$$F = \int \nabla\phi \cdot (\bar{\bar{\varepsilon}}\nabla\phi)\, d\Omega - 2\int \phi\rho\, d\Omega \tag{3.56}$$

which will be minimized by the correct potential provided

that all trial functions satisfy the given Dirichlet conditions.

In the course of this treatment, we have extended the operator's domain to include functions which can only be differentiated once [18, p. 15]. The significance of this will become apparent when we wish to generate finite elements using a linear basis.

Mixed and Neumann Boundaries

The general form for the mixed boundary condition is given by

$$\hat{n} \cdot (\bar{\bar{\varepsilon}}\nabla\phi)\Big|_S + \sigma\phi\Big|_S = h(s) \tag{3.57}$$

The last terms of (3.49) are rewritten as

$$\begin{aligned} F^* &= \langle\phi, Lw\rangle - \langle L\phi, w\rangle \\ &= \int [w(\bar{\bar{\varepsilon}}\nabla\phi) - \phi(\bar{\bar{\varepsilon}}\nabla w)] \cdot \hat{n}\, ds \qquad (3.58) \\ &= \int [w(h - \sigma\phi) - \phi(h - \sigma w)]\, ds \end{aligned}$$

which simplifies to

$$F^* = \int (wh - \phi h)\, ds \tag{3.59}$$

As before, the first term of (3.59) may be dropped creating the new functional:

$$F = \langle L\phi, \phi\rangle - 2\langle\phi, \rho\rangle - \int \phi h\, ds \tag{3.60}$$

By Green's second identity

$$\langle L\phi,\phi\rangle = \int \nabla\phi \cdot (\bar{\bar{\varepsilon}}\nabla\phi)\, d\Omega - \int \phi(\bar{\bar{\varepsilon}}\nabla\phi) \cdot \hat{n}\, ds \tag{3.61}$$

and so

$$F = \int \nabla\phi \cdot (\bar{\bar{\varepsilon}}\nabla\phi)\, d\Omega - 2\int \phi\rho\, d\Omega - \int \phi(h - \sigma\phi)\, ds - \int \phi h\, ds \tag{3.62}$$

or

$$F = \int \nabla\phi \cdot (\bar{\bar{\varepsilon}}\nabla\phi)\, d\Omega - 2\int \phi\rho\, d\Omega - 2\int \phi h\, ds + \int \sigma\phi^2\, ds \tag{3.63}$$

Note the similarity between the volume source ρ and the surface source h. Note also the formal similarity between the scalar and dual vector cases [17] (i.e. the curl operator will replace the gradient operator). With a pure Neumann boundary, the last term of the functional would vanish.

3.4 INTERFACE CONDITIONS

There are two well known conditions which must be met at media interfaces:

$$\phi_1\Big|_i = \phi_2\Big|_i \tag{3.64}$$

and

$$\hat{n} \cdot (\vec{D}_1 - \vec{D}_2)\Big|_i = Q(i) \tag{3.65}$$

The finite-element method, which is described in Chapter IV, will automatically enforce (3.64). After demonstrating how to include condition (3.65), we shall show how certain boundary conditions occur naturally without being explicitly specified in the functional.

Interior Sheet Charges

In order to demonstrate how the second interface condition is satisfied, consider Figure 3.1. The total region R is bounded by the outer surface S_0. The boundary on R_1 includes part of S_0 plus all of S_i. A sheet (or "interior surface") charge density Q exists on S_i.

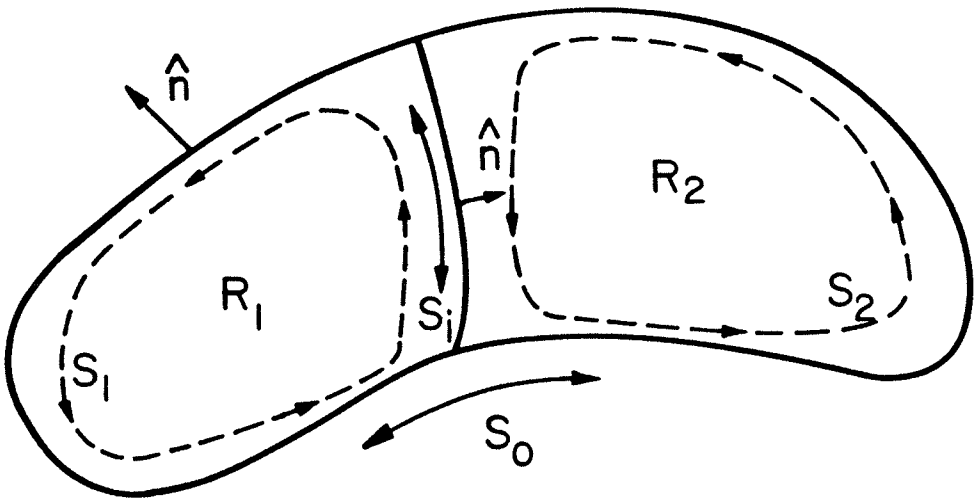

Figure 3.1: Simple Region with Two Elements

To restate the second interface condition,

$$(\hat{n} \cdot \vec{D}_1 - \hat{n} \cdot \vec{D}_2)\Big|_i = Q(i) \tag{3.66}$$

or

$$\hat{n} \cdot \overline{\overline{\varepsilon}}_1 \nabla\phi\Big|_i - \hat{n} \cdot \overline{\overline{\varepsilon}}_2 \nabla\phi\Big|_i = Q(i) \tag{3.67}$$

where we assume a sheet charge density Q exists along the interface. Rewriting F* as

$$\begin{aligned} F^* &= \langle\phi, Lw\rangle - \langle L\phi, w\rangle \\ &= \int [w(\overline{\overline{\varepsilon}}\nabla\phi) - \phi(\overline{\overline{\varepsilon}}\nabla w)] \cdot \hat{n}\, ds \\ &= \int_{S_1} [w(\overline{\overline{\varepsilon}}_1\nabla\phi) - \phi(\overline{\overline{\varepsilon}}_1\nabla w)] \cdot \hat{n}\, ds \\ &\quad - \int_{S_2} [w(\overline{\overline{\varepsilon}}_2\nabla\phi) - \phi(\overline{\overline{\varepsilon}}_2\nabla w)] \cdot \hat{n}\, ds \end{aligned} \tag{3.68}$$

and using (3.67)

$$\langle L\phi, \phi\rangle = \int \nabla\phi \cdot (\overline{\overline{\varepsilon}}\nabla\phi)\, d\Omega - \int \phi(\overline{\overline{\varepsilon}}\nabla\phi) \cdot \hat{n}\, ds \tag{3.69}$$

the surface integral may be split between each region as

$$\begin{aligned} &\int \phi(\overline{\overline{\varepsilon}}\nabla\phi) \cdot \hat{n}\, ds \\ &= \int_{S_1} \phi(\overline{\overline{\varepsilon}}_1\nabla\phi) \cdot \hat{n}\, ds - \int_{S_2} \phi(\overline{\overline{\varepsilon}}_2\nabla\phi) \cdot \hat{n}\, ds \end{aligned} \tag{3.70}$$

where the minus sign(s) result from the choice of an inward normal within R_2. Substituting (3.69) and (3.70) into

(3.49)

$$F = \int \nabla\phi \cdot (\bar{\bar{\varepsilon}}\nabla\phi)\, d\Omega - 2\int \phi\rho\, d\Omega$$
$$+ \int_{S_1} [w(\bar{\bar{\varepsilon}}_1\nabla\phi) - \phi(\bar{\bar{\varepsilon}}_1\nabla w)] \cdot \hat{n} - \phi(\bar{\bar{\varepsilon}}_1\nabla\phi) \cdot \hat{n}\, ds \qquad (3.71)$$
$$+ \int_{S_2} -[w(\bar{\bar{\varepsilon}}_2\nabla\phi) - \phi(\bar{\bar{\varepsilon}}_2\nabla w)] \cdot \hat{n} + \phi(\bar{\bar{\varepsilon}}_2\nabla\phi) \cdot \hat{n}\, ds$$

and applying the interface condition (3.67) gives

$$F = \int \nabla\phi \cdot (\bar{\bar{\varepsilon}}\nabla\phi)\, d\Omega - 2\int \phi\rho\, d\Omega$$
$$- 2\int_{S_i} \phi Q\, ds + \int_{S_i} wQ\, ds \qquad (3.72)$$

where the surface integrals are now taken over the intersection of S_1 and S_2. As the last term is not a function of ϕ, it may be dropped giving

$$F = \int \nabla\phi \cdot (\bar{\bar{\varepsilon}}\nabla\phi)\, d\Omega - 2\int \phi\rho\, d\Omega - 2\int_{S_i} \phi Q\, ds \qquad (3.73)$$

as the required functional.

Collecting common terms from (3.56), (3.63) and (3.73) leads to a functional which will allow for inhomogeneous Dirichlet, Neumann and mixed boundaries as well as interior sheet charges.

Finite-element discretization of the field will lead to a matrix equation of the form

$$S\underline{\phi} = \underline{b} \qquad (3.74)$$

where S is associated the Laplacian operator, $\underline{\phi}$ is the discretized potential, and $\underline{b}$ is a column vector due to source terms. The matrix operator S is positive-definite under all valid boundary conditions. In summary, the final form of the functional is:

$$F = \int [\nabla\phi \cdot (\bar{\bar{\varepsilon}}\nabla\phi) - 2\phi\rho]\, d\Omega + \int_{S_o} (\sigma\phi^2 - 2h\phi)\, ds - 2\int_{S_i} \phi Q\, ds \tag{3.75}$$

3.5 NATURAL BOUNDARY AND INTERFACE CONDITIONS

Although the functional of (3.75) was derived from a number of proven variational principles, there is (as yet) no guarantee that the function which makes F stationary is the actual solution to the original physical problem. By writing, and subsequently minimizing, the related Euler equations, we shall see that all required boundary and interface conditions are satisfied naturally by the variational process.

Assume a trial function of the form

$$\phi = \phi_o + \alpha\eta \tag{3.76}$$

where α is a number and η is an arbitrary function. For the moment, ϕ_0 and η can be taken as functions that are discon-

tinuous across the element boundary S_i. By hypothesis,

$$\left.\frac{\partial F}{\partial \alpha}\right|_{\alpha=o} = 0 \tag{3.77}$$

Substituting (3.76) into (3.75), differentiating with respect to α, evaluating at $\alpha=0$, and equating the result to zero gives:

$$\begin{aligned}&\int [\nabla\eta \cdot (\bar{\bar{\varepsilon}}\nabla\phi_o) - \eta\rho]\, d\Omega \\ &+ \int_{S_o} \eta(\sigma\phi_o - h)\, ds - \int_{S_i} \eta Q\, ds = 0\end{aligned} \tag{3.78}$$

To avoid including the algebra required to obtain this result, readers are referred to Refs. [8, pp. 6.22 - 6.25] and Appendix A of [17] for details on the treatment of similar problems.

Now consider the compound region of Figure 3.1. For clarity, two elements (R_1 and R_2) form the total region R. Green's identity, written for each region R_n, becomes:

$$\begin{aligned}\sum_{n=1}^{2}\int_{S_n} \eta(\bar{\bar{\varepsilon}}\nabla\phi_o) \cdot \hat{n}\, ds &= \sum_{n=1}^{2} \int_{R_n} \nabla\eta \cdot (\bar{\bar{\varepsilon}}\nabla\phi_o)\, d\Omega \\ &+ \sum_{n=1}^{2} \int_{R_n} \eta\nabla \cdot (\bar{\bar{\varepsilon}}\phi_o)\, d\Omega\end{aligned} \tag{3.79}$$

Note that η will vanish wherever a Dirichlet boundary ex-

ists. Substituting (3.79) into (3.78) produces:

$$\sum_{n=1}^{2} \int_{R_n} \eta_n[-\nabla \cdot (\bar{\bar{\varepsilon}}_n \nabla\phi_o) - \rho]\, d\Omega$$

$$+ \sum_{n=1}^{2} \int_{S_o} \eta_n[(\bar{\bar{\varepsilon}}_n \nabla\phi_o) \cdot \hat{n} + \sigma\phi_o - h]\, ds \qquad (3.80)$$

$$+ \sum_{n=1}^{2} \int_{S_n} \eta_n(\bar{\bar{\varepsilon}}_n \nabla\phi_o) \cdot \hat{n}\, ds$$

$$+ \int_{S_i} \eta Q\, ds = 0$$

Now examine the third term of (3.80). Observing that S_n includes part of S_0 plus S_i:

$$\sum_{n=1}^{2} \int_{S_n} \eta_n(\bar{\bar{\varepsilon}}_n \nabla\phi_o) \cdot \hat{n}\, ds \qquad (3.81)$$

$$= \int_{S_1} \eta_1(\bar{\bar{\varepsilon}}_1 \nabla\phi_o) \cdot \hat{n}\, ds - \int_{S_2} \eta_2(\bar{\bar{\varepsilon}}_2 \nabla\phi_o) \cdot \hat{n}\, ds$$

The negative sign on the last term of (3.81) is due to the choice of an inward normal for region two.

If continuity of ϕ is enforced across the boundary (and certainly within individual elements)

$$\eta_1(s_i) = \eta_2(s_i) = \eta \qquad (3.82)$$

so (3.81) implies

$$\int \eta[-\nabla \cdot (\bar{\bar{\varepsilon}}\nabla\phi_o) - \rho]\, d\Omega + \int_{S_o} \eta[(\bar{\bar{\varepsilon}}\nabla\phi_o) \cdot \hat{n} + \sigma\phi_o - h]\, ds + \int_{S_i} \eta[\hat{n} \cdot (\bar{\bar{\varepsilon}}_1\nabla\phi_o - \bar{\bar{\varepsilon}}_2\nabla\phi_o) - Q]\, ds = 0 \tag{3.83}$$

As η is completely arbitrary, it is apparent that

$$-\nabla \cdot (\bar{\bar{\varepsilon}}\nabla\phi_o) = \rho \tag{3.84}$$

$$\hat{n} \cdot (\bar{\bar{\varepsilon}}\nabla\phi_o) + \sigma\phi_o = h \tag{3.85}$$

and

$$\hat{n} \cdot (\bar{\bar{\varepsilon}}_1\nabla\phi_o) - \hat{n} \cdot (\bar{\bar{\varepsilon}}_2\nabla\phi_o) = Q \tag{3.86}$$

must all be true when the functional is stationary.

In summary, equations (3.84) through (3.86) verify that the original problem, along with all necessary boundary conditions, have been satisfied. In addition, if the surface charge density h and surface permittivity σ were not included in the functional, the natural Neumann boundary condition becomes

$$\hat{n} \cdot (\bar{\bar{\varepsilon}}\nabla\phi_o) = \vec{D}_n = 0 \tag{3.87}$$

Similarly, the well known homogeneous interface condition

$$\vec{D}_{n1} = \vec{D}_{n2} \tag{3.88}$$

also occurs naturally.

Chapter IV

THE FINITE-ELEMENT METHOD

Having formed an energy functional for use with the Laplacian operator, we shall now discretize the problem's region by the Rayleigh-Ritz technique. In a simple linear problem, this would lead to a set of linear equations that must be solved for a vector of node potentials:

$$S\underline{\phi} = \underline{b} \tag{4.1}$$

The total field would then be given by interpolating those nodes using the basis functions chosen during the original discretization process.

When considering the semiconductor transport equations, an initial guess to the true solution -- in terms of the electrostatic and quasi-Fermi potentials -- is used as the starting estimate for a Newton-Raphson iteration scheme. Using that guess, a matrix equation is formed and solved for a vector of displacement potentials. As the iterations proceed, the displacements approach zero and the process terminates. As both the media and sources can be functions of potential, the matrix equation must be re-evaluated on each iteration.

4.1 VARIATIONAL FORMULATION

Consider the operator equation

$$L\phi = -\nabla \cdot (\bar{\bar{\varepsilon}}\nabla\phi) = \rho \tag{4.2}$$

where, for the moment, L is assumed to be linear, self-adjoint, and positive-definite. The solution to (4.2) can be obtained by minimizing the functional

$$F = \langle L\phi,\phi\rangle - 2\langle\phi,\rho\rangle \tag{4.3}$$

Through the use of Green's theorem, (4.3) becomes

$$F = \int (\nabla\phi) \cdot \bar{\bar{\varepsilon}}(\nabla\phi)\, d\Omega - 2\int \phi\rho\, d\Omega \tag{4.4}$$

As stated, (4.3) is valid only under the Dirichlet

$$\phi\Big|_S = g(s) \tag{4.5}$$

and homogeneous Neumann

$$\hat{n} \cdot (\bar{\bar{\varepsilon}}\nabla\phi)\Big|_S = 0 \tag{4.6}$$

boundary conditions but the extension to the case of general boundaries is straightforward. Discretizing ϕ by

$$\phi = \underline{\alpha}^T\underline{\phi} = \underline{\phi}^T\underline{\alpha} \tag{4.7}$$

and substituting (4.7) into (4.4) while enforcing

$$\frac{\partial F}{\partial \underline{\alpha}} = \underline{0} \tag{4.8}$$

results in the linear system (4.1) where

$$S = \int (\nabla \underline{\alpha}) \cdot \overline{\overline{\varepsilon}} (\nabla \underline{\alpha}^T) \, d\Omega \tag{4.9}$$

and

$$\underline{b} = \int \underline{\alpha} \rho \, d\Omega \tag{4.10}$$

The above scheme describes a purely variational approach for some arbitrary basis functions $\underline{\alpha}$. By choosing $\underline{\alpha}$ such that only small, piecewise continuous regions of space are covered, we obtain what is known as the finite-element method.

4.2 MATRIX GENERATION

Assuming implied summation over repeated subscripts, (4.1) may be rewritten as

$$\sum_j S_{ij} \phi_j = S_{ij} \phi_j = b_i \tag{4.11}$$

The system matrix is given by

$$S_{ij} = \int (\nabla \alpha_i) \cdot \overline{\overline{\varepsilon}} (\nabla \alpha_j) \, d\Omega \tag{4.12}$$

and the right-hand side by

$$b_i = \int \alpha_i \rho \, d\Omega \tag{4.13}$$

Modelling the medium by the same basis used for the poten-

tial allows $\overline{\overline{\varepsilon}}$ to be expressed as

$$\overline{\overline{\varepsilon}} = \overline{\overline{\alpha}}^{T} \underline{\varepsilon} \tag{4.14}$$

Rewriting (4.12) as

$$S_{ij} = \int \vec{\beta}_i \cdot \overline{\overline{\varepsilon}} \vec{\beta}_j \, d\Omega \tag{4.15}$$

with the vector $\vec{\beta}$ representing the gradient of the scalar shape functions, substituting (4.14), and factoring out $\underline{\varepsilon}$ yields

$$S_{ij} = \int \vec{\beta}_i \cdot \overline{\overline{\alpha}}^{T} \vec{\beta}_j \, d\Omega \tag{4.16}$$

Expanding the vectors into equivalent matrices

$$S^{*}_{ijk} = \int (\nabla\alpha_i) \cdot \overline{\overline{\alpha}}_k (\nabla\alpha_j) \, d\Omega \tag{4.17}$$

and therefore

$$S_{ij} = S^{*}_{ijk} \varepsilon_k \tag{4.18}$$

Similarly, the source terms of (4.13) may be factored as

$$b_i = B_{ij} \rho_j \tag{4.19}$$

where

$$B_{ij} = \int \alpha_i \alpha_j \, d\Omega \tag{4.20}$$

It is important to observe that matrices S* and B are dependent only on the choice of $\underline{\alpha}$ and not on medium or source characteristics. Other terms of the functional, such as

those describing the Neumann and mixed boundaries, are factored into matrix products in a similar manner. In all cases, terms involving sources will appear on the right-hand side of (4.1) while terms involving media migrate into the S matrix.

Until now, little was said about the form of the α's. Each element represents a single, independent component of the basis used to expand the potential, source, and medium. In a purely variational context, one might utilize an (even) Fourier series so that $\alpha_n=\cos(nx)$ would be an appropriate choice.

In the finite-element method, the interpolation functions are defined over localized domains. These "shape functions" are usually built from polynomic terms (i.e. Lagrangian or Hermitian forms) but other, related structures exist [19, 20, 21].

For development of the MANIFEST system, a combination of Lagrangian and Serendipity[4] elements were used. In one-dimensional calculations, both linear and quadratic Lagrangian elements are available. In two dimensions, quasi-linear Lagrange and the eight-node Serendipity element are employed. During initial development, a nine-node, bi-quadratic Lagrange element was tested but it proved less reliable (tend-

---

[4] Serendipity elements are named after the Three Princes of Serendip who were famous for their chance discoveries. Unlike Lagrange or Hermitian elements, which use their corresponding polynomials as a basis, Serendipity elements were developed by accident [22, p. 89].

ing to generate spurious oscillations) than the Serendipity form. At present, the three-dimensional version of MANIFEST only implements a quasi-linear Lagrange element.

As a general comment, the author feels that element structures of degree greater than two are not cost effective for this kind of simulation. Spline-like basis functions have been studied by others [23, 24] but their complexity and cost seems to outweigh any advantages gained. In Chapter III, only continuity of potential was assumed in deriving the functionals. In some cases, most notably when a physical discontinuity of field exists, higher-order continuity may actually hinder the variational process by restricting the set of trial functions available for energy minimization.

The node-numbering scheme displayed in Figure 4.1 leads to the scalar shape functions listed in Table 4.1. As all shape functions are regular polynomials, the integrals of (4.18) and (4.20) can be evaluated via a Gauss-quadrature scheme [25]. Three, nine, and eight gauss-points are used in one, two and three dimensions, respectively.

In addition to using the same basis functions for modelling the potential, media, and sources, the shape of each element can be modified by defining a simple coordinate transformation between global space (i.e. X, Y) and local space (i.e. ξ, η). For a given element, the mapping is giv-

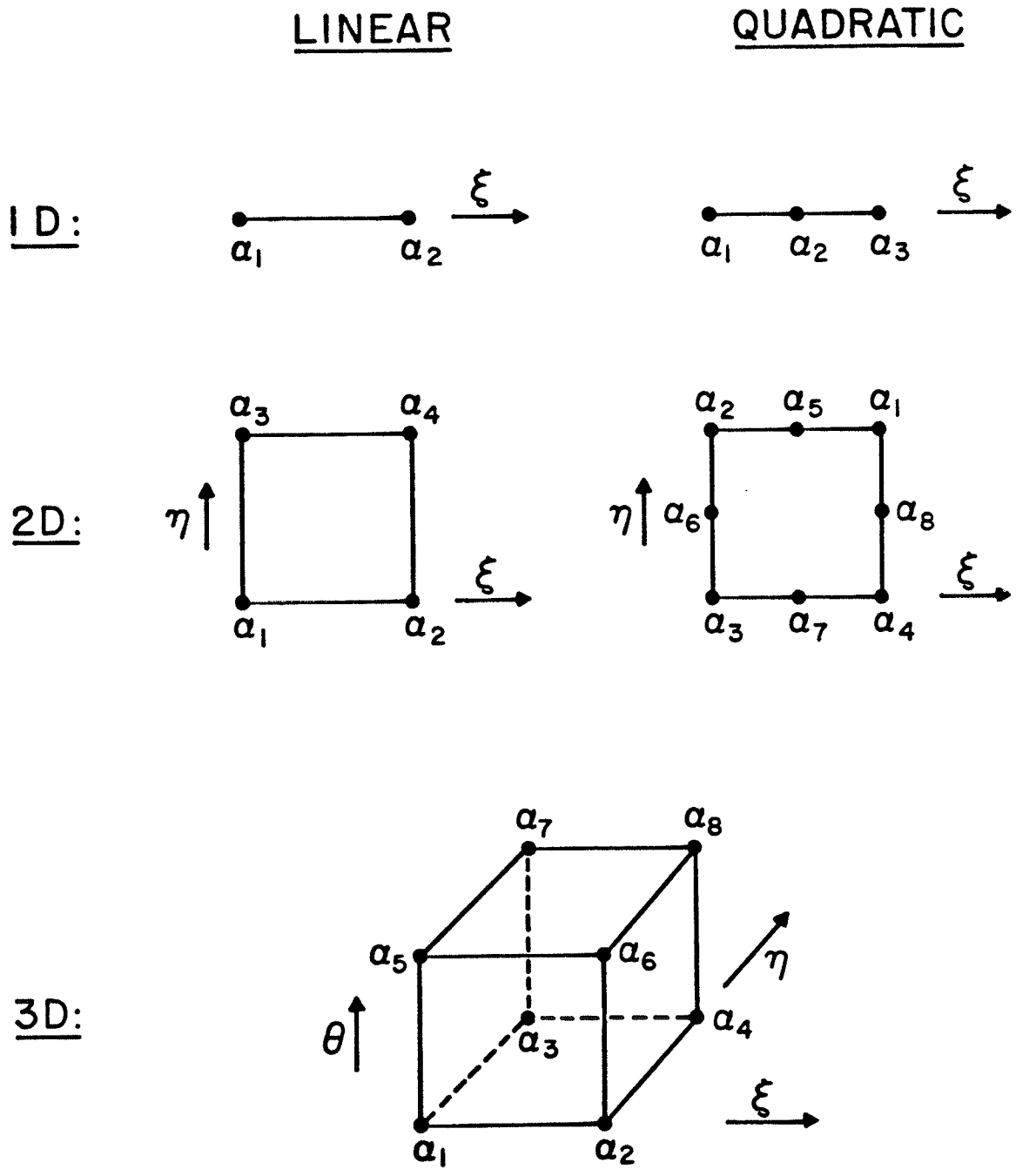

Figure 4.1: Local Node-Numbering Scheme

TABLE 4.1

Scalar Shape Functions

(local coordinates)

1D:	$\alpha_1 = (1 - \xi)$	$\alpha_1 = 2\xi^2 - 3\xi + 1$
[0,1]	$\alpha_2 = (\xi)$	$\alpha_2 = 4(\xi - \xi^2)$
		$\alpha_3 = 2\xi^2 - \xi$

2D:	$\alpha_1 = (1 - \xi)(1 - \eta)$	$\alpha_1 = \frac{1}{4}(1 + \xi)(1 + \eta) - \frac{1}{2}\alpha_5 - \frac{1}{2}\alpha_8$
	$\alpha_2 = (\xi)(1 - \eta)$	$\alpha_2 = \frac{1}{4}(1 - \xi)(1 + \eta) - \frac{1}{2}\alpha_5 - \frac{1}{2}\alpha_6$
	$\alpha_3 = (1 - \xi)(\eta)$	$\alpha_3 = \frac{1}{4}(1 - \xi)(1 - \eta) - \frac{1}{2}\alpha_6 - \frac{1}{2}\alpha_7$
	$\alpha_4 = (\xi)(\eta)$	$\alpha_4 = \frac{1}{4}(1 + \xi)(1 - \eta) - \frac{1}{2}\alpha_7 - \frac{1}{2}\alpha_8$
		$\alpha_5 = \frac{1}{2}(1 - \xi^2)(1 + \eta)$
		$\alpha_6 = \frac{1}{2}(1 - \eta^2)(1 - \xi)$
		$\alpha_7 = \frac{1}{2}(1 - \xi^2)(1 - \eta)$
		$\alpha_8 = \frac{1}{2}(1 - \eta^2)(1 + \xi)$
	[0,1]	[-1,1]

3D:	$\alpha_1 = (1 - \xi)(1 - \eta)(1 - \theta)$	$\alpha_5 = (1 - \xi)(1 - \eta)(\theta)$
[0,1]	$\alpha_2 = (\xi)(1 - \eta)(1 - \theta)$	$\alpha_6 = (\xi)(1 - \eta)(\theta)$
	$\alpha_3 = (1 - \xi)(\eta)(1 - \theta)$	$\alpha_7 = (1 - \xi)(\eta)(\theta)$
	$\alpha_4 = (\xi)(\eta)(1 - \theta)$	$\alpha_8 = (\xi)(\eta)(\theta)$

en by

$$x = \underline{\alpha}^T \underline{x} = \underline{x}^T \underline{\alpha} \tag{4.21}$$

$$y = \underline{\alpha}^T \underline{y} = \underline{y}^T \underline{\alpha} \tag{4.22}$$

The required integrations are now performed over local space only. Note that a (geometry-dependent) Jacobian will appear inside all integrands. If the same shape functions are chosen to model the region as the field, the transformation is said to be isoparametric. Other schemes may be used to over or underdefine the element's geometry, but unless one has specific knowledge of the problems to be solved, the above technique seems to be most common. References [8, 19] describe the appropriate transformation algorithms in detail.

4.3 THE NEWTON-RAPHSON ALGORITHM

If we now discard the assumption of linearity, equation (4.2) can still be solved by means of the Newton-Raphson-Kantorovitch[5] algorithm. Assuming $\overline{\overline{\varepsilon}}$ and ρ can be written as functions of the potential, the residual vector $\underline{R}$ is defined as

$$\underline{R} = S\underline{\phi} - \underline{b} \tag{4.23}$$

The aim of Newton's method is to reduce $\underline{R}$ to zero through

[5] Kantorovitch's contribution to the Newton-Raphson technique is that of demonstrating the validity of the functional during each iteration [26].

successive iterations of the following form:

$$J^n(\underline{\phi}^n - \underline{\phi}^{n+1}) = J^n(\underline{\Delta\phi}^{n+1}) = \underline{R}^n \tag{4.24}$$

Equation (4.24) is well known and its validity will not be discussed further. Interested readers are referred to [27, 28, 29] for more information.

The Jacobian matrix

$$J^n = \frac{\partial \underline{R}^n}{\partial \underline{\phi}^n} \tag{4.25}$$

must be evaluated for each iteration. Differentiating by parts and using implied summation:

$$J^n_{ij} = \frac{\partial R^n_i}{\partial \phi^n_j} = S^*_{ijk}\,\epsilon^n_k + \left[S^*_{ilk}\left(\frac{\partial \epsilon^n_k}{\partial \phi^n_j}\right)\right]\phi^n_l - B_{ik}\left(\frac{\partial \rho^n_k}{\partial \phi^n_j}\right) \tag{4.26}$$

Note that the constituent parts of J involve no new matrices. Once a finite-element mesh has been specified, S* and B are known for all subsequent problems. One should also observe that although S is sparse and symmetrical, J is sparse (and of the same topology as S) but asymmetrical. Futhermore, the structure of J does not change as the iterations proceed.

If field (i.e. potential derivative) dependence is eliminated from $\overline{\overline{\epsilon}}$ and ρ, a very significant simplification occurs in J. The medium and source sub-Jacobians take the form of diagonal matrices rather than general tensors. Hence (4.26)

may be rewritten as:

$$J_{ij}^{n} = S_{ij}^{n} + \left[S_{ikj}^{*} \left(\frac{\partial \epsilon_j^n}{\partial \phi_j^n} \right) \right] \phi_k^n - B_{ij} \left(\frac{\partial \rho_j^n}{\partial \phi_j^n} \right) \tag{4.27}$$

Provided the field dependence is not extreme, (4.27) may still work quite well. The ultimate solution to (4.2) depends only on the validity of (4.1) and not on the actual Jacobian used. In effect, the Jacobian only governs the rate of convergence. The final result depends solely on the S* and B matrices.

4.4 MULTIPLE EQUATIONS

As indicated in Chapter II, three coupled Poisson-like equations describe electronic transport in semiconductors. Combining ϕ_s, ϕ_n, and ϕ_p into one complex vector

$$\underline{\phi}_T = \begin{bmatrix} \underline{\phi}_s \\ \underline{\phi}_n \\ \underline{\phi}_p \end{bmatrix} \tag{4.28}$$

allows us to write:

$$\begin{bmatrix} \underline{R}_s \\ \underline{R}_n \\ \underline{R}_p \end{bmatrix} = \begin{bmatrix} S_s & 0 & 0 \\ 0 & S_n & 0 \\ 0 & 0 & S_p \end{bmatrix} \begin{bmatrix} \underline{\phi}_s \\ \underline{\phi}_n \\ \underline{\phi}_p \end{bmatrix} - \begin{bmatrix} B & 0 & 0 \\ 0 & B & 0 \\ 0 & 0 & B \end{bmatrix} \begin{bmatrix} \underline{\rho}_s \\ \underline{\rho}_n \\ \underline{\rho}_p \end{bmatrix} \tag{4.29}$$

The new Newton-Raphson equation then becomes:

$$\begin{bmatrix} \frac{\partial R_s}{\partial \phi_s} & \frac{\partial R_s}{\partial \phi_n} & \frac{\partial R_s}{\partial \phi_p} \\ \frac{\partial R_n}{\partial \phi_s} & \frac{\partial R_n}{\partial \phi_n} & \frac{\partial R_n}{\partial \phi_p} \\ \frac{\partial R_p}{\partial \phi_s} & \frac{\partial R_p}{\partial \phi_n} & \frac{\partial R_p}{\partial \phi_p} \end{bmatrix}^n \begin{bmatrix} \Delta\underline{\phi}_s \\ \Delta\underline{\phi}_n \\ \Delta\underline{\phi}_p \end{bmatrix}^{n+1} = \begin{bmatrix} \underline{R}_s \\ \underline{R}_n \\ \underline{R}_p \end{bmatrix}^n \qquad (4.30)$$

The explicit form of J remains as in (4.27) but the subscripts now run over the expanded Hilbert space spanned by $\underline{\phi}_T$.

As with ordinary (i.e. linear) finite elements, the global S (or in our case J) matrix is formed by considering each elemental submatrix independently. On each iteration, (4.30) is treated as a complete, linear problem in its own right. Hence, it is legitimate to build J (global) from a large set of smaller, linear subsystems.

4.5 IMPLEMENTATION DETAILS

A series of computer programs were written to implement the above algorithm. The resulting package, known as MANIFEST, allows for the solution of up to three nonlinear, Poisson-like equations. Time-dependent terms are handled with a simple backward-difference formula.

Although a complete desciption of this package is given in the "MANIFEST User's Guide" [10] some of the more fundamental aspects of the programs' code are discussed here.

Source listings (in FORTRAN IV) for MANIFEST are given in the "MANIFEST Installation Guide" [11]. Related manuals describing the mesh generator and plotting programs are available through Refs. [30, 31, 32].

Dirichlet Nodes

Unlike Neumann or mixed boundaries, which involve the addition of extra terms to the functional, Dirichlet boundaries require the trial functions to be pre-specified. Since, at all Dirichlet nodes, ϕ_i is known in all iterations of (4.30) $\Delta\phi_i$ must always be zero for those nodes. Eliminating the i'th row and column from the matrix equation automatically ensures that the i'th ϕ is held at its initial (and final!) value.

Transient Analysis

Time-dependence in MANIFEST is handled by maintaining two copies of the total potential vector (ϕ_s, ϕ_n, and ϕ_p): the working copy currently being solved, and the previous set of potentials from the last "time-step". As only time-dependences of the form

$$\frac{\partial n}{\partial t} \tag{4.31}$$

and

$$\frac{\partial p}{\partial t} \tag{4.32}$$

occur in the recombination expressions R_n and R_p, a simple backward-difference approximation is applied [33]:

$$\frac{\partial n}{\partial t} \approx \frac{(n^i - n^{i-1})}{\Delta t} \tag{4.33}$$

$$\frac{\partial p}{\partial t} \approx \frac{(p^i - p^{i-1})}{\Delta t} \tag{4.34}$$

Although higher-order expressions could be used, these would require extra copies of the potential vector. Other methods, such as those based on the Crank-Nicolson-Galerkin formulation [34], might be attempted; but this simple Euler-like scheme gives acceptable results with minimal programming and computational effort.

Step-Limiting

Unless one is sufficiently close to the final solution, the Newton-Raphson algorithm may fail to converge. In these circumstances, the user has only two choices: restart the process with a better initial guess, or modify the algorithm to improve convergence. Although in some instances, the user may be forced to give a more accurate initial estimate, MANIFEST provides a step-limiting option in response to the second alternative.

When invoked, the step-limiter monitors the algorithm for

divergence. If the relative displacement norm

$$\frac{\| \Delta\phi^{n} \|}{\| \Delta\phi^{n+1} \|} = \frac{\sum_k \left| \phi_k^{n} - \phi_k^{n+1} \right|}{\sum_k \left| \phi_k^{n+1} \right|} \tag{4.35}$$

should happen to diverge, a new potential is calculated by limiting the maximum absolute value of $\Delta\phi_i^n$ to the previous value of the displacement norm. If the algorithm is converging, no modifications are made. This form of automated under-relaxation generally works quite well and is much simpler to use than methods which require the user to supply their own relaxation parameters [5].

Disk-Swapping

The elemental matrices S* and B are determined solely by the finite-element mesh. Rather than (numerically) recalculating the associated integrals on each Newton iteration, it may be advantageous to store the submatrices on a temporary disk file and swap them into core as required [17, 35]. The two and three-dimensional versions‘ of MANIFEST allow the user to invoke such a feature. Clearly, a tradeoff exists between the cost of execution time and I/O counts. This technique appears most favorable when the integration costs are high (i.e. for three-dimensional elements) and the com-

---

‘ Due to the manner in which one-dimensional elements are defined, MANIFEST-1D does not require the disk-swapping feature.

puter can be "tuned" for efficient I/O (i.e. on a dedicated mini-computer with a hard disk). As only sequential files are created by the disk-swapping routines, the efficency of the I/O routines can become quite high.

Precision

As presently documented, MANIFEST is written in standard FORTRAN IV (IBM level H) with single-precision variables. It was found that double precision (i.e. 16 decimal digits per floating point word) is required to achieve convergence for heavily doped semiconductor devices (e.g. N_{dope} > 1.0E16 cm-3). It is believed that only variables associated with the potentials and the matrix inversion routines (ASYMPAK) need be converted, but this has not yet been fully proven.

Matrix Solution

Approximately half of the cost of each Newton-Raphson iteration is associated with the inversion of the global Jacobian matrix. Although sparse, the Jacobian is generally not symmetrical or definite. Hence simple SOR (successive over-relaxation) methods tend to be unstable in these circumstances [36].

The method chosen for matrix solution is based on bifactorization. The particular algorithm used (ASYMPAK [37, 38]) is adapted from a paper of Zollenkopf's which incorporates prepivotal factoring and sparse-storage techniques.

Other semi-iterative algorithms, such as those based on conjugate-gradient methods (CG, ICCG, or pre-conditioned ICCG), may prove to be more suitable as the Newton scheme is already iterative [39, 40].

4.6 EXTENSIONS

Future versions of MANIFEST should provide for improvements in algorithmic performance, accuracy, and ease of use. Clearly, there are virtually an infinite number of extensions possible for a program such as this. Although it is impossible to satisfy the needs and preferences of all users equally, some of the more desirable aspects of future implementations are discussed below.

Interactive Graphics

In the author's opinion, the major disadvantage to MANIFEST is the difficulty in guiding the solution process. When solving any large nonlinear problem, a certain amount of user interaction can be of great benefit to the algorithm. As an initial guess is always required, spurious or nonphysical solutions can -- and frequently do -- occur. Ideally the user should be able to run MANIFEST interactively with the option to modify solutions, data, and job parameters. To efficiently implement such a scheme, a graphical display of the mesh and fields must be provided. Presently available pre- and post-processors (MANDAP [30, 31] and

CONTOUR [32]) do not adequately fulfill these needs. Of course, far more computer resources would be required to realize this level of integration.

Field-Dependent Mobility

In Section 2.2, an expression for carrier mobility was given which involved the electrostatic field. Unfortunately, only the potential ϕ_s (rather than $\vec{E}$) is directly available at the finite-element nodes.[7] When field-dependent mobilities are required, the MANIFEST user has two alternatives:

1. Calculate the fields directly by differentiating the shape functions. Although technically simple and theoretically correct, this method will inevitably lead to poor field estimates.
2. Derive an empirical mobility formula based on the boundary conditions and the value of ϕ_s.

It is generally recognized that neither scheme is entirely satisfactory. Ultimately, as one requires accurate electric-field estimates throughout the region of interest, the use of modern integral-equation formulations may aid in the calculation of field-dependent mobilities [41, 42].

---

[7] In MANIFEST-1D, facilities exist for calculating the derivatives of the electostatic and quasi-Fermi potentials for use with the mobility expressions. However, the nonlinear effects of these fields are not reflected in the Jacobian matrix. Hence the convergence rate of the algorithm will be degraded when field-dependent mobilities are used.

Capacitance Calculations

One of the fundamental characteristics of a semiconductor device is its capacitance. The capacitance between two electrodes -- with all others held at some specified potential -- is given by

$$C = \frac{dQ}{dV} \tag{4.36}$$

where dQ is the incremental stored charge resulting from an incremental applied voltage of dV. Although simple to write, equation (4.36) is nontrivial to implement.

In principle, one may produce a Q-V curve for the terminal potential range of interest. The derivative of that curve will then be C(V). Stepping the electrode voltage is a standard process in MANIFEST, but to obtain the appropriate Q requires an complicated algorithm [43].

The incremental charge is constructed from the sum of all volume charge densities ρ and all surface (including interior interfaces) charge density's σ. One must split all such charges into two parts: positive charges $\rho+$ and $\sigma+$; and negative charges $\rho-$ and $\sigma-$. The appropriate Q used in (4.36) is then given by

$$Q = \int_{\Omega} \rho^{+}\, dv + \int_{\Omega} \sigma^{+}\, ds \tag{4.37}$$

Although the volume charge density is simply the source term of Poisson's equation, the surface charge density must be

evaluated from:

$$\sigma = \hat{n} \cdot (\bar{\bar{\varepsilon}} \nabla \phi_s) \tag{4.38}$$

To simplify the above process, the following relation is used by MANIFEST:

$$C = \frac{d^2E}{d^2V} \tag{4.39}$$

Both the electrostatic energy and applied bias voltage are accurately known in the program. Taking the second derivative of the E-V curve, even with a spline based algorithm, may introduce large errors into the C(V) characteristic. For rigorous capacitance calculations, the first method is preferred.

Adaptive Mesh-Solving

One of the most useful, yet most difficult, extensions to MANIFEST would be the addition of an adaptive mesh-generator. With such a device, the user would only need to specify an initial coarse mesh and the program would refine and, if necessary, redefine the mesh as the solutions proceed.

To date, few researchers have attempted such a scheme [44, 45]. Possible techniques for deciding where to refine the mesh rely on monitoring the magnitude of the electric field (difficult) or the local error in the residuals (easier). Methods based on residual calculations (the $\underline{R}$ in (4.23)) seem most promising as local mesh refinement would then be applied where the algorithm is failing to converge.

Multi-Step Extrapolation

When characterizing a device, one or more device parameters are varied (i.e. stepped) as MANIFEST computes the electrostatic and quasi-Fermi potentials under the given operating conditions. Presently, the initial guess for the next calculation is taken as the last valid set of potentials. By defining a step-extrapolation parameter as some combination of all varying device parameters (e.g. bias voltage, time, temperature, etc.), an improved potential estimate could be obtained via a suitable extrapolation scheme. As MANIFEST already stores two copies of all potential vectors (from current and previous solutions), simple linear extrapolation would seem the most natural technique.

Chapter V

CHARACTERIZATION OF CONVENTIONAL DEVICES

This chapter serves to illustrate how MANIFEST can be used to aid in the characterization of conventional semiconductor devices. The solution strategies presented here are not the only ones possible and certainly they are not optimal. Users of the MANIFEST system must realize that proper application of such a complicated design tool may take many months to master and should be considered partially as an art as well as a science.

All programs were written in FORTRAN IV (IBM level H) and run on an AMDAHL 470/V8 computer at the University of Manitoba. As well, MANIFEST has been successfully implemented on a DEC VAX/750 at Xerox's PARC facility. Two and three-dimensional meshes were generated with the aid of the MANDAP package. Contour and perspective plots are provided by the CONTOUR program.

To gain insight into the MANIFEST system, the first example is a series of analytic tests where the program can be easily evaluated for accuracy and computational efficiency. The remaining examples include various diodes and transistors operating under both steady-state and transient conditions. Additional examples can be found in Ref. [10].

5.1 ANALYTIC TESTS

This section demonstrates the MANIFEST program for a number of test cases where the exact solution is known in closed form. In the following examples, we seek a solution to

DIV(k*GRAD(PHI))=f

where k represents an inhomogeneous isotropic medium and f signifies an appropriate source. These tests were devised by selecting a solution PHI and medium k, and subsequently deriving the correct expression for f. In general, both k and f may be functions of position, time, and potential. Table 5.1 summarizes the media and source properties for these examples. Unless stated otherwise, spatial regions for the one-dimensional problems are defined for X in the range (0,1) while the two-dimensional tests require both X and Y to be within (0,1).

The first three tests involve MANIFEST in a series of one-dimensional studies (i.e. examples 1D1, 1D2, and 1D3). Case 1D1 is concerned with the solution of a simple diffusion equation where, for simplicity, both the medium and source are independent of the potential. To study the convergence properties of the backward-difference time-derivative approximation, a set of energy/time curves were generated using three, six, and twelve time-steps.[8]

[8] Times from zero to three natural-time-units were used for these examples. One natural-time-unit is defined as the

TABLE 5.1

Analytic Test Cases

1D Tests

1D1

```
k= 1                                    0 < X < PI
f= D(PHI)/D(T)                          0 < T < 3
PHI = SIN(X)*EXP(-T)
```

1D2

```
k= 1 + (X*PHI**2)/2)
f= (1+(X*PHI**2)/2)*(BETA*(6*X-2))
   + (X*PHI*(BETA*(3*X**2-2*X)+PHI0)+(PHI**2)/2)
   * (BETA*(3*X**2-2*X)+PHI0)
BETA := SCALE*(1-PHI0)
PHI= SCALE*(1-PHI0)*(X-1)*(X**2) + (PHI0*X)
```

1D3

```
k= 1 + (GRAD(PHI)/E0)**2
f= (2.*SCALE*(-81.*X**5*PHI0**3*SCALE**2+243.*X**5*PHI0**2*SCALE
 **2-243.*X**5*PHI0*SCALE**2+81.*X**5*SCALE**2+135.*X**4*PHI0**3*
 SCALE**2-405.*X**4*PHI0**2*SCALE**2+405.*X**4*PHI0*SCALE**2-135.
 *X**4*SCALE**2-72.*X**3*PHI0**3*SCALE**2+54.*X**3*PHI0**3*SCALE
 216.*X**3*PHI0**2*SCALE**2-108.*X**3*PHI0**2*SCALE-216.*X**3*PHI0
 *SCALE**2+54.*X**3*PHI0*SCALE+72.*X**3*SCALE**2+12.*X**2*PHI0**3
 *SCALE**2-54.*X**2*PHI0**3*SCALE-36.*X**2*PHI0**2*SCALE**2+108.*
 X**2*PHI0**2*SCALE+36.*X**2*PHI0*SCALE**2-54.*X**2*PHI0*SCALE-
 12.*X**2*SCALE**2+12.*X*PHI0**3*SCALE-9.*X*PHI0**3-24.*X*PHI0**2*
 SCALE+9.*X*PHI0**2+12.*X*PHI0*SCALE-3.*X*PHI0*E0**2+3.*X*E0**2
 3.*PHI0**3-3.*PHI0**2+PHI0*E0**2-E0**2))/E0**2
PHI= SCALE*(1-PHI0)*(X-1)*(X**2) + (PHI0*X)
```

2D Tests (2D1 and 2D2)

```
k= 1 + (PHI**2)
f= 2*(5*X*(PHI**2) + (Y**4)*PHI + X)
PHI= X*(Y**2)
```

Figure 5.1 depicts the calculated solutions at times of 0, 1, 2, and 3 time-units when only three time-steps were used. The time-integration scheme incorporated into MANIFEST ensures stable convergence for constant or increasing time-steps [46, 47]. The example was run with a grid consisting of 10 quadratic elements and 21 nodes. The total CPU time for this test was less than 0.34 seconds. Figure 5.2 is a plot of energy density versus time when three, six, and twelve time-steps were used. The solutions appear to converge towards the exact solution (i.e. the bottom curve) as the number of steps increases. A semi-log plot of the same set of curves is shown in Figure 5.3. As expected, the system's energy decays exponentially with a time constant of unity.

The second test attempts to solve a nonlinear (time independent) differential equation by incrementing one of the boundary potentials (at X=1) much as an electrode on a two terminal semiconductor device might be swept. As well as studing the behavior of the system's energy, we shall calculate the "capacitance" (defined here as the second derivative of the energy-voltage curve) of this "device". As before, this problem was run with a mesh consisting of 10 quadratic elements and 21 nodes slighty skewed towards X=1. The calculated solutions -- with the bias potential (i.e. PHI0 at X=1) swept from 0 to 1.5 volts in steps of 0.25

time required for an exponentially decaying curve to fall by a factor of e.

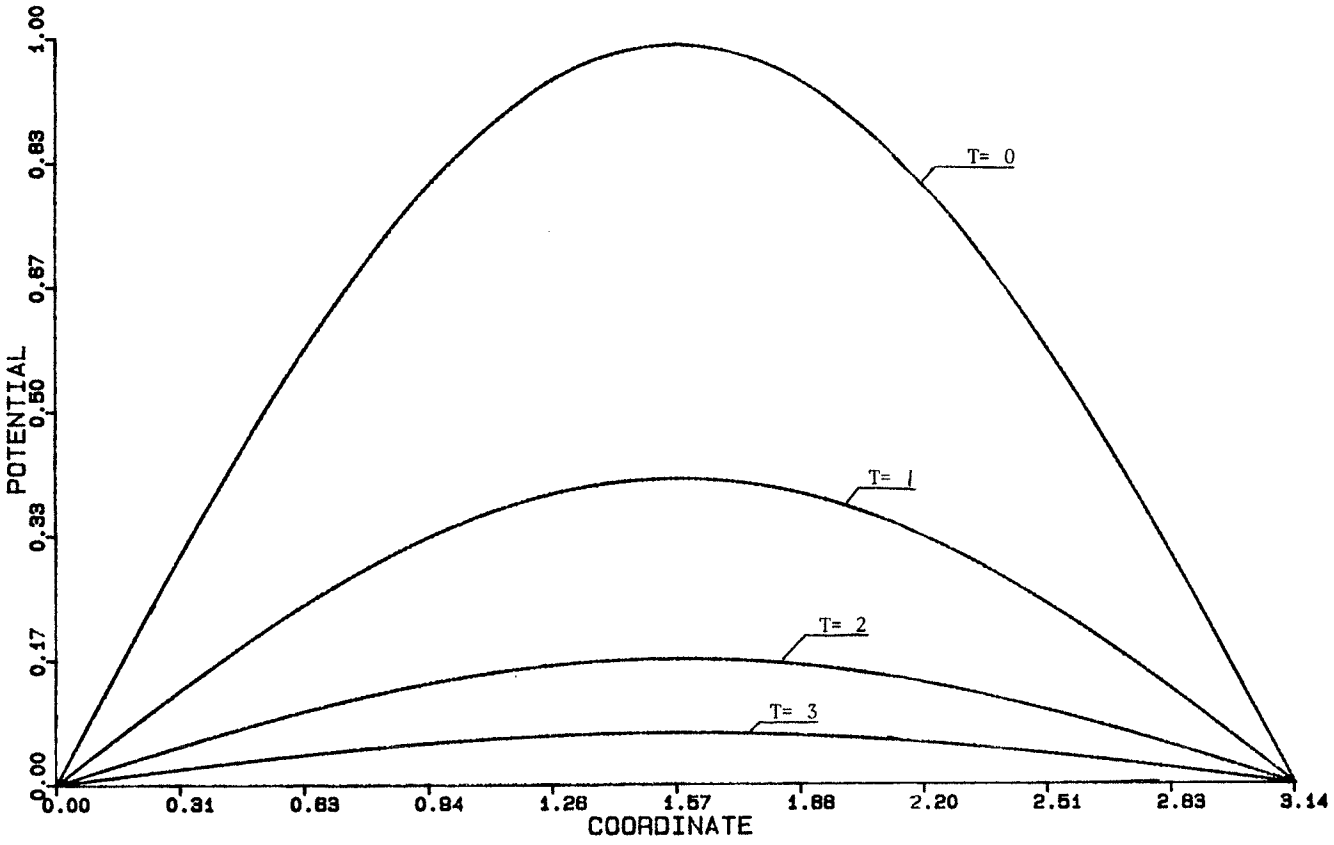

Figure 5.1: Calculated Potentials (1D1)

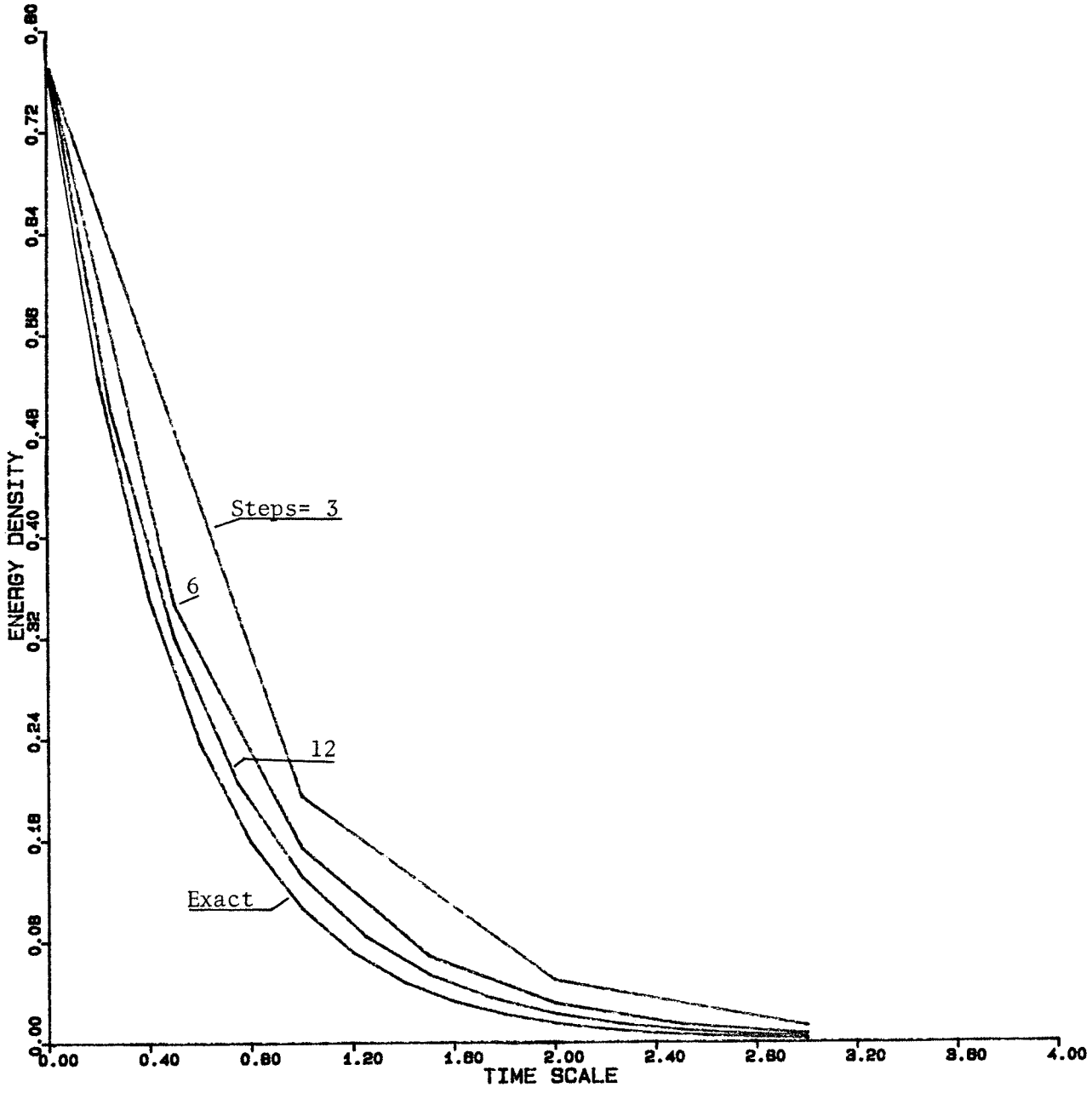

Figure 5.2: Energy vs. Time (1D1)

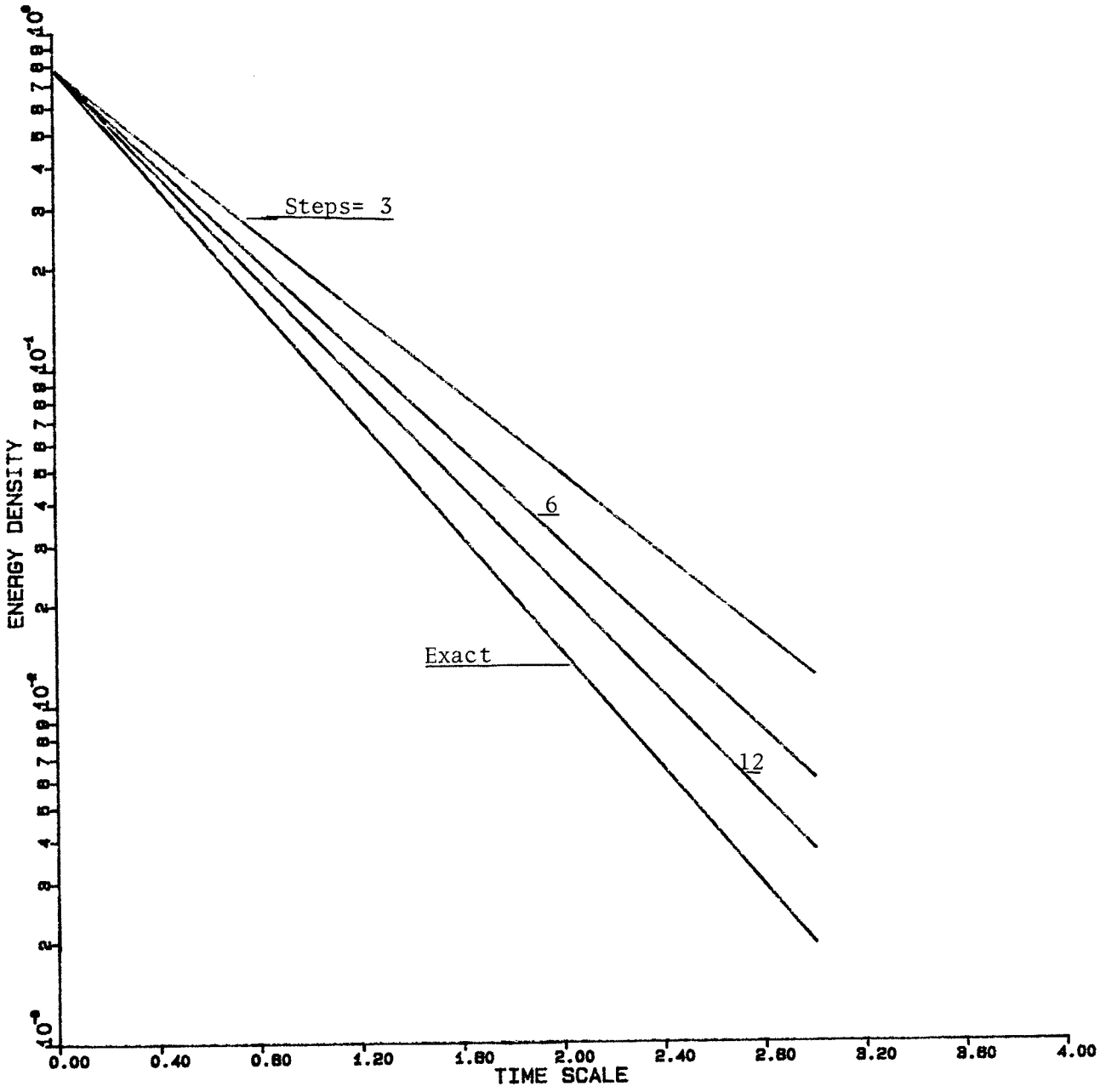

Figure 5.3: Energy vs. Time [semi-log] (1D1)

volts and SCALE= 5.0 -- are shown in Figure 5.4. Each solution converged quadratically using only three iterations from the previously calculated solution. The required CPU time was approximately 0.38 seconds. Table 5.2 summarizes the error for the final solution. Plots of stored energy and capacitance versus bias potential are given in Figures 5.5 and 5.6 respectively. The energy curves agree exceptionally well with the exact calculations. Considering MANIFEST must obtain a second derivative numerically from an energy-potential curve of only seven data points, the calculated capacitance is also seen to agree quite well.

The final one-dimensional test involves solving a series of field-dependent problems. At each Newton-Raphson iteration, the electric field is calculated by a second-order finite-difference formula at each node of the mesh. Since the Jacobian matrix does not explicity handle potential derivatives (all derivative information was set to zero) a quadratic convergence rate was not expected. Using the same mesh and SCALE factor as above, a number of tests were performed while varying the field-strength factor E0. For large values of this constant (e.g. E0 > 10.0), the medium term is weakly dependent upon the field strength. Hence the Newton-Raphson algorithm works very well. For intermediate values (e.g. 10.0 > E0 > 4.0), the field dependence of k becomes strong enough so that one notices a significant increase in the number of iterations required before the solu-

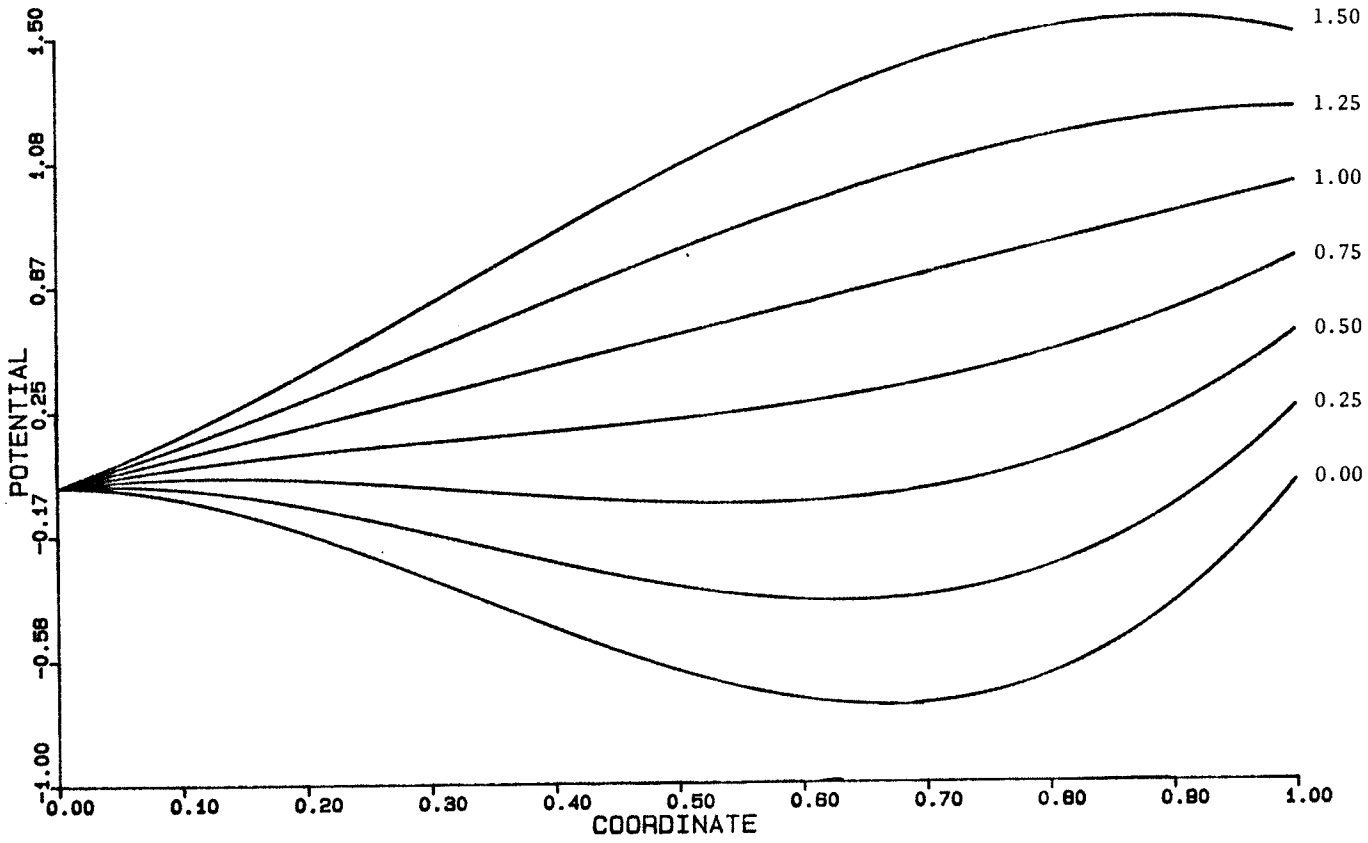

Figure 5.4: Calculated Potentials (1D2)

TABLE 5.2

Exact vs. Calculated Potentials (1D2)

MANIFEST VERSION 1.8-1D DATE= 7/09/83 TIME= 3:29 PM

ANALYTIC TEST (1D3)

PROCESSING ==> USER

PROCESS CODE: 2

SOLUTION

NODE	EXACT	CALCULATED	DELTA
1	0.0	0.0	0.0
2	0.5679E-01	0.5664E-01	0.1483E-03
3	0.1193E+00	0.1193E+00	0.4625E-04
4	0.1962E+00	0.1963E+00	-0.1383E-04
5	0.2787E+00	0.2787E+00	-0.6002E-04
6	0.3831E+00	0.3832E+00	-0.7755E-04
7	0.4922E+00	0.4923E+00	-0.8219E-04
8	0.6075E+00	0.6075E+00	-0.2587E-04
9	0.7241E+00	0.7240E+00	0.4971E-04
10	0.8400E+00	0.8399E+00	0.1141E-03
11	0.9534E+00	0.9533E+00	0.1354E-03
12	0.1062E+01	0.1062E+01	0.9537E-04
13	0.1165E+01	0.1165E+01	0.1144E-04
14	0.1260E+01	0.1260E+01	-0.9727E-04
15	0.1345E+01	0.1345E+01	-0.2050E-03
16	0.1419E+01	0.1420E+01	-0.2899E-03
17	0.1479E+01	0.1480E+01	-0.3586E-03
18	0.1528E+01	0.1528E+01	-0.4168E-03
19	0.1551E+01	0.1552E+01	-0.4005E-03
20	0.1544E+01	0.1545E+01	-0.4311E-03
21	0.1500E+01	0.1500E+01	-0.9537E-06

RELATIVE NORM: 0.1654E-03

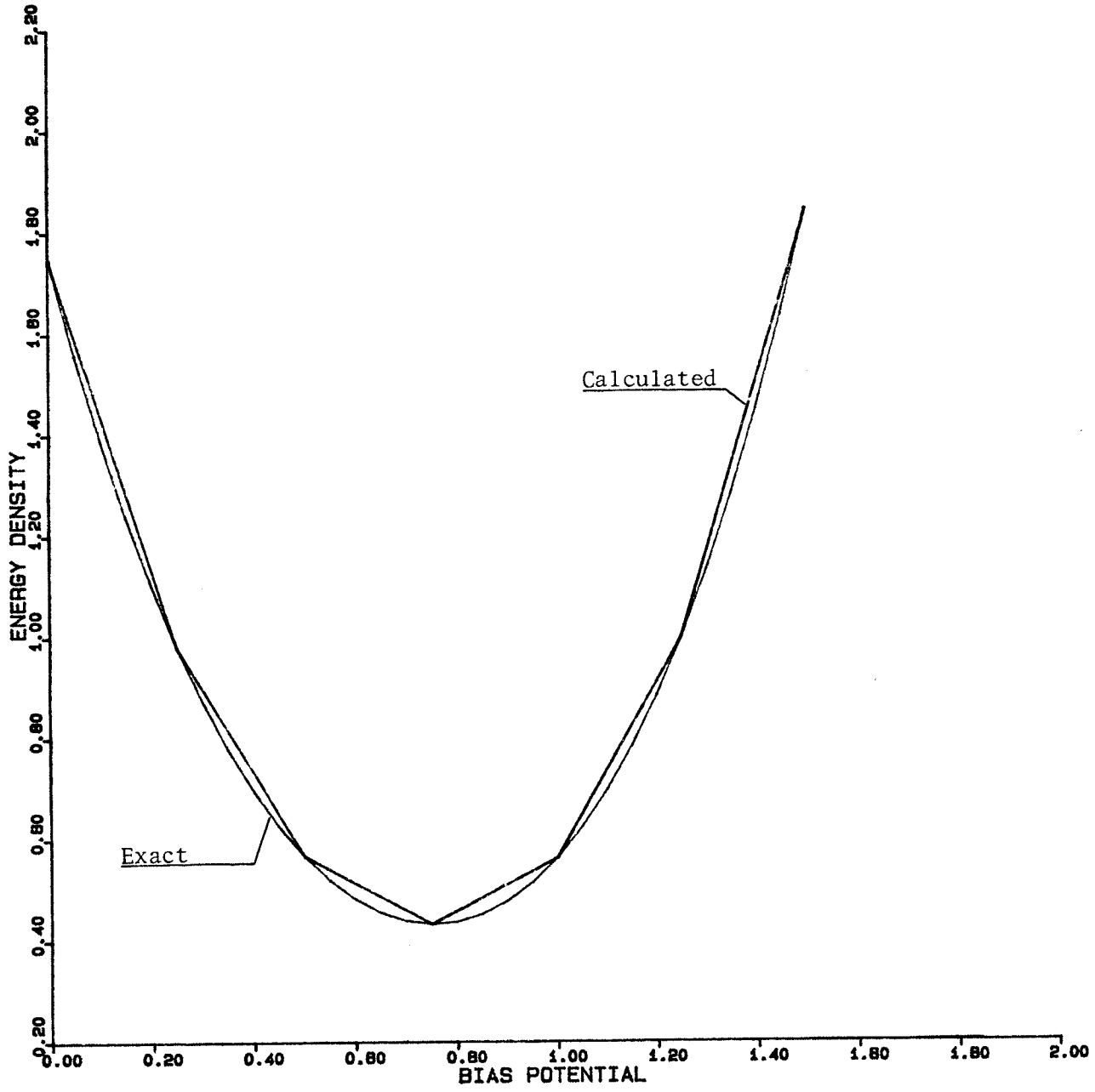

Figure 5.5: Energy vs. Bias Potential (1D2)

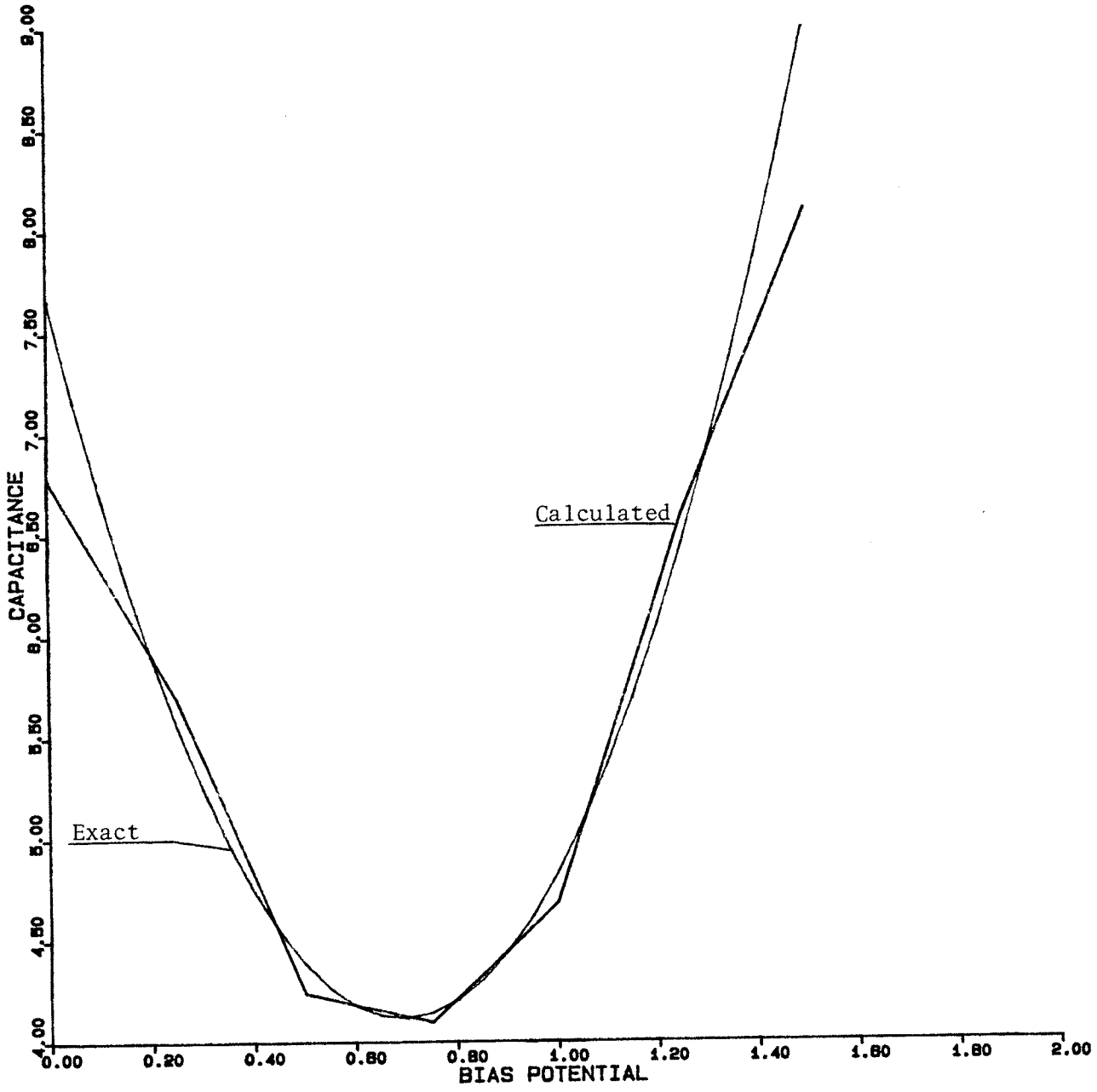

Figure 5.6: Capacitance vs. Bias Potential (1D2)

tion converges. If E0 is made sufficiently small, the solution may fail to converge even if one starts very near the exact answer. Note that the potentials of examples 1D2 and 1D3 were purposely chosen to be the same. The calculated potentials (for the case of E0= 5.0) are shown in Figure 5.7 while the energy-potential curve is given by Figure 5.8 and the capacitance-potential curve by Figure 5.9. The energy and capacitance curves for this example are NOT the same as those for the previous test.

A set of two-dimensional problems (examples 2D1 and 2D2) were devised to evaluate MANIFEST-2D. The two meshes, using quasi-linear and quadratic elements, of Figures 5.10 and 5.11 were used to generate the potential contour plots in Figures 5.12 and 5.13. Quadratic convergence was observed for both runs (using three iterations from a constant starting potential). Table 5.3 summarizes some of the global characteristics for these tests. It is interesting to note that the quadratic test 2D2 (with 96 nodes and 25 elements) required less CPU time than the linear test 1D2 (with 144 nodes and 121 elements) yet produced slightly more accurate results. The source integrals, which should equal the sum of all normal fluxes, was calculated independently of those fluxes.

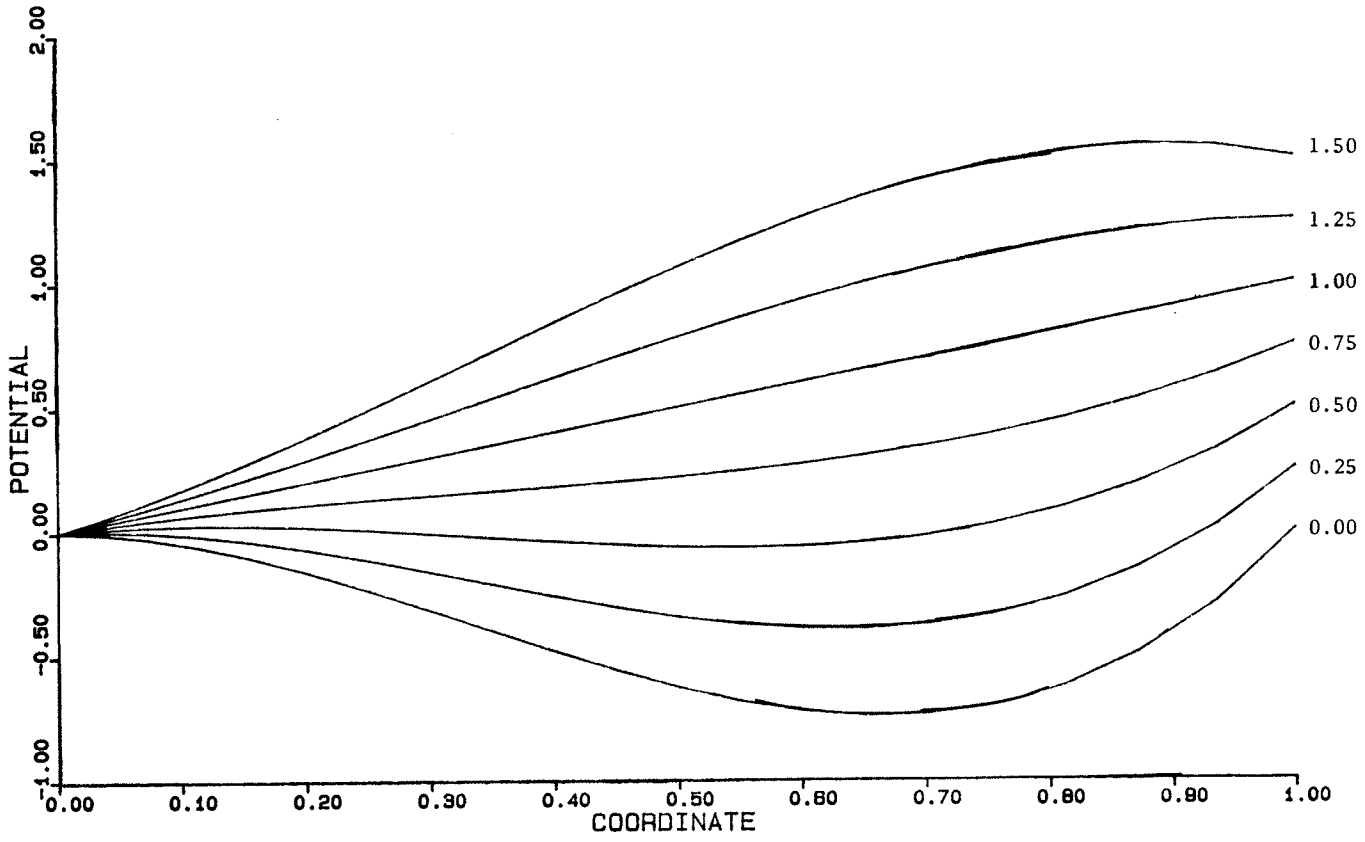

Figure 5.7: Calculated Potentials (1D3)

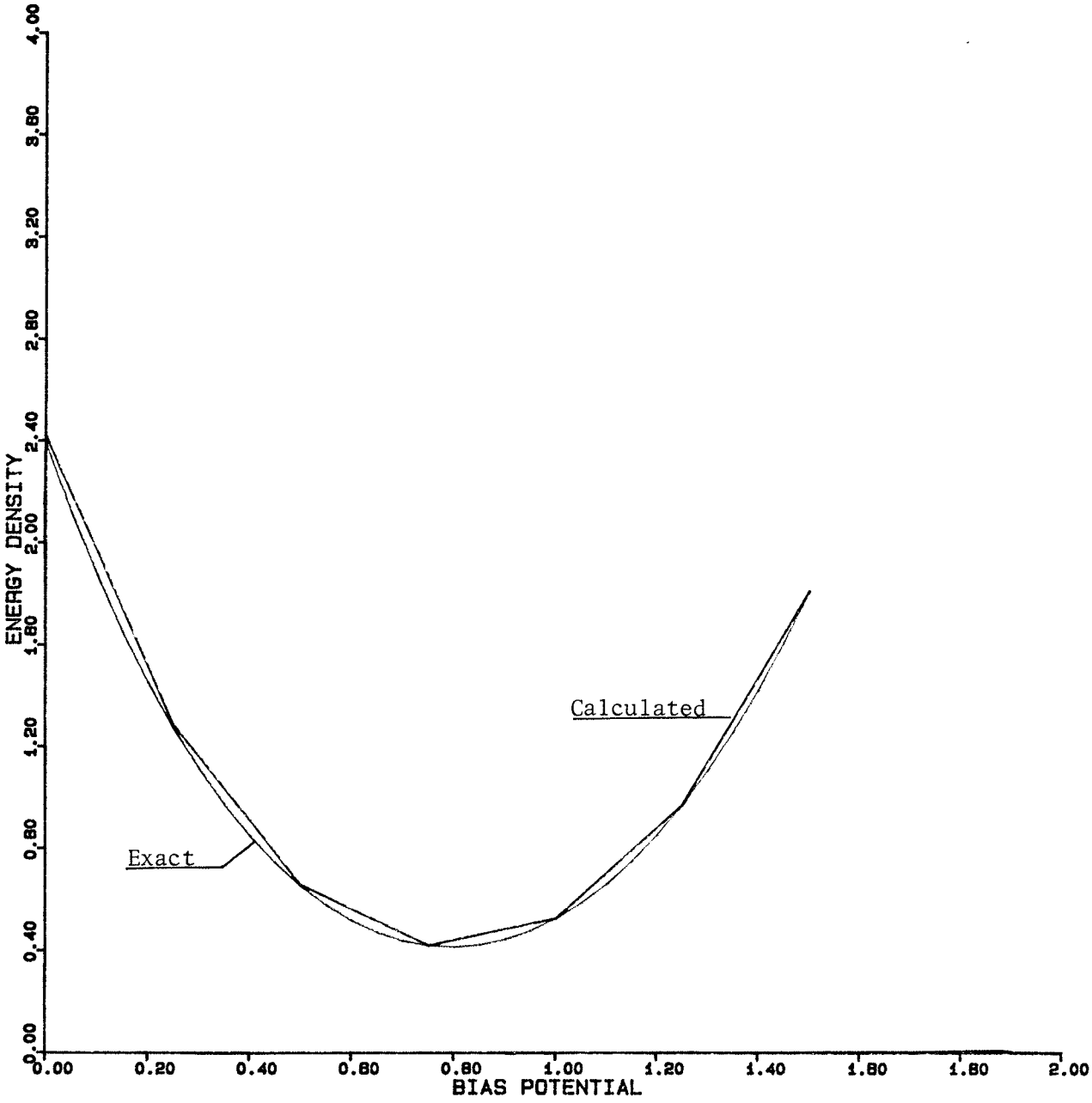

Figure 5.8: Energy vs. Bias Potential (1D3)

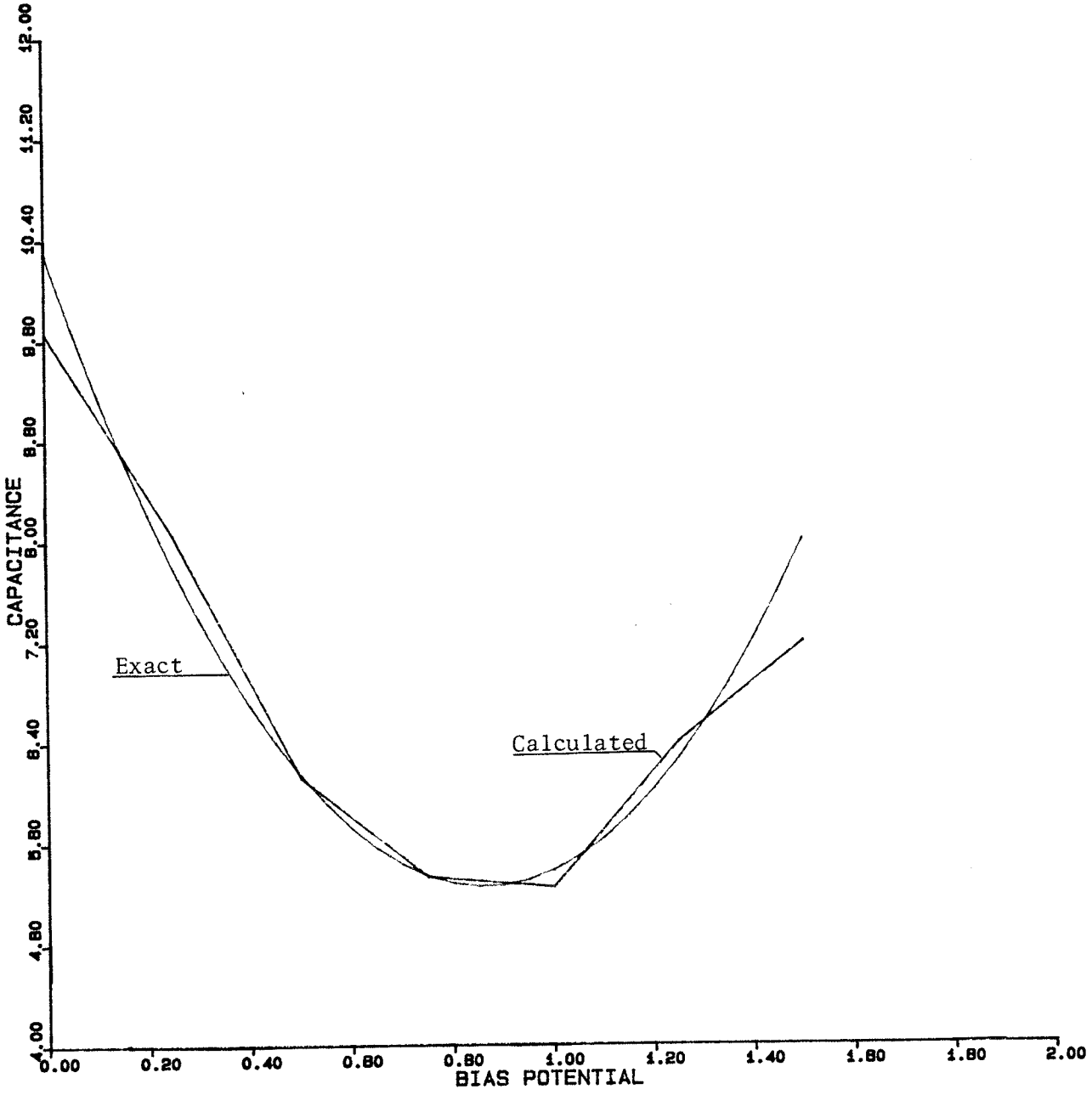

Figure 5.9: Capacitance vs. Bias Potential (1D3)

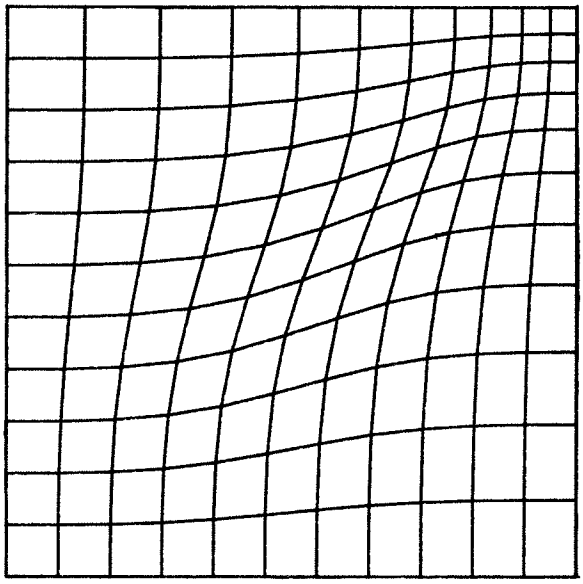

Figure 5.10: Linear Finite-Element Mesh (2D1)

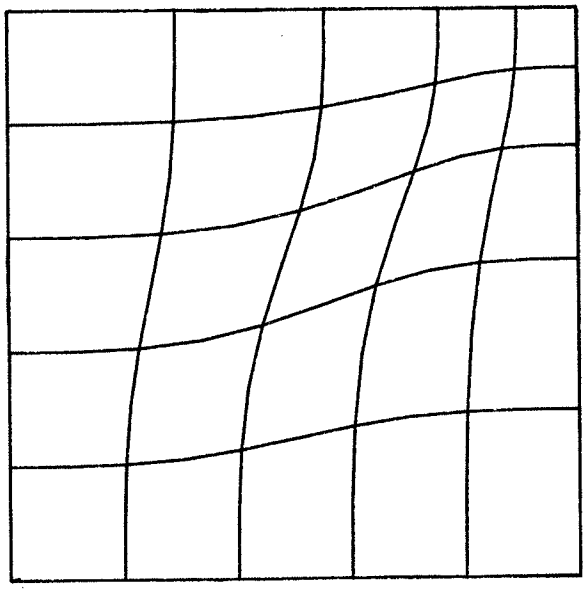

Figure 5.11: Quadratic Finite-Element Mesh (2D2)

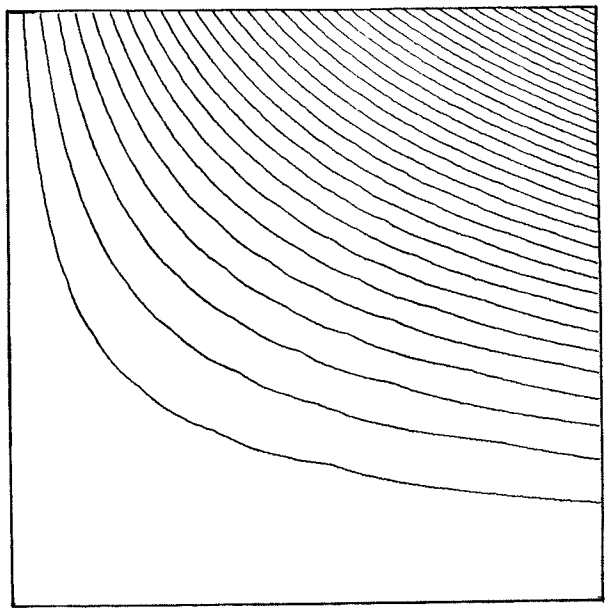

Figure 5.12: Calculated Potentials (2D1)

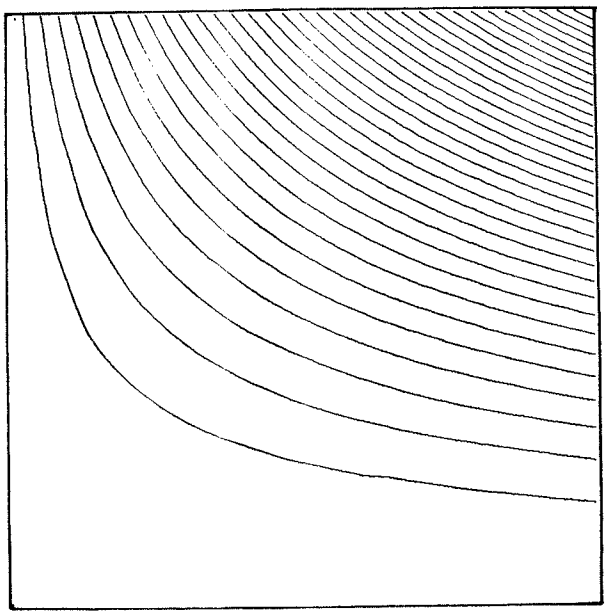

Figure 5.13: Calculated Potentials (2D2)

TABLE 5.3

Two-Dimensional Analytic Test Results

Exact Solution

Energy= 1/2 * (1/5 + 4/9 + 1/27 + 4/35) = 0.3979E+00

Source Integral= 3/2 - 1/3 + 10/21 = 0.1643E+01

Flux (top) = 3/2 = 0.1500E+01
Flux (LHS) = -1/3 = -0.3333E+00
Flux (bot) = 0 = 0.0000E+00
Flux (RHS) = 10/21 = 0.4762E+00

2D1

Energy= 0.3987E+00

Source Integral= 0.1657E+01

Flux (top) = 0.1455E+01
Flux (LHS) = -0.3342E+00
Flux (bot) = -0.6117E-01
Flux (RHS) = 0.4809E+00

CPU time = 2.9 seconds.

2D2

Energy= 0.3979E+00

Source Integral= 0.1643E+01

Flux (top) = 0.1513E+01
Flux (LHS) = -0.3308E+00
Flux (bot) = -0.2238E-02
Flux (RHS) = 0.4837E+00

CPU time = 1.8 seconds.

5.2 THE P-N JUNCTION

As our first example of semiconductor device characterization, we shall consider two versions of a one-dimensional P-N junction. Rather than displaying the electrostatic and quasi-Fermi potentials, we shall show carrier concentrations (cm-3) versus spatial coordinate (cm). Unless otherwise stated, the CGS system of units will be assumed for all diagrams. These examples were developed with the assistance of Mr. D. Quail as part of an undergraduate research project.

Table 5.4 lists the important parameters' which define a simple step junction. Figure 5.14 illustrates the carrier profiles (n and p) under forward biases of 0.0, 0.57, and 1.12 volts. The results of a transient analysis response to a unit step function in potential of 0.2 volts are presented in Figure 5.15. Plots of current density (A cm-2) versus bias potential are given in Figures 5.16 and 5.17. The second curve in Figure 5.16 is obtained from a simple analytic model devised by Mr. Quail. The rapid rise in current density near 0.22 volts, as predicted by MANIFEST, is attributed to the filling of mid-bandgap traps in the semiconductor [13].

' The names given within the parameter tables reflect FORTRAN variables used when these examples were run.

TABLE 5.4

Abrupt P-N Junction Parameters

Parameter	Value	Units
TAUN	1.0E-9	s
TAUP	1.0E-9	s
T	300.0	K
NI	1.6E10	cm-3
UN	1500.0	cm2/v/s
UP	600.0	cm2/v/s
DOPE	1.0E16	cm-3
EPSON	11.8	

TABLE 5.5

Diffused P-N Junction Parameters

Parameter	Value	Units
TAUN	2.0E-9	s
TAUP	1.0E-9	s
T	300.0	K
NI	1.6E10	cm-3
UN	1500.0	cm2/v/s
UP	600.0	cm2/v/s
EPSON	11.8	

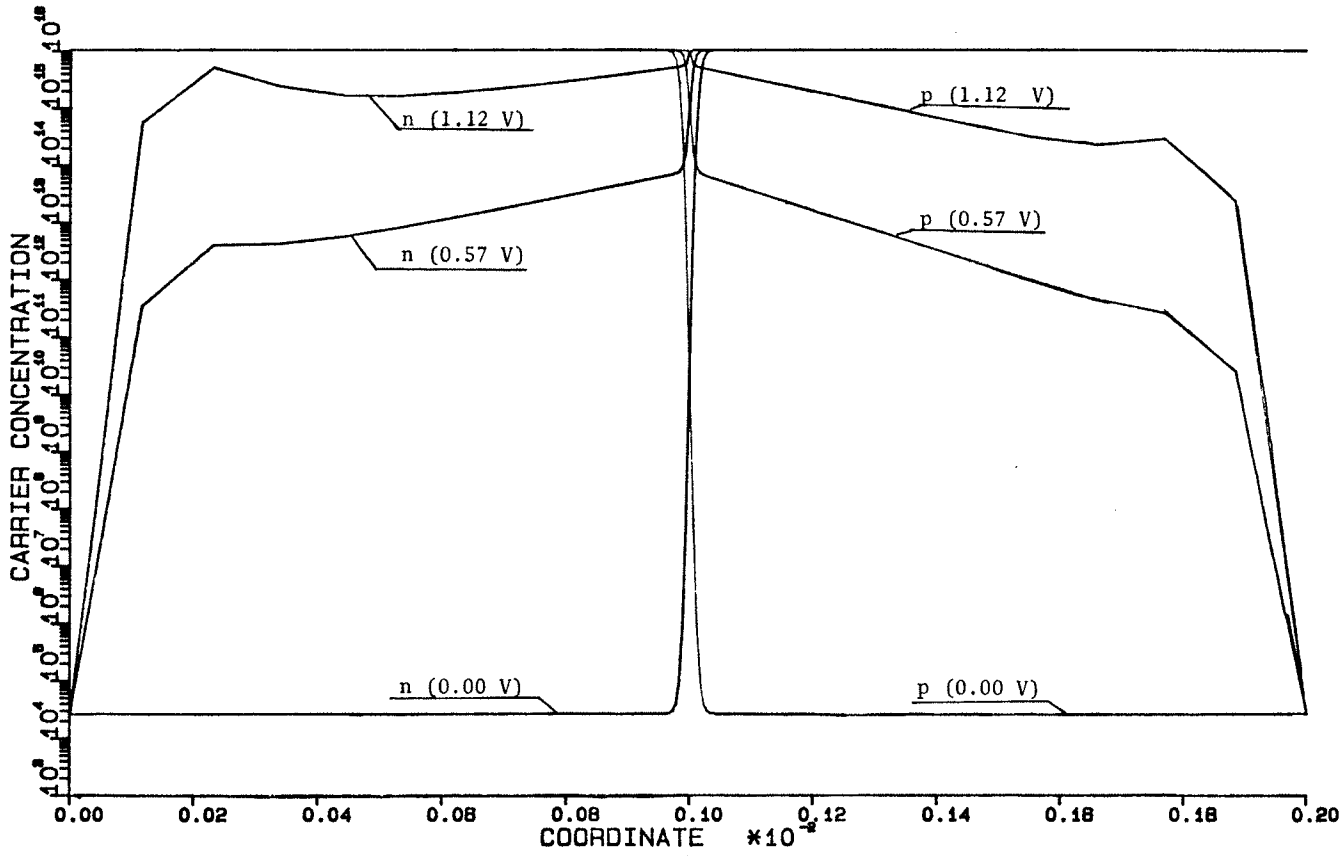

Figure 5.14: Carrier Concentration (Abrupt Junction)

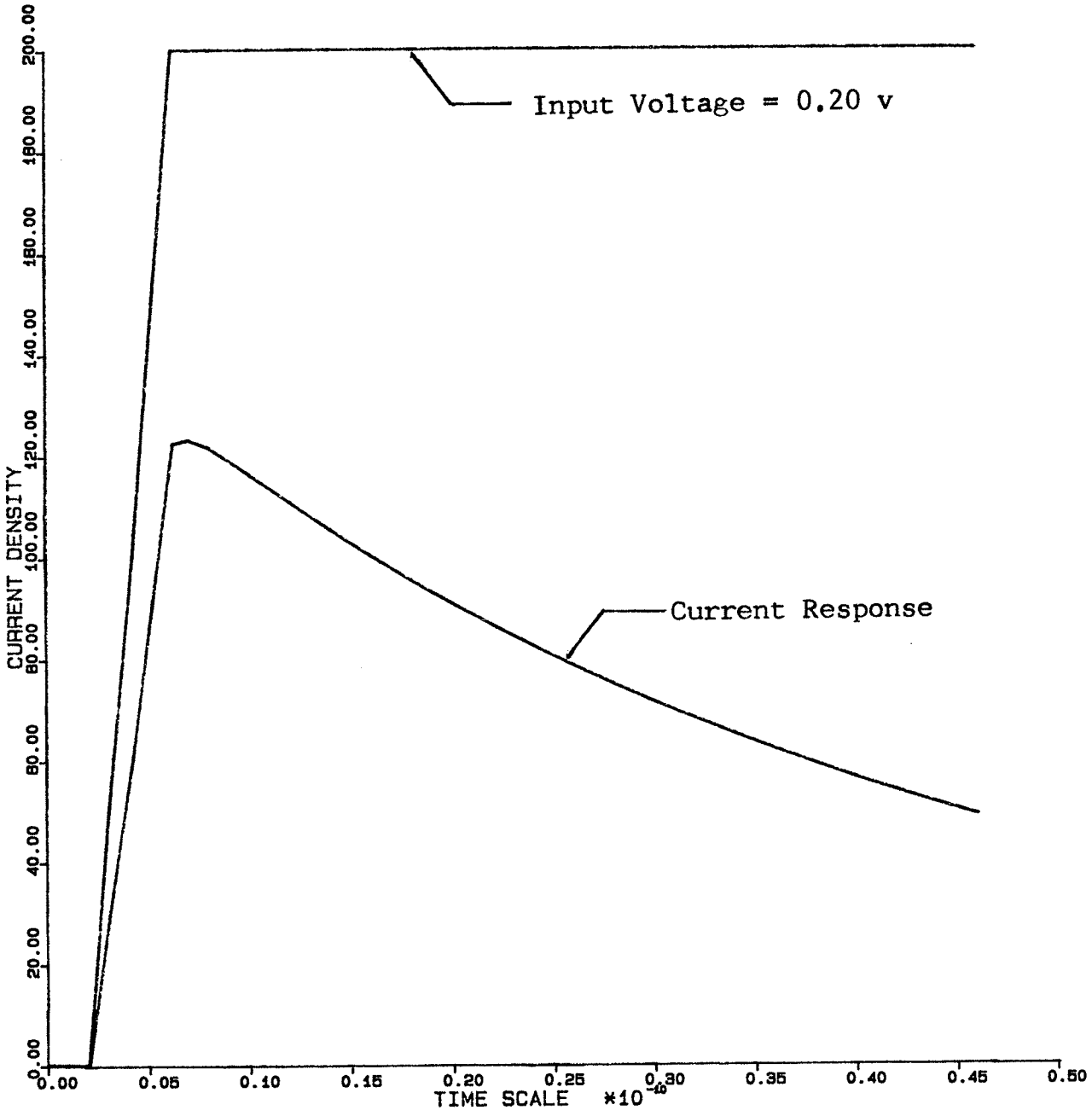

Figure 5.15: Transient Analysis (Abrupt Junction)

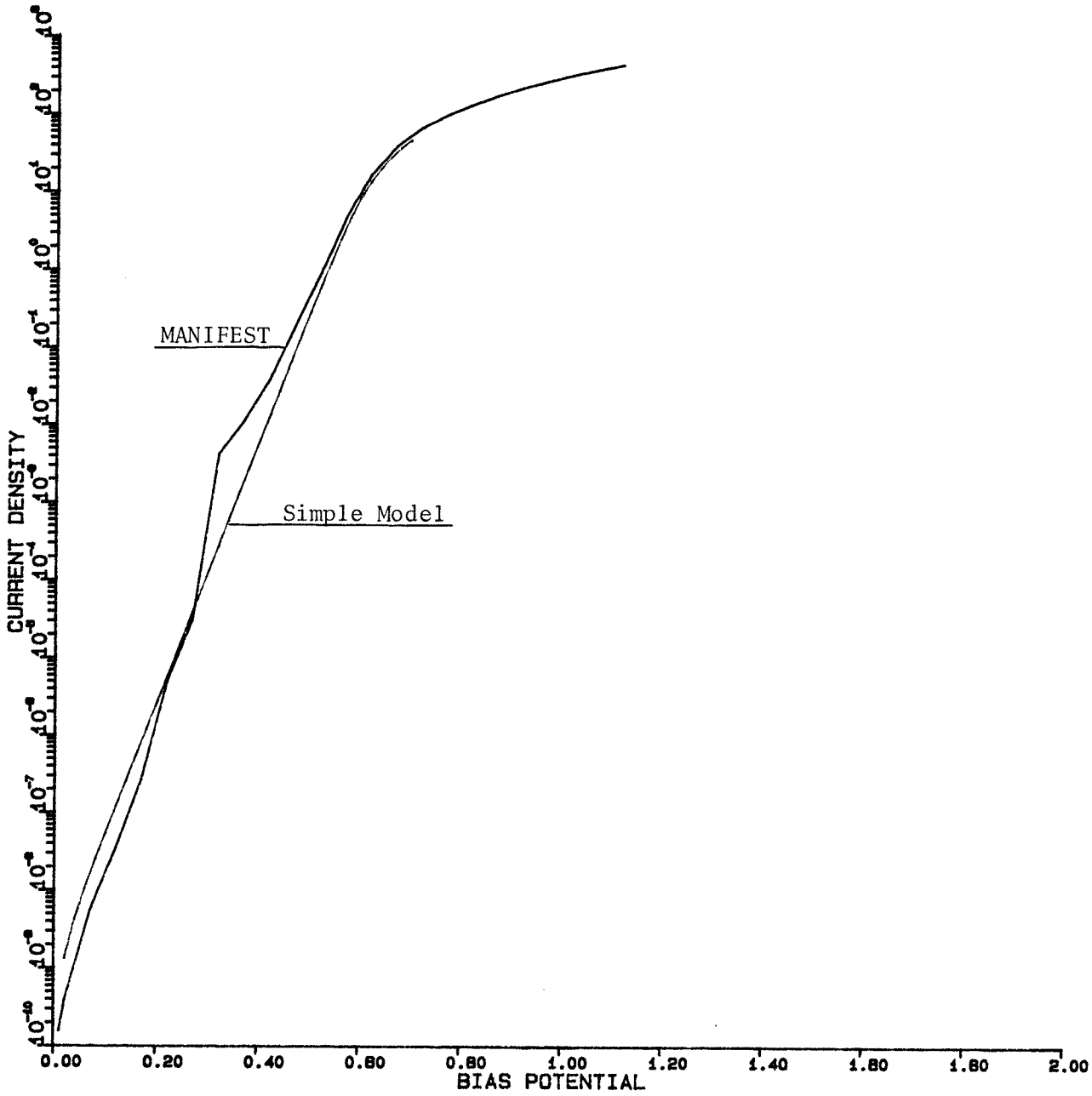

Figure 5.16: J_f vs. Voltage (Abrupt Junction)

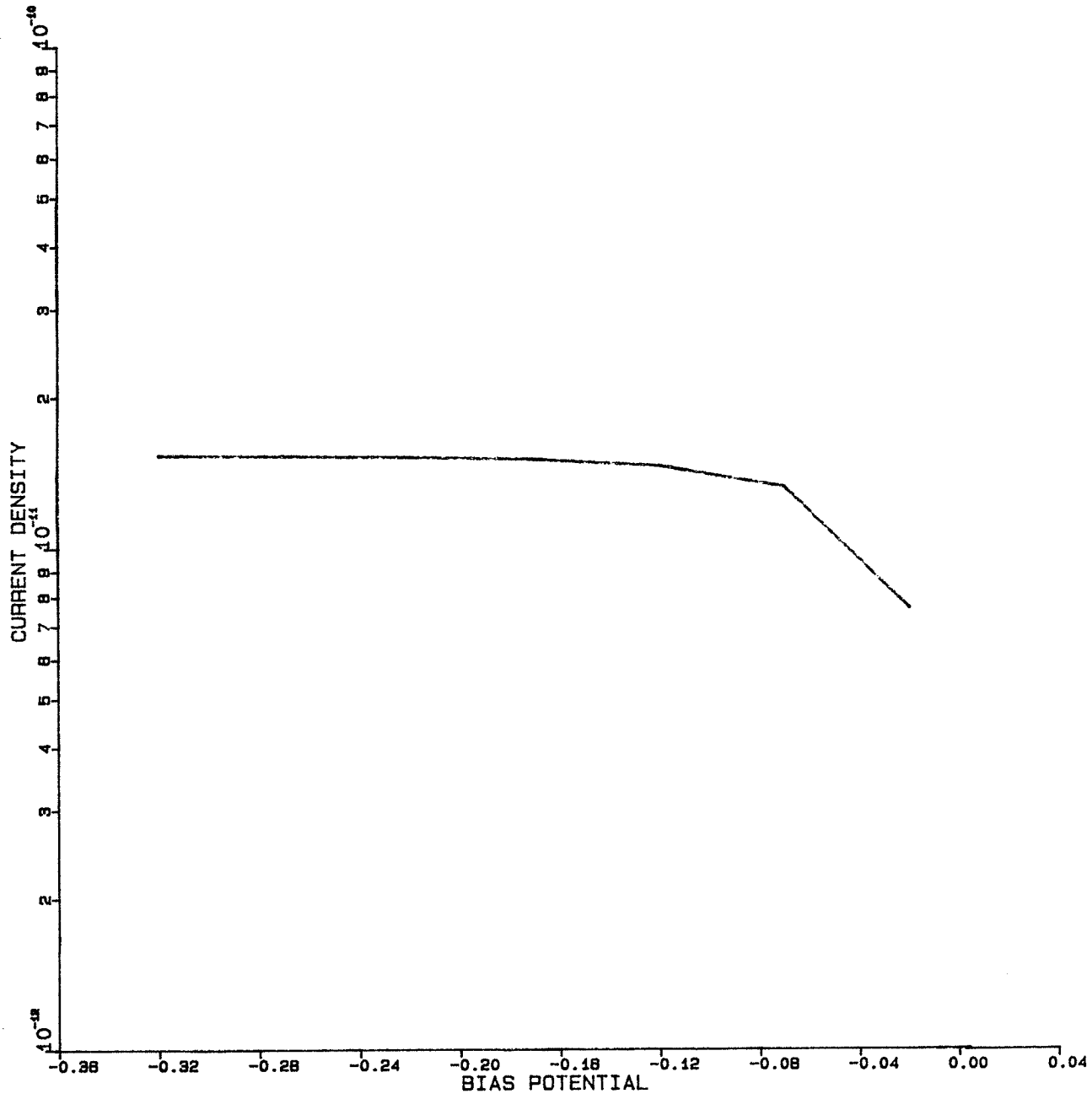

Figure 5.17: J_r vs. Voltage (Abrupt Junction)

The second P-N junction we shall consider has been studied by others [3, 48] and represents a device which is quite difficult to solve numerically. The doping profile is given by:

```
DOPE=(8.0E15)-(1.0E18*EXP(-(X**2)/1.864E-10)
```

for X between 0.0 and 2.0E-4 cm. The difficulty stems from the fact that the metal contacts are placed very close to the junction region. This, coupled with the chosen device parameters (see Table 5.5), leads to a very high recombination rate at the electrodes. These high recombination rates force the quasi-Fermi levels to undergo rapid changes near the device's boundaries. The finite-element method has difficulty modelling such phenomena.

Figure 5.18 illustrates the carrier profiles under forward bias potentials of 0.0 and 0.416 volts. In Figure 5.19, the result of a transient simulation for a step bias change of 0.3 volts is shown. Figures 5.20 and 5.21 present the forward and reverse current-voltage characteristics of the diffused junction diode. As with the abrupt-junction diode, the jump in current density near 0.25 volts (forward bias) is due to a high concentration of mid-bandgap traps.

Both of these diodes were modelled with a relatively large number of unknowns (93 nodes for the abrupt junction and 181 nodes for the diffused junction). In addition, 20 to 30 run-steps (i.e. increments in applied bias potential

or time) were used for each test. The total CPU time (on the Amdahl) ranged from 10 to 20 seconds for each complete solution.

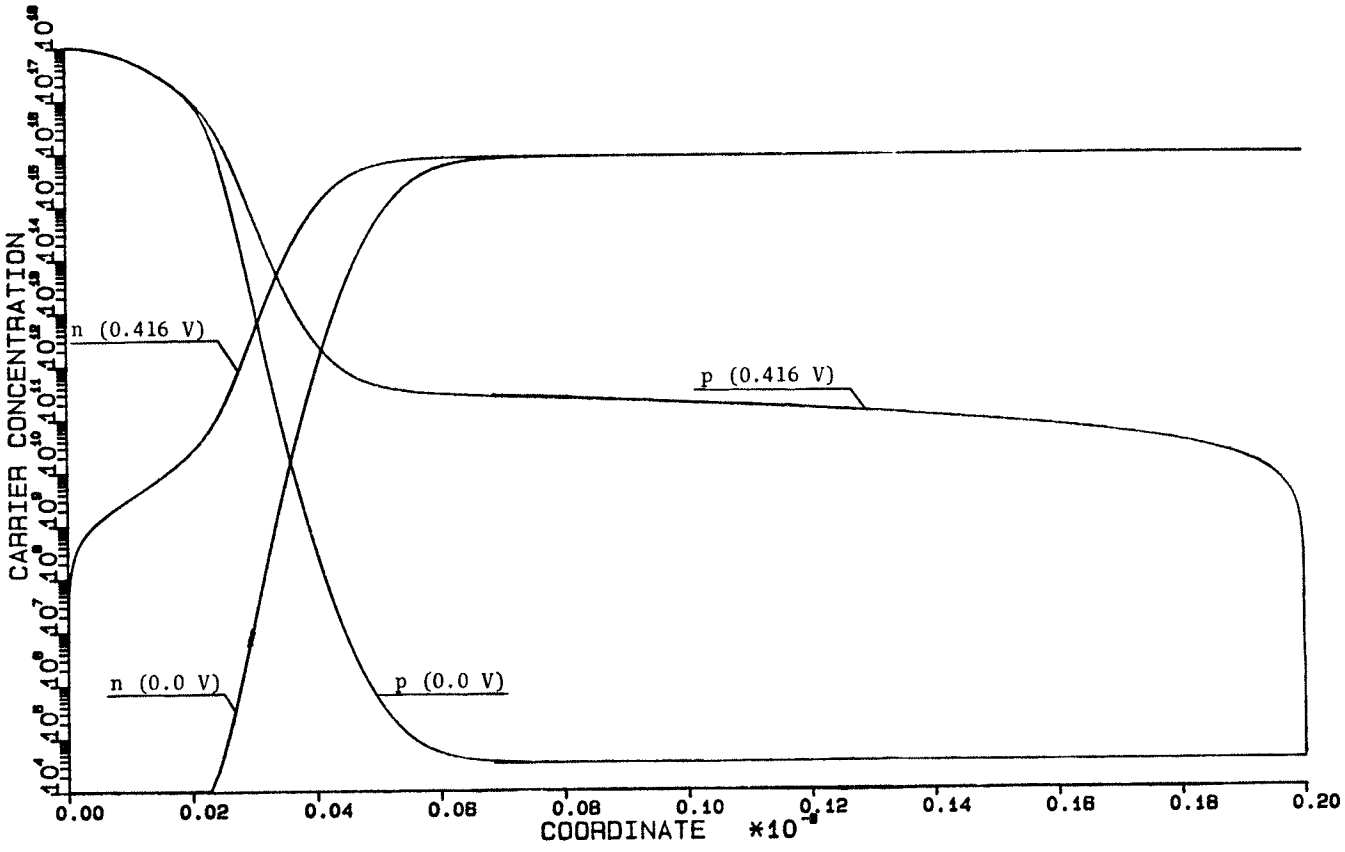

Figure 5.18: Carrier Concentration (Diffused Junction)

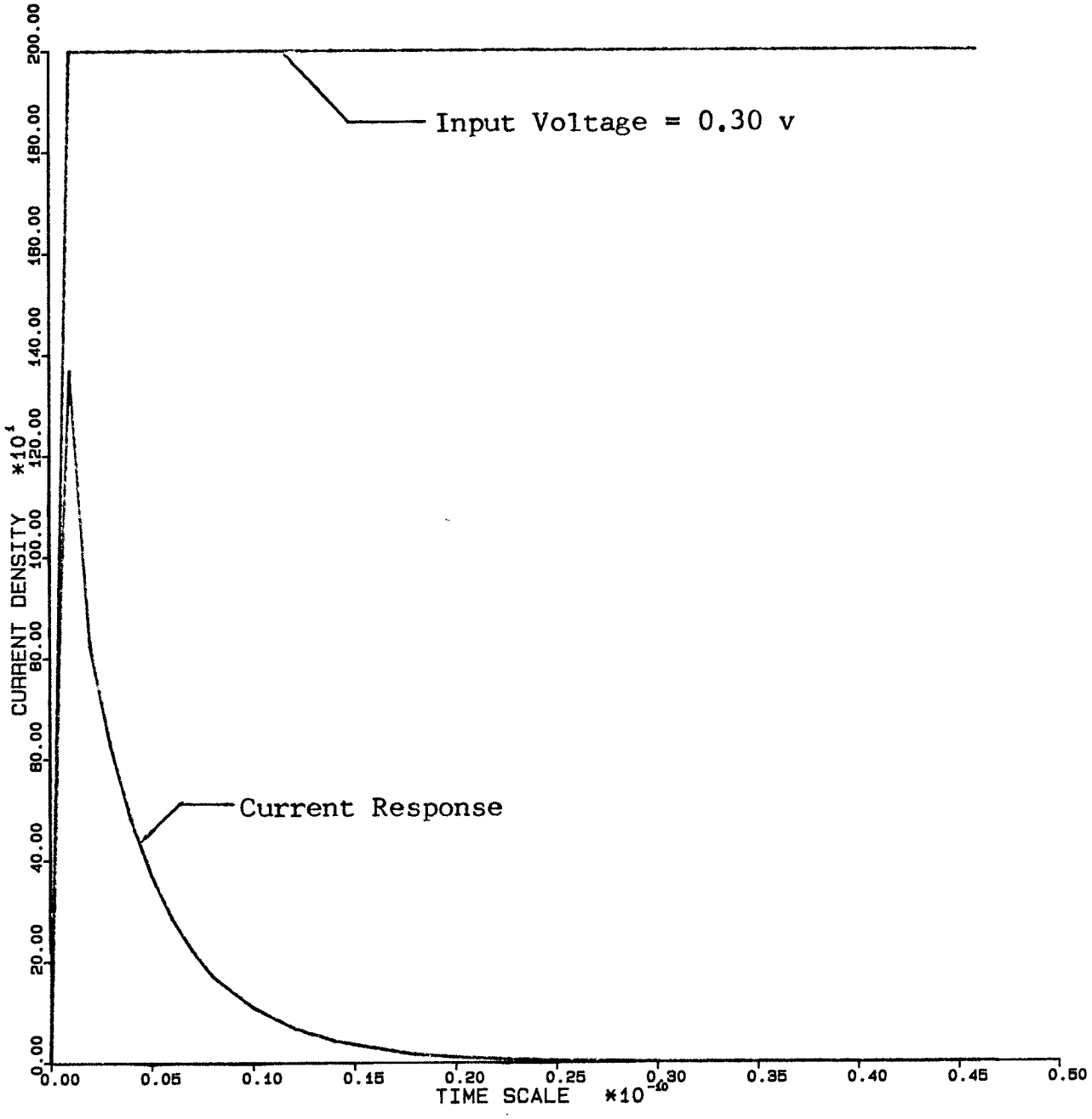

Figure 5.19: Transient Analysis (Diffused Junction)

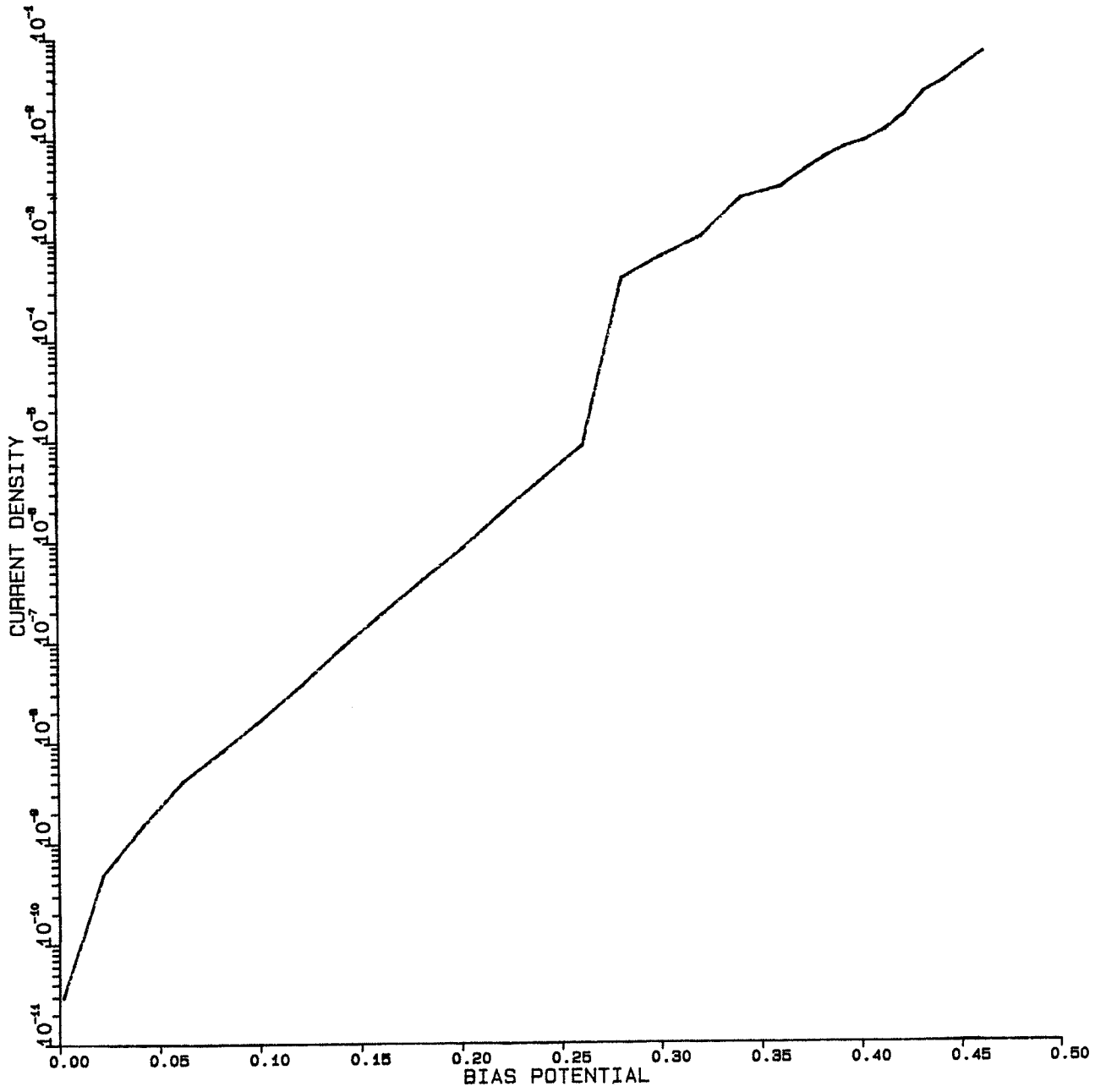

Figure 5.20: J_f vs. Voltage (Diffused Junction)

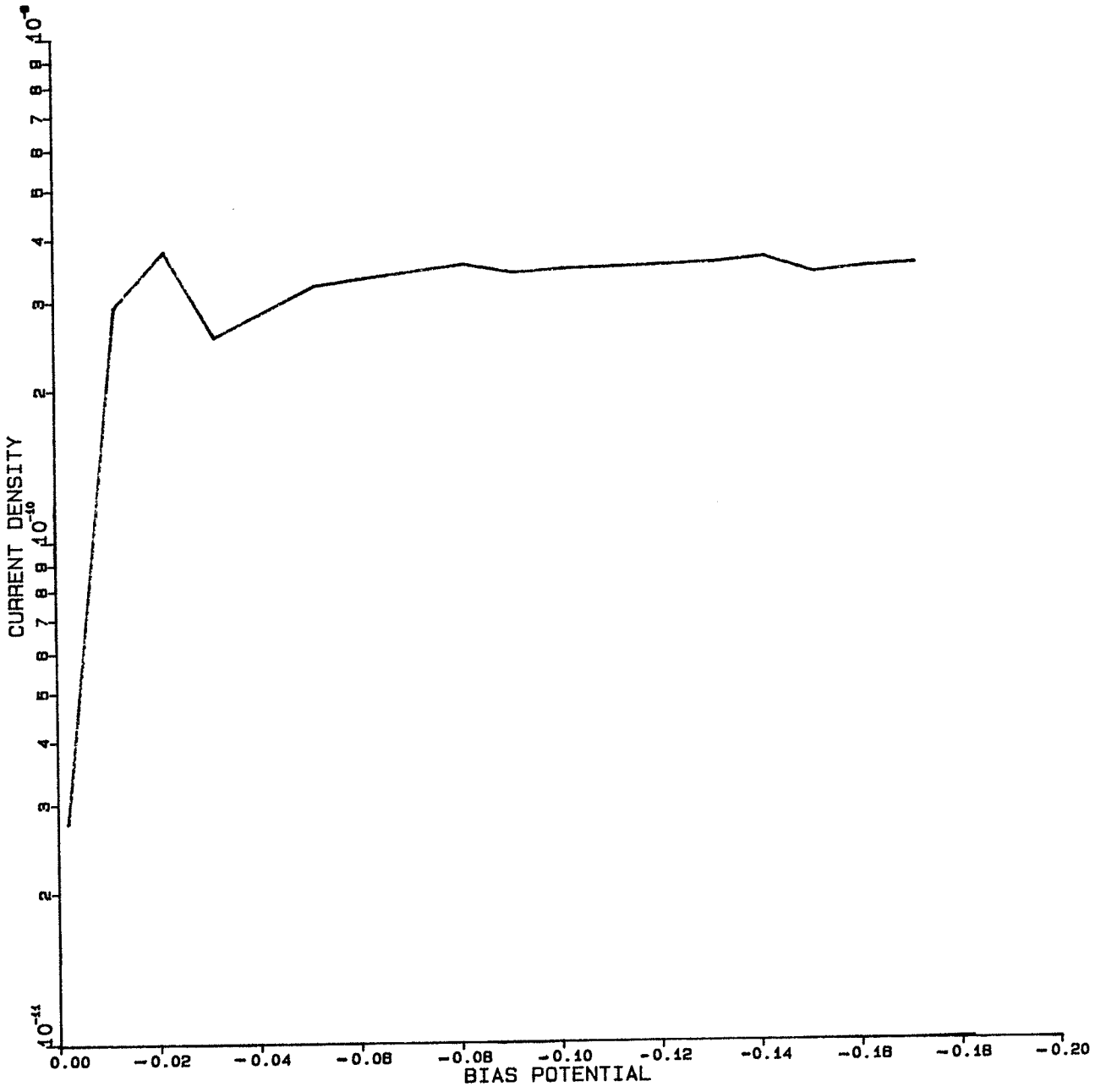

Figure 5.21: J_r vs. Voltage (Diffused Junction)

5.3 THE THYRISTOR

This example demonstates how one may obtain multivalued current-voltage characteristics using MANIFEST. Consider the one-dimensional thyristor shown in Figure 5.22. The doping profile for this device is similar to a thyristor model given by Kurata [9, pp. 116] except that all dimensions have been reduced by a factor of ten (i.e. the total device length is now 70 microns) and the relative width of the base region (W_{pb}) is somewhat narrower than in Kurata's case. Considering the high doping concentrations involved in this example, a total of 147 nodes were used in the mesh. All relevant system parameters are given by Table 5.6.

The complete J-V characteristics, illustrated in Figure 5.23, were obtained in two parts. The lower curve -- when the device is "off" -- is simply traced by incrementing the forward bias voltage (interactively) until the program failed to converge. By this technique, the forward blocking voltage (V_{bo}) was found to be approximately 1.07 volts. To obtain the upper curve -- where the device is "on" -- the base region is replaced by an equivalently doped n-region and this new "diode" is stepped up to a large forward bias (1.30 volts). At this point, the base region is gradually switched from n-type silicon to p-type silicon and the bias is decreased until a lower cutoff voltage is obtained (V_{co}=0.56 volts). This procedure is a legitimate approach

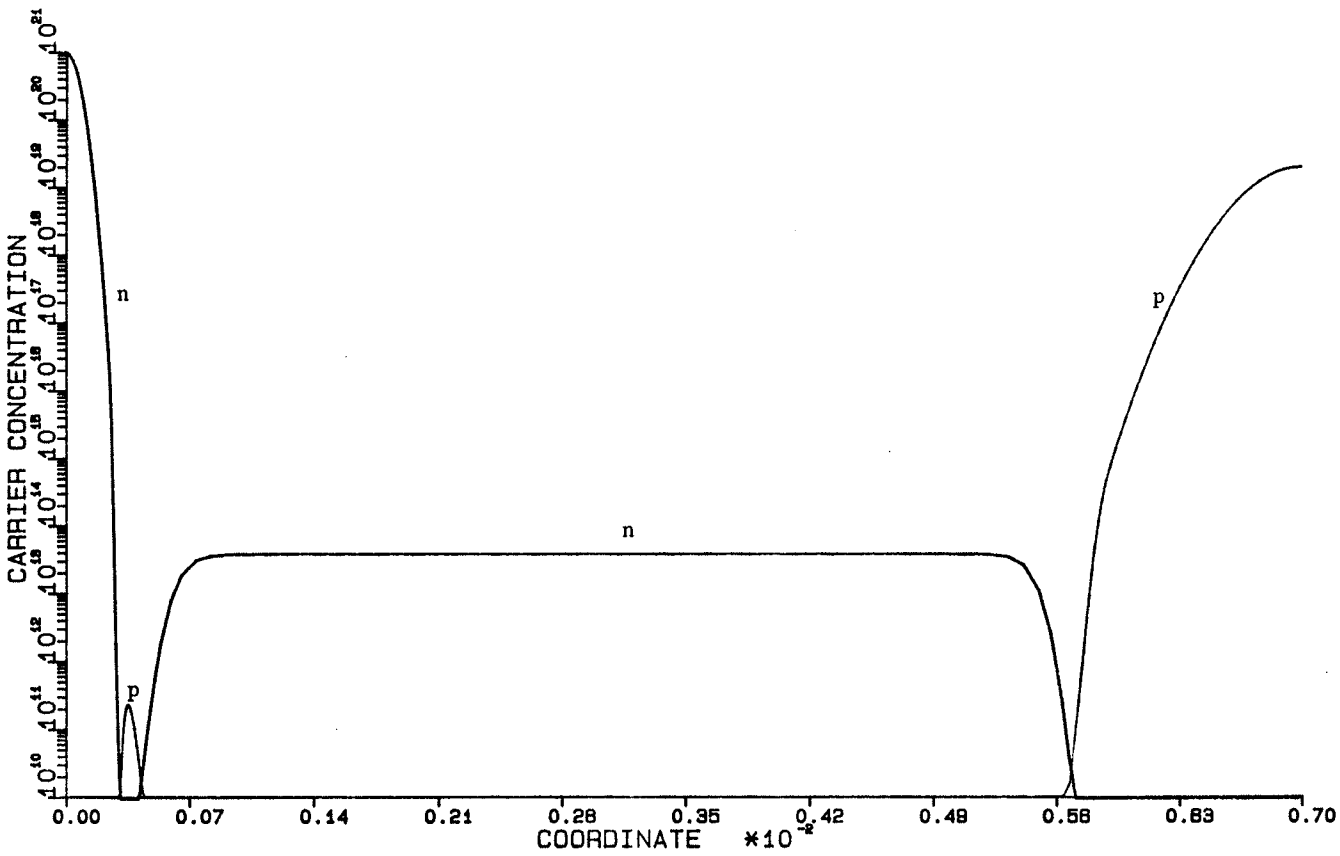

Figure 5.22: One-Dimensional Thyristor

TABLE 5.6

Thyristor Parameters

Parameter	Value	Units
TAU	1.0E-7	s
CNE	1.0E21	cm-3
CPB	5.0E18	cm-3
CNE	4.0E13	cm-3
CPE	2.0E19	cm-3
T	300.0	K
NI	1.6E10	cm-3
W	700.0E-5	cm
WOFF	38.0E-5	cm
WNE	27.5E-5	cm
WPE	15.5E-5	cm
UN	1500.0	cm2/v/s
UP	450.0	cm2/v/s
EPSON	11.8	

to obtaining bistable characteristics [9]. In general, V_{bo} and V_{co} can only be considered as lower and upper bounds to the true turning points in the S-type negative-resistance curve of the actual thyristor. Figure 5.24 gives the carrier concentrations at a forward voltage of 0.7 volts for which case the thyristor is "on" (i.e. conducting). Figure 5.25 gives an equivalent plot (again at 0.7 volts) when the thyristor is "off" (i.e. non-conducting).

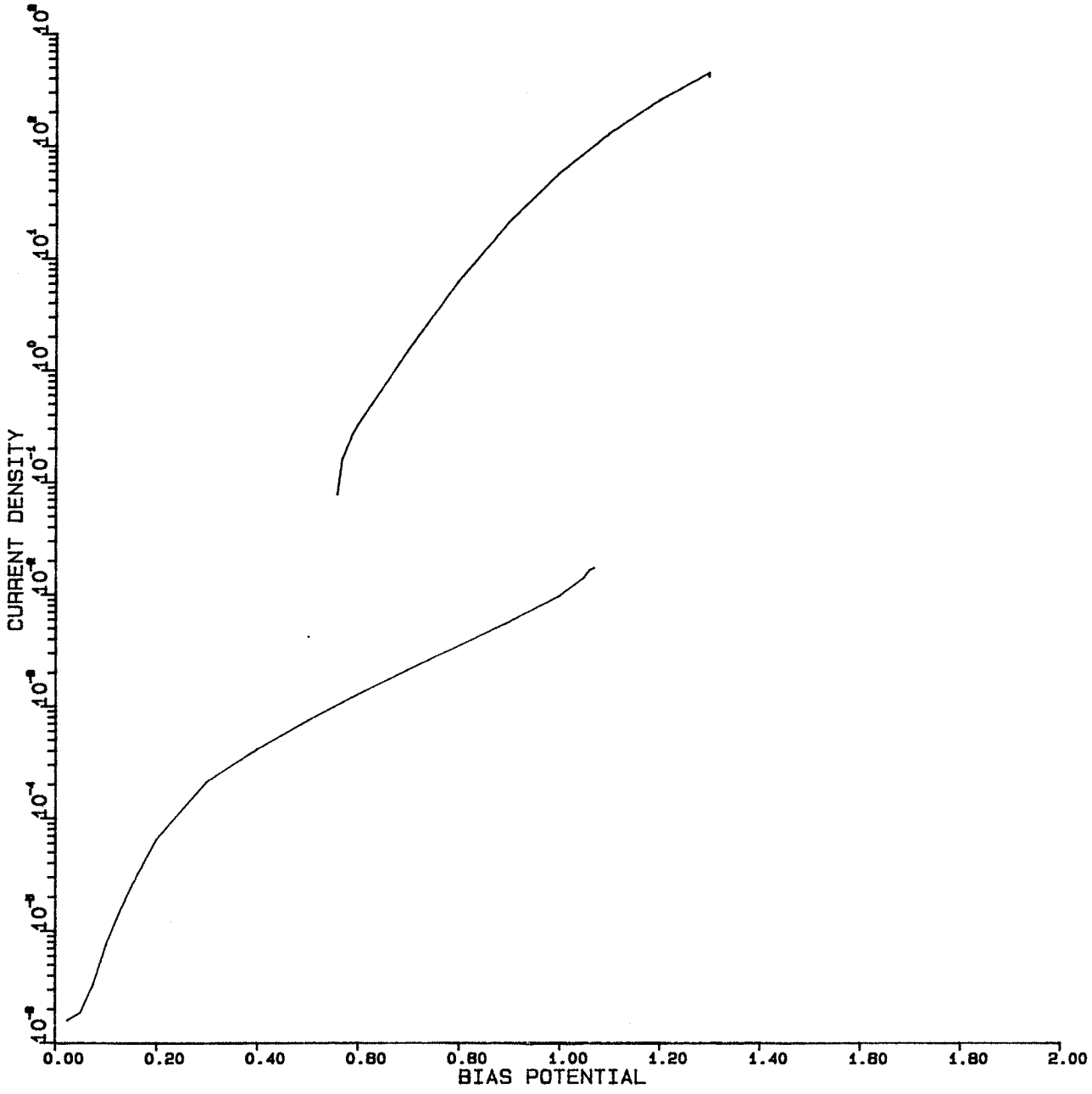

Figure 5.23: J-V Characteristics of Thyristor

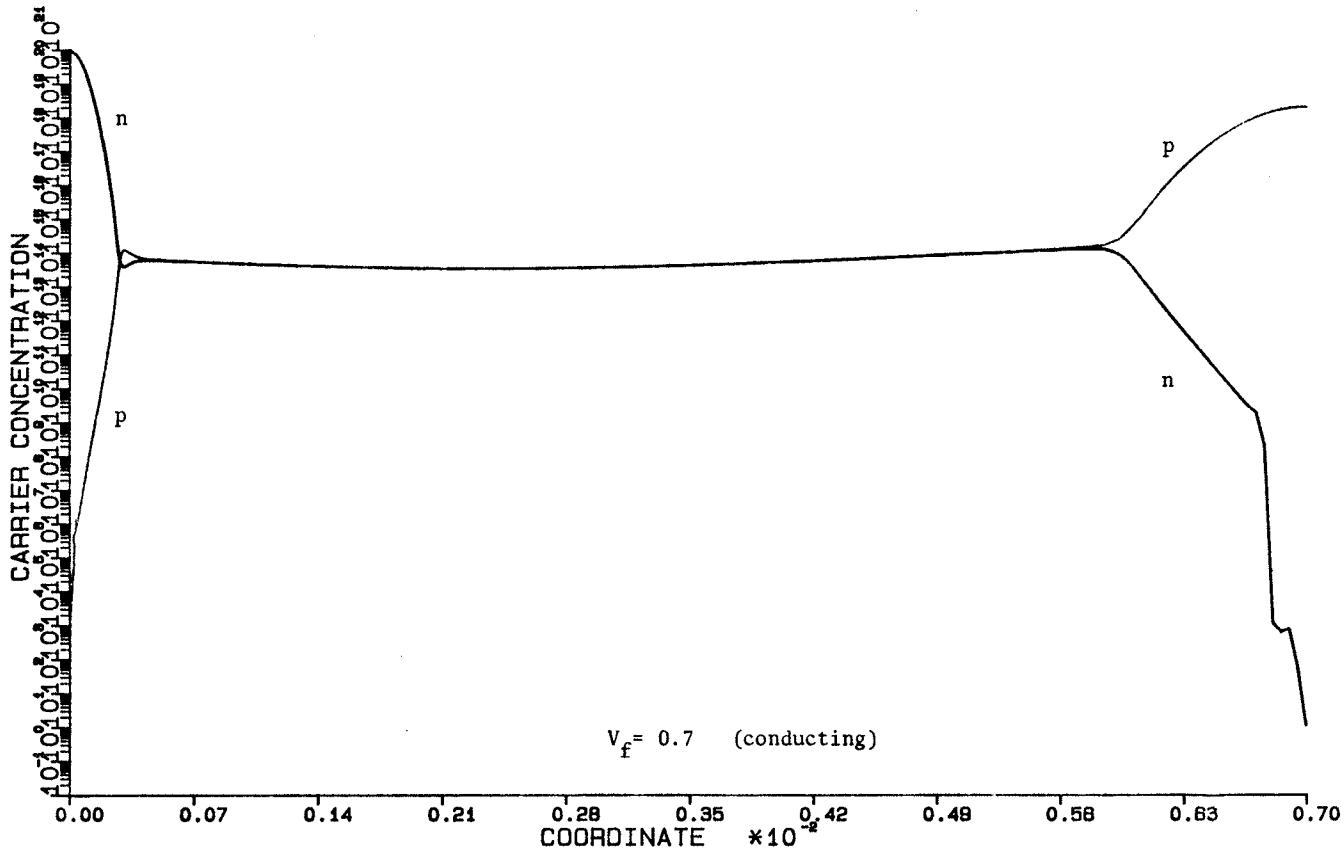

Figure 5.24: Carrier Concentrations of Thyristor (ON)

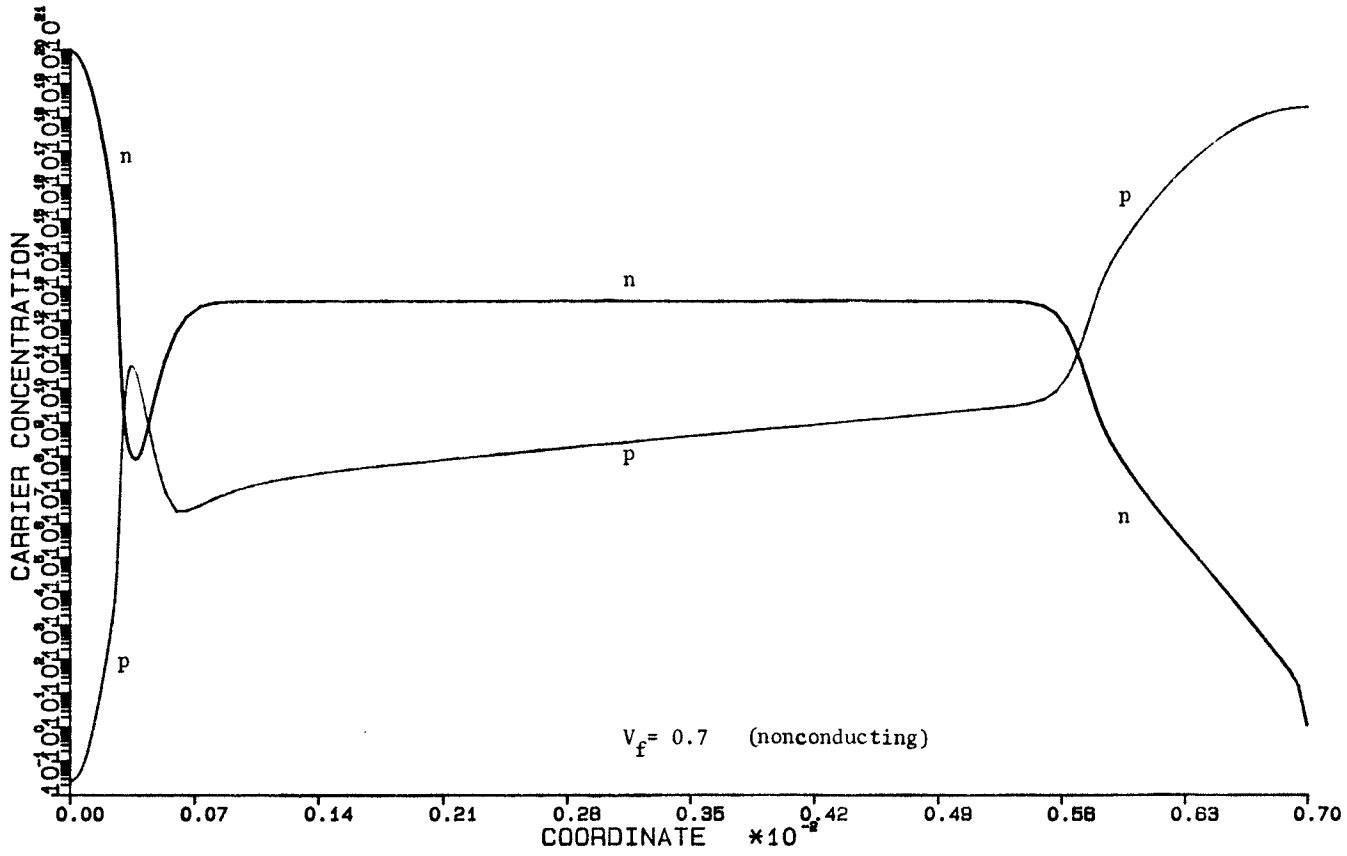

Figure 5.25: Carrier Concentrations of Thyristor (OFF)

5.4 GALLIUM ARSENIDE MESFET

As an example of the solution of a two-dimensional unipolar device, a GaAs MESFET was simulated using the mesh of Figure 5.26. A total of 433 nodes and 128 bi-quadratic elements form a nearly rectangular grid of 1.0 by 0.15 microns. Although the source and drain contacts would normally be placed along the top of the FET (i.e. parallel to the gate), we assume that they are sufficiently far from the active region that artificial contacts and be placed at S' and D' as indicated [49]. All other surfaces are treated as perfect insulators and modelled with a homogeneous Neumann boundary condition.

Assuming majority carriers dominate in the transport process, we solve only Poisson's equation and the steady-state (electron) current-continuity equation with the minority carrier term (i.e. p) set to zero. As a direct consequence, there will not be any significant bulk recombination. Hence the two equations needed to solve this problem may be written as:

$$\nabla \cdot (\varepsilon \nabla \Phi_s) = -q (N_d - n) \tag{5.1}$$

$$\nabla \cdot (q \mu_n n \nabla \Phi_n) = 0 \tag{5.2}$$

Table 5.7 summarizes the important device parameters used in this simulation.

TABLE 5.7

MESFET Parameters

Parameter	Value	Units
NI	1.8E6	cm-3
UN	5000	cm2/v/s
T	300	K
DOPE	1.0E16	cm-3
EPSON	12.5	

For this example, a Schottky barrier of height V_{bi} = -0.2 volts was established under the gate region. Three separate MANIFEST jobs were run with gate bias voltages of $V_{gs'}$ = -0.1, 0.0, and +0.1 volts. In each case, $V_{d's'}$ was stepped from 0.0 to 0.4 volts.

Figures 5.27 and 5.28 show the electrostatic (PHIS) and electron quasi-Fermi (PHIN) potentials under forward biases of $V_{d's'}$ = 0.025 and 0.4 volts with $V_{gs'}$ = 0.0 volts. Figure 5.29 is a current-density versus voltage plot for the three values of $V_{gs'}$. Each current-voltage curve required approximately 130 seconds of CPU time on the Amdahl computer.

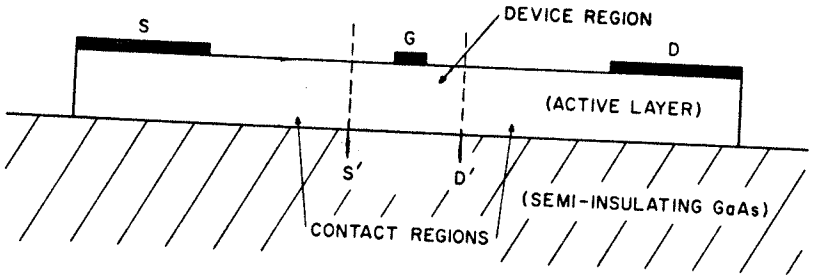

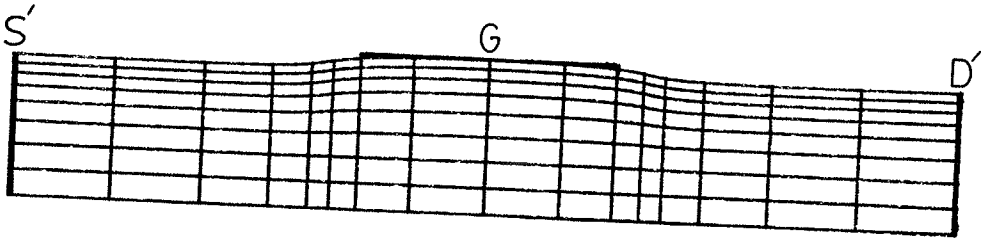

Figure 5.26: The GaAs MESFET

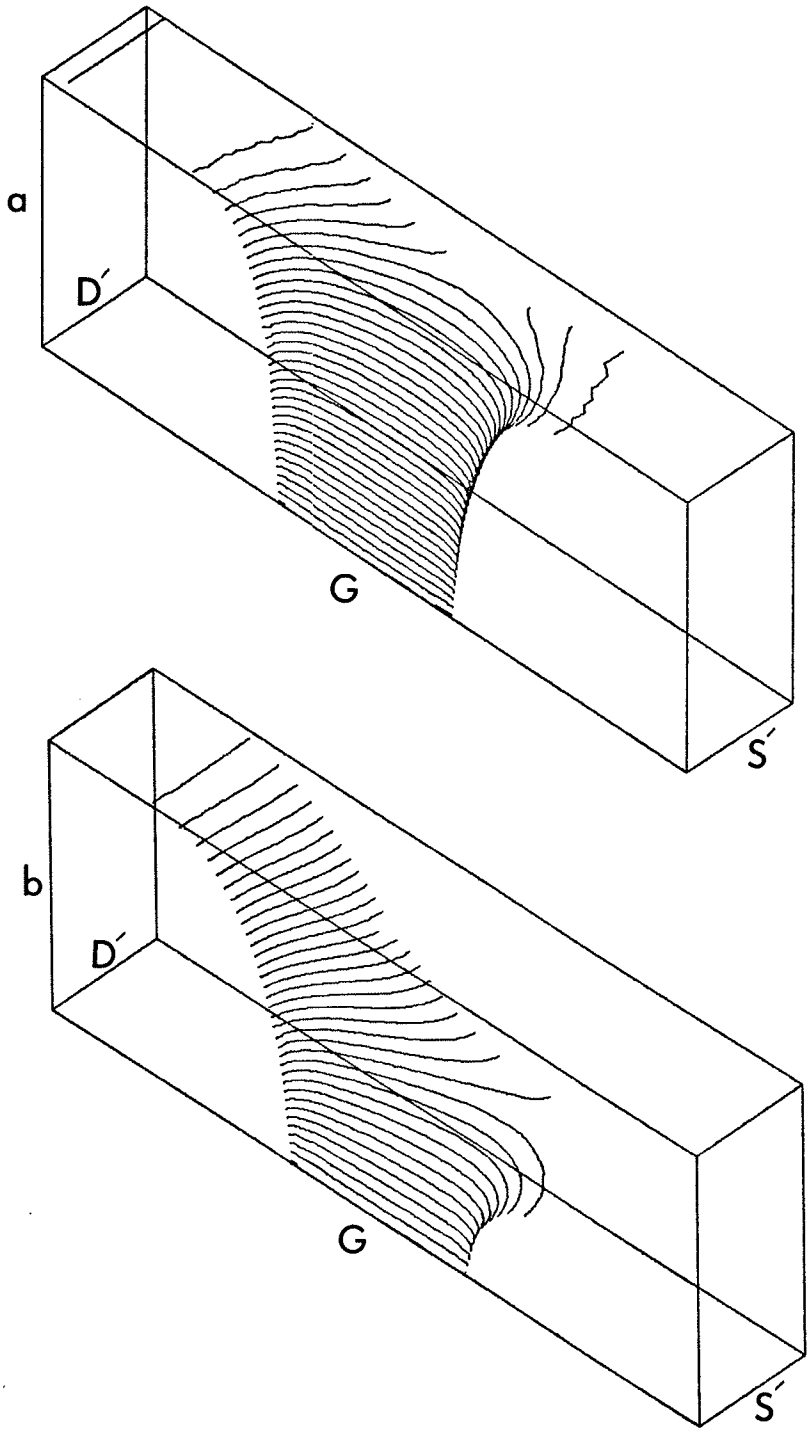

Figure 5.27: Electrostatic Potentials for MESFET (PHIS)

a) $V_{ds}' = 0.025$
b) $V_{ds}' = 0.400$
} $V_{gs}' = 0.0$ volts

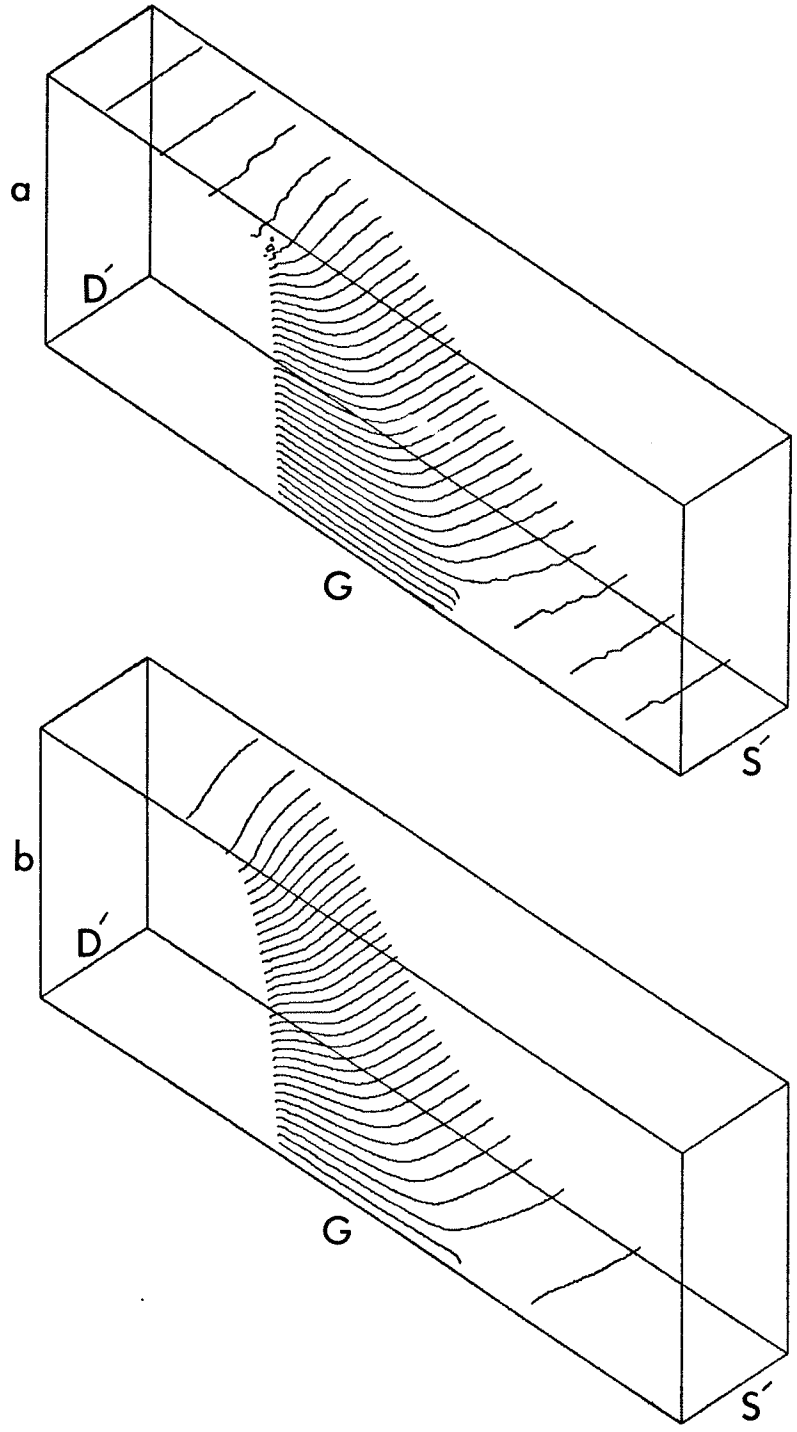

Figure 5.28: Fermi-Potentials for MESFET (PHIN)

a) $V_{ds}' = 0.025$
b) $V_{ds}' = 0.400$
} $V_{gs}' = 0.0$ volts

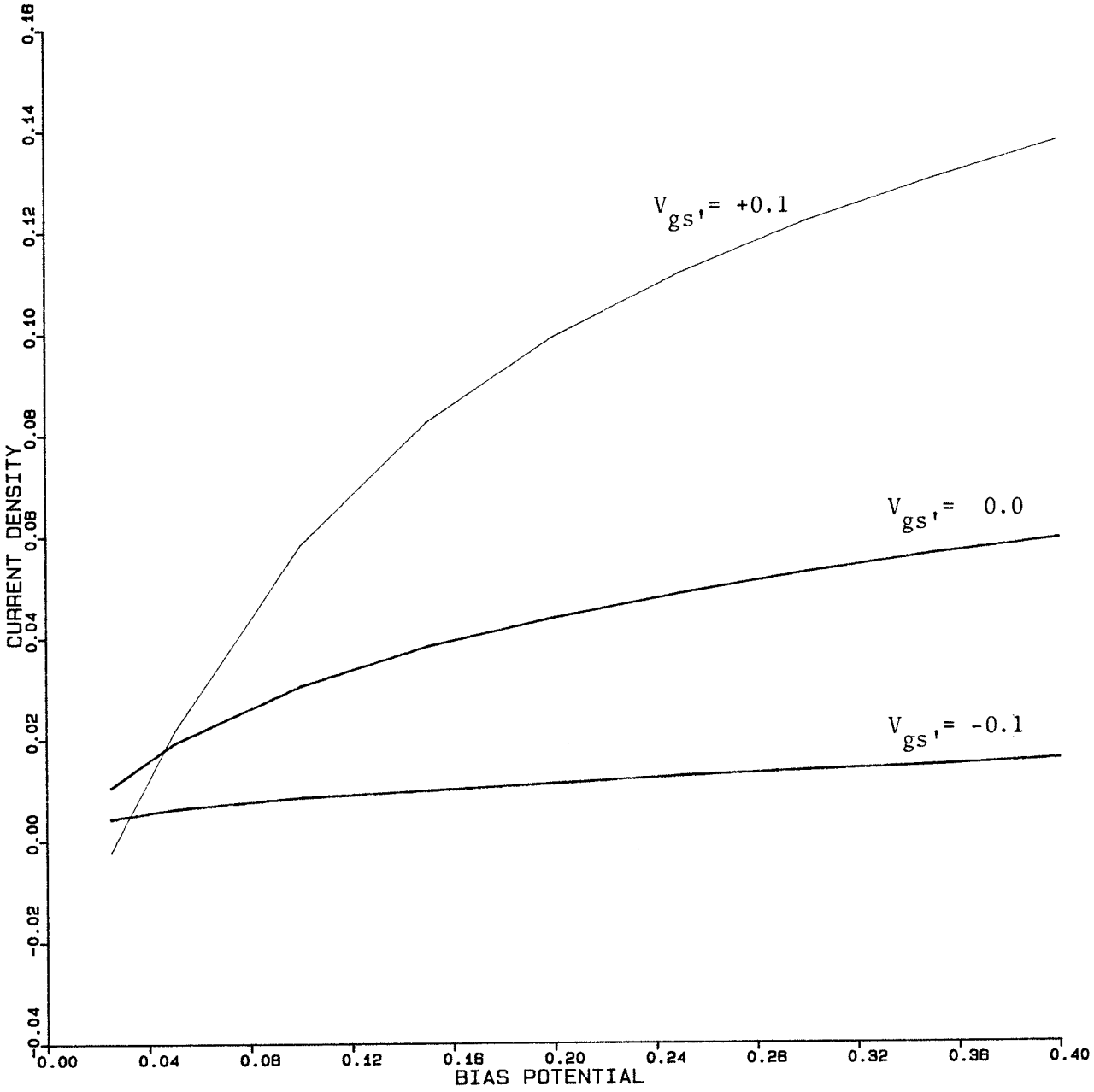

Figure 5.29: $J_{d'}$ vs. $V_{d's'}$ for MESFET

5.5 AXISYMMETRIC BIPOLAR TRANSISTOR

As an example of analyzing a three-dimensional device with MANIFEST-2D, consider the axisymmetric transistor in Figure 5.30. When described in cylindrical coordinates, there will be no variation of the device in one spatial dimension. Hence a 2D simulation will suffice for modelling this 3D problem.

TABLE 5.8

Transistor Parameters

Parameter	Value	Units
NI	1.4E10	cm-3
DOPE(E)	8.0E15	cm-3
DOPE(B)	(varying)	cm-3
DOPE(C)	2.0E15	cm-3
T	300	K
EPSON	11.8	

Rather than characterizing the transistor by deriving its current-voltage curves, we shall examine the behavior of the energy bands (under equilibrium conditions) as a function of the doping concentration in the base layer. These results provide a useful diagnostic tool to device designers [60]. The device's maximum radius is 1.5 microns and its thickness is 1.0 microns. As seen from Table 5.8, the emitter region (top) is doped to N_d= 8.0E15 cm-3 while the collector is

doped to N_d= 2.0E15 cm-3. Selected electrostatic potential plots are shown in Figures 5.31 and 5.32. The base region's doping level was increased in five steps of: N_a= 1.0E14, 1.0E15, 5.0E15, 1.0E16, and 2.0E16 cm-3.

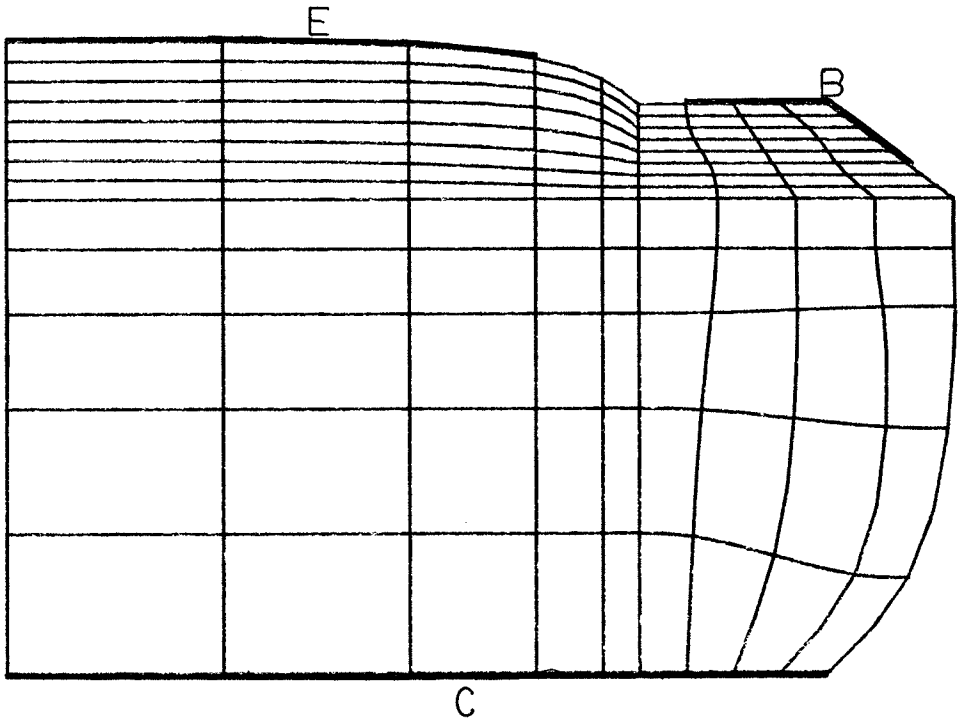

Figure 5.30: Axisymmetrical Bipolar Transistor

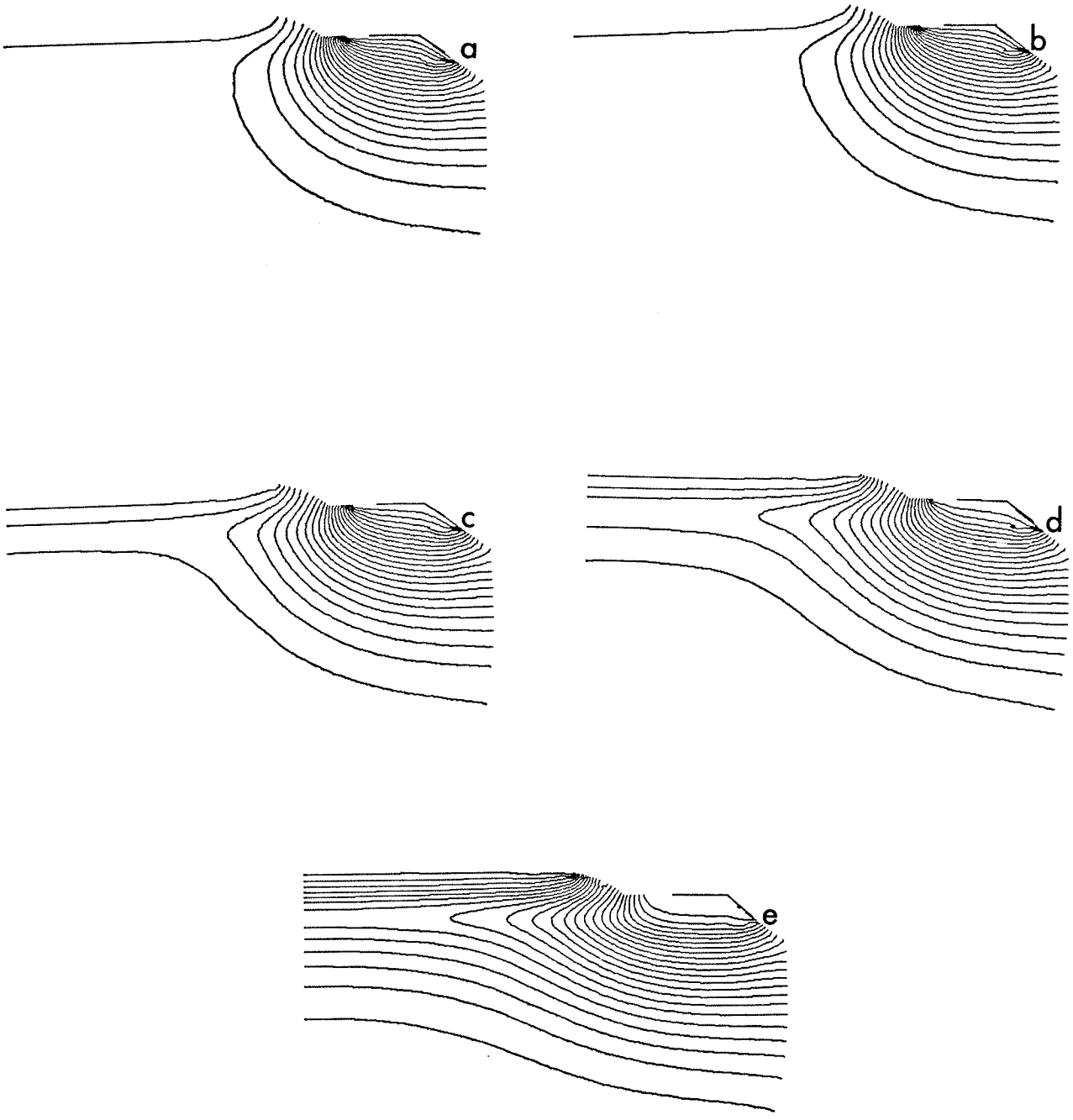

Figure 5.31: PHIS vs. N_a(base) for Transistor

a) Na= 1.0E14
b) Na= 1.0E15
c) Na= 5.0E15
d) Na= 1.0E16
e) Na= 2.0E16

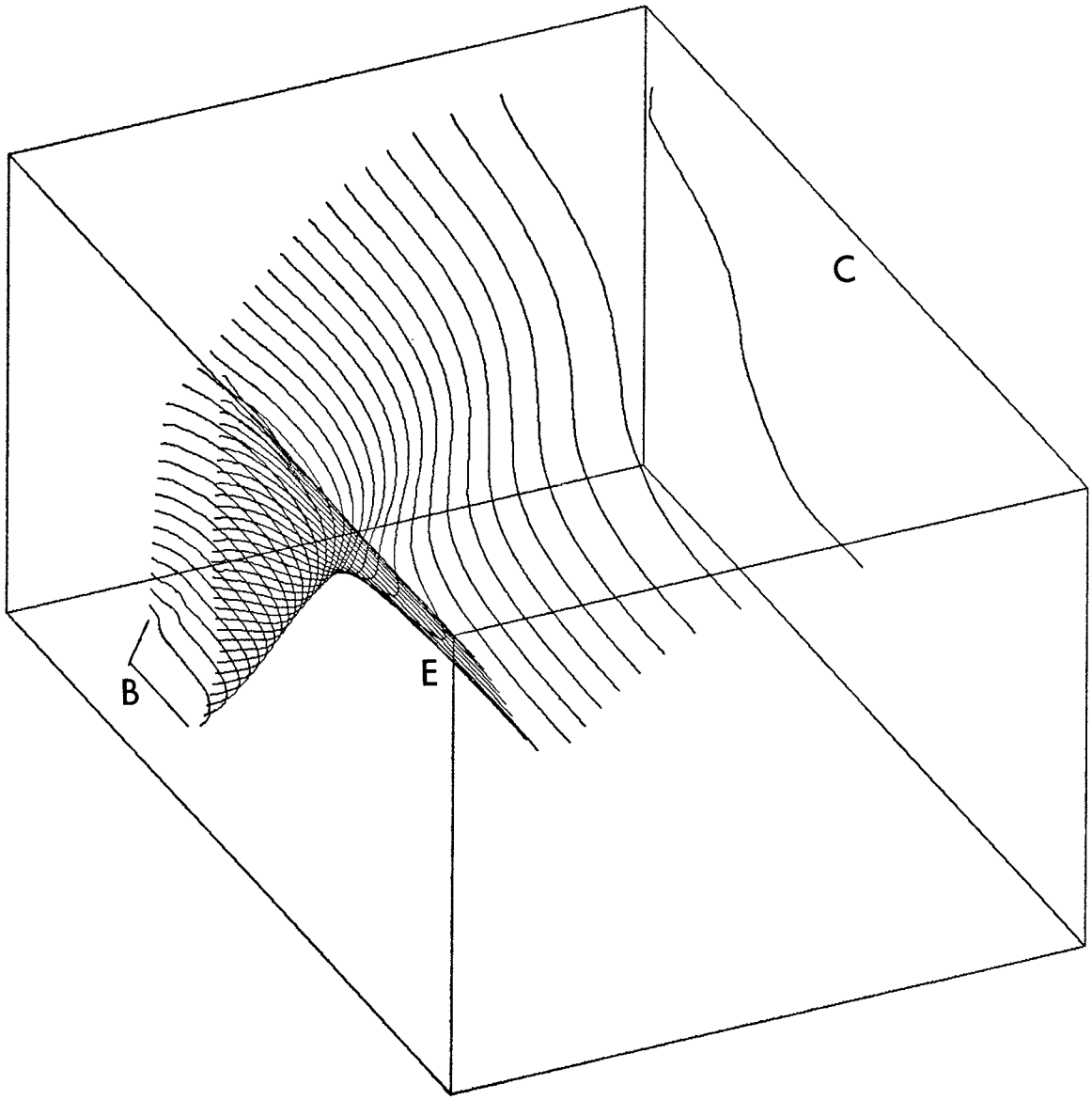

Figure 5.32: PHIS at N_a(base)= 2.0E16 cm-3

5.6 SMALL SCHOTTKY-BARRIER CONTACTS

To demonstrate the solution of a truly three-dimensional problem, the fields near the corner of a small Schottky contact were studied using MANIFEST-3D. In addition, an equivalent 1D model was used to show how leakage fields affect the capacitance of small devices. Figure 5.33 depicts this problem's geometry. Each side of the cubical region is 1.0 microns long.

The 2D mesh of Figure 5.34 was duplicated 10 times vertically to yield a 3D grid of 144 elements and 250 nodes. An eqivalent 1D grid of 9 linear elements and 10 nodes (with a total length of 1.0 micron) was used in the one-dimensional analysis. A GaAs substrate was doped to N_d= 1.0E15 cm-3 (n-type) and Dirichlet contacts were placed along the bottom and over a small square region on the top surface (0.5 by 0.5 microns giving an area of 0.25E-8 cm2). Assuming no additional fluxes can leak from the device, we have placed homogeneous Neumann boundaries everywhere else. In all, four barriers with V_{bi}= 0.0, -0.1, -0.2, and -0.3 volts were studied. A list of important device parameters is given in Table 5.9.

Both models (1D and 3D) were stepped from V= 0.0 to 0.4 volts forward bias. The Fermi-potentials for the one-dimensional case where V_{bi}= -0.2 volts and V= 0.2 volts is shown in Figure 5.35. Figures 5.36 through 5.38 illustrate the

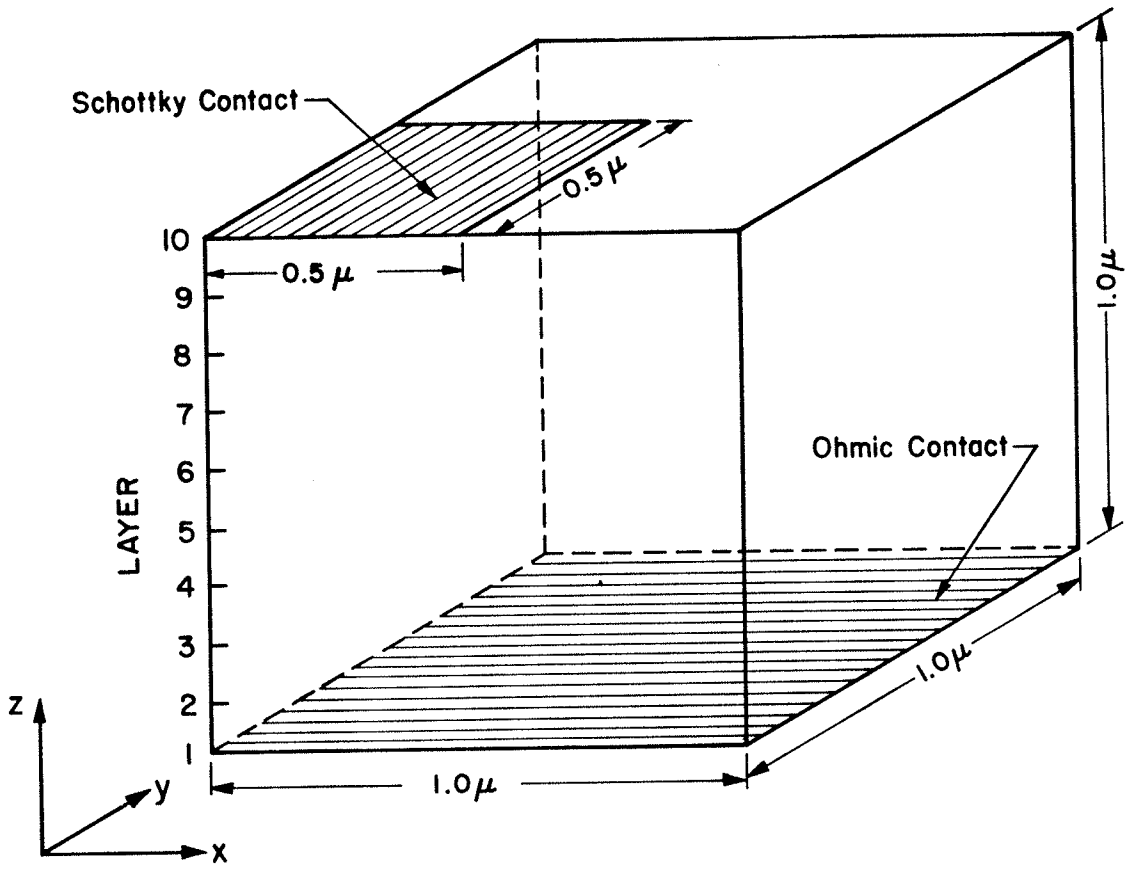

Figure 5.33: Three-Dimensional Schottky Contact

Fermi-potentials for the 3D model under equivalent conditions. A plot of energy content versus applied bias potential is given by Figure 5.39. To account for flux leakage in the 3D case, the energies were normalized by adjusting the effective area of the 1D model so as to ensure that the E-V curves matched when V_{bi} = 0.0 volts. This condition (in which the barrier height is zero) is equivalent to modelling a leaky, linear capacitor. The effective area required to convert the energy-density of the 1D model to energy-content of the 3D model was found to be 0.68E-8 cm2. The theoretical capacitance evaluates to approximately 0.77E-16 F (per-

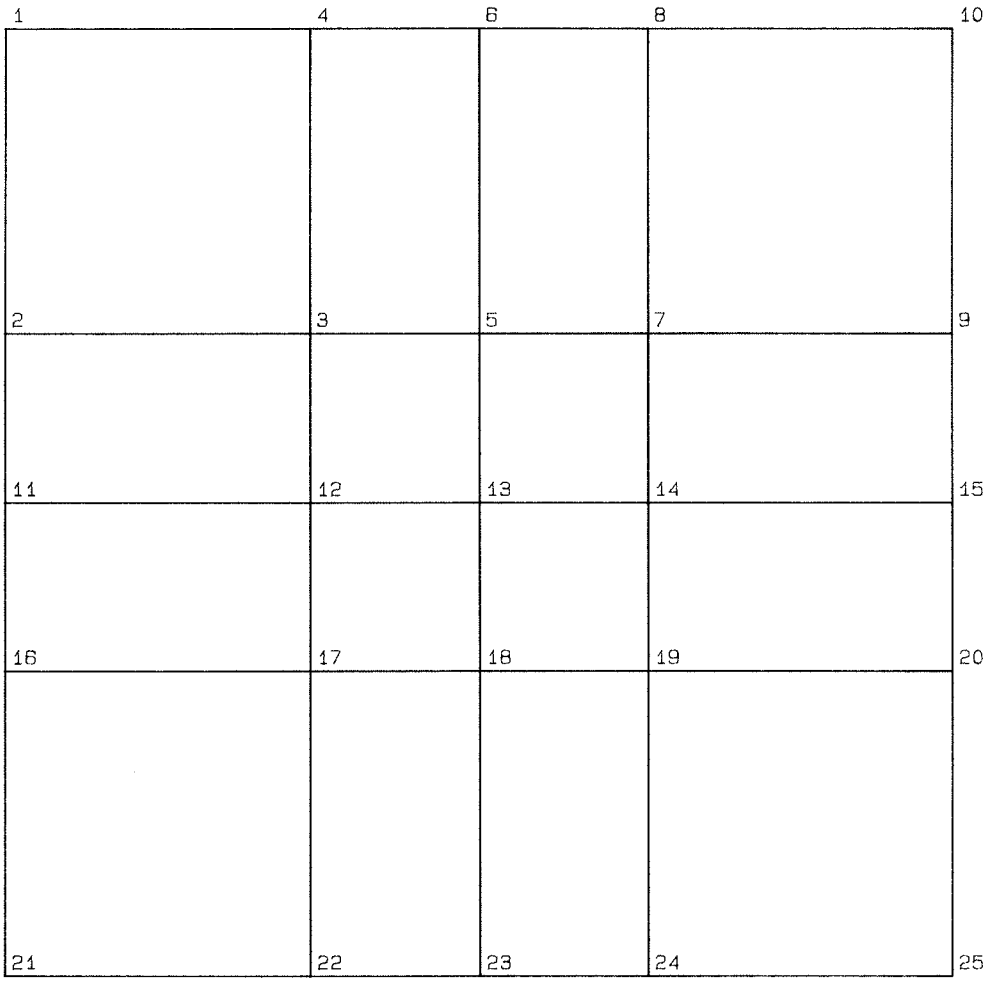

Figure 5.34: Fundamental 2D Mesh for 3D Grid

TABLE 5.9

Schottky Barrier Parameters

Parameter	Value	Units
TAU	5.0E-9	s
T	300.0	K
NI	1.8E6	cm-3
UN	8500.0	cm2/v/s
UP	400.0	cm2/v/s
DOPE	1.0E15	cm-3
EPSON	12.5	

mittivity times effective area divided by depth). As presented, there are four pairs of energy-voltage curves corresponding to the specified barrier height. The upper curve of each pair is for the 1D model while the lower curve is for the 3D device. Although the energy curves appear to be quite close, the capacitance plots in Figures 5.40 and 5.41 have qualitatively different behavior. This is because these capacitance curves are dependent upon the second derivative of the E-V curves. The C-V characteristics for the 1D case are similar to those measured for appreciable forward bias voltages on large Schottky contacts [61].

CPU times on the Amdahl varied between 10 and 15 minutes for each capacitance curve.

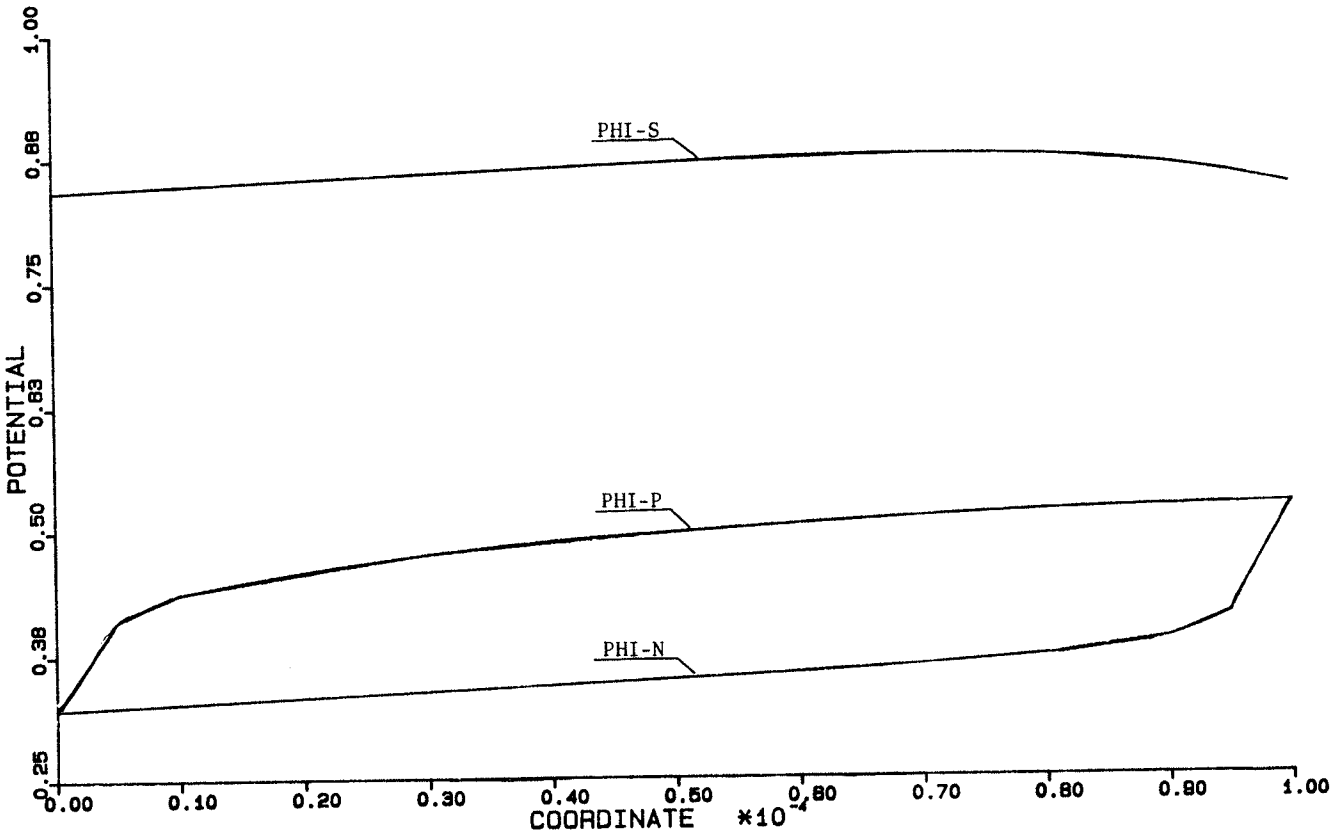

Figure 5.35: Fermi-Potentials of 1D Schottky Contact

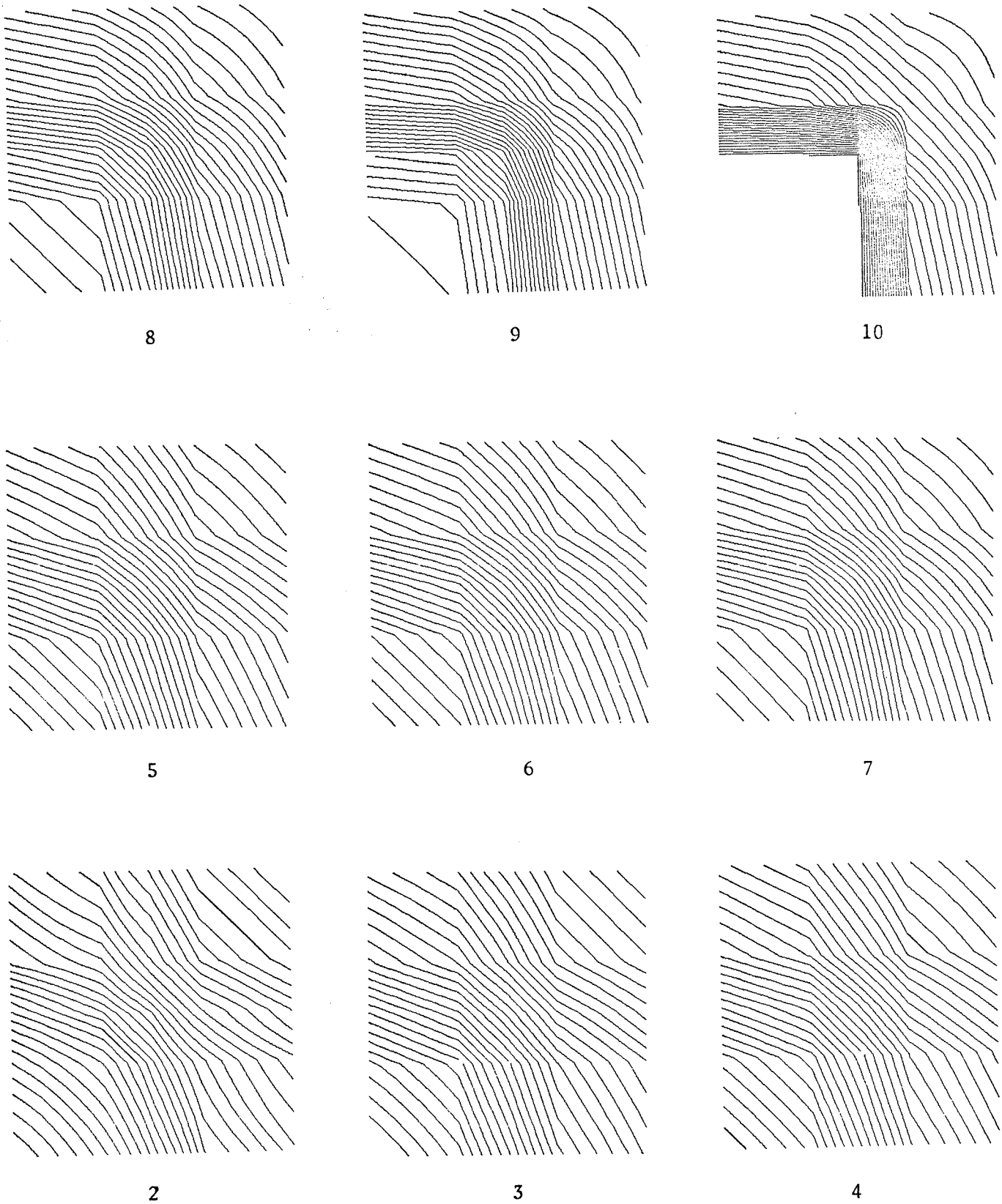

Figure 5.36: Potential of 3D Schottky Contact (PHIS)

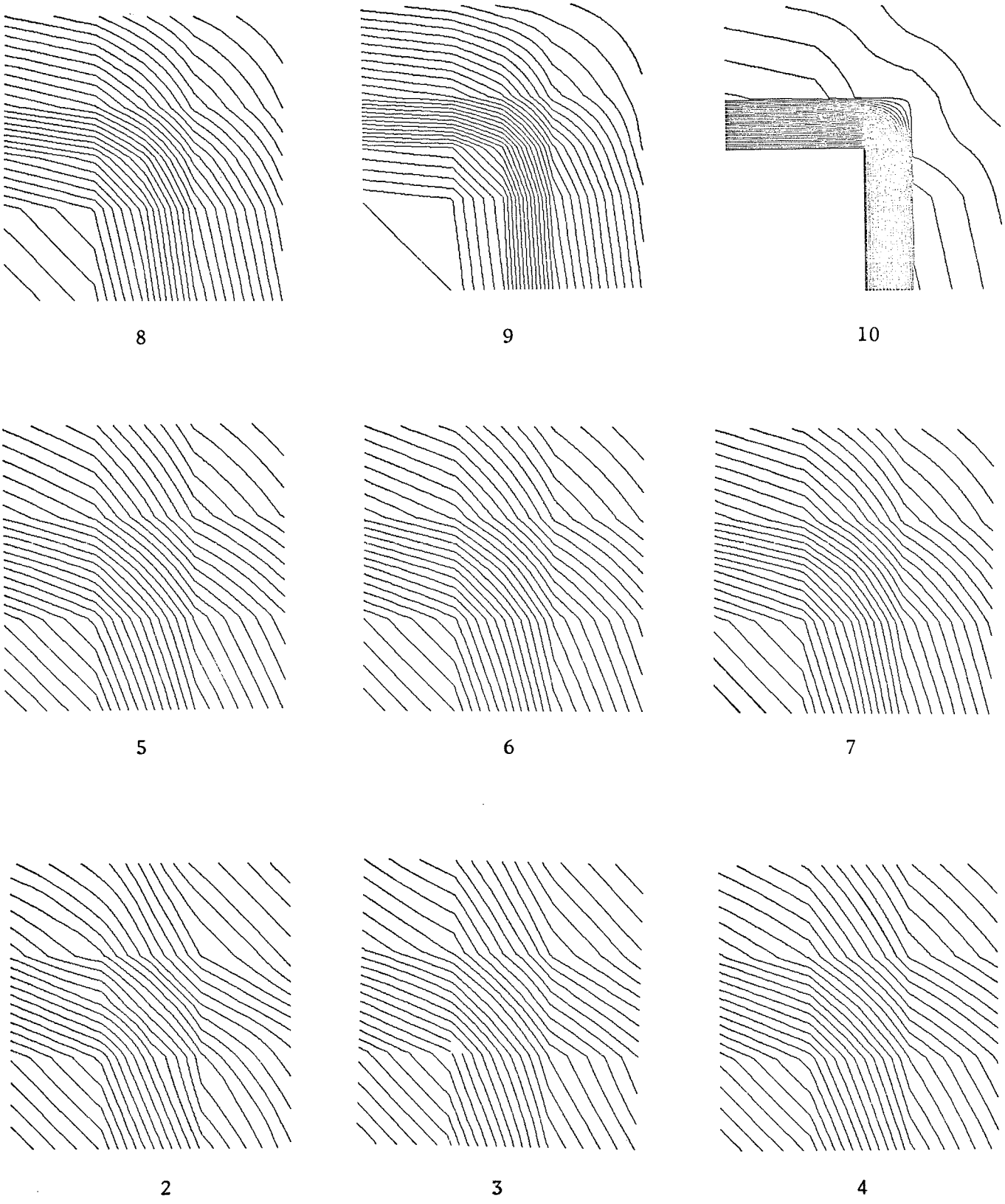

Figure 5.37: Fermi-Potential of 3D Schottky Contact (PHIN)

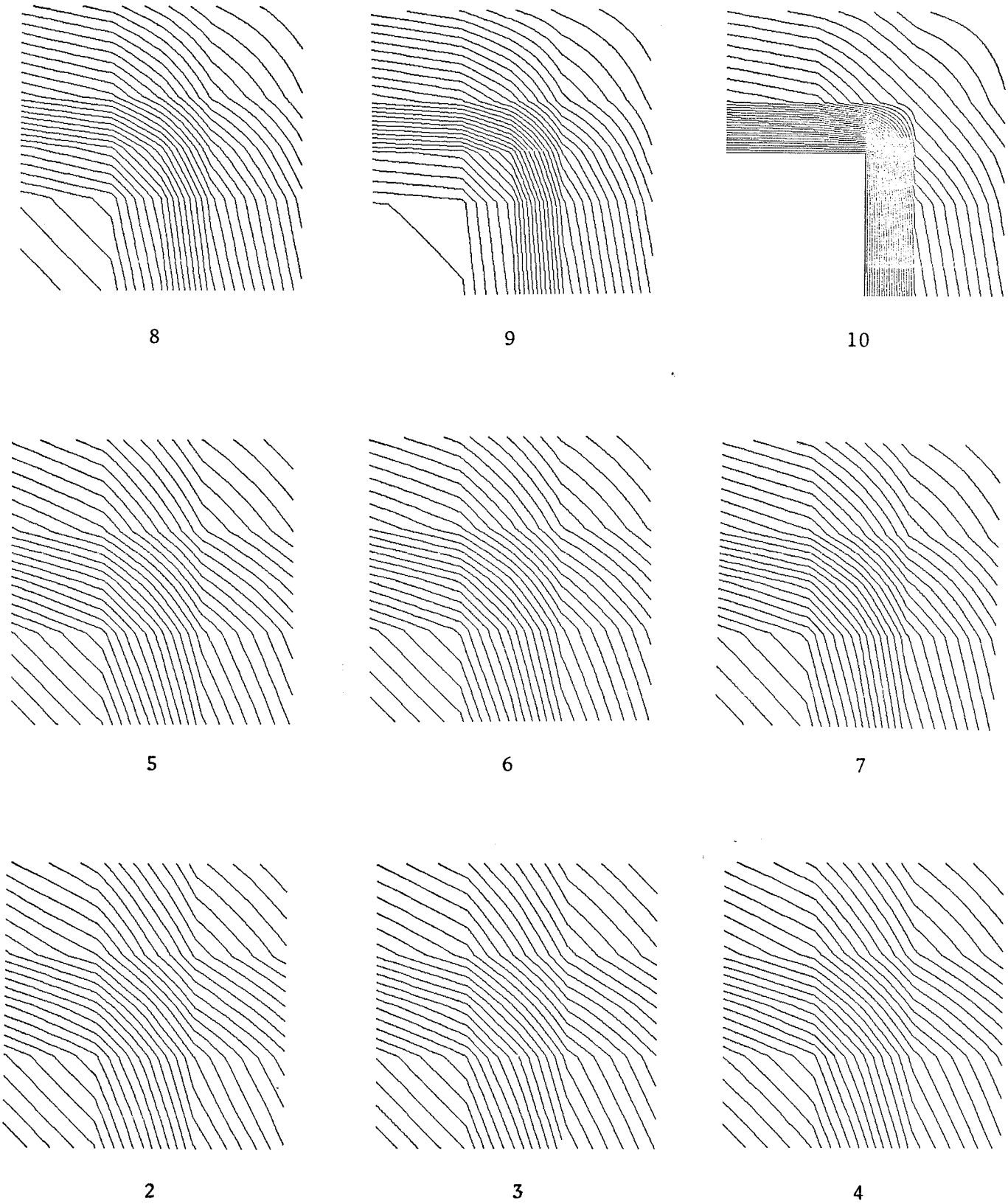

Figure 5.38: Fermi-Potential of 3D Schottky Contact (PHIP)

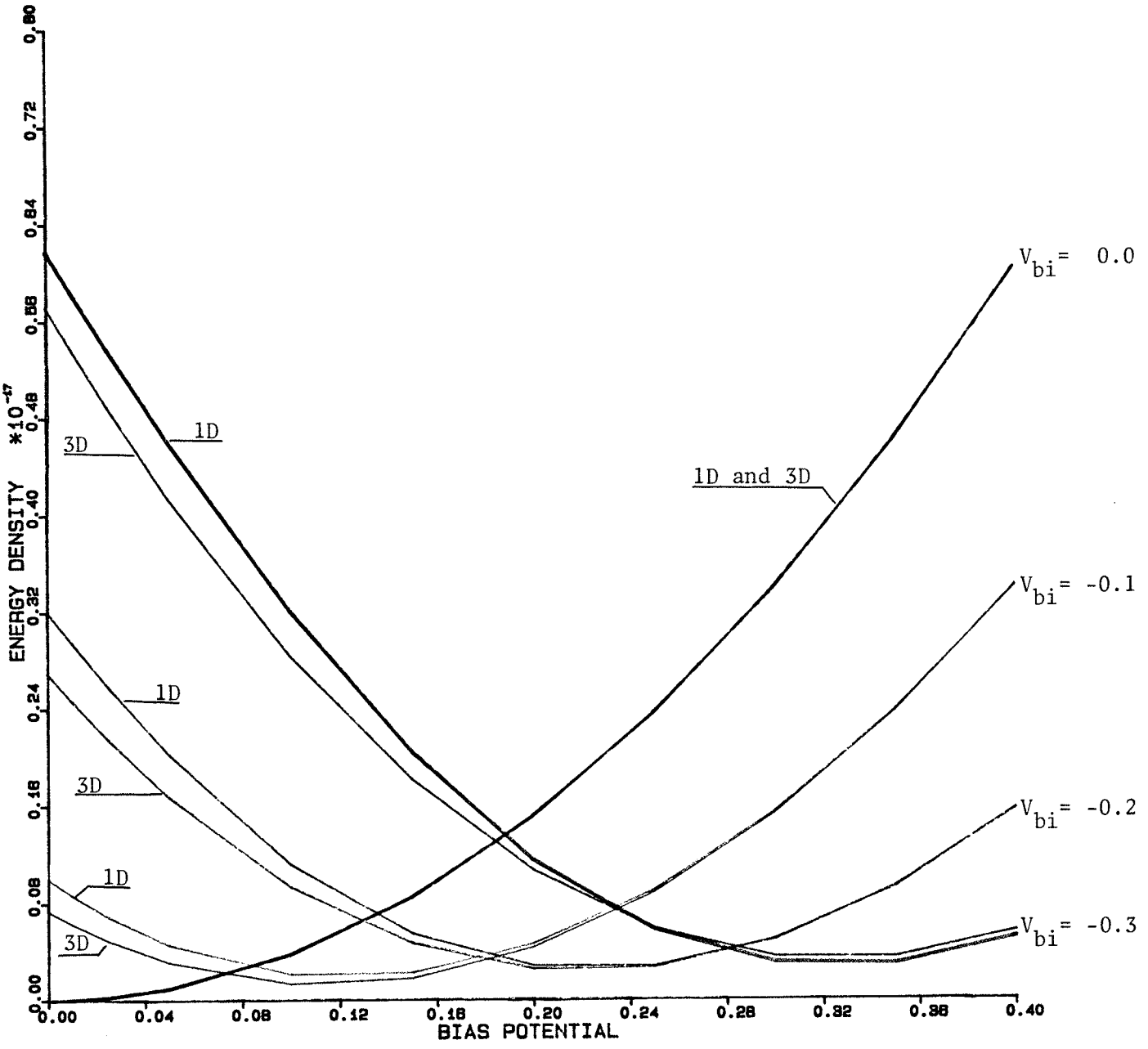

Figure 5.39: Energy vs. Bias for Schottky Contacts

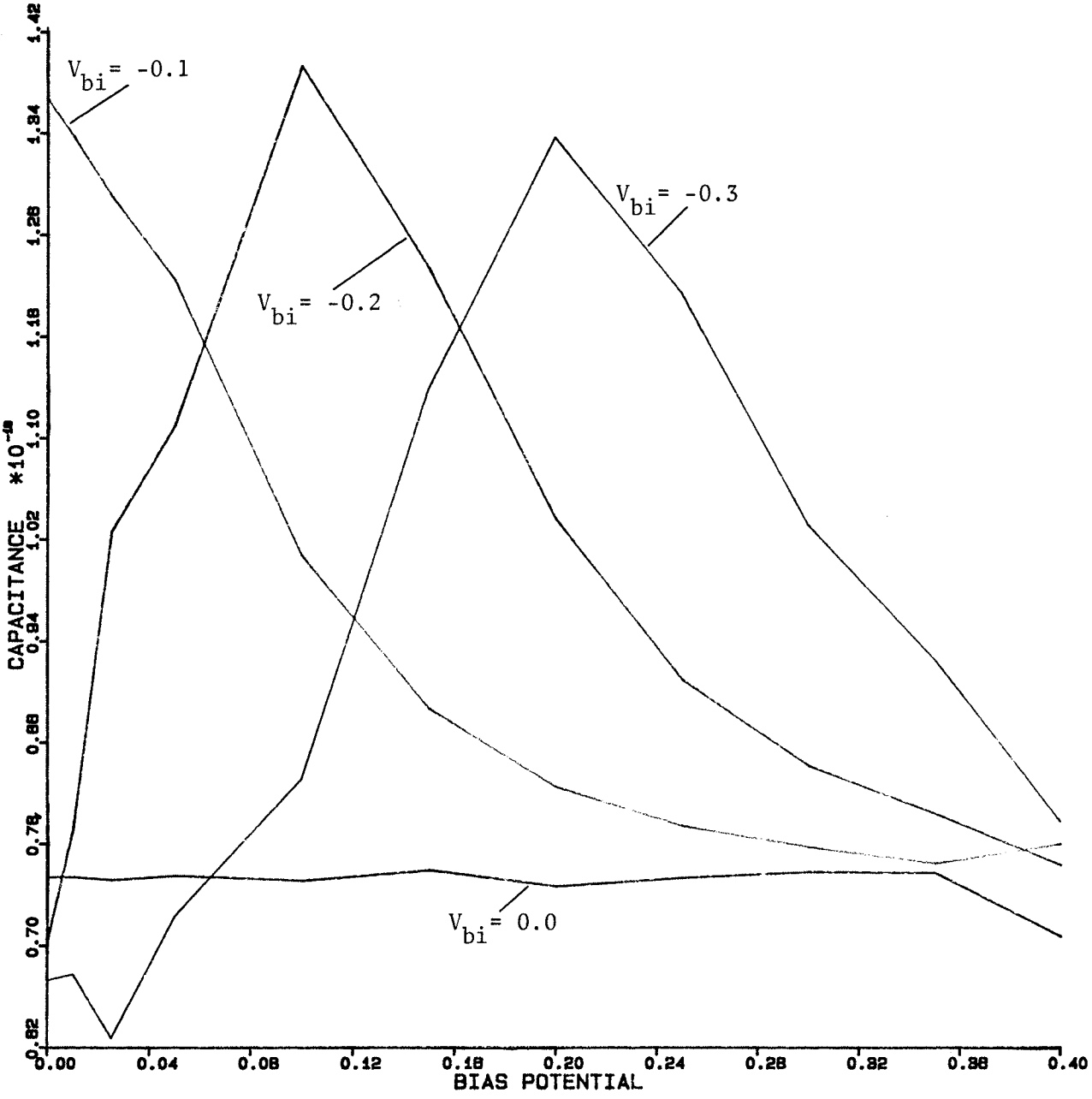

Figure 5.40: Capacitance of 1D Schottky Contact

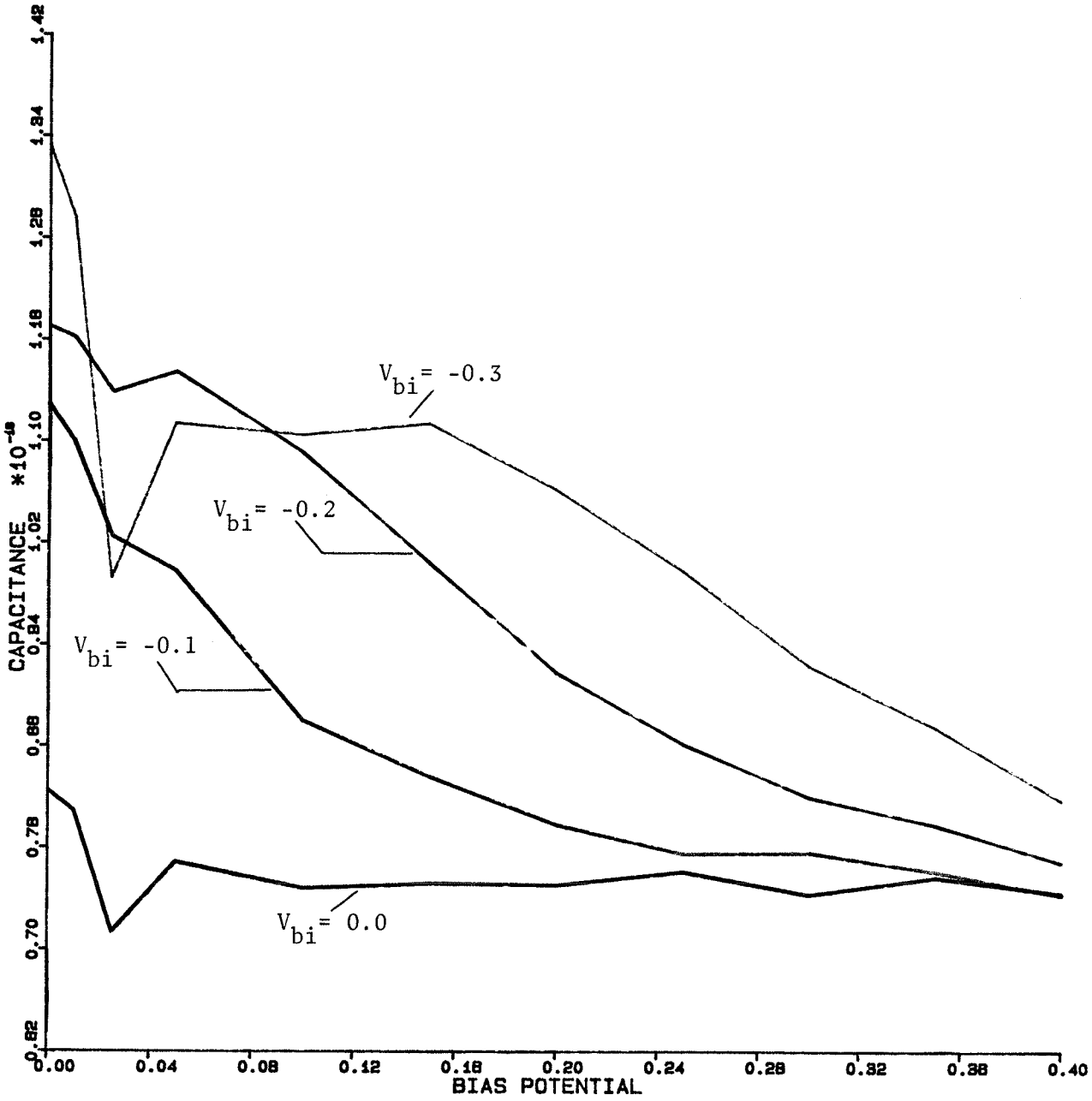

Figure 5.41: Capacitance of 3D Schottky Contact

Chapter VI

APPLICATIONS IN EXPLORATORY PHYSICS

The transport properties of electrons and holes at grain boundaries in polycrystalline semiconductors is of considerable present interest, both for academic and practical reasons. The grain boundary differs from other semiconductor interface systems in that the orientation but not the crystal structure changes across this interface; this can give rise to behavior which is unique to this type of interface and as such is of scientific importance. Electronic and optical processes at grain boundaries are of current practical importance as a result of their effects on the photovoltaic conversion efficiency of thin-film polycrystalline semiconductor solar cells [50].

Pioneering work on the characterization of electronic mechanisms at grain boundaries has been carried out recently by Seager and co-workers at Sandia Laboratories [51-54]. These workers have investigated the effects of grain-boundary interface states on the majority carrier transport in n-type polycrystalline silicon. From measurements of current-voltage characterists performed on isolated grain boundaries, they have been able to extract the energy distribution of interface states.

Here we present the results of a numerical investigation of transport phenomena at grain boundaries in silicon. The major departure from previous work reqards the assumption that carrier transport can be modelled by a simple diffusion model at the grain boundaries. Using the finite-element techniques developed during the course of this thesis, we solve the complete set of transport equations governing the flow of electrons and holes both in the bulk silicon and at the simulated grain boundaries. Several observations, involving experimental as well as numerical measuments, indicate that the transport at grain boundaries can be a rather complex process [63].

6.1 THE GRAIN-BOUNDARY INTERFACE

The grain boundary in a polycrystalline semiconductor is an interface between two identical crystals of different orientation. The mismatch in bonding between the two crystals results in bond defects (e.g. distorted bond angles, dilated or compressed bonds, broken bonds) at the grain boundary. These defects are expected to exist primarily on a single plane of atoms, and to a lesser extent on the neighbouring planes. We consider the width of the grain boundary region to be negligible on the scale of variations in the potential in the adjacent space-charge regions.

The bonding defects at the grain boundary translate into localized electronic states or interface states. The energy

distribution of these states is of importance in the determination of carrier transport processes. There is in general a net charge associated with the grain-boundary interface states, which is modified by a voltage applied across the grain boundary. The interface states also function as recombination centers for excess electrons and holes at the boundary. It has been observed that for grain boundaries in n-type silicon, the interface states inevitably contribute a net negative charge [55]. In p-type silicon, the interface states contribute a net positive charge [55]. The reason for this difference in n and p-type silicon is the difference in the postion of the Fermi energy relative to the interface state distribuion in the two cases.

In order to be specific we restrict out discussion to the case of grain boundaries in p-type silicon. This is the case which pertains to the energy-band diagram of Figure 6.1. It is assumed that positive charge associated with the interface states is balanced by a net negative charge due to uncompensated ionized acceptor impurities. These acceptor impurities are located in space-charge regions adjacent to the grain boundary in the crystalline regions to either side. Furthermore, we have also assumed that the interface charge is uniformly distributed over the area of the grain boundary plane. The magnitude of the potential barrier at the grain boundary for zero applied bias voltage (V_{do} in Figure 6.1) is referred to as the diffusion potential of the grain boundary.

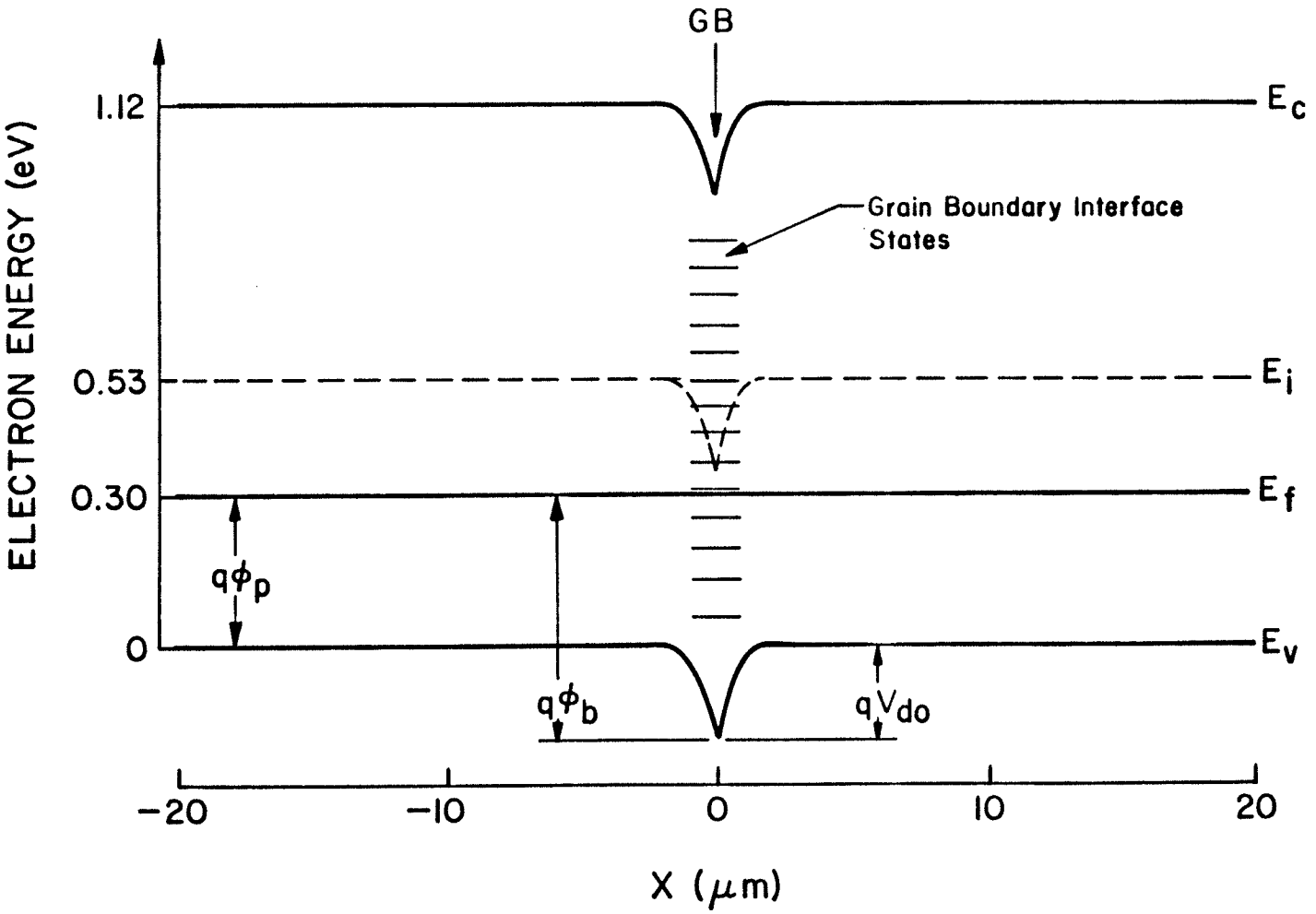

Figure 6.1: Energy-Band Diagram of Grain Boundary

Poisson's equation relates the charge distribution to the electrostatic potential. This may be expressed as

$$\nabla^2\phi_i = -\frac{\rho}{\varepsilon} \tag{6.1}$$

where ϕ_i is the electrostatic potential, ε is the permittivity of the semiconductor, and p is the charge density given by

$$\rho = q(p - n + N_d^+ - N_a^-) + Q_{is} \tag{6.2}$$

In (6.1), Q_{is} is the net charge in the grain boundary interface states and N_d^+, N_a^- are the ionized donor, acceptor impurity concentrations (assumed uniformly distributed in space). For p-type material, $N_d = 0$ in (6.1). In general, Q_{is} is a function of n and p, the concentrations of electrons and holes at the grain boundary. These carrier concentrations are given by

$$n = n_i \exp\left(\frac{E_{fn} - E_i}{kT}\right) \tag{6.3}$$

$$p = n_i \exp\left(\frac{E_i - E_{fp}}{kT}\right) \tag{6.4}$$

where E_{fn}, E_{fp} are the quasi-Fermi levels for electrons and holes respectively. In (6.1) the potential ϕ_i may be replace by $-E_i/q$ where the energy E_i, which appears in (6.3) and (6.4), is known as the intrinsic level (see Figure 6.1).

The charge Q_{is} in grain boundary interface states is dependent upon the energy distribution of these states, and

also upon their charge state when occupied by an electron (donorlike or acceptorlike).

6.2 CARRIER TRANSPORT ACROSS GRAIN BOUNDARIES

In the previous section, we have described the processes which contribute to the formation of a diffusion potential, or potential barrier against the transport of majority carriers across grain boundaries in semiconductors such as silicon. We have also introduced the localized interface states, which act as recombination centers for electrons and holes, and which modify the diffusion potential by adjusting their charge according to the concentrations of electrons and holes at the grain boundary. We now address the electron and hole transport processes.

In order to model the transport of electrons and holes analytically, an appropriate transport model must be adopted. To guide this procedure, we have performed a simulation of grain-boundary transport using our finite-element methods of numerical analysis, which employ the Newton-Raphson algoritm. In particular, both one and two-dimensional versions of MANIFEST were used to analyze isolated grain boundaries and portions of solar cells constructed of polycrystalline material.

Originally, to simplify the interpretation of these numerical results, we have solved for the case where the charge in grain-boundary interface states Q_{is} is fixed, and

does not depend on bias voltage applied across the boundary. In addition, we ignore recombination through grain-boundary interface states. While it was realized that these assumptions are unphysical, they provided for the analysis of electron and hole transport uncomplicated by the effects of recombination at the interface. Subsequent numerical calculations have included these effects.

An example of the results of the numerical calculations is given in Figure 6.2, which shows the dependence of the electron and hole quasi-Fermi potentials (imrefs), and of the electrostatic potential, upon position for a voltage V applied across the grain boundary. The effect of this voltage is to lower the potential barrier, or band bending, on the forward-biased side of the boundary and to increase it on the opposite (reverse-biased) side. The voltage division between these two sides depends, among other things, upon the charge in grain-boundary interface states Q_{is}, and in particular on the manner in which this charge changes under applied bias voltage. However, in the calculation of Figure 6.2, the effects of changing Q_{is} are not considered as discussed above.

We consider the mechanism by which holes cross the grain boundary is similar generally to the earlier treatment of metal-semiconductor contacts, or Schottky barriers [56]. The holes must negotiate the space-charge region by the usual drift and diffusion mechanisums and upon arriving at the

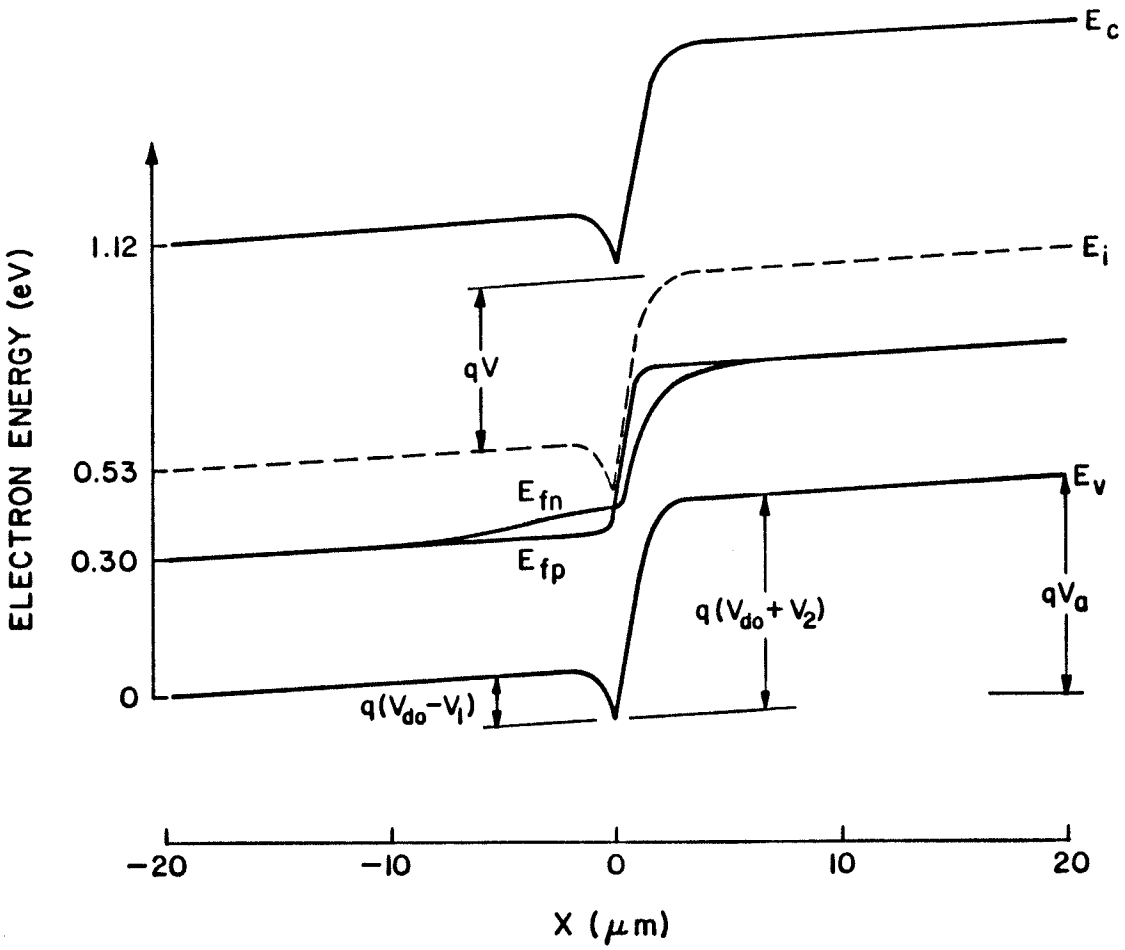

Figure 6.2: Fermi-Potentials for Grain Boundary

grain boundary either be accepted into the other side, or be reflected. The opposite side of the grain boundary is the same semiconductor, but with a different crystal orientation. The acceptance of the holes can be regarded as a process of interface emission characterized by a collection velocity v_r, which is in series with the drift and diffusion processes.

In the Schottky barrier, at least for high mobility semiconductors such as silicon, the thermionic emission of the majority carriers (holes) into the metal becomes the bottleneck to current flow. This has been discussed by Gossick [57], and more recently by Rhoderick [58]. In that case the diffusion potential is generally very large. In addition, there are very few available states in the metal with momentum parallel to the surface to match those of the holes from the semiconductor. This is because the energy at which the holes are transferred is close to the conduction band edge in the semiconductor, but remote from the band edges in the metal.

In the present problem, however, the diffusion potentials are typically much smaller that those of the Schottky barrier. Also, the states on either side of the grain boundary have the same energy relative to the band edges. The limitations due to conservation of parallel momentum are greatly relaxed. In addition there exists, on the reverse-biased side, a large electric field which is attractive to the ma-

jority carriers. The consequence of these factors is that holes, upon reaching the grain-boundary interface, are collected efficiently and the supply of these carriers through the space-charge region may become the limiting factor in determining the current. Following the work of Rhoderick [58] and of Crowell and Sze [56], we consider the energy diagram of Figure 6.3 and the extremes of hole concentration at the grain boundary when transport is limited by diffusion (case 1, curve D) or by emission (case 2, curve E).

We suggest that a general approximate expression for the intermediate case may, on the basis of Refs. [52, 56], be written

$$J_p = \frac{q N_v V_r}{1 + \frac{V_r}{V_d}} \exp(-\frac{\phi_b}{V_T})[\exp(\frac{V_1}{V_T}) - \exp(-\frac{V_2}{V_T})]$$

$$= \frac{q N_v V_r}{1 + \frac{V_r}{V_d}} \exp(-\frac{\phi_b}{V_T}) \exp(\frac{V_1}{V_T})[1 - \exp(-\frac{V}{V_T})] \qquad (6.5)$$

since $V = V_1 + V_2$ where V is the total voltage applied across the grain boundary, V_1 is the forward bias on the left side of the grain boundary in Figure 6.2 which is so far an undetermined portion of V, and V_2 is the reverse bias on the right side of the boundary. V_d and V_r are the diffusion and interface recombination (or in our case collection) velocities for the holes. ϕ_b is the equilibrium barrier height which is independent of V (Figure 6.1); N_v is the effective

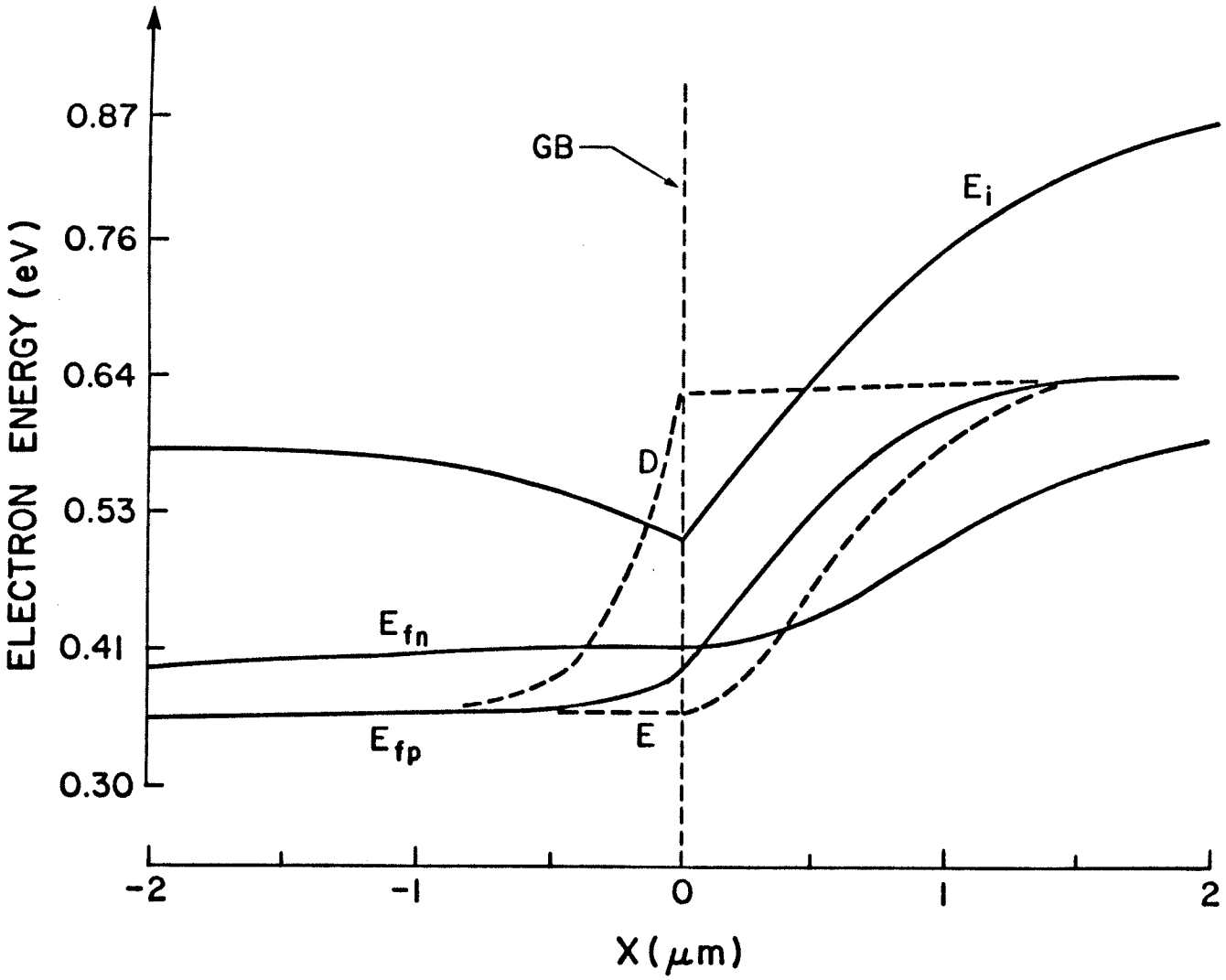

Figure 6.3: Emission and Diffusion at Grain Boundaries

density of states in the valence band. In the present case $v_d = \mu\xi_{m1}$ with ξ_{m1} the maximum field on the reversed-biased side of the boundary. For any appreciable voltage across the boundary, $\xi_{m2} >> \xi_{m1}$ and $V_r >> V_d$ in Eqn. (6.5).

In case 1 (shown schematically as D in Figure 6.3), the interface collection velocity v_r is considered to be large. The hole current is then limited by diffusion through the (forward-biased) space-charge region and the concentration of holes at the grain boundary remains small under applied voltage. This is illustrated by a rise in the hole quasi-Fermi level E_{fp}, as the grain boundary is approached from the forward-biased side. The schematic line in Figure 6.3 shows the extreme case; in practice if E_{fp} rises by more than kT or so the transport may be considered to be diffusion-limited [58]. The transfer of holes across the grain boundary which in this case is proportional to their concentration at x=0, p(0), is kept small by the limited supply to the boundary. On the other hand, if the collection velocity v_r is small (case 2 and E in Figure 6.3) holes arriving at the grain boundary are not immediately removed by the reverse-biased side. The supply of holes to the grain boundary is bountiful and p(0) increases to its maximum value determined by by the hole Fermi level on the forward-biased side. In this case E_{fp} is relatively flat up to the grain boundary. This corresponds to the emission-limited case. As we observe in Figures 6.2 and 6.3 which show the results

of an exact calculation, the true situation is intermediate between these two extremes, with E_{fp} rising (in this case by more than kT) as the grain boundary is approached.

On the basis of the results from the numerical analysis (shown in Figures 6.2 and 6.3), we believe that the diffusion model ($V_r \gg V_d$), as originally described by Stratton [59], is the appropriate approximation for the interpretation of majority-carrier transport across grain boundaries. This model is employed in the analysis of the experimental data as reported in [62].

6.3 THE GRAIN-BOUNDARY PROGRAM

A one-dimensional grain-boundary program, which allows a potential-dependent charge in grain-boundary interface states, is listed in Appendix C. Appendix D provides a sample of its generated output. The model incorporated into the program is divided into two sectons: a portion to describe electronic transport in bulk silicon, and a portion to describe transport across the grain-boundary interface.

Transport in the bulk is handled in a similar fashion to the other examples shown in this thesis. Recombination is assumed to occur through mid-bandgap traps (of density N_t) and is modelled via Shockley-Read-Hall statistics. As before, the mobilities are assumed to be independent of the electric field strength. The following parameters apply to all subsequent simulations: T= 300 K, N_d= 3.0E15 cm-3 (n-

type Si), μ_n= 1350 cm2 v-1 s-1, μ_p= 475 cm2 v-1 s-1, σ_n= 1.0E-16 cm2, σ_p= 1.0E-14 cm2, V_{th}= 1.0E7 cm s-1, and N_t= 1.0E17 cm-3 (resulting in a minority carrier lifetime of 0.1 nanoseconds). When a photogeneration rate is specified, it is assumed uniform over the entire device.

The charge on the grain-boundary is given by:

$$Q_{is} = -q*(Q_{vb}*f + Q_{fx})$$

where q is the electronic charge, Q_{vb} is a constant factor reflecting the density of interface states whose charge is dependent upon the electrostatic potential and the concentrations of electrons and holes at the grain boundary, Q_{fx} is a constant factor reflecting the density of fixed charge, and f ($0<f<1$) determines the probability of occupation of a grain-boundary trap by an electron. The recombination expressions at the grain boundary are similar to those employed in the bulk material except that Q_{vb} replaces N_t to account for interface traps.

A finite-element mesh consisting of 61 nodes and 30 quadratic elements is used to discretize the area near the grain boundary (located at X=0) from -1.0 to +1.5 microns. Care must be taken to insure that an element does not cross the boundary as the electrostatic field must be discontinuous there. As shown in Appendix C, the bias voltage is stepped from 0.0 to 1.2 volts with Q_{fx} = 2.0E11 and Q_{vb}= 1.5E11 cm-2. No excess (photo) generation was applied during the sample

run shown in Appendix D. Figures 6.4 and 6.5 show plots of the grain-boundary potentials and of the carrier concentrations for the case of V= 1.2 volts.

The first sequence of tests presented in this section involve fixing Q_{fx} at 2.0E11 cm-2 and varying Q_{vb} without any excess generation rate (i.e. dark conditions). Plots of current density versus applied bias potential are shown in Figures 6.6 and 6.7, the latter being a semilogarithmic plot. Three values of Q_{vb} (1.0E11, 1.5E11, and 2.0E11 cm-2) were used for this example. A plot of capacitance (F cm-2) versus bias potential is presented in Figure 6.8. The steady-state capacitance of a grain-boundary interface is observed to be affected more modestly than current density by changes in the charge on the boundary.

In the next test, we reverse the roles of Q_{vb} and Q_{fx} and hold Q_{vb}= 2.0E11 cm-2 constant while Q_{fx} is varied over 1.0E11, 1.5E11, and 2.0E11 cm-2. Again, there is no excess (photo) generation rate. Figures 6.9 and 6.10 show current density versus voltage for this case. Note that the current densities are somewhat higher than in the previous case. Capacitance versus voltage is plotted in Figure 6.11.

From the observations in Figures 6.6 to 6.11, one may conclude that an increase in the fixed grain-boundary interface charge has the affect of reducing the magnitude of the majority carrier current. This is the result of an increase in the potential barrier (i.e. the diffusion potential) at

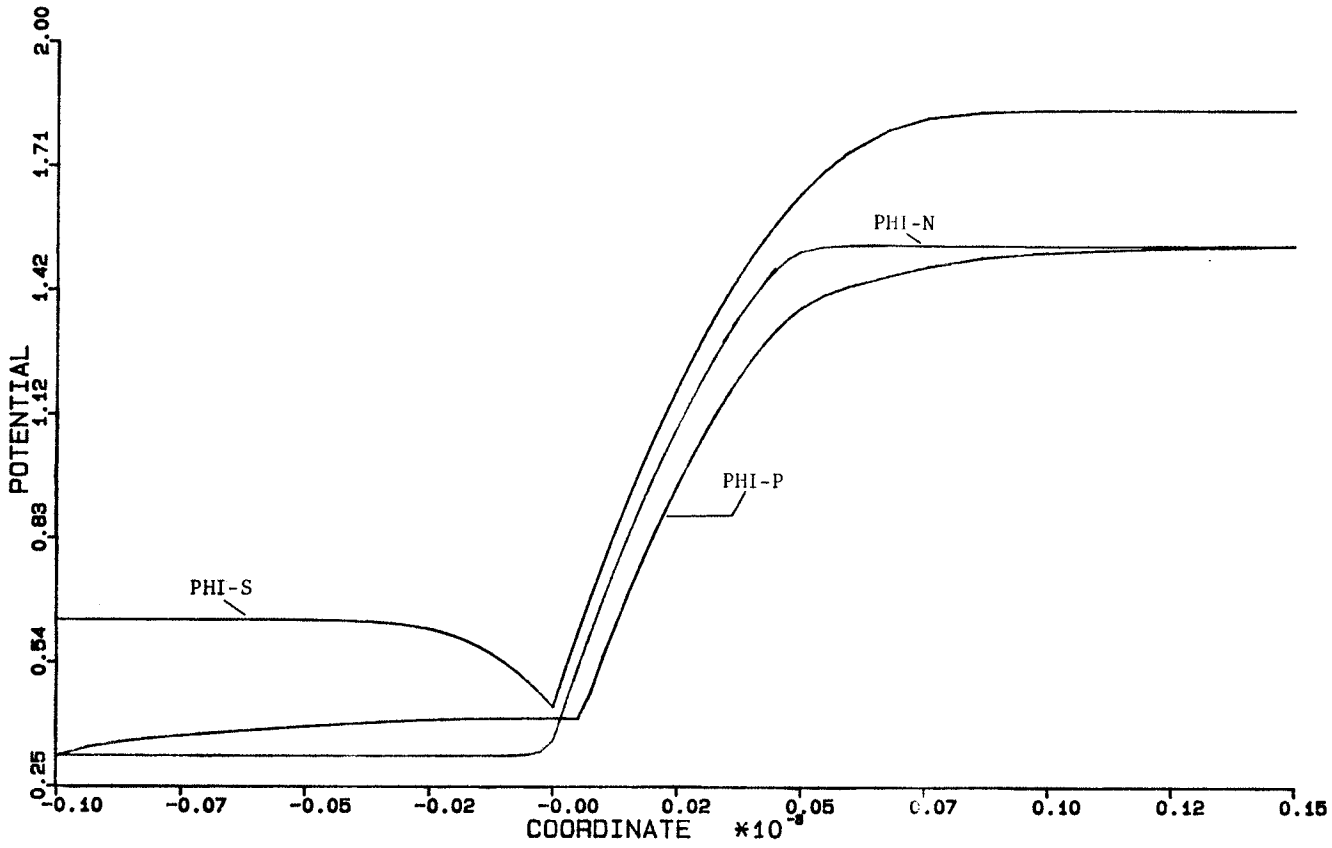

Figure 6.4: Grain-Boundary Potentials

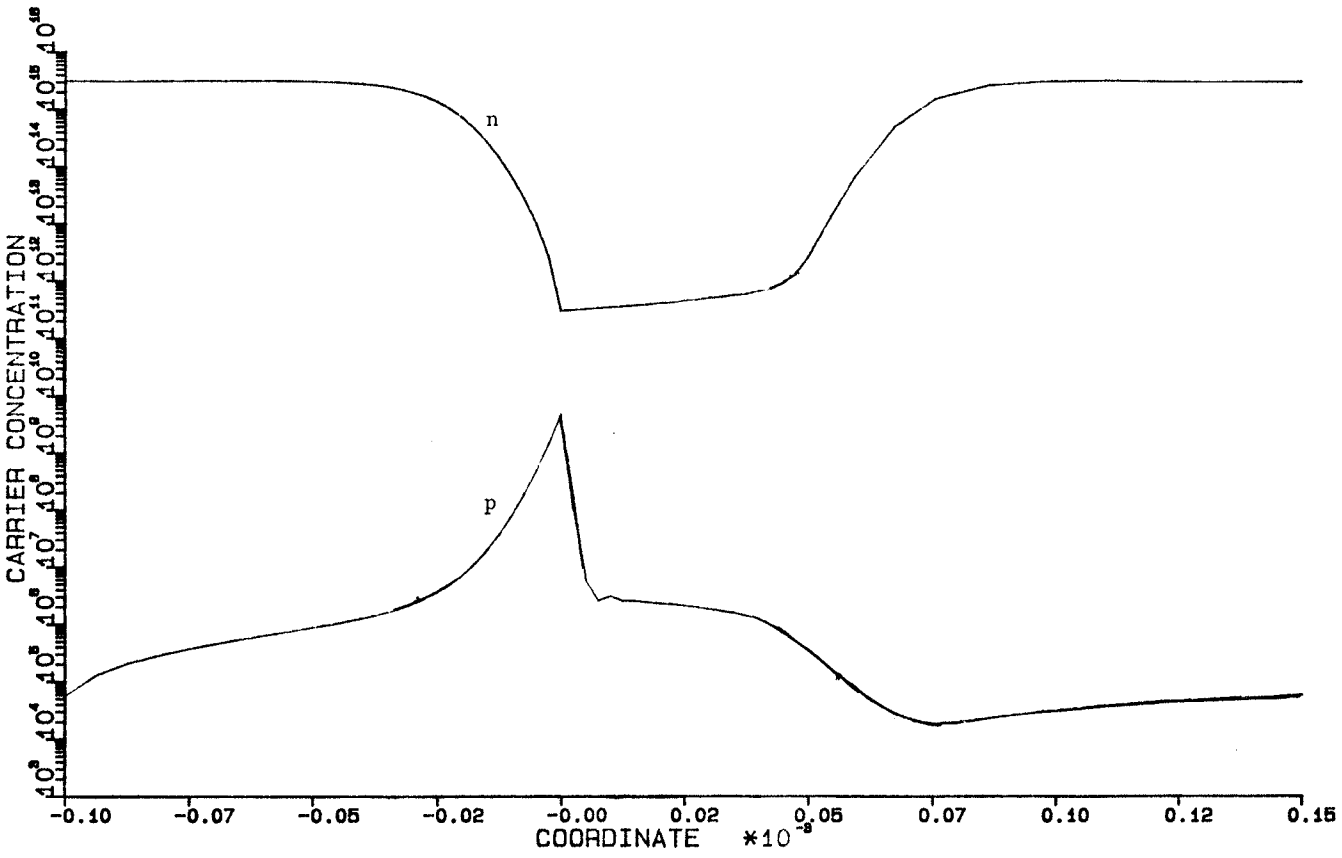

Figure 6.5: Grain-Boundary Carrier Concentrations

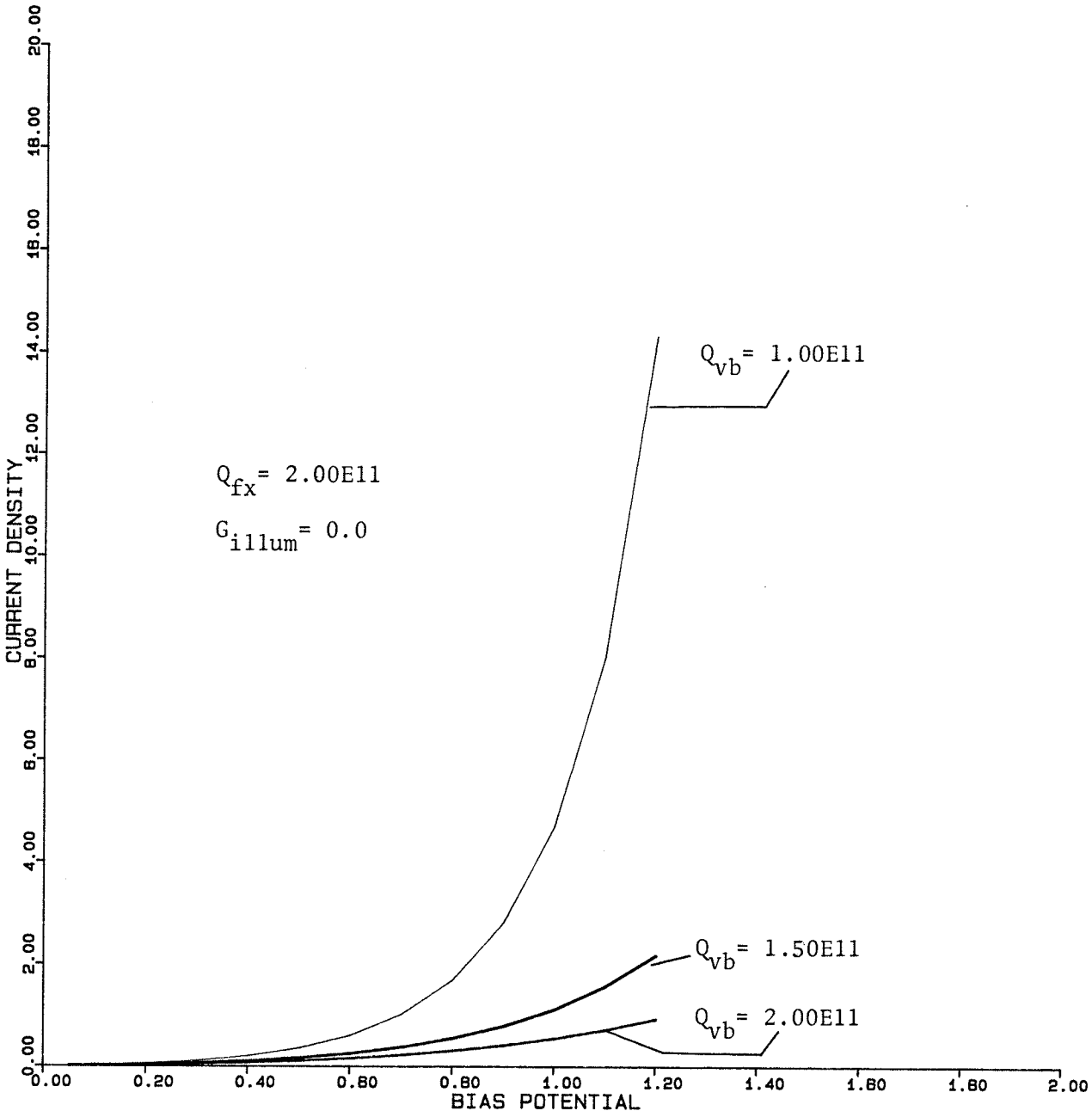

Figure 6.6: J vs. V for Grain Boundary (GB1)

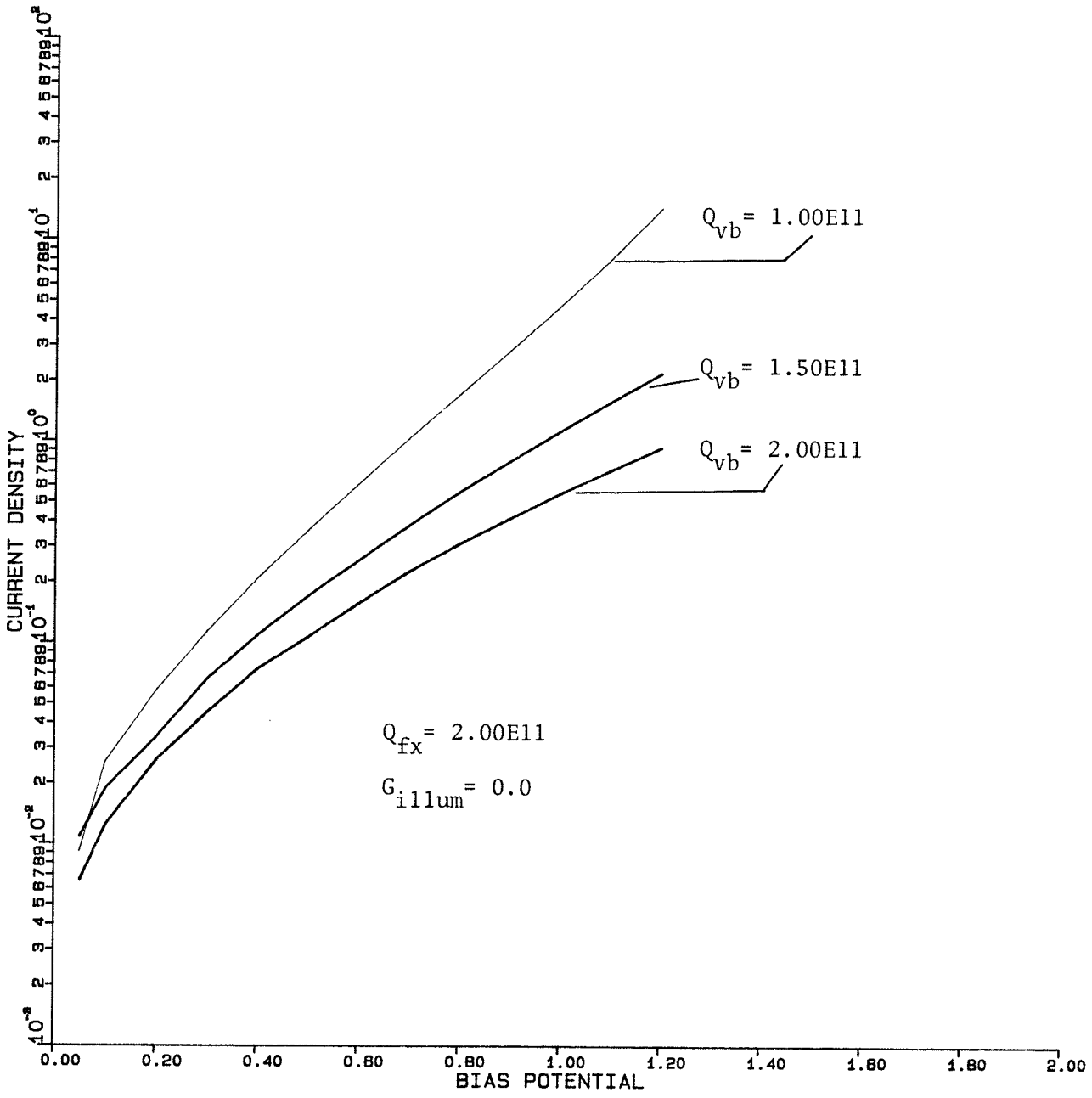

Figure 6.7: J vs. V for Grain Boundary [semi-log] (GB1)

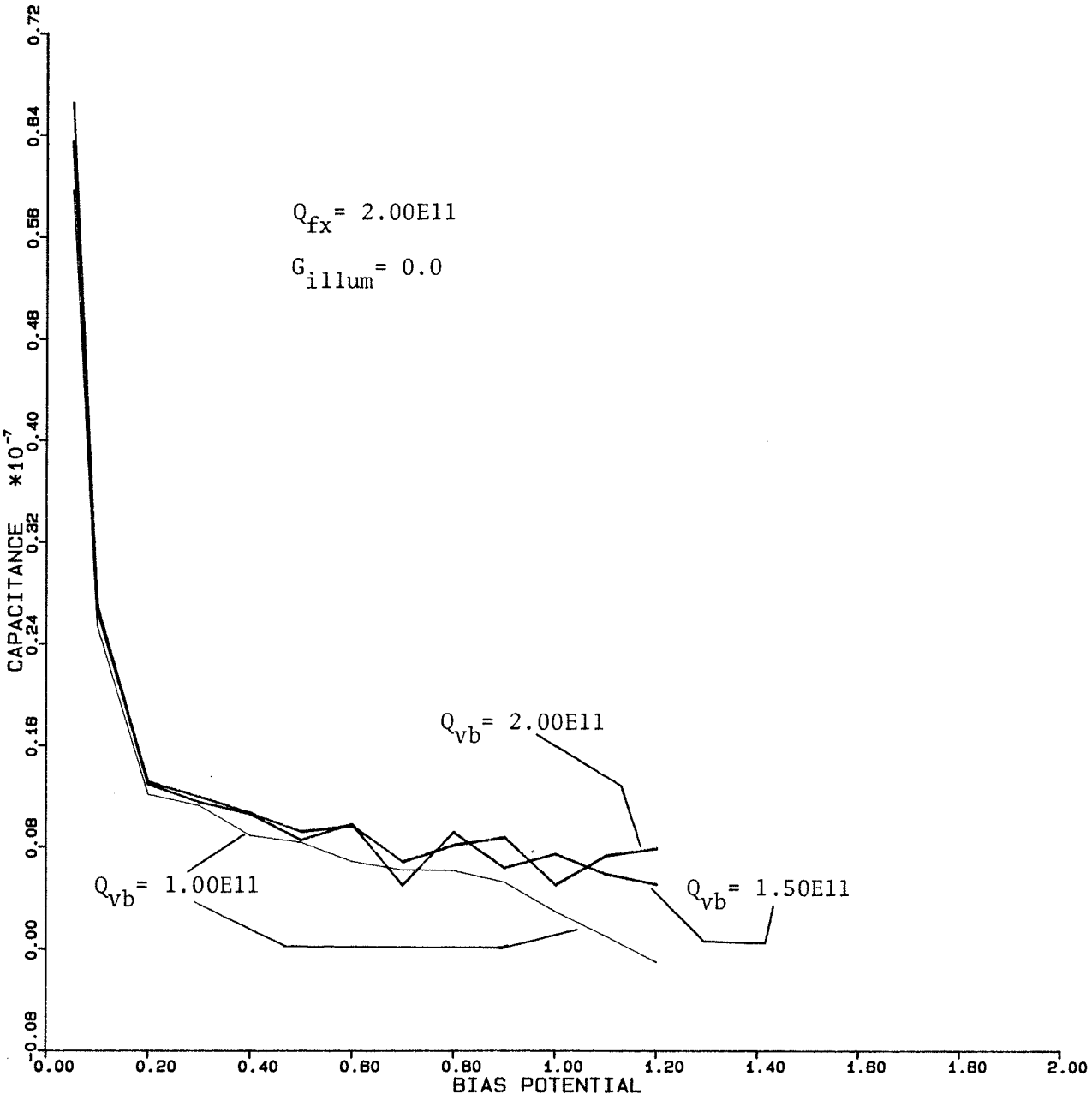

Figure 6.8: C vs. V for Grain Boundary (GB1)

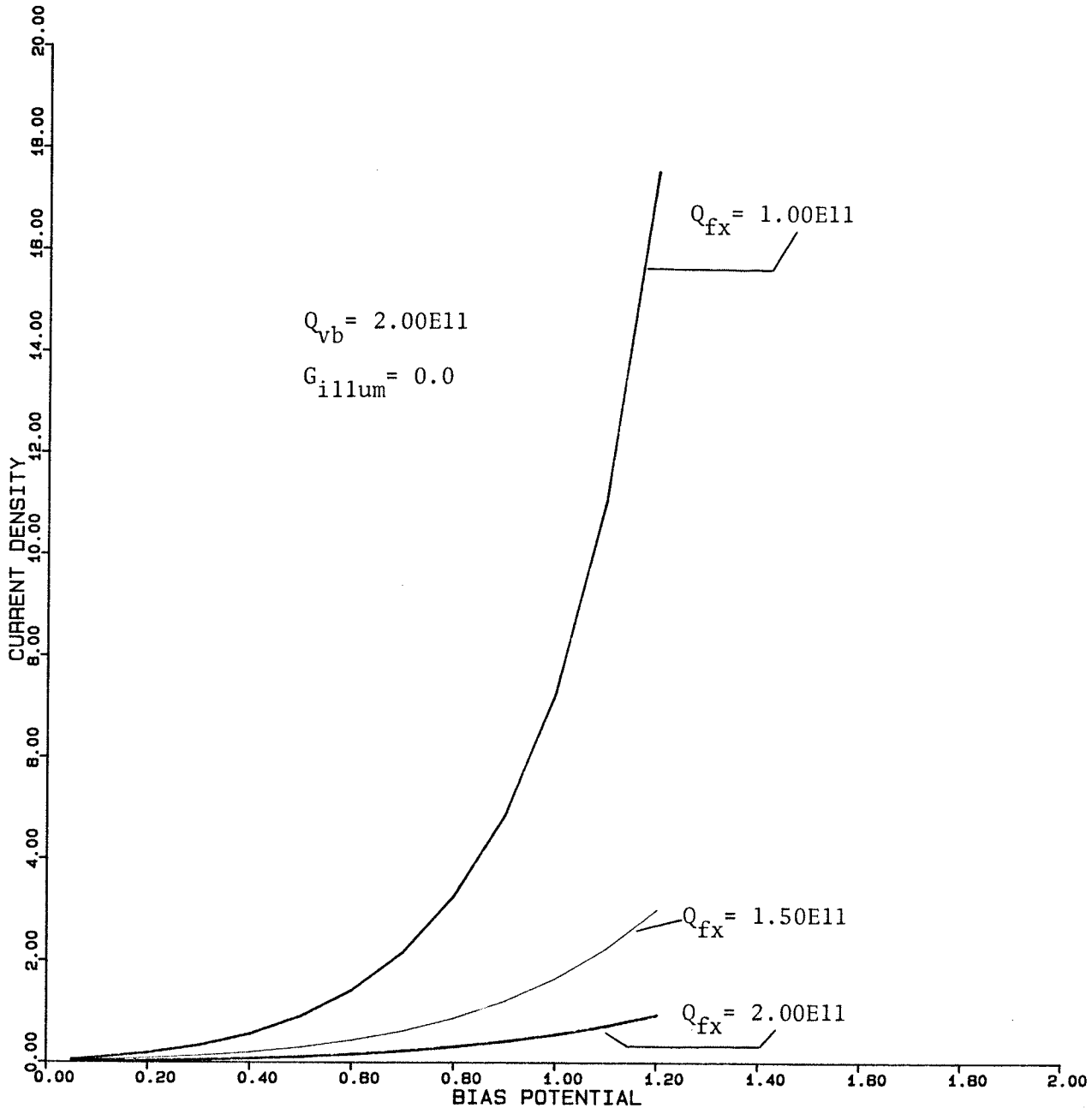

Figure 6.9: J vs. V for Grain Boundary (GB2)

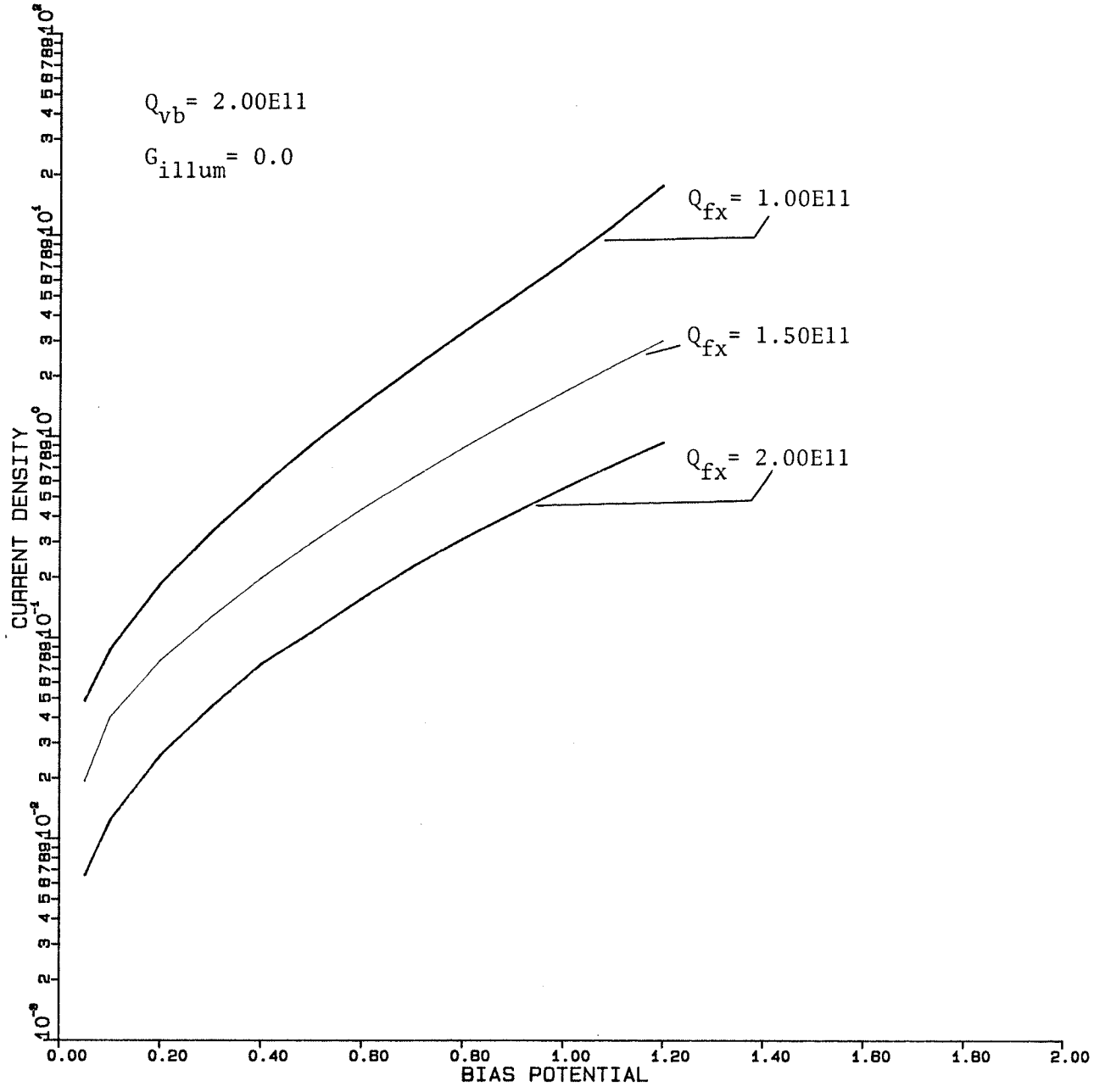

Figure 6.10: J vs. V for Grain Boundary [semi-log] (GB2)

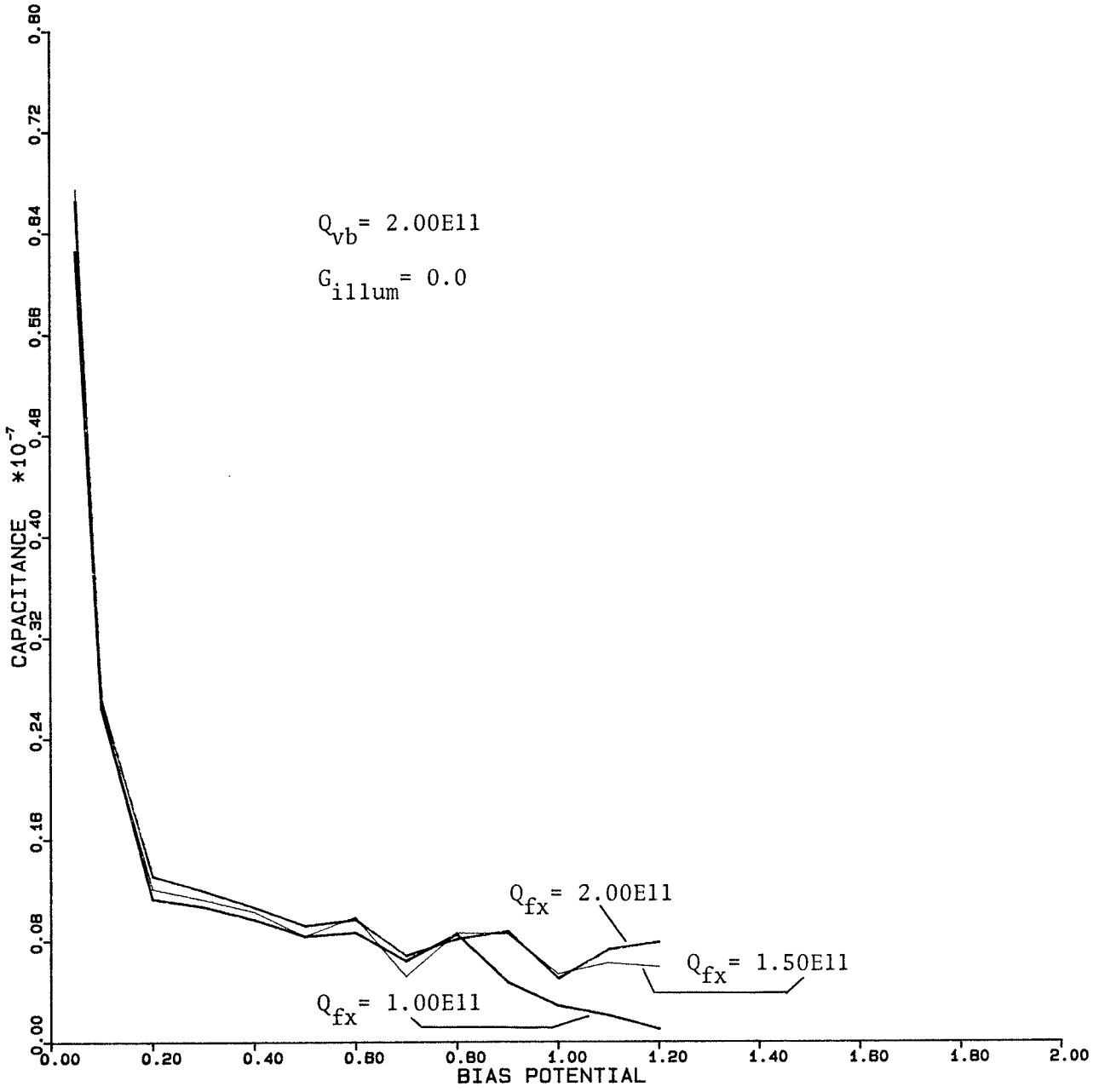

Figure 6.11: C vs. V for Grain Boundary (GB2)

the grain boundary. In addition, the presence of interface states with charge dependent upon the bias voltage (Figures 6.6 to 6.8) gives rise to a reduced voltage dependence as compared to the case of fixed interface charge (Figures 6.9 to 6.11). This is a consequence of the pinning of the majority carrier quasi-Fermi potential at the grain boundary by the interface states [62].

The final set of tests considers the effects of optical illumination on an isolated grain boundary. Holding both Q_{vb} and Q_{fx} at 1.5E11 cm-2, a photogeneration rate was applied to the device. A plot of the carrier concentrations (n and p) for various generation rates between 1.0E15 and 1.0E20 cm-3 s-1 is given (under zero bias) in Figure 6.12.

The upper set of curves in Figure 6.12 represents the majority carrier concentration for various photogeneration rates. The concentration of majority carriers at the grain boundary is independent of photogeneration rate up to G= 1.0E17 cm-3 s-1. Above this rate, conditions of high-level injection occur, in which the minority-carrier concentration (lower curves in Figure 6.12) at the grain boundary becomes equal to the majority-carrier concentration. Further increases in photogeneration rate cause the diffusion potential at the grain boundary to decrease (as shown in Figure 6.13), giving rise to an appreciable photoconduction effect [66].

For each specified photogeneration rate, a current-voltage curve was produced. Figure 6.14 illustrates how the carrier profiles change with increasing bias potential at a photogeneration rate of G= 1.0E20 cm-3 s-1. Figures 6.15 and 6.16 show current density versus voltage for photogeneration rates between 1.0E15 and 1.0E20 cm-3 s-1. The capacitance characteristics for this device are shown in Figure 6.17. Under low applied bias voltages, the effect of illumination is to reduce the height of the potential barrier at the grain boundary, and hence reduce the capacitance of the device.

Under applied bias voltage, which varies from 0.0 to 1.2 volts in 0.2 volt increments in Figure 6.14, the majority-carrier concentration (upper curves) remains well above the minority-carrier concentration. Majority carriers are injected across the grain boundary at a rate controlled by the diffusion potential V_{do} and hence by the photogeneration rate G. For high photogeneration rates, V_{do} is small. As shown in Figures 6.15 and 6.16, the current in this case increases rapidly with applied voltage. This is the photoconduction effect discussed above.

In summary, it has been shown that the numerical techniques discussed in this thesis are of great value in obtaining quantitative exploratory information about device phenomina such as grain-boundary transport. More details on the application of these tools in interpreting experimental re-

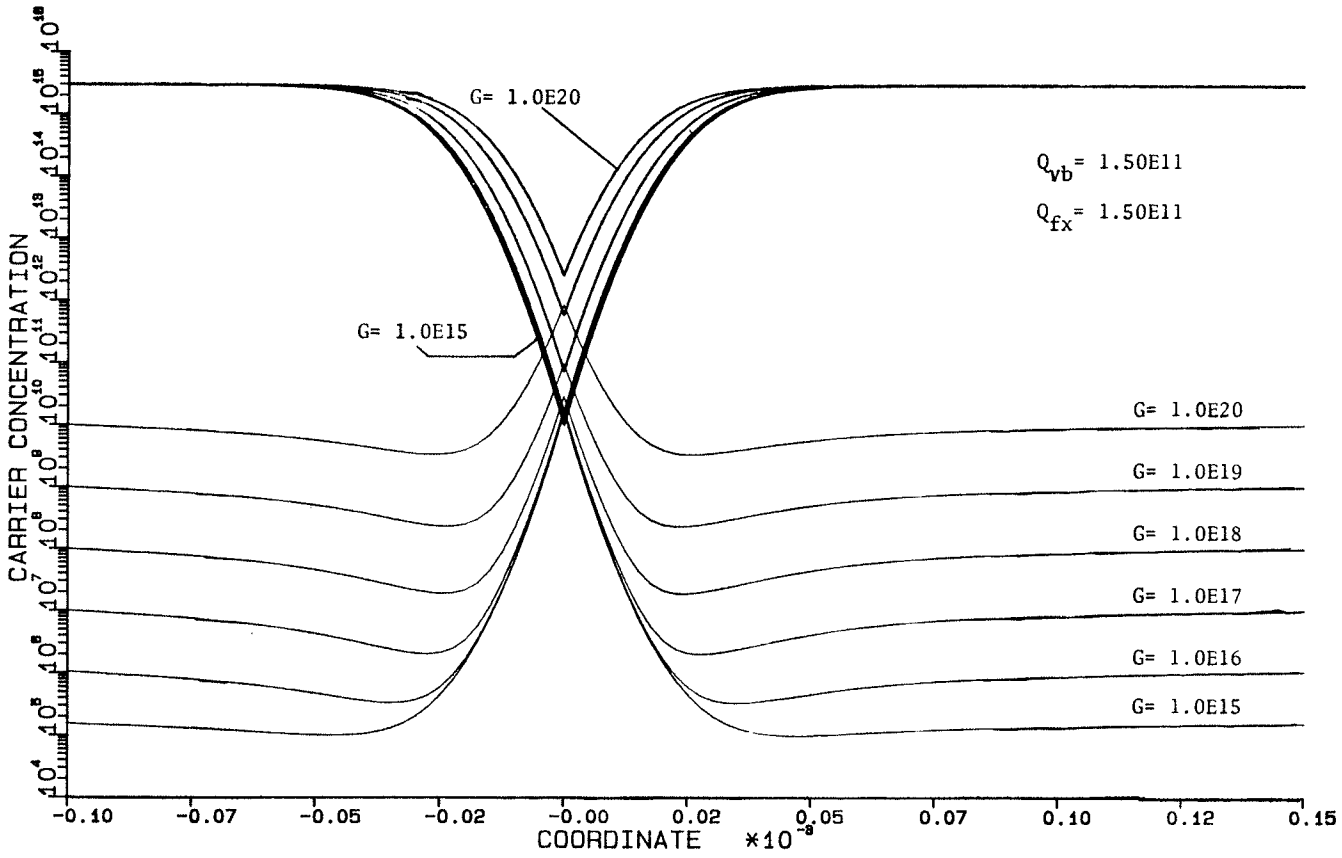

Figure 6.12: Carrier Concentrations Under Illumination

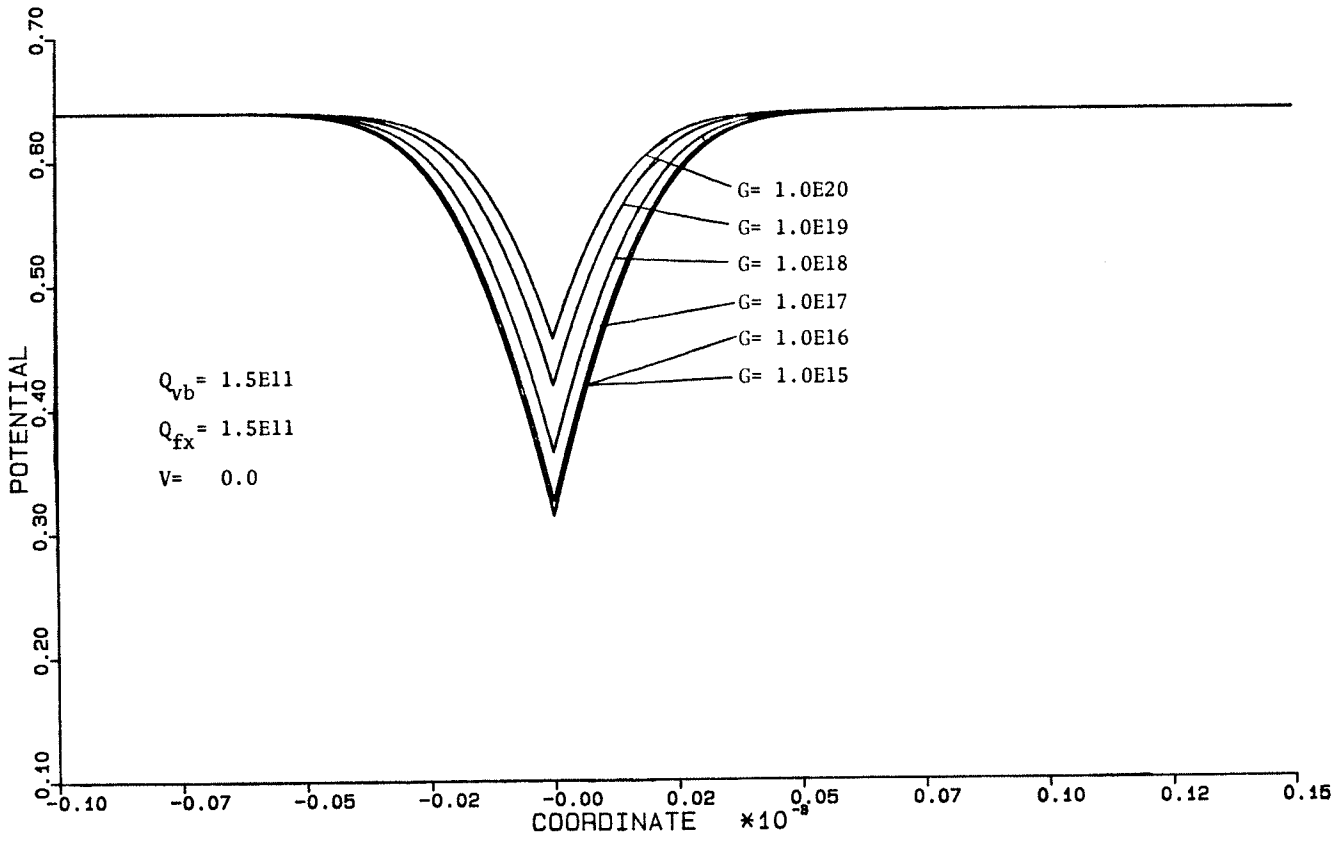

Figure 6.13: Electrostatic Potential Under Illumination

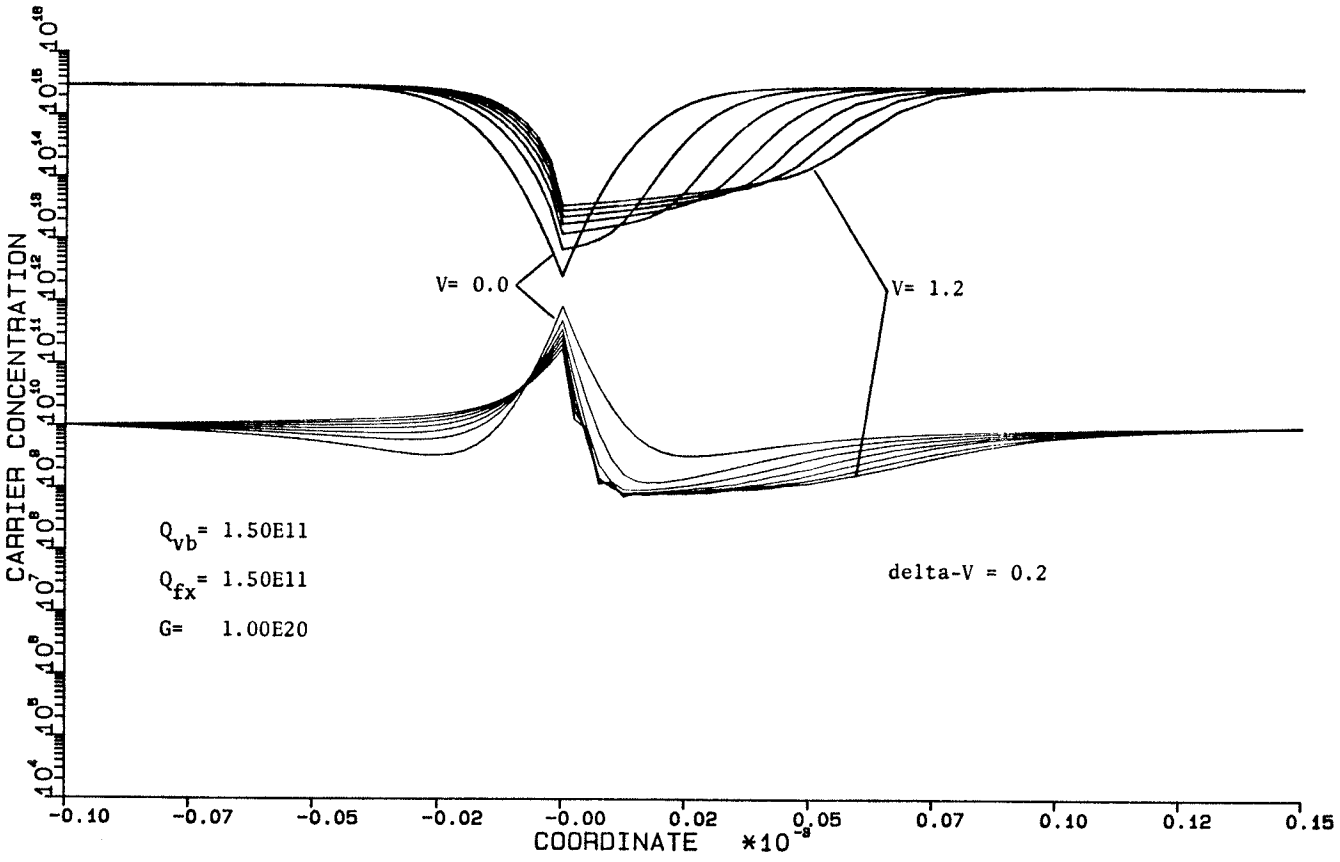

Figure 6.14: Carrier Concentrations Under Bias

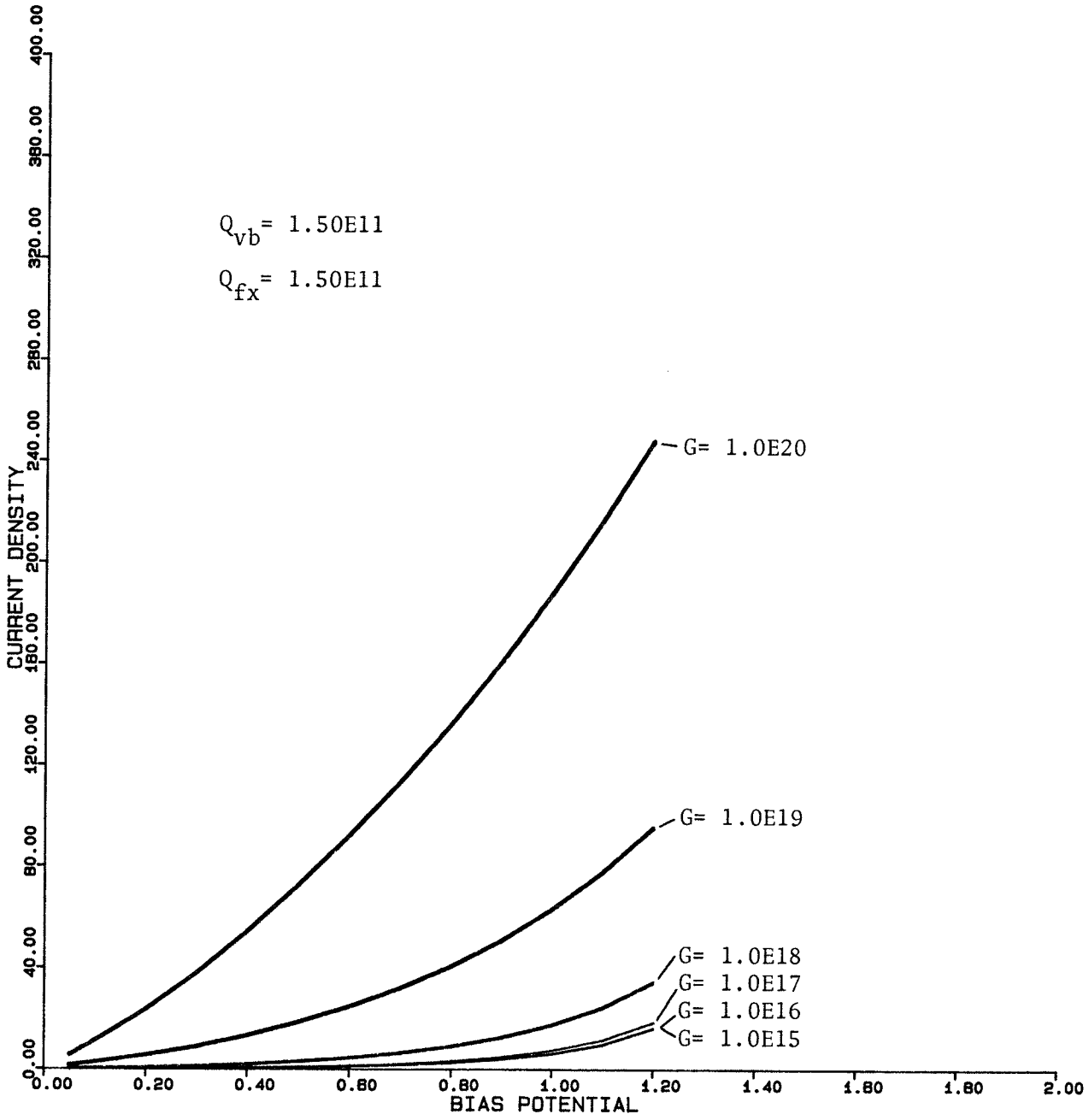

Figure 6.15: J vs. V for Grain Boundary (GB3)

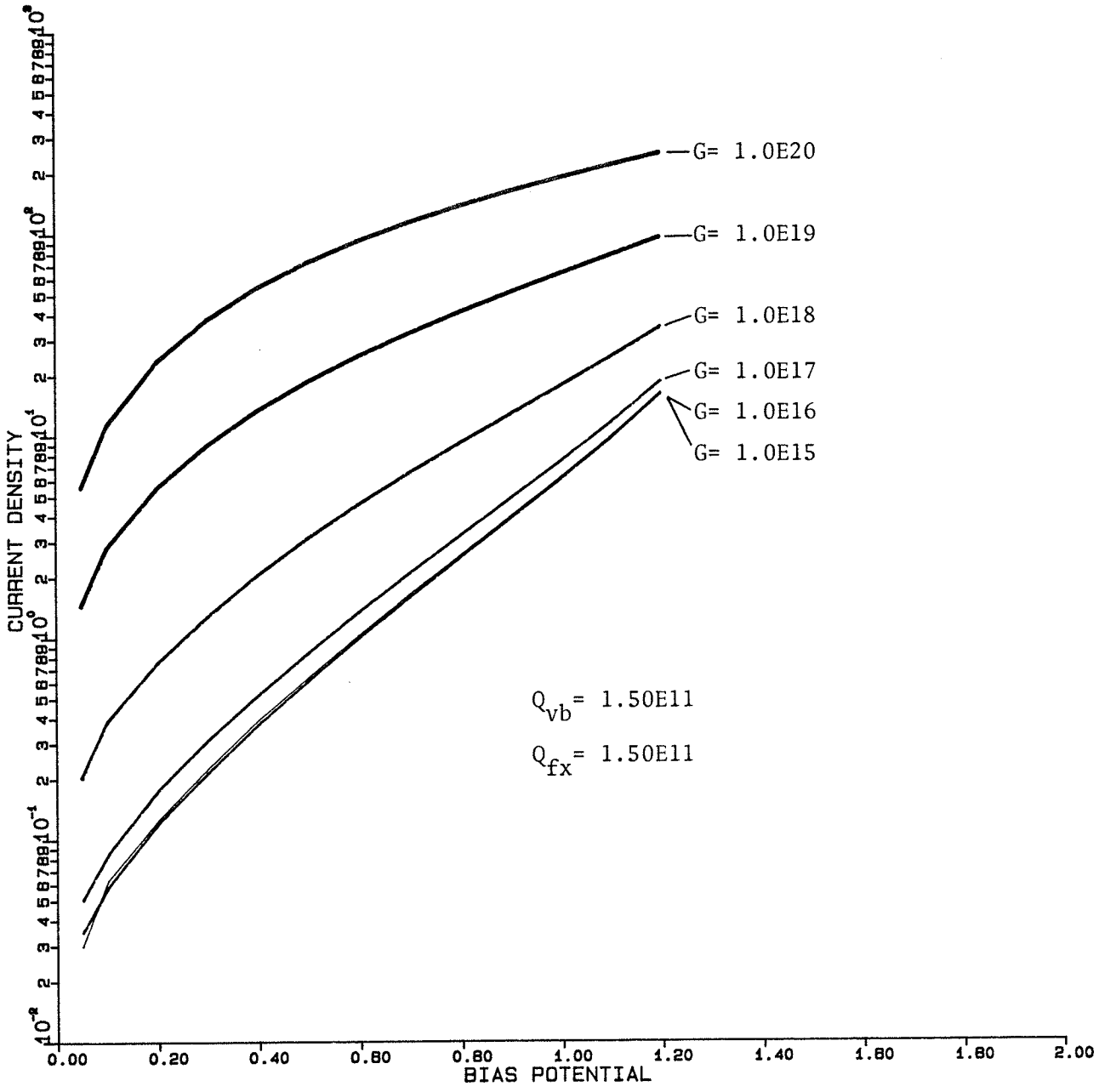

Figure 6.16: J vs. V for Grain Boundary [semi-log] (GB3)

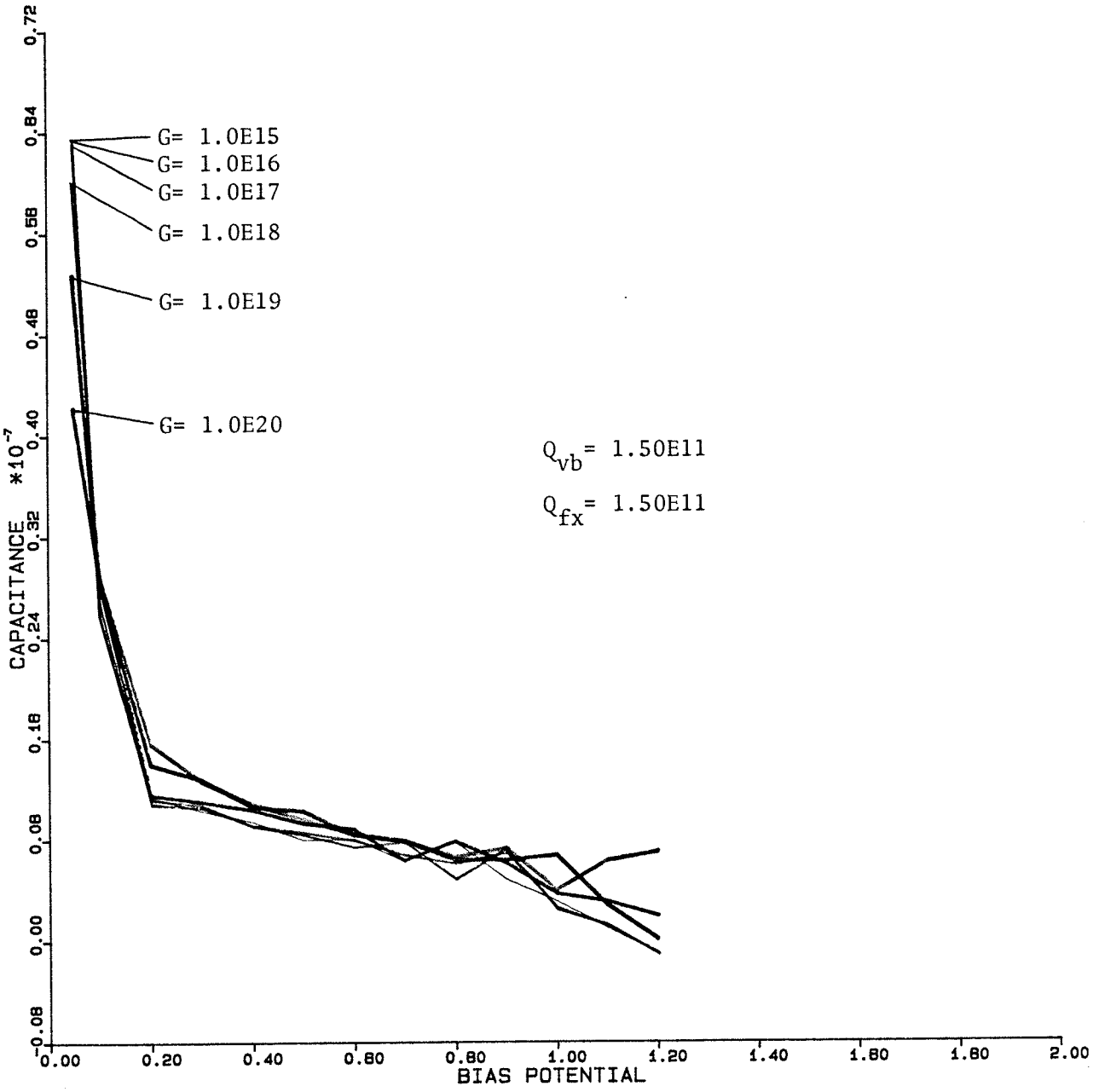

Figure 6.17: C vs. V for Grain Boundary (GB3)

sults on grain-boundary samples has been published elsewhere [62, 63]. Appendix E is a reprint of the paper "Electronic Transport at Grain Boundaries in Silicon" which appears in Physical Review B.

Chapter VII

CONCLUSIONS AND RECOMMENDATIONS

The present approach has proven to be a novel and efficient method of solving the transport equations associated with semiconductor devices. Starting with Poisson's equation and the current continuity equations, a set of three nonlinear partial differential equations are derived. The solution to these equations, in terms of the electrostatic and quasi-Fermi potentials, is obtained through the use of a combined finite-element, Newton-Raphson algorithm. A CAD system, called MANIFEST, was written to test the techniques developed in the thesis.

To fully exploit the elegance of the finite-element method, variational analysis (as applied to Poisson's equation) has been shown to be an appropriate numerical method of solution. Having derived an energy functional which is valid under Dirichlet, Neumann, and mixed boundary conditions, a matrix equation is obtained by Rayleigh-Ritz discretization. The functional -- which allows for an inhomogeneous, anisotropic medium -- is shown to be both positive-definite and self-adjoint under the stated boundary conditions. Additionally, all media and sources may be functions of the potentials ϕ_s, ϕ_n, and ϕ_p. Due to the nonlinearity of the problem, no guarantee of uniqueness exists.

The residual vector, defined as the difference between the left and right-hand sides of the matrix equation, is then forced to zero using a vector form of Newton's method. Various extensions to the above process, such as transient analysis and automatic step-limiting are possible. In practice one finds that the above algorithm works quite well. Quadratic convergence, as predicted for Newton's method, is observed as the solution is approached. At this point, it is useful to consider several key issues regarding the design of MANIFEST and this thesis.

The first question to answer is, why were finite-elements chosen over finite-difference techniques? Virtually all seasoned numerical analysts who have solved complicated field problems will agree that finite-differences, no matter how convoluted or evolved, are obsolete and antiquated. Over the years, people have repeatedly reported high-order difference formulas and multi-armed operaters which are designed to cater for curved and/or irregular boundaries. In practice, one finds hopelessly complicated programs which are very limited in scope. More seriously, it becomes unduly difficult to understand how or why such methods (don't) work in relation to specific problems and geometries. On the other hand, the finite-element method is based on sound mathematical and physical principles. Use of a variational approach, be it with an energy functional or not, gives the user confidence in his or her answers and allows better in-

sight into the convergence properties of the algorithm. The elements not only describe the geometry of the device in a simple and accurate fashion, but expedite specification of source, medium, boundary, and interface properties. In summary, finite elements represent a complete and unified approach to solving a wide varity of related problems within the context of a single (group) of computer programs.

Having decided the basic method of solution, one next must consider how to handle the nonlinearity of the semiconductor transport equations. The general principle behind the numerical solution of a nonlinear equation is to guess at a possible solution, invert a related quasi-linear system matrix (evaluated with the most recent potentials), and iterate the above process until the sequence of solutions appears to converge (i.e. this is the "contraction mapping" approach). Such a scheme may or may not converge depending primarily on how "nonlinear" the original problem is. For the case at hand, the degree of nonlinearity is strongly dependent upon the magnitude of the concentration of the dopants. As a general rule, any problem of interest or practical importance will probably not converge. It was this observation that prompted the decision to employ a Newton-Raphson algorithm rather than a simple successive-approximation scheme.

Even within the context of Newton's method, several researchers have published reports of various modifications

and algorithmic improvements. Most have aimed at reducing the cost of each iteration rather than increasing convergence rates or accuracy. Having studied (and often tried) many such modificatons, it is the author's opinion that one should concentrate on mathematically correct and justifiable algorithms. Most forms of modification will improve convergence rates for a given set of problems, but in the long run they often increase the user's costs due to useless attempts at "improving" problems outside of the scope of the modification. Although MANIFEST retains a few refinement parameters (e.g. the acceleration factor, auto-step limiting), one should be very careful with their use.

When considering the coupling of the three Poisson-like equations, again two choices are available: simple iteration or a full Newton-Raphson scheme. If the degree of coupling (i.e. related to the magnitude of the current density) is sufficiently low, simple iteration between the equations may be stable and hence cost less than a complete Newton's approach. However, we have observed quadratic convergence with Newton's method whereas the simpler technique will, at best, only converge linearly. Of course each iteration is much more expensive due to the much larger matrix which must be inverted. As the device under study departs from equilibrium, the continuity equations become tightly coupled and Newton's method is required to retain convergence.

One possibility which, with care, could increase convergence and stability would be to implement a reliable interstep interpolation scheme. Presently, MANIFEST uses the previous solution as its guess to the next solution. By using information from earlier solution steps, it is possible to provide an improved estimate for the forthcomming iteration. Originally, a linear extrapolation routine was included in MANIFEST. For very simple devices (i.e. lightly doped diodes) there was a marked improvement in algorithmic stability. Unfortunately, as the device became more nonlinear the extrapolation process provided less accurate estimates than those without extrapolation. Hence, the above scheme (which was in any case not very general) was deleted.

Within MANIFEST, two element structures were tested: those using linear and quadratic basis functions. As expected, a grid of quadratic elements produces smoother and more accurate results than an equivalent mesh of linear elements. Of course processing costs will rise with the increase in accuracy (even for the same number of unknowns) as a quadratic element generates a rather large bandwidth in the system matrix. Unfortunately, extra care must be applied when using quadratic meshes as the potentials may occasionally overshoot their true values near regions of high electric fields. This phenomenon, which cannot easily occur with linear elements, may lead to spurious oscillations in the solution and can seriously affect the convergence properties of the Newton-Raphson algorithm.

The reader will note the use of quadrilaterals rather than triangles in the two-dimensional version of MANIFEST. Although nearly any shape could be used for element design (and different shapes can be intermixed), quadrilaterals allow for a straightforward and uniform extension to three-dimensional programs. A recent review of newly developed finite-element programs indicates a trend away from triangular forms [20].

When solving semiconductor device problems with MANIFEST, the user should attempt to extract as must useful information about the device as possible with a one-dimensional model before proceeding with a two or three-dimensional analysis. The cost of analyzing a device increases dramatically as the number of spatial dimensions increase. Not only are more nodes involved (hence there are more equations to process) but the cost of matix inversion also increases with its size. As opposed to the obvious use of such a design tool, i.e. generating terminal operating characteristics, the most interesting and potentially useful information is contained in the solution potentials. In general, the electrostatic and quasi-Fermi potentials will be known far more accurately that current density or capacitance characteristics. In future, researchers using such simulation tools should concentrate on studing device physics from the potentials (or energy bands) rather than relying solely on measured terminal behavior.

There are several areas where MANIFEST could be substantially improved. For any field problem, one is always faced with producing a suitable finite-element mesh which represents the best tradeoff between node density and running time. Usually, the mesh density is increased near regions where one expects a large field gradient (as near geometic singularities). The semiconductor problem compounds mesh design in two respects: devices tend to be split into domains of low gradient potentials which are coupled by high gradient ridges (e.g. the emitter, base, and collector regions of a transistor); and these high-field ridges may migrate through the device as the operating conditions change. Both points can be solved (although not easily) with an adaptive mesh-refinement algorithm. Ideally, the algorithm would monitor local convergence (via the residuals) and field strength, adding (or deleting) nodes where necessicary. Another possible solution would make use of "intelligent elements" which monitor their gradient and introduce field singularities if the gradient becomes too high. Such a scheme would be useful for a wide variety of field problems, linear or otherwise.

As a final advance towards a completely automated program, the run-step sequencer could be designed to pick optimal steps (of time, bias potential, etc.) so as to trace a characteristic curve for some device with minimal cost and operator intervention. In general, future developments in

device modelling programs should strive towards techniques which are simple to use and are guaranteed to produce reasonably accurate results. As these programs will be primarily used by highly trained design engineers, computer costs will not be a major factor when evaluating their performance.

The finite-element method, when combined with a Newton-Raphson algorithm, allows a complete and unified treatment of electronic transport in semiconductor devices. Higher-order, isoparametric elements permit accurate modelling of geometry, media, and source characteristics over a wide range of operating conditions. For many existing and forthcoming devices, this method provides a viable alternative to other analysis schemes.

Appendix A

THE MANIFEST USER'S GUIDE

The "MANIFEST Users's Guide" describes the first version of the Manitoba Finite-Element Semiconductor Tool which was developed by the author during the course of this thesis at the University of Manitoba from 1982 to 1983.

After reviewing the basic THEORY of the finite-element and Newton-Raphson algorithms in Chapter I, a detailed description of GENERAL USAGE AND PROGRAMMING PHILOSOPHY is given in Chapter II. The user is introduced to the various subroutines, variables, common blocks, and data files which comprise the system. Details of essential user programming (such as allocating computer storage and writing problem dependent subroutines) are discussed and various pre- and post-processing facilities are introduced. In Chapter III, all relevant COMMAND DESCRIPTIONS are presented. Chapter IV gives several detailed programming EXAMPLES (with complete data and output listings) while a number of important LIMITATIONS AND EXTENSIONS are discussed in Chapter V.

Copies of the "MANIFEST User's Guide" (TR82-6) may be obtained by contacting the Department of Electrical Engineering at the University of Manitoba (Winnipeg, Manitoba, Canada, R3T 2N2).

Appendix B

DEVICE PARAMETERS

The following parameters may be used with expression (2.6) to describe carrier mobility in silicon. This table is reproduced from Kurata [9, p. 11].

Parameter	μ_p	μ_n
N_{ref} (cm-3)	6.30E16	8.50E16
α	7.60E-1	7.20E-1
μ_{max} (cm2/v/s)	4.95E02	1.33E03
μ_{min} (cm2/v/s)	4.77E01	6.50E01
E^{c} cm-1)	1.95E04	8.00E03
β	1.0	2.0

These ionization-rate parameters are to be used with expressions (2.27) and (2.28). This table is also adapted from Kurata [9, p. 14].

Parameter	A (cm-1)	b (v cm-1)
Electron	3.80E6	1.75E6
Hole	2.25E7	3.26E6

Appendix C

THE GRAIN-BOUNDARY PROGRAM

This appendix provides the source listing for a one-dimensional grain-boundary simulation program. Users can easily vary parameters relating to the bulk semiconductor (n-type silicon in this case) and the grain-boundary interface. In particular, the interface is modelled as an infinitely thin sheet of charge located at X=0. The total charge is given by:

$$Q_{is} = -q*(Q_{vb}*f + Q_{fx})$$

where q is the charge of an electron (1.6022E-19 C), Q_{vb} is a constant factor reflecting the density of interface states with charge dependent upon the potentials, Q_{fx} is a constant factor reflecting the density of fixed charge, and f ($0<f<1$) determines the probability of occupation of a grain-boundary trap by an electron. A sample run of this program is provided in Appendix D.

```
10. , //GRAIN1D JOB ',,,F=45,I=10,R=512K,T=9,L=4,C=O',SHAW
20.  //STEP1 EXEC FORTXCG,OPT=2,MAP=NOMAP,S=NOS,
30.  //  PARM.GO='SIZE=512K,EP=MAIN',REGION=512K,
40.  //  USERLIB='SHAW.MANIFEST.DBL.LOAD',P=D,AD=DBLPAD4
50.  //FORT.SYSPRINT DD DUMMY
60.  //FORT.SYSIN DD *
70.  C
80.  C     MANIFEST --- MANITOBA FINITE-ELEMENT SEMICONDUCTOR TOOL
90.  C                  ONE-DIMENSIONAL VERSION
100. C
110. C     GRAIN-BOUNDARY PROGRAM
120. C
130.       CALL MANGO1
140.       STOP
150.       END
160.       SUBROUTINE EVAL1(TPHI,XPOSN)
170. C
180. C     PROCESS MEDIA AND VOLUME SOURCES FOR
190. C     1D GRAIN-BOUNDARY MODEL
200. C
210.       REAL TPHI(MAXNOD,3,2),XPOSN(MAXNOD),NI,NCHRG,NT,KT
220. C
230.       COMMON /PARMS/TEMPER,DOPE,EPSON,UN,UP,SIGN,SIGP,VTH,NT,QVB,GENER,
240.      &QFX
250.       COMMON /PARMS2/NI,KT,ECHRG
260.       COMMON /MISC1/MAXNOD,MAXELM,MAXEC1,MAXEC2,N,NV,NNODES,NELEMS
270.       COMMON /MISC2/P1,P2,P3,P1P,P2P,P3P,X,NODNUM,IELEM,IEQNUM
280.       COMMON /MISC4/RK1,RK2,RK3,S1,S2,S3,DRK1,DRK1N,DRK1P,DRK2,DRK2N,
290.      &DRK2P,DRK3,DRK3N,DRK3P,DS1,DS1N,DS1P,DS2,DS2N,DS2P,DS3,DS3N,DS3P
300. C
310.       CALL GPARMS(TPHI,XPOSN)
320.       NCHRG=NI*EXP((P1-P2)/KT)
330.       PCHRG=NI*EXP((P3-P1)/KT)
340. C
350.       S1=-ECHRG*(PCHRG-NCHRG+DOPE)
360.       DS1=ECHRG*((PCHRG+NCHRG)/KT)
370.       DS1N=-ECHRG*NCHRG/KT
380.       DS1P=-ECHRG*PCHRG/KT
390. C
400.       S2=(ECHRG*NI**2*SIGN*SIGP*VTH*NT-ECHRG*SIGN*SIGP*VTH*NT*PCHRG*
410.      &NCHRG)/(NI*SIGN+NI*SIGP+SIGN*NCHRG+SIGP*PCHRG)+ECHRG*GENER
420.       DENOM=(KT*NI**2*SIGN**2+2.*KT*NI**2*SIGN*SIGP+KT*NI**2*SIGP**2+2.*
430.      &KT*NI*SIGN**2*NCHRG+2.*KT*NI*SIGN*SIGP*(PCHRG+NCHRG)+2.*KT*NI*SIGP
440.      &**2*PCHRG+KT*SIGN**2*NCHRG**2+2.*KT*SIGN*SIGP*PCHRG*NCHRG+KT*SIGP*
450.      &*2*PCHRG**2)
460.       DS2=(-ECHRG*NI**2*SIGN**2*SIGP*VTH*NT*NCHRG+ECHRG*NI**2*SIGN*SIGP*
470.      &*2*VTH*NT*PCHRG+ECHRG*SIGN**2*SIGP*VTH*NT*PCHRG*NCHRG**2-ECHRG*
480.      &SIGN*SIGP**2*VTH*NT*PCHRG**2*NCHRG)/DENOM
490.       DS2N=(ECHRG*NI**2*SIGN**2*SIGP*VTH*NT*NCHRG+ECHRG*NI*SIGN**2*SIGP*
500.      &VTH*NT*PCHRG*NCHRG+ECHRG*NI*SIGN*SIGP**2*VTH*NT*PCHRG*NCHRG+ECHRG*
510.      &SIGN*SIGP**2*VTH*NT*PCHRG**2*NCHRG)/DENOM
520.       DS2P=(-ECHRG*NI**2*SIGN*SIGP**2*VTH*NT*PCHRG-ECHRG*NI*SIGN**2*SIGP
530.      &*VTH*NT*PCHRG*NCHRG-ECHRG*NI*SIGN*SIGP**2*VTH*NT*PCHRG*NCHRG-ECHRG
540.      &*SIGN**2*SIGP*VTH*NT*PCHRG*NCHRG**2)/DENOM
550. C
560.       S3=S2
570.       DS3=DS2
580.       DS3N=DS2N
590.       DS3P=DS2P
600. C
610. C     DEFINE PERMITTIVITY OF MEDIA
620. C
630.       RK1=(8.8542E-14)*EPSON
```

```
      DRK1=0.0
      DRK1N=0.0
      DRK1P=0.0
C
      RK2=UN*NCHRG*ECHRG
      DRK2=RK2/KT
      DRK2N=-DRK2
      DRK2P=0.0
C
      RK3=-UP*PCHRG*ECHRG
      DRK3=-RK3/KT
      DRK3N=0.0
      DRK3P=-DRK3
C
      RETURN
      END
      SUBROUTINE USRRUN(TPHI,D1,MAP)
C
C     UPDATE DIRICHLET BOUNDARYS FOR ILLUMINATION CHANGES
C     VALID ONLY UNDER LOW INJECTION CONDITIONS
C
C     I.E. ASSUME:  GENER= (PCHRG-NI) * (VTH*NT*SIGP)
C
      REAL TPHI(MAXNOD,3,2),NI,NT,KT
      INTEGER MAP(MAXNOD)
C
      COMMON /PARMS/TEMPER,DOPE,EPSON,UN,UP,SIGN,SIGP,VTH,NT,QVB,GENER,
     &QFX
      COMMON /PARMS2/NI,KT,ECHRG
      COMMON /MISC1/MAXNOD,MAXELM,MAXEC1,MAXEC2,N,NV,NNODES,NELEMS
C
      DELTP=KT*ALOG((GENER/(SIGP*VTH*NT)+NI**2/DOPE)/NI)
      DELTN=KT*ALOG(DOPE/NI)
      DELT=DELTP+DELTN
      IF (MAP(1).EQ.0) TPHI(1,3,1)=TPHI(1,2,1)+DELT
      IF (MAP(NNODES).EQ.0) TPHI(NNODES,3,1)=TPHI(NNODES,2,1)+DELT
C
      RETURN
      END
      SUBROUTINE USER(TPHI,XPOSN)
C
C     INITIALIZE POTENTIALS AND PARMS FOR GB
C
      REAL TPHI(MAXNOD,3,2),XPOSN(MAXNOD),NI,NT,KT
C
      COMMON /PARMS/TEMPER,DOPE,EPSON,UN,UP,SIGN,SIGP,VTH,NT,QVB,GENER,
     &QFX
      COMMON /PARMS2/NI,KT,ECHRG
      COMMON /MISC1/MAXNOD,MAXELM,MAXEC1,MAXEC2,N,NV,NNODES,NELEMS
C
C     READ FUNCTION SWITCH
C
      READ (5,*) ISWT
      IF (ISWT.NE.1) GO TO 10
C
C     DEFINE FIXED PARMS (HELMUT WOLF / SIZ)
C
      EGO=1.119
      DEGDT=-2.3E-4
      ECHRG=1.6022E-19
      KT=8.61708E-5*TEMPER
      EG=EGO+DEGDT*(TEMPER-300.0)
      NI=6.190E15*(TEMPER**1.5)*EXP(-EG/(2.0*KT))
```

```
1270.         PRINT 40,TEMPER,KT,EG,NI
1280.   C
1290.   10    IF (ISWT.NE.2) GO TO 30
1300.   C
1310.   C     INIT TPHI
1320.   C
1330.         PHIS=2.0*KT*ALOG(DOPE/NI)
1340.         PHIN=PHIS/2.0
1350.         PHIP=PHIS+KT*ALOG((GENER/(SIGP*VTH*NT)+NI**2/DOPE)/NI)
1360.         DO 20 I=1,NNODES
1370.         TPHI(I,1,1)=PHIS
1380.         TPHI(I,2,1)=PHIN
1390.         TPHI(I,3,1)=PHIP
1400.   20    CONTINUE
1410.   C
1420.   30    RETURN
1430.   40    FORMAT (/' PROPERTIES OF SILICON'//' TEMPERATURE =',F5.0/' KT =',
1440.        &E12.4/' EG =',E12.4/' NI =',E12.4)
1450.         END
1460.         SUBROUTINE EVAL2(TPHI,XPOSN)
1470.   C
1480.   C     PROCESS GRAIN-BOUNDARY SOURCE TERMS (QVB AND QFX)
1490.   C
1500.   C     QVB IS PROPORTIONAL TO VARIABLE CHARGE ON THE GB
1510.   C       (I.E.  NIS= QVB*F)
1520.   C     QFX IS PROPORTIONAL TO FIXED CHARGE ON THE GB
1530.   C     TOTAL CHARGE IS:  QIS= ECHRG * (QVB*F + QFX)
1540.   C
1550.         COMMON /PARMS/TEMPER,DOPE,EPSON,UN,UP,SIGN,SIGP,VTH,NT,QVB,GENER,
1560.        &QFX
1570.         COMMON /PARMS2/NI,KT,ECHRG
1580.         COMMON /MISC1/MAXNOD,MAXELM,MAXEC1,MAXEC2,N,NV,NNODES,NELEMS
1590.         COMMON /MISC2/P1,P2,P3,P1P,P2P,P3P,X,NODNUM,IELEM,IEQNUM
1600.         COMMON /MISC5/CURT1,CURT2,CURT3,DC1,DC1N,DC1P,DC2,DC2N,DC2P,DC3,
1610.        &DC3N,DC3P
1620.   C
1630.         REAL TPHI(MAXNOD,3,2),XPOSN(MAXNOD),NI,KT,NT,NCHRG
1640.   C
1650.         CALL GPARMS(TPHI,XPOSN)
1660.         NCHRG=NI*EXP((P1-P2)/KT)
1670.         PCHRG=NI*EXP((P3-P1)/KT)
1680.   C
1690.         F=(NI*SIGP+SIGN*NCHRG)/(NI*SIGN+NI*SIGP+SIGN*NCHRG+SIGP*PCHRG)
1700.         DENOM=(KT*NI**2*SIGN**2+2.*KT*NI**2*SIGN*SIGP+KT*NI**2*SIGP**2+2.*
1710.        &KT*NI*SIGN**2*NCHRG+2.*KT*NI*SIGN*SIGP*(PCHRG+NCHRG)+2.*KT*NI*SIGP
1720.        &**2*PCHRG+KT*SIGN**2*NCHRG**2+2.*KT*SIGN*SIGP*PCHRG*NCHRG+KT*SIGP*
1730.        &*2*PCHRG**2)
1740.         DF1=(NI*SIGN**2*NCHRG+NI*SIGP**2*PCHRG+2.*SIGN*SIGP*PCHRG*NCHRG)/
1750.        &DENOM
1760.         DF2=(-NI*SIGN**2*NCHRG-SIGN*SIGP*PCHRG*NCHRG)/DENOM
1770.         DF3=(-NI*SIGP**2*PCHRG-SIGN*SIGP*PCHRG*NCHRG)/DENOM
1780.   C
1790.         CURT1=-ECHRG*(QVB*F+QFX)
1800.         DC1=-ECHRG*QVB*DF1
1810.         DC1N=-ECHRG*QVB*DF2
1820.         DC1P=-ECHRG*QVB*DF3
1830.   C
1840.         CURT2=(ECHRG*NI**2*SIGN*SIGP*VTH*QVB-ECHRG*SIGN*SIGP*VTH*QVB*PCHRG
1850.        &*NCHRG)/(NI*SIGN+NI*SIGP+SIGN*NCHRG+SIGP*PCHRG)
1860.         DENOM=(KT*NI**2*SIGN**2+2.*KT*NI**2*SIGN*SIGP+KT*NI**2*SIGP**2+2.*
1870.        &KT*NI*SIGN**2*NCHRG+2.*KT*NI*SIGN*SIGP*(PCHRG+NCHRG)+2.*KT*NI*SIGP
1880.        &**2*PCHRG+KT*SIGN**2*NCHRG**2+2.*KT*SIGN*SIGP*PCHRG*NCHRG+KT*SIGP*
1890.        &*2*PCHRG**2)
```

```
1900.         DC2=(-ECHRG*NI**2*SIGN**2*SIGP*VTH*QVB*NCHRG+ECHRG*NI**2*SIGN*SIGP
191C.        &**2*VTH*QVB*PCHRG+ECHRG*SIGN**2*SIGP*VTH*QVB*PCHRG*NCHRG**2-ECHRG*
1920.        &SIGN*SIGP**2*VTH*QVB*PCHRG**2*NCHRG)/DENOM
1930.         DC2N=(ECHRG*NI**2*SIGN**2*SIGP*VTH*QVB*NCHRG+ECHRG*NI*SIGN**2*SIGP
1940.        &*VTH*QVB*PCHRG*NCHRG+ECHRG*NI*SIGN*SIGP**2*VTH*QVB*PCHRG*NCHRG+
1950.        &ECHRG*SIGN*SIGP**2*VTH*QVB*PCHRG**2*NCHRG)/DENOM
1960.         DC2P=(-ECHRG*NI**2*SIGN*SIGP**2*VTH*QVB*PCHRG-ECHRG*NI*SIGN**2*
1970.        &SIGP*VTH*QVB*PCHRG*NCHRG-ECHRG*NI*SIGN*SIGP**2*VTH*QVB*PCHRG*NCHRG
1980.        &-ECHRG*SIGN**2*SIGP*VTH*QVB*PCHRG*NCHRG**2)/DENOM
1990.  C
2000.         CURT3=CURT2
2010.         DC3=DC2
2020.         DC3N=DC2N
2030.         DC3P=DC2P
2040.  C
2050.         RETURN
2060.         END
2070.  //*
2080.  //GO.SYSLOUT DD DUMMY
2090.  //GO.FT02F001 DD DSN=&&SYSWRK,UNIT=SYSDA,SPACE=(TRK,(1,1)),
2100.  //      DISP=(NEW,DELETE),DCB=(RECFM=FB,LRECL=80,BLKSIZE=8000)
2110.  //GO.FT03F001 DD DSN=SHAW.PHI.DATA,DISP=SHR
2120.  //GO.FT04F001 DD DSN=SHAW.PARM.DATA,DISP=SHR
2130.  //GO.SYSIN DD *
2140.  TITLE    /* DEFINE PROBLEM'S TITLE */
2150.  GRAIN BOUNDARY
2160.  COMMENT
2170.         * * * * *  G R A I N - 1 D  * * * * *
2180.
2190.        GRAIN BOUNDARY PROBLEM WITH THE
2200.        FOLLOWING PARAMETERS:
2210.
2220.          1     TEMPER    TEMPERATURE (K)
2230.          2     DOPE      DOPING CONCENTRATION (DONOR) (CM-3)
2240.          3     EPSON     RELATIVE PERMITTIVITY
2250.          4     UN        ELECTRON MOBILTIY (CM2 V-1 S-1)
2260.          5     UP        HOLE MOBILITY (CM2 V-1 S-1)
2270.          6     SIGN      CAPTURE CROSS SECTION ELECTRONS (CM2)
2280.          7     SIGP      CAPTURE CROSS SECTION HOLES (CM2)
2290.          8     VTH       THERMAL CARRIER VELOCITY (CM S-1)
2300.          9     NT        TRAP CONCENTRATION (BULK) (CM-3)
2310.          10    QVB       TRAP CONCENTRATION FACTOR (GB) (CM-2)
2320.          11    GENER     GENERATION RATE (SEC-1 CM-3)
2330.          12    QFX       FIXED CHARGE FACTOR ON GB (CM-2)
2340.
2350.  NOCOMMENT
2360.  GRID     /* SET UP FE MESH FROM -1.0 TO +1.5 MICRONS */
2370.  5  3
2380.  7      1.0E-4
2390.  1      -1.0
2400.  11     -0.5
2410.  21     -0.25
2420.  31      0.0
2430.  41      0.25
2440.  51      0.50
2450.  61      1.50
2460.  DEFINE  /* GND=1, V(+)=2, GB=3 */
2470.  3
2480.    1 1 1  /* ELEC 1 IS ALWAYS GROUND */
2490.      1
2500.    2 1 1  /* V(+) */
2510.      61
2520.    3 2 1  /* ELEC 3 IS GB */
```

```
2530.       31
2540.   PARMS    /* USE CGS UNITS THROUGHOUT */
2550.   12
2560.   1       300.0    TEMPER
2570.   2       3.0E15   DOPE
2580.   3       11.8     EPSON (SI)
2590.   4       1350.0   UN
2600.   5       475.0    UP
2610.   6       1.0E-16   SIGN
2620.   7       1.0E-14   SIGP
2630.   8       1.0E7    VTH
2640.   9       1.0E17   NT   (TAUP= 1.0E-10 SEC)
2650.   10      0.0      QVB
2660.   11      0.0      GENER
2670.   12      0.0      QFX
2680.   USER     /* INITIALIZE "PARMS2" */
2690.   1
2700.   USER     /* INITIALIZE TPHI */
2710.   2
2720.   NOLIST
2730.   RUN      /* EXTABLISH GB */
2740.   3     0 0 0 0 0
2750.     0.0 1
2760.     -12 1        +1.00E11     0.0         0.0         (QFX)
2770.     0.0 1
2780.     -12 1        +2.00E11     0.0         0.0         (QFX)
2790.     0.0 1
2800.     -10 1        +1.50E11     0.0         0.0         (QVB)
2810.   CLASS
2820.   3
2830.   RUN      /* SWEEP GB BIAS POTENTIAL */
2840.   14    0 1 0 1 0
2850.     0.0 1
2860.       2  2          0.0         0.0         0.0         1     <== COUNT STEPS
2870.     0.0 1
2880.       2  2          0.05        0.05        0.05        2
2890.     0.0 1
2900.       2  2          0.05        0.05        0.05        3
2910.     0.0 1
2920.       2  2          0.10        0.10        0.10        4
2930.     0.0 1
2940.       2  2          0.10        0.10        0.10        5
2950.     0.0 1
2960.       2  2          0.10        0.10        0.10        6
2970.     0.0 1
2980.       2  2          0.10        0.10        0.10        7
2990.     0.0 1
3000.       2  2          0.10        0.10        0.10        8
3010.     0.0 1
3020.       2  2          0.10        0.10        0.10        9
3030.     0.0 1
3040.       2  2          0.10        0.10        0.10        10
3050.     0.0 1
3060.       2  2          0.10        0.10        0.10        11
3070.     0.0 1
3080.       2  2          0.10        0.10        0.10        12
3090.     0.0 1
3100.       2  2          0.10        0.10        0.10        13
3110.     0.0 1
3120.       2  2          0.10        0.10        0.10        14
3130.   GENERATE    /* CALCULATE  PARMS */
3140.   1 1 1
3150.   1 31
3160.   CAPACITANCE
3170.   FINISH
3180.   //
```

Appendix D

SAMPLE OUTPUT

```
- - - - - - - - - - - - - - - - - - - - - - - - - - - - - - - - - - - - - - -

MANIFEST VERSION 1.8-1D


PROCESSING ==> TITLE   /* DEFINE PROBLEM'S TITLE */

     PROBLEM TITLE: GRAIN BOUNDARY

- - - - - - - - - - - - - - - - - - - - - - - - - - - - - - - - - - - - - - -

MANIFEST VERSION 1.8-1D

GRAIN BOUNDARY


PROCESSING ==> COMMENT

       * * * * *  G R A I N - 1 D  * * * * *

      GRAIN BOUNDARY PROBLEM WITH THE
      FOLLOWING PARAMETERS:

        1     TEMPER    TEMPERATURE (K)
        2     DOPE      DOPING CONCENTRATION (DONOR) (CM-3)
        3     EPSON     RELATIVE PERMITTIVITY
        4     UN        ELECTRON MOBILTIY (CM2 V-1 S-1)
        5     UP        HOLE MOBILITY (CM2 V-1 S-1)
        6     SIGN      CAPTURE CROSS SECTION ELECTRONS (CM2)
        7     SIGP      CAPTURE CROSS SECTION HOLES (CM2)
        8     VTH       THERMAL CARRIER VELOCITY (CM S-1)
        9     NT        TRAP CONCENTRATION (BULK) (CM-3)
        10    QVB       TRAP CONCENTRATION FACTOR (GB) (CM-2)
        11    GENER     GENERATION RATE (SEC-1 CM-3)
        12    QFX       FIXED CHARGE FACTOR ON GB (CM-2)

NOCOMMENT

- - - - - - - - - - - - - - - - - - - - - - - - - - - - - - - - - - - - - - -

MANIFEST VERSION 1.8-1D

GRAIN BOUNDARY


PROCESSING ==> GRID    /* SET UP FE MESH FROM -1.0 TO +1.5 MICRONS */

     INPUT UNIT(S) =   5
     OPTION #(S) =   3
     # OF ELEMENTS =  30
     # OF NODES =  61
     SCALE FACTOR =  0.1000D-03


ELEM(S)    NODE(S)

    1         1    2    3
    2         3    4    5
    3         5    6    7
    4         7    8    9
    5         9   10   11
    6        11   12   13
    7        13   14   15
    8        15   16   17
    9        17   18   19
   10        19   20   21
   11        21   22   23
   12        23   24   25
   13        25   26   27
   14        27   28   29
   15        29   30   31
   16        31   32   33
   17        33   34   35
   18        35   36   37
   19        37   38   39
   20        39   40   41
   21        41   42   43
   22        43   44   45
   23        45   46   47
   24        47   48   49
   25        49   50   51
```

```
  26        51   52   53
  27        53   54   55
  28        55   56   57
  29        57   58   59
  30        59   60   61

NODE(S)    COORDINATE(S)

   1      -0.1000D-03
   2      -0.9380D-04
   3      -0.8760D-04
   4      -0.8170D-04
   5      -0.7580D-04
   6      -0.7050D-04
   7      -0.6520D-04
   8      -0.6080D-04
   9      -0.5640D-04
  10      -0.5320D-04
  11      -0.5000D-04
  12      -0.4750D-04
  13      -0.4500D-04
  14      -0.4250D-04
  15      -0.4000D-04
  16      -0.3750D-04
  17      -0.3500D-04
  18      -0.3250D-04
  19      -0.3000D-04
  20      -0.2750D-04
  21      -0.2500D-04
  22      -0.2250D-04
  23      -0.2000D-04
  24      -0.1750D-04
  25      -0.1500D-04
  26      -0.1250D-04
  27      -0.1000D-04
  28      -0.7500D-05
  29      -0.5000D-05
  30      -0.2500D-05
  31       0.0
  32       0.2500D-05
  33       0.5000D-05
  34       0.7500D-05
  35       0.1000D-04
  36       0.1250D-04
  37       0.1500D-04
  38       0.1750D-04
  39       0.2000D-04
  40       0.2250D-04
  41       0.2500D-04
  42       0.2750D-04
  43       0.3000D-04
  44       0.3250D-04
  45       0.3500D-04
  46       0.3750D-04
  47       0.4000D-04
  48       0.4250D-04
  49       0.4500D-04
  50       0.4750D-04
  51       0.5000D-04
  52       0.5460D-04
  53       0.5920D-04
  54       0.6740D-04
  55       0.7560D-04
  56       0.8650D-04
  57       0.9740D-04
  58       0.1101D-03
  59       0.1228D-03
  60       0.1364D-03
  61       0.1500D-03

- - - - - - - - - - - - - - - - - - - - - - - - - - - - - - - - - - - - - - -

MANIFEST VERSION 1.8-1D

GRAIN BOUNDARY

PROCESSING ==> DEFINE  /* GND=1, V(+)=2, GB=3 */

     # OF ELECTRODES TO PROCESS =   3

     ELECTODE # =   1     TYPE =   1     # OF NODES =   1

NODE(S)
```

```
   1

     ELECTODE # =   2     TYPE =   1     # OF NODES =   1
NODE(S)
  61

     ELECTODE # =   3     TYPE =   2     # OF NODES =   1
NODE(S)
  31

- - - - - - - - - - - - - - - - - - - - - - - - - - - - - - - - - - - - - -
MANIFEST VERSION 1.8-1D
GRAIN BOUNDARY

PROCESSING ==> PARMS   /* USE CGS UNITS THROUGHOUT */
     # PARMS TO READ =  12

 NO.        PARMAMETER(S)

   1        0.3000D+03
   2        0.3000D+16
   3        0.1180D+02
   4        0.1350D+04
   5        0.4750D+03
   6        0.1000D-15
   7        0.1000D-13
   8        0.1000D+08
   9        0.1000D+18
  10        0.0
  11        0.0
  12        0.0

- - - - - - - - - - - - - - - - - - - - - - - - - - - - - - - - - - - - - -
MANIFEST VERSION 1.8-1D
GRAIN BOUNDARY

PROCESSING ==> USER    /* INITIALIZE "PARMS2" */

PROPERTIES OF SILICON

TEMPERATURE = 300.
KT =  0.2585D-01
EG =  0.1119D+01
NI =  0.1282D+11

- - - - - - - - - - - - - - - - - - - - - - - - - - - - - - - - - - - - - -
MANIFEST VERSION 1.8-1D
GRAIN BOUNDARY

PROCESSING ==> USER    /* INITIALIZE TPHI */


- - - - - - - - - - - - - - - - - - - - - - - - - - - - - - - - - - - - - -
MANIFEST VERSION 1.8-1D
GRAIN BOUNDARY

PROCESSING ==> NDLIST


- - - - - - - - - - - - - - - - - - - - - - - - - - - - - - - - - - - - - -
MANIFEST VERSION 1.8-1D
```

```
GRAIN BOUNDARY

PROCESSING ==> RUN      /* EXTABLISH GB */

     # OF STEPS =   3
     MAX. # OF ITERATIONS =  10
     MAXIMUM DISPLACEMENT NORM =  0.1000D-02
     ACCELERATION FACTOR =  0.1000D+01
     OPTION #(S) =   0   0   0   0   0


STEP NUMBER =   1
TIME =  0.0
NUMBER OF ELECTRODES =   1

     ELECTRODE #: -12      PROCESS CODE =   1
     VALUE(S):  0.1000D+12

BIAS =  0.0


RECORD OF CONVERGENCE

ITER       DISP. NORM
```

```
SPARSE MATRIX SOLUTION BY ZOLLENKOPF BIFACTORIZATION.


LOCATIONS USED BEFORE SIMAS =   172

MAXIMUM LOCATIONS USED =   172

NUMBER OF FILL-INS =     0

LOCATIONS USED AFTER SIMAS =    86
```

```
   1        0.9305D-02
   2        0.7209D-02
   3        0.1811D-02
   4        0.7613D-04

BIAS =  0.0


STEP NUMBER =    2
TIME =  0.0
NUMBER OF ELECTRODES =    1

     ELECTRODE #: -12      PROCESS CODE =    1
     VALUE(S):  0.2000D+12

BIAS =  0.0


RECORD OF CONVERGENCE

ITER        DISP. NORM

   1        0.3427D-01
   2        0.2506D-01
   3        0.6419D-02
   4        0.3786D-03

BIAS =  0.0


STEP NUMBER =    3
TIME =  0.0
NUMBER OF ELECTRODES =    1

     ELECTRODE #: -10      PROCESS CODE =    1
     VALUE(S):  0.1500D+12

BIAS =  0.0


RECORD OF CONVERGENCE

ITER        DISP. NORM

   1        0.4235D-01
   2        0.8812D-02
   3        0.2004D-02
   4        0.7833D-04

BIAS =  0.0

- - - - - - - - - - - - - - - - - - - - - - - - - - - - - - - - - - - - -

MANIFEST VERSION 1.8-1D

GRAIN BOUNDARY


PROCESSING ==> CLASS

     PROBLEM CLASS STRUCTURE =    3

- - - - - - - - - - - - - - - - - - - - - - - - - - - - - - - - - - - - -

MANIFEST VERSION 1.8-1D

GRAIN BOUNDARY


PROCESSING ==> RUN      /* SWEEP GB BIAS POTENTIAL */

     # OF STEPS =  14
     MAX. # OF ITERATIONS =  10
     MAXIMUM DISPLACEMENT NORM =  0.1000D-02
     ACCELERATION FACTOR =  0.1000D+01
     OPTION #(S) =   0   1   0   1   0


STEP NUMBER =    4
TIME =  0.0
NUMBER OF ELECTRODES =    1

     ELECTRODE #:    2      PROCESS CODE =    2
     VALUE(S):  0.0          0.0          0.0
```

```
BIAS =  0.0

RECORD OF CONVERGENCE
ITER        DISP. NORM


SPARSE MATRIX SOLUTION BY ZOLLENKOPF BIFACTORIZATION.

LOCATIONS USED BEFORE SIMAS =  1902

MAXIMUM LOCATIONS USED =  1902

NUMBER OF FILL-INS =  126

LOCATIONS USED AFTER SIMAS =  1014
```

```
   1       0.5081D-07

BIAS =  0.0


STEP NUMBER =   5
TIME =  0.0
NUMBER OF ELECTRODES =   1

     ELECTRODE #:   2     PROCESS CODE =   2
     VALUE(S):  0.5000D-01  0.5000D-01  0.5000D-01

BIAS =  0.5000D-01


RECORD OF CONVERGENCE

ITER       DISP. NORM

   1       0.5856D-01
   2       0.4268D-02
   3       0.2671D-03

BIAS =  0.5000D-01


STEP NUMBER =   6
TIME =  0.0
NUMBER OF ELECTRODES =   1

     ELECTRODE #:   2     PROCESS CODE =   2
     VALUE(S):  0.5000D-01  0.5000D-01  0.5000D-01

BIAS =  0.1000D+00


RECORD OF CONVERGENCE

ITER       DISP. NORM

   1       0.4848D-01
   2       0.2867D-02
   3       0.1465D-03

BIAS =  0.1000D+00


STEP NUMBER =   7
TIME =  0.0
NUMBER OF ELECTRODES =   1

     ELECTRODE #:   2     PROCESS CODE =   2
     VALUE(S):  0.1000D+00  0.1000D+00  0.1000D+00

BIAS =  0.2000D+00


RECORD OF CONVERGENCE

ITER       DISP. NORM

   1       0.8414D-01
   2       0.7186D-02
   3       0.1472D-02
   4       0.3253D-03

BIAS =  0.2000D+00


STEP NUMBER =   8
TIME =  0.0
NUMBER OF ELECTRODES =   1

     ELECTRODE #:   2     PROCESS CODE =   2
     VALUE(S):  0.1000D+00  0.1000D+00  0.1000D+00

BIAS =  0.3000D+00


RECORD OF CONVERGENCE

ITER       DISP. NORM

   1       0.7649D-01
   2       0.2255D-02
   3       0.3003D-03
```

```
BIAS =  0.3000D+00


STEP NUMBER =   9
TIME =  0.0
NUMBER OF ELECTRODES =   1

     ELECTRODE #:   2     PROCESS CODE =   2
     VALUE(S):  0.1000D+00  0.1000D+00  0.1000D+00

BIAS =  0.4000D+00


RECORD OF CONVERGENCE

ITER       DISP. NORM

   1       0.6897D-01
   2       0.1876D-02
   3       0.3675D-03

BIAS =  0.4000D+00


STEP NUMBER =  10
TIME =  0.0
NUMBER OF ELECTRODES =   1

     ELECTRODE #:   2     PROCESS CODE =   2
     VALUE(S):  0.1000D+00  0.1000D+00  0.1000D+00

BIAS =  0.5000D+00


RECORD OF CONVERGENCE

ITER       DISP. NORM

   1       0.6240D-01
   2       0.1482D-02
   3       0.1491D-03

BIAS =  0.5000D+00


STEP NUMBER =  11
TIME =  0.0
NUMBER OF ELECTRODES =   1

     ELECTRODE #:   2     PROCESS CODE =   2
     VALUE(S):  0.1000D+00  0.1000D+00  0.1000D+00

BIAS =  0.6000D+00


RECORD OF CONVERGENCE

ITER       DISP. NORM

   1       0.5651D-01
   2       0.1180D-02
   3       0.9925D-04

BIAS =  0.6000D+00


STEP NUMBER =  12
TIME =  0.0
NUMBER OF ELECTRODES =   1

     ELECTRODE #:   2     PROCESS CODE =   2
     VALUE(S):  0.1000D+00  0.1000D+00  0.1000D+00

BIAS =  0.7000D+00


RECORD OF CONVERGENCE

ITER       DISP. NORM

   1       0.5168D-01
   2       0.1029D-02
   3       0.7601D-04

BIAS =  0.7000D+00


STEP NUMBER =  13
```

```
TIME =  0.0
NUMBER OF ELECTRODES =   1

     ELECTRODE #:   2     PROCESS CODE =   2
     VALUE(S):  0.1000D+00  0.1000D+00  0.1000D+00

BIAS =  0.8000D+00


RECORD OF CONVERGENCE

ITER       DISP. NORM

   1       0.4753D-01
   2       0.8857D-03

BIAS =  0.8000D+00


STEP NUMBER =  14
TIME =  0.0
NUMBER OF ELECTRODES =   1

     ELECTRODE #:   2     PROCESS CODE =   2
     VALUE(S):  0.1000D+00  0.1000D+00  0.1000D+00

BIAS =  0.9000D+00


RECORD OF CONVERGENCE

ITER       DISP. NORM

   1       0.4400D-01
   2       0.7824D-03

BIAS =  0.9000D+00


STEP NUMBER =  15
TIME =  0.0
NUMBER OF ELECTRODES =   1

     ELECTRODE #:   2     PROCESS CODE =   2
     VALUE(S):  0.1000D+00  0.1000D+00  0.1000D+00

BIAS =  0.1000D+01


RECORD OF CONVERGENCE

ITER       DISP. NORM

   1       0.4088D-01
   2       0.7262D-03

BIAS =  0.1000D+01


STEP NUMBER =  16
TIME =  0.0
NUMBER OF ELECTRODES =   1

     ELECTRODE #:   2     PROCESS CODE =   2
     VALUE(S):  0.1000D+00  0.1000D+00  0.1000D+00

BIAS =  0.1100D+01


RECORD OF CONVERGENCE

ITER       DISP. NORM

   1       0.3812D-01
   2       0.6755D-03

BIAS =  0.1100D+01


STEP NUMBER =  17
TIME =  0.0
NUMBER OF ELECTRODES =   1

     ELECTRODE #:   2     PROCESS CODE =   2
     VALUE(S):  0.1000D+00  0.1000D+00  0.1000D+00

BIAS =  0.1200D+01
```

```
RECORD OF CONVERGENCE

ITER       DISP. NORM

   1       0.3564D-01
   2       0.6616D-03

BIAS =  0.1200D+01

- - - - - - - - - - - - - - - - - - - - - - - - - - - - - - - - - - - - - -

MANIFEST VERSION 1.8-1D

GRAIN BOUNDARY


PROCESSING ==> GENERATE   /* CALCULATE  PARMS */

     OPTION #(S) =   1   1   1
     CURRENT DENSITY SELECTION NODES:   1  31


STEP NUMBER =   4
TIME =  0.0000D-78
BIAS =  0.0000D-78

     ENERGY(S):  0.4112D-08 -0.2562D-10  0.2181D-16
     SOURCE INTEGRAL(S): -0.3651D-07  0.6411D-21  0.6411D-21

     CURRENT DENSITY:  0.7001D-38
        STANDARD DEVIATION:  0.3316D-37
        CASES PROCESSED:  19%
        EXIT VALUE:  0.4773D-02
        EXIT CRITERIUM:  0.1000D-01


STEP NUMBER =   5
TIME =  0.0000D-78
BIAS =  0.5000D-01

     ENERGY(S):  0.4214D-08  0.2220D-03 -0.1926D-09
     SOURCE INTEGRAL(S): -0.3677D-07 -0.6617D-08 -0.6617D-08

     CURRENT DENSITY:  0.1086D-01
        STANDARD DEVIATION:  0.9557D-04
        CASES PROCESSED:   4%
        EXIT VALUE:  0.2984D+00
        EXIT CRITERIUM:  0.1000D-01


STEP NUMBER =   6
TIME =  0.0000D-78
BIAS =  0.1000D+00

     ENERGY(S):  0.4468D-08  0.8665D-03 -0.1176D-08
     SOURCE INTEGRAL(S): -0.3736D-07 -0.1950D-07 -0.1950D-07

     CURRENT DENSITY:  0.1873D-01
        STANDARD DEVIATION:  0.1124D-03
        CASES PROCESSED:   4%
        EXIT VALUE:  0.2568D+00
        EXIT CRITERIUM:  0.1000D-01


STEP NUMBER =   7
TIME =  0.0000D-78
BIAS =  0.2000D+00

     ENERGY(S):  0.5184D-08  0.3692D-02 -0.1718D-07
     SOURCE INTEGRAL(S): -0.3882D-07 -0.5578D-07 -0.5578D-07

     CURRENT DENSITY:  0.3398D-01
        STANDARD DEVIATION:  0.1108D-03
        CASES PROCESSED:   4%
        EXIT VALUE:  0.2057D+01
        EXIT CRITERIUM:  0.1000D-01


STEP NUMBER =   8
TIME =  0.0000D-78
BIAS =  0.3000D+00

     ENERGY(S):  0.6050D-08  0.1003D-01 -0.8165D-07
     SOURCE INTEGRAL(S): -0.4027D-07 -0.1079D-06 -0.1079D-06

     CURRENT DENSITY:  0.6619D-01
```

```
        STANDARD DEVIATION:  0.1238D-03
        CASES PROCESSED:    4%
        EXIT VALUE:  0.4159D+00
        EXIT CRITERIUM:  0.1000D-01


STEP NUMBER =   9
TIME =  0.0000D-78
BIAS =  0.4000D+00

     ENERGY(S):  0.7032D-08  0.2190D-01 -0.1793D-06
     SOURCE INTEGRAL(S): -0.4165D-07 -0.1755D-06 -0.1755D-06

     CURRENT DENSITY:  0.1089D+00
        STANDARD DEVIATION:  0.1817D-03
        CASES PROCESSED:    4%
        EXIT VALUE:  0.9585D+00
        EXIT CRITERIUM:  0.1000D-01


STEP NUMBER =  10
TIME =  0.0000D-78
BIAS =  0.5000D+00

     ENERGY(S):  0.8118D-08  0.4280D-01 -0.3617D-06
     SOURCE INTEGRAL(S): -0.4298D-07 -0.2575D-06 -0.2575D-06

     CURRENT DENSITY:  0.1697D+00
        STANDARD DEVIATION:  0.1179D-03
        CASES PROCESSED:    4%
        EXIT VALUE:  0.6367D+00
        EXIT CRITERIUM:  0.1000D-01


STEP NUMBER =  11
TIME =  0.0000D-78
BIAS =  0.6000D+00

     ENERGY(S):  0.9295D-08  0.7770D-01 -0.5588D-06
     SOURCE INTEGRAL(S): -0.4423D-07 -0.3572D-06 -0.3572D-06

     CURRENT DENSITY:  0.2549D+00
        STANDARD DEVIATION:  0.6825D-04
        CASES PROCESSED:    4%
        EXIT VALUE:  0.6600D+00
        EXIT CRITERIUM:  0.1000D-01


STEP NUMBER =  12
TIME =  0.0000D-78
BIAS =  0.7000D+00

     ENERGY(S):  0.1056D-07  0.1338D+00 -0.7810D-06
     SOURCE INTEGRAL(S): -0.4542D-07 -0.4753D-06 -0.4753D-06

     CURRENT DENSITY:  0.3798D+00
        STANDARD DEVIATION:  0.3717D-04
        CASES PROCESSED:    4%
        EXIT VALUE:  0.6045D+01
        EXIT CRITERIUM:  0.1000D-01


STEP NUMBER =  13
TIME =  0.0000D-78
BIAS =  0.8000D+00

     ENERGY(S):  0.1189D-07  0.2235D+00 -0.1019D-05
     SOURCE INTEGRAL(S): -0.4655D-07 -0.6241D-06 -0.6241D-06

     CURRENT DENSITY:  0.5571D+00
        STANDARD DEVIATION:  0.1594D-03
        CASES PROCESSED:    4%
        EXIT VALUE:  0.6856D+00
        EXIT CRITERIUM:  0.1000D-01


STEP NUMBER =  14
TIME =  0.0000D-78
BIAS =  0.9000D+00

     ENERGY(S):  0.1330D-07  0.3582D+00 -0.1259D-05
     SOURCE INTEGRAL(S): -0.4763D-07 -0.7785D-06 -0.7785D-06

     CURRENT DENSITY:  0.7934D+00
        STANDARD DEVIATION:  0.1125D-03
        CASES PROCESSED:    4%
        EXIT VALUE:  0.2573D+00
        EXIT CRITERIUM:  0.1000D-01
```

```
STEP NUMBER =  15
TIME =  0.0000D-78
BIAS =  0.1000D+01

     ENERGY(S):  0.1478D-07  0.5627D+00 -0.1490D-05
     SOURCE INTEGRAL(S): -0.4865D-07 -0.9528D-06 -0.9528D-06

     CURRENT DENSITY:  0.1121D+01
        STANDARD DEVIATION:  0.2992D-04
        CASES PROCESSED:   4%
        EXIT VALUE:  0.2992D+01
        EXIT CRITERIUM:  0.1000D-01


STEP NUMBER =  16
TIME =  0.0000D-78
BIAS =  0.1100D+01

     ENERGY(S):  0.1633D-07  0.8667D+00 -0.1694D-05
     SOURCE INTEGRAL(S): -0.4962D-07 -0.1139D-05 -0.1139D-05

     CURRENT DENSITY:  0.1573D+01
        STANDARD DEVIATION:  0.7532D-04
        CASES PROCESSED:   4%
        EXIT VALUE:  0.1578D+01
        EXIT CRITERIUM:  0.1000D-01


STEP NUMBER =  17
TIME =  0.0000D-78
BIAS =  0.1200D+01

     ENERGY(S):  0.1794D-07  0.1311D+01 -0.1854D-05
     SOURCE INTEGRAL(S): -0.5055D-07 -0.1323D-05 -0.1323D-05

     CURRENT DENSITY:  0.2183D+01
        STANDARD DEVIATION:  0.1505D-03
        CASES PROCESSED:   4%
        EXIT VALUE:  0.1005D+01
        EXIT CRITERIUM:  0.1000D-01

- - - - - - - - - - - - - - - - - - - - - - - - - - - - - - - - - - - - -

MANIFEST VERSION 1.8-1D

GRAIN BOUNDARY


PROCESSING ==> CAPACITANCE


STEP         BIAS       CAPACITANCE

   4       0.0000D-78  0.8427D-07
   5       0.5000D-01  0.6345D-07
   6       0.1000D+00  0.2671D-07
   7       0.2000D+00  0.1294D-07
   8       0.3000D+00  0.1152D-07
   9       0.4000D+00  0.1058D-07
  10       0.5000D+00  0.8552D-08
  11       0.6000D+00  0.9810D-08
  12       0.7000D+00  0.5007D-08
  13       0.8000D+00  0.9161D-08
  14       0.9000D+00  0.6349D-08
  15       0.1000D+01  0.7445D-08
  16       0.1100D+01  0.5873D-08
  17       0.1200D+01  0.5064D-08


- - - - - - - - - - - - - - - - - - - - - - - - - - - - - - - - - - - - -

MANIFEST VERSION 1.8-1D

GRAIN BOUNDARY


PROCESSING ==> FINISH

     TOTAL CPU TIME USED =   5.37 SECONDS.
```

Appendix E

ELECTRONIC TRANSPORT AT GRAIN BOUNDARIES

This appendix presents a reprint of the paper Electronic Transport at Grain Boundaries in Silicon which is to appear (as of September 1983) in Physical Review B. As the paper was written early in the development of this thesis, there are several minor variations in notation and technique regarding the numerical analysis of grain-boundary phenomina. Readers should note that -- in the paper -- Qis is independent of the potentials and carrier concentrations.

Electronic transport at grain boundaries in silicon

G. C. McGonigal, D. J. Thomson, J. G. Shaw, and H. C. Card
Materials and Devices Research Laboratory, Department of Electrical Engineering, University of Manitoba, Winnipeg, Manitoba R3T 2N2, Canada
(Received 9 April 1982; revised manuscript received 25 October 1982)

An experimental investigation is reported on carrier transport across isolated grain boundaries in large-grain cast silicon material. Continuous interface-state densities in the 10^{15}–10^{16}-$m^{-2}eV^{-1}$ range are measured for the lower part of the silicon energy gap. The grain-boundary diffusion potentials for this material are shown in some cases to vary appreciably over a single grain-boundary plane; this is thought to be due to a nonuniform spatial distribution of interface charge at the grain boundaries. Numerical calculations by finite-element methods, of the quasi-Fermi potentials in the vicinity of the grain boundary, suggest that the supply of majority carriers by diffusion to this interface may be the limiting factor controlling their transport. The experiments have consequently been interpreted according to the diffusion model rather than the customary thermionic-emission model of majority-carrier transport across grain boundaries.

I. INTRODUCTION

The transport properties of electrons and holes at grain boundaries in polycrystalline semiconductors is of considerable present interest, both for academic and practical reasons. The grain boundary differs from other semiconductor interface systems in that the orientation but not the crystal structure changes across this interface; this can give rise to behavior which is unique to this type of interface and as such is of scientific importance. Electronic and optical processes at grain boundaries are of current practical importance as a result of their effects on the photovoltaic conversion efficiency of thin-film polycrystalline semiconductor solar cells.[1]

Pioneering work on the characterization of electronic mechanisms at grain boundaries has been carried out recently by Seager and co-workers at Sandia Laboratories.[2–5] These workers have investigated the effects of grain-boundary interface states on the majority carrier transport in *n*-type polycrystalline silicon. From measurements of current-voltage characteristics performed on isolated grain boundaries, they have been able to extract the energy distribution of interface states.

In this paper we present the results of an experimental investigation of transport phenomena at grain boundaries in silicon. The present work differs from the work of Seager *et al.* in several ways.

One difference is that our investigations are of grain boundaries in *p*-type silicon so that the information obtained concerning grain-boundary interface states corresponds to the energy distribution of these states in the lower half of the energy gap, whereas Seager has obtained data for the upper half of the energy gap by using *n*-type silicon samples. We are also studying a somewhat different material: cast silicon from Wacker Chemitronic Ltd. of the "Silso" type as opposed to their case of neutron-transmutation doped polycrystalline CVD silicon of smaller grain size and higher doping concentration. We further include in our study the cases of both high and low grain-boundary potential barriers. Optical illumination intensity is employed in addition to bias voltage and temperature as experimental parameters: With the exception of some recent work concerning grain-boundary recombination velocity[5] most of the earlier studies involved dark measurements.[2–4]

This paper also provides a departure from previous work in its treatment of the data in terms of a diffusion model of carrier transport at grain boundaries. This intepretation is guided by results obtained in the present work by simulation of grain boundaries using finite-element techniques of numerical analysis. In the course of the experimental investigations, we have also discovered that, in the Wacker material at least, the grain-boundary potential cannot generally be regarded as uniform over the grain-boundary plane. Several other observations of a presently qualitative nature indicate that the carrier transport at grain boundaries can be a rather complex process.

II. THE GRAIN-BOUNDARY INTERFACE

The grain boundary in a polycrystalline semiconductor is an interface between two identical crystals of different orientation. The mismatch in bonding between the two crystals results in bond defects (e.g., distorted bond angles, dilated or compressed bonds, broken bonds) at the grain boundary. These defects are expected to exist primarily on a single plane of atoms, and to a lesser extent on the neighboring planes. We consider the width of the grain-boundary region to be negligible on the scale of variations in the potential in the adjacent space-charge regions.

The bonding defects at the grain boundary translate into localized electronic states or interface states. The energy distribution of these states is of importance in the determination of carrier-transport processes. There is in general a net charge associated with the grain-boundary interface states, which is modified by a voltage applied across

the grain boundary. The interface states also function as recombination centers for excess electrons and holes at the grain boundary. It has been observed that for grain boundaries in n-type silicon, the interface states inevitably contribute a net negative charge.[6] In p-type silicon the grain-boundary interface states contribute a positive charge.[6] The reason for this difference in n- and p-type silicon is the difference in the position of the Fermi energy relative to the interface-state distribution in the two cases.

In order to be specific we restrict our discussion to the case of grain boundaries in p-type silicon. This is the case which pertains to the experimental work reported below, and to the energy-band diagram of Fig. 1. It is assumed that positive charge associated with the interface states is balanced by a net negative charge due to uncompensated ionized acceptor impurities. These acceptor impurities are located in space-charge regions adjacent to the grain boundary in the crystalline regions to either side. It is assumed that the interface charge is uniformly distributed over the area of the grain boundary. The magnitude of the potential barrier at the grain boundary for zero-applied bias voltage (V_{d0} in Fig. 1) is referred to as the diffusion potential of the grain boundary.

Poisson's equation relates the charge distribution to the electrostatic potential. This may be expressed as

$$\nabla^2\phi_i = -\frac{\rho}{\epsilon}\,, \tag{1}$$

where ϕ_i is the electrostatic potential, ϵ is the permittivity of the semiconductor, and ρ is the charge density given by

$$\rho = q(p - n + N_d^+ - N_a^-) + Q_{is}\,. \tag{2}$$

In Eq. (2), Q_{is} is the net charge in the grain-boundary interface states and N_d^+, N_a^- are the ionized donor, acceptor impurity concentrations in the semiconductor (assumed uniformly distributed in space). For the p-type material discussed in this paper, $N_d = 0$ in Eq. (2). In general Q_{is} is a function of n and p, the concentrations of electrons and holes, at the grain boundary. These carrier concentrations are given by

$$n = n_i \exp\left[\frac{E_{fn} - E_i}{kT}\right], \tag{3}$$

$$p = n_i \exp\left[\frac{E_i - E_{fp}}{kT}\right], \tag{4}$$

where E_{fn}, E_{fp} are the quasi-Fermi levels for electrons and holes, respectively. In Eq. (1) the potential ϕ_i may be replaced by $-E_i/q$ where the energy E_i, which appears in (3) and (4), is known as the intrinsic level (see Fig. 1). The charge Q_{is} in grain-boundary interface states is dependent upon the energy distribution of these states, and also upon their charge state when occupied by an electron (donorlike or acceptorlike).

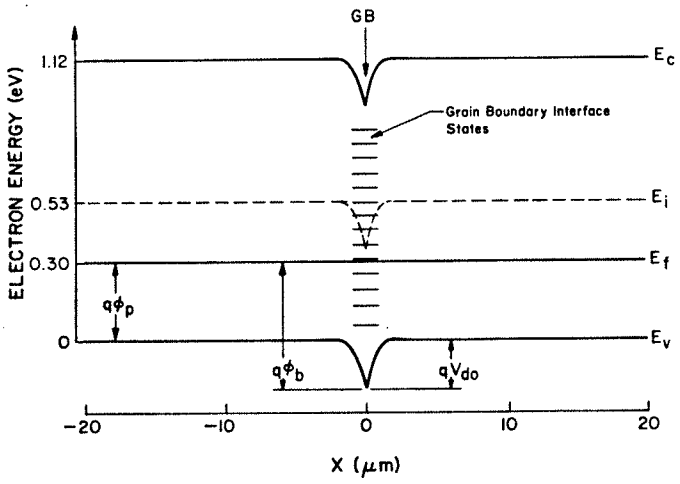

FIG. 1. Numerical calculations of electron energy-band diagram of grain boundary under equilibrium conditions ($V=0$, dark), showing the diffusion potential V_{d0}, barrier height ϕ_b, bulk Fermi potential ϕ_p, intrinsic energy level E_i, and interface states present at $X=0$; $N_a = 10^{20}$ m^{-3}, $T=300$ K, $Q_{is} = .15\times10^{14} q$ C m^{-2}.

III. CARRIER TRANSPORT ACROSS GRAIN BOUNDARIES

In the previous section, we have described the processes which contribute to the formation of a diffusion potential, or potential barrier against the transport of majority carriers across grain boundaries in semiconductors such as silicon. We have also introduced the localized interface states, which act as recombination centers for electrons and holes, and which modify the diffusion potential by adjusting their charge according to the concentrations of electrons and holes at the grain boundary. In this section we address the major theme of this work: electron and hole transport processes.

In order to model the transport of electrons and holes analytically, an appropriate transport model must be adopted. To guide this procedure, we have performed a simulation of grain-boundary transport using finite-element methods of numerical analysis, which employ the Newton-Raphson algorithm (Appendix A).

To simplify the interpretation of these numerical results, we have solved for the case where the charge in grain-boundary interface states Q_{is} is fixed, and does not depend on bias voltage applied across the boundary. In addition, we ignore recombination through grain-boundary interface states. While it is realized that these assumptions are unphysical in a real grain boundary, they provide for the analysis of electron and hole transport uncomplicated by the effects of recombination at this interface.

An example of the results of the numerical calculations is given in Fig. 2, which shows the dependence of the electron and hole quasi-Fermi potentials, and of the electrostatic potential, upon position for a voltage V applied across the grain boundary. Note that in this figure, as well as Fig. 3, the quasi-Fermi level $E_{fn} \neq E_{fp}$ as a consequence of dark generation-recombination currents.[17] The effect of this voltage is to lower the potential barrier, or band bending, on the forward-biased side of the boundary and to increase it on the opposite (reverse-biased) side. The voltage division between these two sides depends, among other things, upon the charge in grain-boundary interface states, Q_{is}, and in particular on the manner in

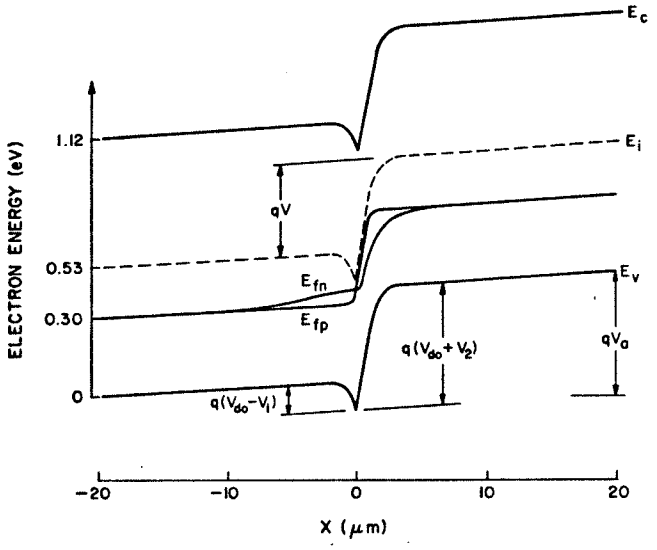

FIG. 2. Numerical calculations of electron energy-band diagram under applied bias voltage V, showing quasi-Fermi levels E_{fn} and E_{fp} for electrons and holes, and voltage division V_1 and V_2 between forward-biased and reversed-biased space-charge regions. (Note: $V=V_1+V_2$.) V_a is the total applied voltage from $X=-20$ to $+20$ μm, which is approximately equal to V except at very large current densities. Slope of energy bands and potentials away from grain boundaries is associated with voltage drop in the series resistance of the grains. This contributes to V_a. $\tau=(\sigma v_{th}N_t)^{-1}=10^{-9}$ s, $N_a=10^{20}$ m^{-3}, $T=300$ K, $Q_{is}=1.5\times10^{14}q$ C m^{-2}.

which this charge changes under applied bias voltage. However, in the calculation of Fig. 2, the effects of changing Q_{is} are not considered, as discussed above.

We consider the mechanism by which holes cross the grain boundary in similar generality to the earlier treatment of the metal-semiconductor contacts, or Schottky barriers.[7] The holes must negotiate the space-charge region by the usual drift and diffusion mechanisms and upon arriving at the grain boundary either be accepted into the other side, or be reflected. The opposite side of the grain boundary is the same semiconductor, but with a different crystal orientation. The acceptance of the holes can be regarded as a process of interface emission characterized by a collection velocity v_r, which is in series with the drift and diffusion processes.

In the Schottky barrier, at least for high-mobility semiconductors such as silicon, the thermionic emission of the majority carriers (holes) into the metal becomes the bottleneck to current flow. This has been discussed by Gossick,[8] and more recently by Rhoderick.[9] The reason is that there are very few available states in the metal with momentum parallel to the surface to match that of the holes from the semiconductor. This is because the energy at which the holes are transferred is close to the valence-band edge in the semiconductor, but remote from the band edges in the metal.

In the present problem, however, the states on either side of the grain boundary have the same energy relative to the band edges. The limitations due to conservation of parallel momentum are greatly relaxed. We also deal with diffusion potentials which are much smaller than those normally encountered in Schottky barriers. In addition there exists, on the reverse-biased side, a large electric field which is attractive to the majority carriers. The consequence of these factors is that holes, upon reaching the grain-boundary interface, are collected efficiently and the supply of these carriers through the space-charge region may become the limiting factor in determining the current. Following the work of Rhoderick[9] and of Crowell and Sze,[7] we consider the energy diagram of Fig. 3 and the extremes of hole concentration at the grain boundary when transport is limited by diffusion (case 1, curve D) or by emission (case 2, curve E).

We suggest that a general approximate expression for the intermediate case may, on the basis of Refs. 7 and 3, be written

$$J_p=\frac{qN_vV_r}{1+\frac{V_r}{V_d}}\exp\left[-\frac{\phi_b}{V_T}\right]\left[\exp\left[\frac{V_1}{V_T}\right]-\exp\left[-\frac{V_2}{V_T}\right]\right]$$

$$=\frac{qN_vN_r}{1+\frac{V_r}{V_d}}\exp\left[-\frac{\phi_b}{V_T}\right]\exp\left[\frac{V_1}{V_T}\right]\left[1-\exp\left[-\frac{V}{V_T}\right]\right], \tag{5}$$

since $V=V_1+V_2$, where V is the total voltage applied across the grain boundary, V_1 is the forward bias on the left side of the grain boundary in Fig. 2 which is so far an undetermined portion of V and V_2 is the reverse bias on the right side of the boundary. V_d and V_r are the diffusion and interface recombination (or in our case collection) velocities for the holes, respectively. ϕ_b is the equilibrium barrier height which is independent of V (Fig. 1); N_v is the effective density of states in the valence band; $v_d=\mu\xi_{m1}$ and ξ_{m1} the maximum electric field in the space-charge region on the forward-biased side of the

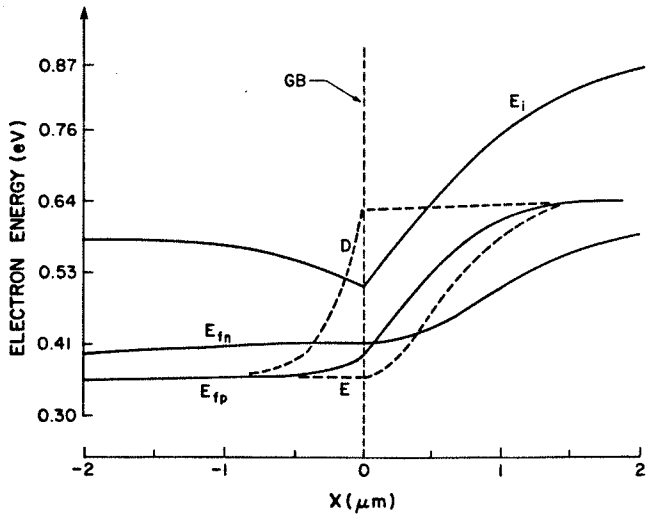

FIG. 3. Expanded view of calculations in neighborhood of grain boundary for case of Fig. 2. Curves D and E show schematically the limiting cases of diffusion- and emission-limited transport.

grain boundary. In the present case $V_r = \mu\xi_{m2}$, with ξ_{m2} the maximum field on the reverse-biased side. For any appreciable voltage across the boundary, $\xi_{m2} \gg \xi_{m1}$ and $V_r \gg V_d$ in Eq. (5).

In case 1 (shown schematically as D in Fig. 3), the interface collection velocity v_r is considered to be large. The hole current is then limited by diffusion through the (forward-biased) space-charge region and the concentration of holes at the grain boundary remains small under applied voltage. This is illustrated by a rise in the hole quasi-Fermi level E_{fp}, as the grain boundary is approached from the forward-biased side. The transfer of holes across the grain boundary which in this case is proportional to their concentration at $x=0$ $p(0)$ is kept small by the limited supply to the boundary. On the other hand, if the collection velocity v_r is small (case 2 and E in Fig. 3) holes arriving at the grain boundary are not immediately removed by the reverse-biased side. The supply of holes to the grain boundary is bountiful and $p(0)$ increases to its maximum value determined by the hole Fermi level on the forward-biased side. In this case E_{fp} is relatively flat up to the grain boundary. As we observe in Figs. 2 and 3 which show the results of an exact calculation, the true situation is intermediate between these extremes, with E_{fp} rising (in this case by more than kT) as the grain boundary is approached.

On the basis of the results of Figs. 2 and 3 from the numerical analysis, we believe that the diffusion model ($V_r \gg V_d$), as originally described by Stratton,[10] is the appropriate basis for the interpretation of majority-carrier transport across grain boundaries. This model is employed in the analysis of the experimental data of the following sections.

IV. SAMPLE FABRICATION AND MEASUREMENTS

The material used in this study was p-type cast silicon of large grain size (typically 1 mm) of the "Silso" type, obtained from Wacker Chemitronic Ltd. The doping concentration N_a from bulk measurements (e.g., C^{-2} vs V of Schottky-barrier capacitance-voltage characteristics for diodes within single grains) was $\simeq 3\times10^{21}$ m^{-3}. The polycrystalline wafers ($100\times100\times0.4$ mm) were cut into strips approximately 1×20 mm. These strips were chemically polished in 3:1:1 HNO_3 (79%), HF (49%), glacial acetic acid, for $\simeq$3 min to eliminate saw damage and to highlight the grain boundaries.[11] Grain boundaries were examined under an optical microscope to identify those which were planar and which extended over the entire cross section of the strip in both the lateral and vertical directions; the latter requirement was determined by examining the back face of the samples.

Aluminum contacts were evaporated in a four-probe configuration (Fig. 4) and were sintered at 600°C for 2 min in N_2 to form ohmic contacts. Aluminum connections were bonded to the (inner two) voltage-measurement contacts. A single grain boundary was then enclosed between the voltage probes. Current was injected and removed at the outer two contacts. Contact potential errors in the determination of the voltage across the grain boundary were avoided by means of this four-probe technique; voltages were measured using a Keithley 610C electrometer with input impedance of 10^{11} ohms. All measurements were made under dc conditions.

Measurements at temperatures from 300 to 200 K were performed in a FTS Systems Inc. Multi-Cool closed-cycle refrigeration unit. For temperatures from 100 to 200 K a cryogenic liquid-nitrogen sample chamber fitted with a

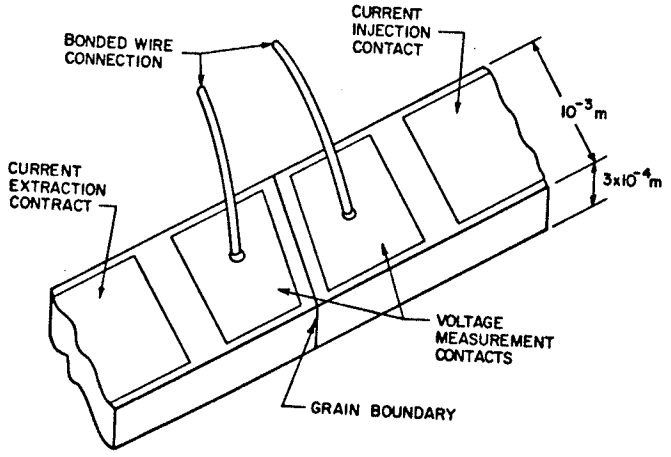

FIG. 4. Sample geometry. Cross-sectional area of all samples $\simeq 3\times10^{-7}$ m^{-2}.

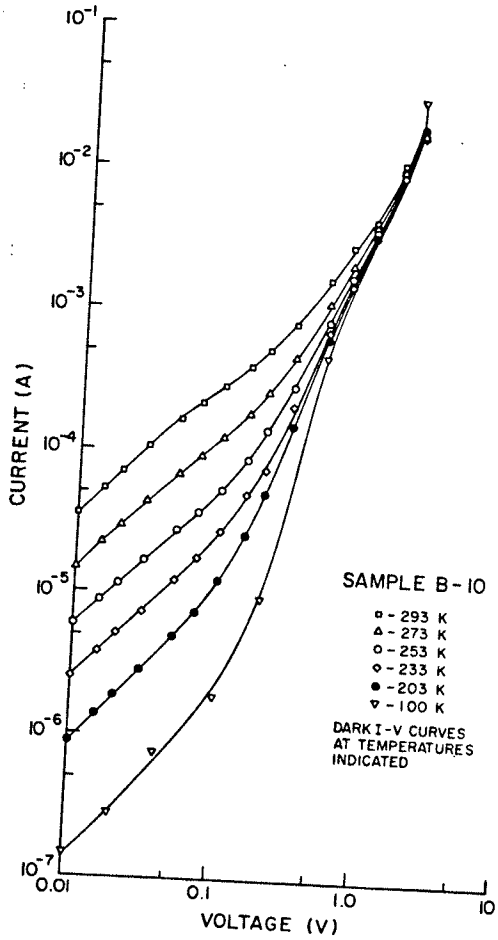

FIG. 5. Experimental dark characteristics of grain boundary B-10 at several measurement temperatures.

heater for temperature variation was employed. Temperatures were measured using Cu-Co thermocouples. Optical illumination was provided by a Sylvania ELH projection lamp with an infrared filter to remove all photon wavelengths $\lambda < 1\ \mu m$. This ensured a relatively uniform photogeneration throughout the sample. The optical intensity was determined using an Optikon Model 550-1 radiometer. The accuracy of this determination was approximately $\pm 30\%$. The reflection from the silicon surface was estimated to be 30%.

The equilibrium grain-boundary diffusion potential, V_{d0}, was observed to vary over a wide range for samples cut from different grain boundaries [V_{d0} values from <0.1 V (electrically inactive) to $\simeq 0.33$ V at 300 K].

V. EXPERIMENTAL RESULTS

Figure 5 shows a typical example of the current-voltage characteristics measured on a grain boundary having a relatively large zero-bias diffusion potential ($V_{d0} \simeq = 0.25$ V at 300 K). Results are given for a number of measurement temperatures. Measurements such as these were performed for a variety of samples over the temperature range $100 \leq T \leq 300$ K. Figure 6 shows a typical example of the corresponding characteristics for a grain boundary with a somewhat smaller (zero bias) diffusion potential. These grain boundaries turn out to exhibit a spatial variation in their properties over the boundary plane. Figure 7 is representative of a different case of grain boundary in which the potential barrier is spatially uniform, as we discuss in a later section.

The effect of optical illumination on the grain-boundary current-voltage characteristics is illustrated in Figs. 8 and 9. This data was obtained for optical powers of 0.2 and 50 $W m^{-2}$, respectively, with $1.0 \leq \lambda \leq 1.1\ \mu m$. A range of optical-illumination intensities was investigated, but the rather complicated behavior observed at higher intensities is still under study at this time.

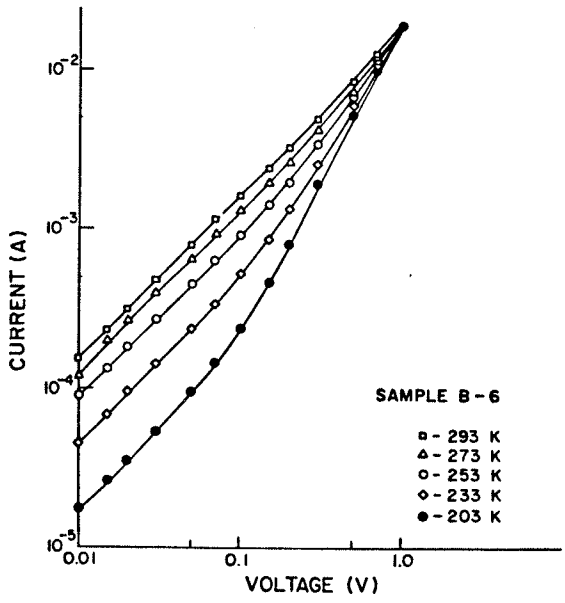

FIG. 6. Experimental dark characteristics of grain boundary B-6 at several measurement temperatures.

In Fig. 10 we show the dependence of the activation energy E_a (defined in Sec. VI) upon the voltage V applied across a boundary region. This activation energy is determined from the temperature dependence of the current-voltage characteristics such as those of Figs. 5–7. Figure 11(a) shows the dependence of E_a upon T (determined at a low value of V) for two of the same samples. From Fig. 11(a) and the expressions of Sec. III we are able to derive the equilibrium (dark, zero-bias) diffusion potential V_{d0}, assuming that this potential is spatially uniform over the boundary plane. This is shown in Fig. 11(b), together with the result expected from a one-dimensional theory. Figures 12(a) and 12(b) give the observed dependence of E_a and V_d upon optical illumination intensity (at 300 K) for the same samples. In this case V_d is no longer the *equilibrium* diffusion potential V_{d0}.

It was also observed that for large grain-boundary voltages, and hence moderately large current densities ($\simeq$10–50 V and $4\times10^5 - 1\times10^6$ $A m^{-2}$) the current exhibited oscillations such as those shown in Fig. 13.

The magnitude of these oscillations was typically on the order of 1% of the dc current. It was observed that a sample biased below the threshold current density for these oscillations could be thermally stimulated into oscillation. Generally, more and larger pulses are observed at higher current densities, and these effects are reversible. We believe these oscillations are due to field emission of carriers from grain-boundary interface states, as discussed in a later section.

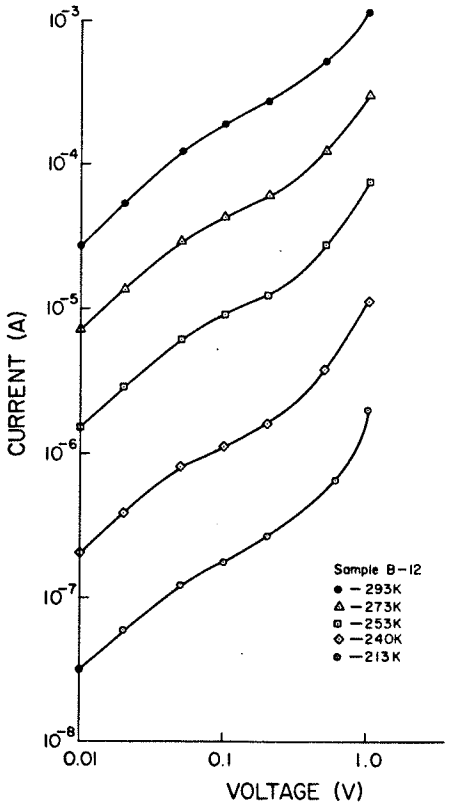

FIG. 7. Experimental dark characteristics of grain boundary B-12 at several measurement temperatures.

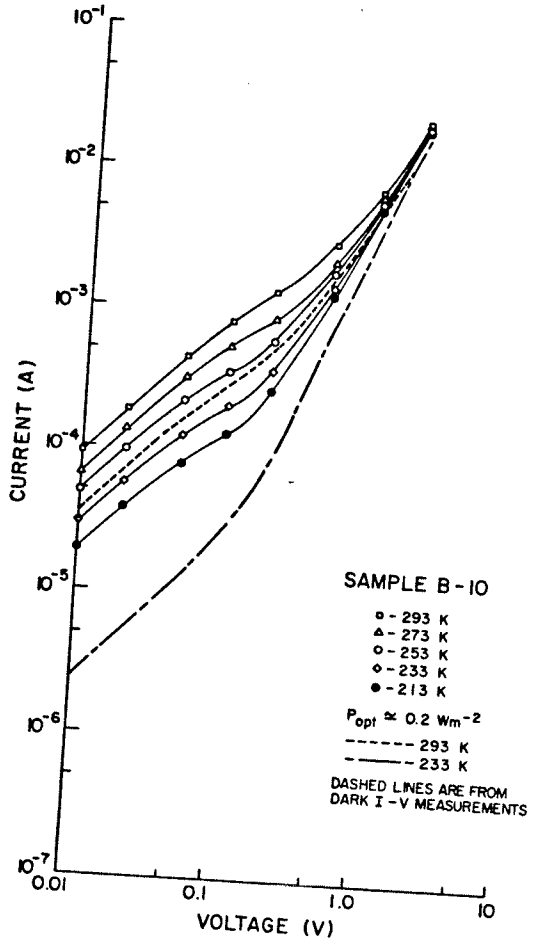

FIG. 8. Experimental characteristics of B-10 under 0.2 W m^{-2} optical illumination ($1.0 < \lambda < 1.1\ \mu m$).

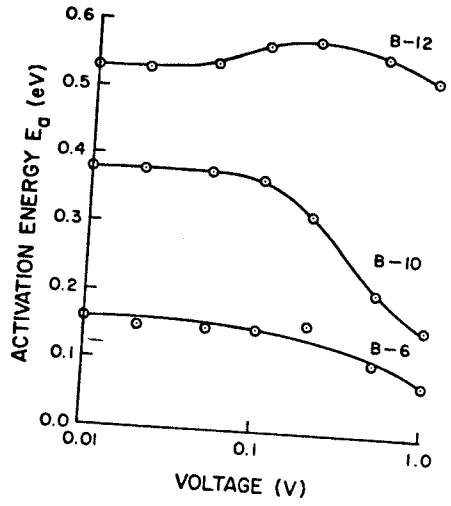

FIG. 10. Activation energy E_a vs V applied to grain boundaries B-10, B-6, and B-12.

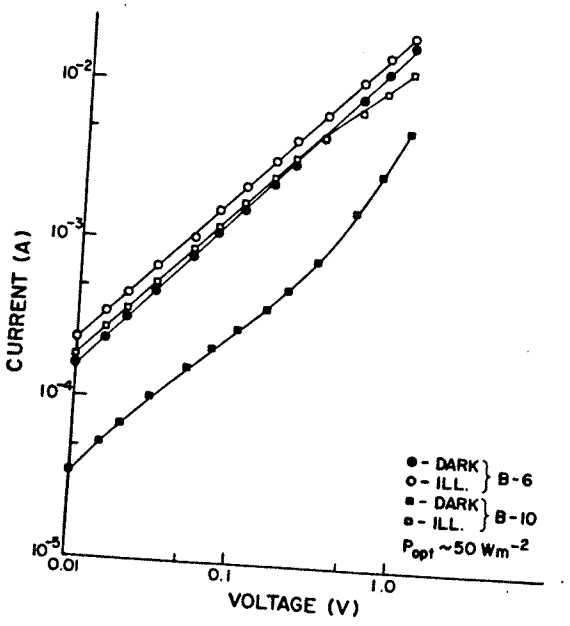

FIG. 9. Experimental characteristics of B-6 and B-10 under 50 W m^{-2} ($1.0 < \lambda < 1.1\ \mu m$) optical illumination.

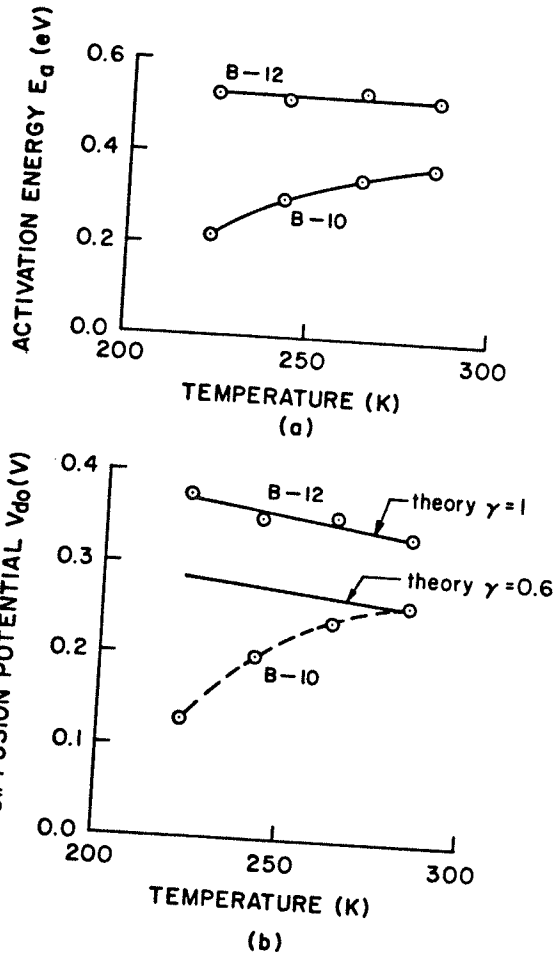

FIG. 11. The dependence of (a) the activation energy and (b) the diffusion potential on temperature for B-10 and B-12 in darkness.

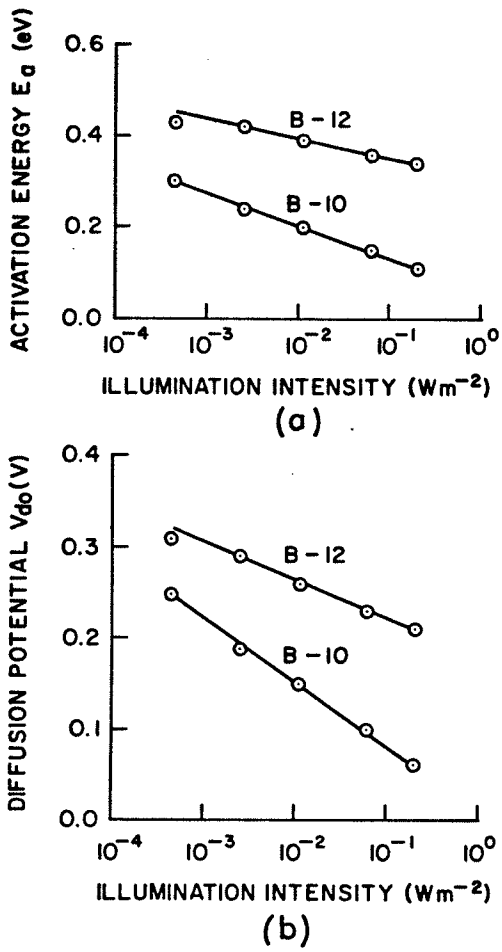

FIG. 12. The dependence of (a) the activation energy and (b) the diffusion potential on illumination intensity for B-10 and B-12. $T=300$ K.

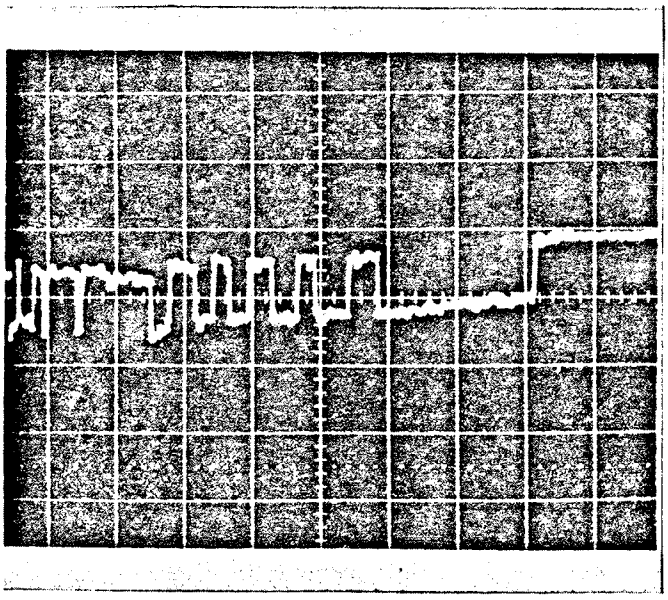

FIG. 13. Current oscillations observed at high dc current densities. Grain-boundary sample B-11. $V=15$ V, $I=150$ mA. Vertical scale: 500 μA/division. Horizontal scale: 1 ms/division.

VI. INTERPRETATION OF RESULTS

The steady-state current-voltage characteristics of the grain boundary in general consist of a component due to the transport of majority carriers over the grain-boundary potential barrier, J_1, a component due to minority carriers transported in the opposite direction, J_2, and finally a component associated with recombination of electrons and holes in grain-boundary interface states, J_3. These three components are illustrated in the energy-band diagram of Fig. 14. Our interpretation of results from the previous section is that the first component is completely dominant over the other two, at least under dark conditions. That is, currents such as those of Figs. 5 to 7 are to be identified with the transport of majority carriers (in our case, holes) over the potential barrier at the grain boundary. (The downward bending of the bands at the grain boundary presents a barrier to holes.) In this interpretation we are in agreement with previous workers.[2-4,12-15] We do, however, consider the other two components in their *indirect* effects upon the majority-carrier current. This will be discussed further below.

In view of the discussion of Sec. III, we adopt the diffusion-limited value of Eq. (5) for the majority-carrier current J_1. In this case ($V_r \gg V_d$), Eq. (5) becomes

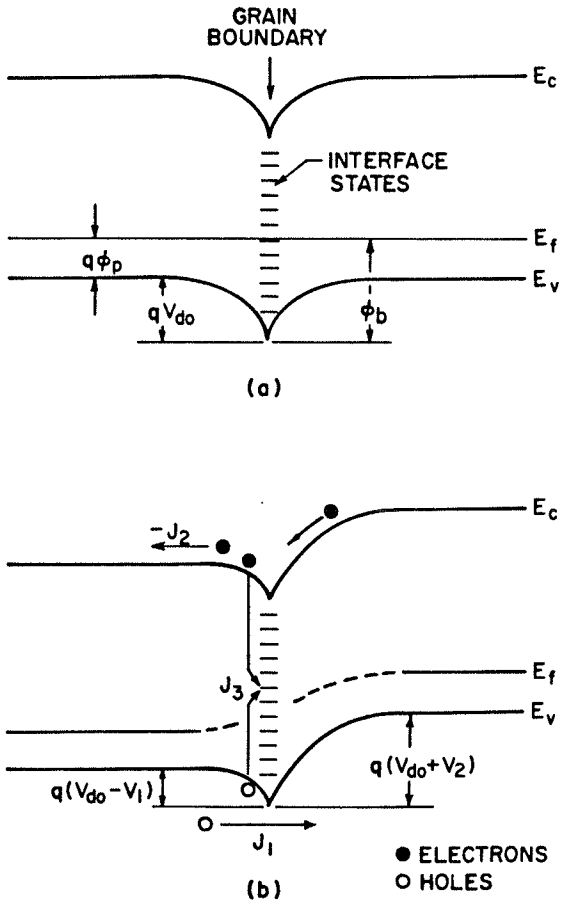

FIG. 14. Electron energy-band diagrams for grain boundary with (zero-bias) diffusion potential V_{d0}. (a) $V=0$; (b) $V>0$. J_1 is the majority-carrier current, J_2 is the minority-carrier current, and J_3 is the recombination current at the grain boundary.

$$J \simeq J_1 \simeq qN_v v_d \exp\left[-\frac{\phi_b}{V_T}\right]\exp\left[\frac{V_1}{V_T}\right]\left[1-\exp\left[-\frac{V}{V_T}\right]\right]$$

$$=qN_v\mu\xi_{m1}\exp\left[-\frac{\phi_p}{V_T}\right]\exp\left[-\frac{V_{d0}}{V_T}\right]\exp\left[\frac{V_1}{V_T}\right]\left[1-\exp\left[-\frac{V}{V_T}\right]\right]$$

$$=qN_a\mu\xi_{m1}\exp\left[-\frac{V_{d0}}{V_T}\right]\exp\left[\frac{V_1}{V_T}\right]\left[1-\exp\left[-\frac{V}{V_T}\right]\right], \tag{6}$$

where $\phi_b = V_{d0}+\phi_p$ (Fig. 14) and we have used $\exp(-\phi_p/V_T)\simeq N_a/N_v$ which is true provided the acceptor impurities (of concentration N_a) remain ionized, i.e., for $T \geq 100$ K in silicon.

For $V \ll V_T$ and $V_1 \ll V_T$ we can simplify (2) to

$$J \simeq qN_a\mu\xi_{m1}\left[\frac{V}{V_T}\right]\exp\left[-\frac{V_{d0}}{V_T}\right], \tag{7}$$

and define an activation energy for the potential barrier at the grain boundary as

$$E_a = -\frac{d\ln\left[\frac{J}{qN_a\mu\xi_{m1}(V/V_T)}\right]}{d(1/kT)}$$

$$=qV_{d0}+q\frac{d(V_{d0})}{d(1/T)}$$

$$=q\left[V_{d0}(T)-T\frac{dV_{d0}}{dT}\right]. \tag{8}$$

Equations (7) and (8) apply for $V \ll V_T$. For relatively large applied voltages, on the other hand, i.e., for $V \gg V_T$, they are replaced by

$$J \simeq qN_a\mu\xi_{m1}\exp\left[-\frac{V_{d0}}{V_T}\right]\exp\left[\frac{V_1}{V_T}\right]$$

$$=qN_a\mu\xi_{m1}\exp\left[-\frac{V_d}{V_T}\right], \tag{7'}$$

where $V_d = V_{d0}-V_1$, and

$$E_a = -\frac{d\ln\left[\frac{J}{qN_a\mu\xi_{m1}}\right]}{d(1/kT)}$$

$$=q(V_{d0}-V_1)+\frac{q}{T}\frac{d(V_{d0}-V_1)}{d(1/T)}$$

$$=q\left[V_d(T)-T\frac{dV_d}{dT}\right]. \tag{8'}$$

Note that the second term on the right-hand sides of Eqs. (8) and (8') turn out to be negative, as discussed below and exactly cancel the temperature dependence of the first term *for spatially-uniform grain boundaries,* so that in this case $E_a \neq E_a(T)$.

We have chosen to take the temperature dependence of the low-field mobility given by[16]

$$\mu(T)=54.3T_n^{-0.57}+\frac{1.36\times10^8 T_n^{-2.23}}{1+[N_a/(2.35\times10^{17}T_n^{2.4})]0.88T_n^{-0.146}} \tag{9}$$

($T_n = T/300$) to the left-hand side in Eqs. (8) and (8'). In these equations, the parameters J, μ, and V_{d0} are temperature dependent, in addition to the explicit appearance of T and $V_T = kT/q$.

The equilibrium diffusion potential V_{d0} in Eq. (8) is temperature dependent for two reasons. First, the temperature dependence of the bulk Fermi potential ϕ_p, given by

$$\phi_p = \frac{kT}{q}\ln(N_v/N_a), \tag{10}$$

gives rise to a temperature dependence of V_{d0} which may be written as

$$\frac{dV_{d0}}{dT} = -\gamma\frac{d\phi_p}{dT}$$

$$\simeq -\frac{\gamma k}{q}\ln\left[\frac{N_v}{N_a}\right], \tag{11}$$

where we have used Eq. (10) and neglected the weak temperature dependence of $\ln N_v$. γ is a parameter which accounts for Fermi-level pinning at the grain boundary by interface states. For examples B-12 and B-10 for example, we have that $\gamma \simeq 0.9$–1.0 and $\gamma \simeq 0.6$, respectively, for the N_{is} measured in these samples (see Appendix B for derivation of γ).

Second, the occurrence of a spatial variation of diffusion potential over the grain-boundary plane will give rise to an "effective V_{d0}" in Eq. (7) which also exhibits a temperature dependence in addition to that of Eq. (11). This is because the current transport through various portions of the grain boundary with different V_{d0} will be weighted by the temperature-dependent factor $\exp(-qV_{d0}/kT)$. At lower temperatures a larger portion of the current will flow through the regions of lowest V_{d0} and the effective V_{d0} will decrease. For a spatially uniform grain boundary dV_{d0}/dT is therefore given by Eq. (11), whereas for a nonuniform boundary, an additional term dependent upon the nature of the spatial nonuniformity contributes to dV_{d0}/dT.

The maximum electric field ξ_{m1} in Eq. (7) corresponds to that close to the grain boundary on the left-hand side of Fig. 14, given in the depletion approximation by[17]

$$\xi_{m1} \simeq \left[\frac{2qN_a}{\epsilon_s}(V_{d0}-V_1-V_T)\right]^{1/2}, \tag{12}$$

where ϵ_s is the silicon permittivity.

As the applied voltage V increase, we have that

$$V=V_1+V_2\,, \tag{13}$$

$$Q_1=-qN_aW_1$$
$$=-[2q\epsilon_sN_a(V_{d0}-V_1-V_T)]^{1/2}\,, \tag{14}$$

$$Q_2=-qN_aW_2$$
$$=-[2q\epsilon_sN_a(V_{d0}+V_2-V_T)]^{1/2}\,, \tag{15}$$

and

$$Q_1+Q_2+Q_{is}=0 \tag{16}$$

for all V. V_{d0}, V_1, and V_2 have been defined above; W_1 and W_2 are the widths of the space-charge regions on the forward- and reverse-biased sides of the grain boundary, respectively. Q_1 and Q_2 are the charge (per unit area) in these space-charge regions (within the depletion approximation), and Q_{is} is the charge per unit area in the grain-boundary interface states.

Let us assume that the grain-boundary interface states remain in equilibrium with the majority carriers (holes) under an applied bias voltage. If we adopt the convention of earlier workers[3,4] that the *change* with bias voltage in the quasi-Fermi level at the grain-boundary interface is approximately equal to the change of its value in the bulk on the forward-biased side, it then follows that

$$Q_{is}(V)=Q_{is}(0)+qN_{is}V_1 \tag{17}$$

for an interface-state density $N_{is}(\mathrm{m^{-2}eV^{-1}})$ which is independent of energy. For an energy-dependent interface-state density, $N_{is}V_1$ in Eq. (17) must be replaced by $\int N_{is}dV_1$.

It is important to realize that the value of N_{is} deduced from measurements using Eq. (17) represents a *lower limit* on the true interface-state density. From our discussion of the majority-carrier transport above, we anticipate a hole transport which is restricted by the supply of holes to the grain boundary (diffusion model) and an appreciable change in the hole quasi-Fermi level E_{fp} across the forward-biased space-charge region. Thus the change in E_{fp} at the grain boundary with applied voltage may be somewhat less than V_1 and N_{is} will be underestimated using Eq. (17) with the experimentally-determined $Q_{is}(V)$.

Finally, we point out that the grain boundaries were modeled as planar interfaces; the possibility of curvature on a macroscopic scale was not accounted for. This may affect the numerical values of N_{is} to some degree.

VII. DISCUSSION OF RESULTS

We have used the diffusion model of Sec. III to analyze the results of Figs. 5–12. This treatment assumes a grain-boundary potential which is spatially uniform over the boundary plane, in accordance with the one-dimensional analysis.

As a general interpretation of the current-voltage characteristics of Figs. 5–7, at very low voltages ($V<V_T$) the curves are near ohmic as expected from Eq. (7). At higher voltages, the increase in J with V originates primarily from the $\exp(V_1/V_T)$ term in Eq. (6). The detailed shape of the characteristic depends upon the variation of V_1 with V, which in turn is controlled by the degree of pinning of the quasi-Fermi level for holes by grain-boundary interface states. The concave nature of these curves at higher V is associated with a high density of interface states N_{is} near midgap (strong pinning), which drops off appreciably towards the valence band. This interpretation is consistent with that offered by Seager *et al.*[2–4] for grain boundaries in *n*-type silicon, in which case N_{is} also falls towards the conduction band.

N_{is} is an important parameter since, among other things, this determines the appropriate value of γ to be used in Eq. (11). We have determined N_{is} as a function of energy by analysis of the current-voltage characteristics at a constant temperature, Fig. 5, in terms of the diffusion theory of the carrier transport. This is in the spirit of the deconvolution scheme of Seager *et al.*,[2–4] and data at three measurement temperatures have been combined to give rise to the N_{is} vs E of Fig. 15. For this sample γ is then determined to be 0.6, as described in the Appendix. Our results for N_{is} agree within an order of magnitude with those obtained by Seager *et al.*,[2–4] in their case in the upper half of the band gap in neutron-transmutation doped silicon. Comparison of $N_{is}(E)$ with earlier workers is made in Fig. 16. The picture which emerges is a peak in the density of interface states of magnitude $N_{is}\simeq 10^{16}$ $\mathrm{m^{-2}eV^{-1}}$ or greater at the peak and of energy spread $\Delta E\simeq 0.1$ eV.

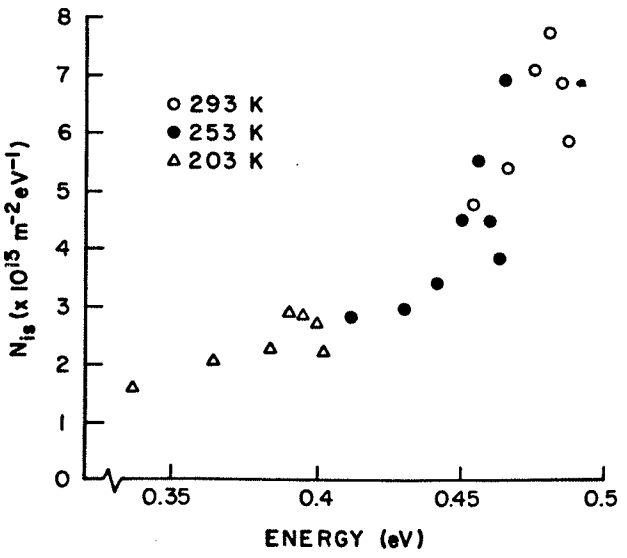

FIG. 15. Density of localized grain-boundary interface states vs energy in band gap of silicon (sample B-10). Points show results obtained from current-voltage characteristics at constant temperature T, for three values of T.

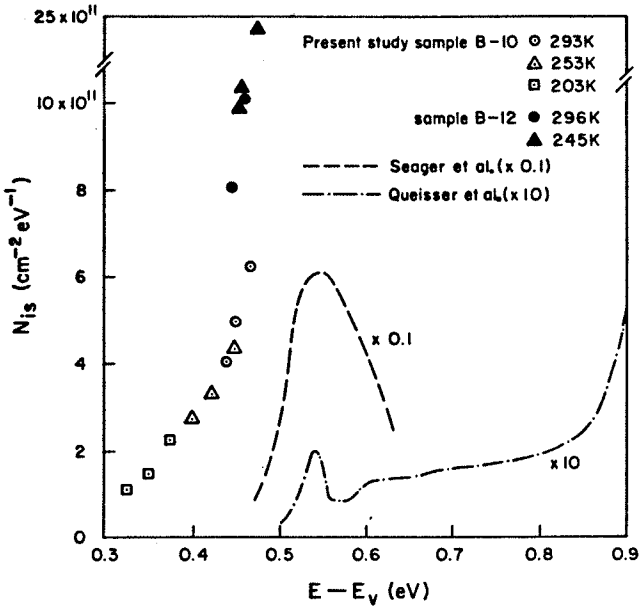

FIG. 16. Comparison of present results for grain-boundary interface states with earlier results for silicon grain boundaries (Refs. 27 and 28). Note units of N_{is} are $cm^{-2}eV^{-1}$ for this figure.

In Fig. 10 we show the dependence of the activation energy E_a (defined in Sec. VI) upon the voltage applied to the grain boundary. In the determination of E_a, the temperature dependence of the mobility, given by Eq. (9), has been removed, i.e., $\ln[J/qN_a\mu(T)\xi_{m1}]$ is plotted vs $1/T$, and the slope used to find E_a in accordance with Eq. (8'). For grain boundaries which are spatially uniform, we can interpret the decrease in E_a at the larger V unambiguously as arising from a decrease in diffusion potential $V_d = V_{d0} - V_1$ due to the increase in V_1 [see Eq. (8')]. As we see below this is the case for grain-boundary sample B-12 but not for B-10 or B-6.

One should realize that the considerably smaller value of E_a for sample B-6 as compared to B-10 and B-12 is a property of the temperature dependence of the current. This does not imply that the absolute value of the current density at a given temperature is much larger. The value of the current density is controlled by the diffusion potential V_{d0}, which for sample B-6 is not significantly lower than for the other samples. The relation between V_{d0} and E_a is strongly dependent on the nonuniformity of the grain boundary.

The increase in E_a with V at low voltages for B-12 in Fig. 10 arises from the preexponential factor in Eq. (6). The temperature dependence of the low-field mobility has been accounted for in arriving at E_a. The temperature dependence of the high-field mobility is smaller than that of the low-field mobility since we are approaching the region of velocity saturation.[17] Since the electric field ξ_{m1} decreases with V, the activation energy at larger V therefore increases.

In the case of grain boundaries B-6 and B-10, arguments which follow indicate that these samples exhibit substantial nonuniformity in their diffusion potentials over the plane of the grain boundary. This prohibits the analysis of the results of Fig. 10 for B-6 and B-10 in terms of the model of Sec. VI, which presupposes spatially uniform grain-boundary potentials.

In Fig. 11 we show how E_a and V_{d0} depend upon temperature for the two grain boundaries B-10 and B-12. For a uniform grain boundary, the activation energy E_a will correspond to V_{d0} for very small N_{is} ($\gamma=0$) and to ϕ_b in Fig. 14 for very large N_{is} ($\gamma\simeq 1$). It must be stressed that, in order to recover the equilibrium diffusion potential V_{d0} from the activation energy E_a, we must employ the analysis of Sec. VI and in particular Eq. (8), since $V < V_T$ in the experimental determination of E_a. Knowing the γ to be used in Eq. (11), we obtain dV_{d0}/dT for Eq. (8) which allows us to determine V_{d0} from E_a. We have therefore implicitly assumed grain boundaries which are *spatially uniform* in their properties. In Fig. 11(b) we show the results of this procedure for B-10 and B-12, together with the dependence of V_{d0} upon T expected theoretically. As we readily observe, B-12 conforms well to the uniform model of Sec. VI with a V_{d0} which decreases slightly with T, in accordance with the temperature dependence of the bulk Fermi potential ϕ_p.

On the other hand, as was discussed in the paragraph following Eq. (11), a grain boundary with spatially nonuniform properties may show a marked *increase* of E_a and V_{d0} with T. This is the case for sample B-10 in Fig. 11. We conclude that while B-12 represents a uniform grain boundary which is suitable for the model of Sec. VI, and which therefore allows an accurate quantitative determination of $V_{d0}(T)$ as in Fig. 11(b), sample B-10 does not. The data of Fig. 11(b) are not expected to be quantitatively correct for B-10, and the most we can say is qualitatively that the apparent V_{d0} increases substantially with increasing temperature as a consequence of its spatially nonuniform grain-boundary potential. Even if Eq. (7) applies with an "effective" $V_{d0}(T)$, the unknown form of the temperature dependence excludes a separation of the two terms on the right-hand side of Eq. (8) for nonuniform samples. We have separately obtained a first-order model for B-10 by assuming a Gaussian distribution of V_{d0} values over the grain-boundary plane.[18] The errors are rather large in this fitting procedure, presumably because a Gaussian distribution of potentials is unphysical in this problem.

The origin of the nonuniformity in diffusion potential for B-10 (also B-6 and others, not shown) is thought to be a spatial variation over the plane of the grain boundary in N_{is}, in N_a, or both. This nonuniformity must be over macroscopic distances (greater than the width W_1, W_2 of the space-charge regions) since otherwise their effects would be integrated electrostatically. The segregation of dopant impurities to the grain boundary can also affect the interface-state distribution in a spatially nonuniform way. We are presently working to quantity this model, which gives a three-dimensional nature to the transport problem. We must point out that in the work of Seager *et al.*,[2-5] the impurities were introduced by neutron-transmutation doping, which is expected to produce a uniform N_a, unlike the present case of cast silicon with dopant introduced into the melt.[19] At any rate, it seems

fairly certain that both uniform and nonuniform grain boundaries exist in the Wacker silicon material of this study.

One possible source of spatial nonuniformity is the surface region of the sample. We are satisfied that this is not important in our samples on the basis of experiments with a zerostat, which allows us to deposit either positive or negative charge on the surface.[20] The deposition of negative charge causes a noticeable temporary increase in the current across the grain boundary, undoubtedly because the potential barrier of this boundary is substantially lowered near the surface by the negative charge. On the other hand, the deposition of positive charge on the surface of a virgin sample has no observable effect, which implies that the grain-boundary barrier near the surface of an undisturbed sample is not substantially lower than in the bulk. The barrier near the surface may instead be higher, of course, but the fraction of the total current-carrying area affected is small enough to be neglected in this case.

It is observed in Figs. 8 and 9, and also in Fig. 12, that the exposure of the samples to optical illumination substantially reduces the diffusion potential at the grain boundary. Comparing B-6 and B-10 in Fig. 9 shows that the grain boundary with the larger V_{d0} (B-10) exhibits a much greater sensitivity to illumination. These effects were predicted earlier[21,22] and may be understood by considering the effects of photogenerated minority carriers (electrons) which are attracted to the grain boundary by the electric field in the adjacent space-charge regions. Electrons accumulate at the grain boundary until their concentration reaches the magnitude at which their capture by the interface states exactly balances the supply by photogeneration within a diffusion length on either side of the grain boundary. Provided this electron concentration (which increases approximately linearly with photogeneration rate) is sufficiently large that $n\sigma_n \simeq p\sigma_p$ (σ_n, σ_p are the capture cross sections of grain-boundary interface states for electrons and holes) the interface charge Q_{is} will decrease.[21,22] More interface states will be occupied by electrons than under dark conditions, and V_d will decrease below its dark value V_{d0}. The effect is reduced in B-6 because the lower V_{d0} implies a larger p, which requires a larger n (higher optical intensity) to meet the $n\sigma_n \simeq p\sigma_p$ condition.

The results of Fig. 12 further indicate that, for each order-of-magnitude change in the photogeneration rate, the value of V_d for $V=0$ decreases by approximately 0.07 eV. Since the majority-carrier concentration at the grain boundary $p \sim \exp(-V_d/V_T)$ and $V_T = 0.026$ V at 300 K, we expect approximately an order-of-magnitude increase in this concentration. This observation is consistent with our earlier theoretical work, and confirms that for appreciable photogeneration, $n\sigma_n \approx p\sigma_p$ at the grain boundary.[21] This condition implies a charge in grain-boundary interface states which is modified by the photogeneration in such a way that the decrease in diffusion potential ΔV_d is one half of the quasi-Fermi-level separation $\Delta E_F = E_{fn} - E_{fp}$ at the grain boundary.[14]

Series-resistance effects from the bulk silicon grains has been found to be negligible in the data presented in Sec. V, except at the largest current densities and lowest V_{d0}. For these currents, the coalescence of the various curves at different temperature and optical-illumination intensities (Fig. 5 to 8) indicate the onset of series-resistance effects. For the nonuniform grain boundaries, this mechanism occurs at lower current densities than would be expected on the basis of a one-dimensional model of the current transport, particularly at low temperature. This is understandable since at the low temperature, the effective area of active grain-boundary conduction is small and under these conditions, the series resistance increases and is explained in terms of a spreading resistance calculation.

Additional support for the notion of characteristic interface defects (a peak in N_{is} near midgap) comes from a consideration of the crystal mismatch at the grain boundary. Let us consider this mismatch on the basis of a simple model such as that of Fig. 17. This represents a realistic mismatch angle for grain boundaries in cast silicon. Note that characteristic defects are periodically repeated along the grain-boundary plane but at distances of many atomic spacings. In the vertical direction, the repetition distance will be much shorter, the dimension of a unit cell. It is clear that not all of these defect sites contribute interface states near midgap (which would correspond to unsatisfied bonds) since $\int N_{is} dE \simeq 10^{15}-10^{16}$ m^{-2} over the energy range corresponding to the midgap peak, whereas the total density of atoms on the boundary plane is 10^3-10^4 times larger. This assumes that the orientational mismatch between adjacent grains is preserved over macroscopic distances.[23]

It is interesting to also note that, by virtue of the periodic nature of the defect structure, a two-dimensional *band* conduction should be possible in the grain-boundary plane. These bands will be rather narrow for momentum parallel to the page in Fig. 17 as a result of the repetition length being several atomic distances, but could be wide for transport in the perpendicular direction.

With regard to the oscillations reported in Sec. V, we believe these to be due to electric-field-enhanced emission from the localized interface states at the grain boundary.

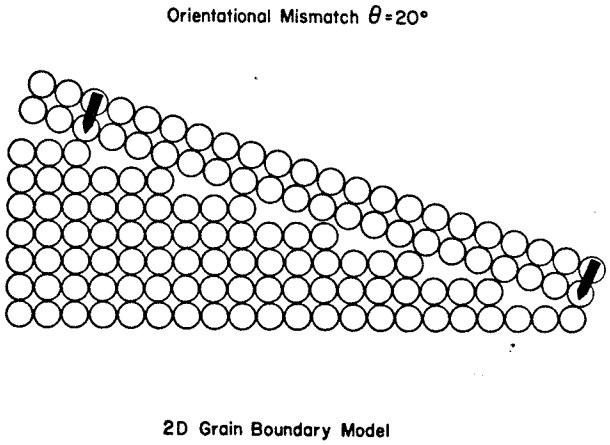

FIG. 17. Periodic nature of defect structure is suggested by this two-dimensional model. Note repetition of approximately equal disorder structure with a period of three atomic spacings along the interface between the two crystals. True periodicity is indicated by the arrows.

The beneficial effect of increased temperature supports this view, as it would provide for thermally-assisted field emission. An alternative explanation which we considered for a time was impact ionization in the localized regions of high electric field that are expected from the spatial nonuniformity of the grain-boundary potentials, but this would be expected to display a negative temperature coefficient. The oscillations appear to reflect the periodic emptying and filling of the interface states with charge, which in turn affects the electric-field distribution. As the states capture holes, the field ξ_{m2} on the reverse-biased side of the boundary is enhanced, and at a particular value, the emission rate increases rapidly. Having released their charge, ξ_{m2} decreases, quenching the emission and refilling of the states begins again.

The relative orientations of the crystals on either side of the interface of sample (B10) of Figs. 5, 8, and 10–12 were measured using x-ray precession photography.[24] The crystals were found to have a 9° mismatch of the (111) planes, and the grain-boundary plane bisected this mismatch angle. These mismatch angles were typical of electrically-active grain boundaries in the silicon material studied in this paper.

VIII. CONCLUSIONS

On the basis of the experimental studies described in this paper, and the theoretical arguments concerning the collection velocity for majority carriers of the grain boundary, the rate-limiting process of majority carrier supply by diffusion to the grain boundary should be incorporated into any transport model. The thermionic emission theory used by previous authors is expected to provide at best an order-of-magnitude estimate of the current across the electrically-biased grain boundary. Grain boundaries with a variety of diffusion potentials exist[25] in Wacker "Silso" silicon, and many of these boundaries contain potential barriers which are spatially nonuniform over macroscopic portions of the grain-boundary plane. Spatially-uniform grain boundaries also exist in this material, and for these samples a reasonable agreement with the theoretical one-dimensional model is obtained. Grain-boundary interface-state densities measured in this material are in the range of $(10^{15}-10^{16})$-$m^{-2}eV^{-1}$ and exhibit an increase with energy away from E_v in the lower half of the energy gap between 0.3 and 0.5 eV. More direct measurements of these interface-state distributions, such as depleted-layer spectroscopy techniques[26] are necessary for accurate determinations, since the results are otherwise transport-model dependent. An adequate understanding of grain-boundary phenomena in cast silicon materials, or vapor-deposited polycrystalline thin films, will challenge research workers for some time to come.

ACKNOWLEDGMENTS

It is a pleasure to acknowledge helpful discussions with Kwan Kao, Lex De Groot, and Alvin Wexler (University of Manitoba), Wei Hwang, Edward Yang, and Ed Poon (Columbia University), and Paul Panayotatos (Rutgers University) on topics described in this paper, and Frank Hawthorne (University of Manitoba) for conducting the x-ray precession photography. The financial support of the Natural Sciences and Engineering Research Council of Canada (NSERC) provided under strategic grant No. G0442 and operating grant No. A1330 are also very much appreciated.

APPENDIX A: NUMERICAL ANALYSIS OF GRAIN BOUNDARIES

The general semiconductor transport problem, neglecting quantum-mechanical effects such as reflection by the grain-boundary interface, is solved self-consistently with the following equations.

Poisson's equation relates the charge distribution to the electrostatic potential. This may be expressed as

$$\nabla^2\phi_i=-\frac{\rho}{\epsilon}\,, \tag{A1}$$

where ϕ_i is the electrostatic potential, ϵ is the permittivity of the semiconductor, and ρ is the charge density given by

$$\rho=q(p-n+N_d^+-N_a^-)+Q_{is}\,. \tag{A2}$$

In Eq. (A2), Q_{is} is the net charge in the grain-boundary interface states (assumed in our results to be independent of n and p, and hence of bias voltage) and N_d^+, N_a^- are the ionized donor, acceptor impurity concentrations. We also have the current-density expressions[17]

$$\vec{J}_n=q\mu_n n\vec{\xi}+qD_n\vec{\nabla}n=\mu_n n\vec{\nabla}E_{fn}\,, \tag{A3}$$

$$\vec{J}_p=q\mu_p p\vec{\xi}-qD_p\vec{\nabla}p=\mu_p p\vec{\nabla}E_{fp}\,, \tag{A4}$$

and current continuity equations

$$\frac{\partial n}{\partial t}=G-U+\frac{1}{q}\vec{\nabla}\cdot\vec{J}_n\,, \tag{A5}$$

$$\frac{\partial p}{\partial t}=G-U-\frac{1}{q}\vec{\nabla}\cdot\vec{J}_p\,, \tag{A6}$$

where G is the generation rate and U is the net recombination rate. For simplicity, we shall restrict ourselves to the steady state ($dn/dt=dp/dt=0$), and in the bulk of the semiconductor, we have employed the usual recombination model,[17]

$$U=\left[\frac{1}{\tau}\right]\frac{pn-n_i^2}{p+n+2n_i}\,, \tag{A7}$$

with $\tau=(\sigma v_{th}N_t)^{-1}$ as the bulk lifetime for minority carriers.

1. Program formulation

A nonuniform, one-dimensional mesh (of 61 nodes) was constructed to simulate an isolated grain boundary in p-type silicon. The boundary is situated at $x=0$, and 20 microns of bulk semiconductor is allowed on either side. Guided by the depletion approximation, one expects a space-chrage region on the order of 1 μm for the doping concentration considered in this paper. Hence elements are more densely packed near the boundary than in the bulk material. Dirichlet boundaries (i.e., those of a fixed,

known potential) are enforced at the regions' edges and the grain boundary is modeled as an interior Neumann interface. The current density is evaluated from

$$\vec{J}=\vec{J}_n+\vec{J}_p=-q(\mu_n n\vec{\nabla}\phi_n+\mu_p p\vec{\nabla}\phi_p)\,, \tag{A8}$$

with the use of the quasi-Fermi *potentials* $\phi_n=-E_{fn}/q$ and $\phi_p=-E_{fp}/q$. The gradients of ϕ_n and ϕ_p are determined by numerical differentiation.

2. Finite-element modeling techniques

In order to efficiently simulate the transport processes associated with semiconductor materials, one requires a model which is both physically accurate and numerically stable. Previous researchers have successfully applied variations of the finite-difference[29,30] and finite-element[31] methods to a number of semiconductor problems. Unfortunately, many of the earlier techniques suffer from lack of generality (e.g., restricted forms of carrier transport) and limited accuracy of solutions.

The method presented here uses quadratic, isoparametric elements together with a fully implicit Newton-Raphson algorithm to achieve accurate Fermi potentials with acceptable computational effort. Although the grain-boundary examples cited within this paper are analyzed in one spatial dimension, the method is equally suited for two- and three-dimensional analysis.

The electronic transport processes describing the behavior of a semiconductor device may be reduced to a set of three simultaneous, nonlinear, Poisson-type equations. A variational scheme is applied along with finite-element discretization to generate a quasilinear system of equations which is then transformed into a suitable residual vector. The final solution to the transport equations is obtained by zeroing that residual vector via Newton's algorithm. The following discussion describes the finite-element method in a very superficial manner. Interested readers are referred to Refs. 32–34 for related mathematical proofs and a more detailed explanation of the technique.

3. The finite-element method

Consider

$$L\phi=-\vec{\nabla}\cdot(\epsilon\vec{\nabla}\phi)=\rho\,, \tag{A9}$$

where, for the moment, the medium ϵ and source ρ are assumed to be functions of position but independent of the potential ϕ. It can be shown that under suitable boundary conditions, the energy functional,

$$F=\langle L\phi,\phi\rangle-2\langle\phi,\rho\rangle\,, \tag{A10}$$

is minimized by the solution of (A9). The triangular brackets denote a suitably defined inner product. Under influence of the Dirichlet,

$$\phi\,|_s=g(s)\,, \tag{A11}$$

and Neumann,

$$\hat{n}\cdot(\epsilon\vec{\nabla}\phi)\,|_s=h(s)\,, \tag{A12}$$

boundary conditions, together with the interface condition,

$$\hat{n}\cdot(\epsilon_1\vec{\nabla}\phi-\epsilon_2\vec{\nabla}\phi)\,|_i=k(i)\,, \tag{A13}$$

the functional may be explicitly written as

$$F=\int_R\epsilon(\vec{\nabla}\phi)^2-2\phi\rho\,d\Omega -2\int_{S_0}\phi h\,dx-\int_{S_i}\phi k\,ds\,. \tag{A14}$$

Providing ϵ is strictly positive, the operator $\mathbf{L}$ will be positive-definite. Choosing a suitable basis set $\underline{\alpha}$ and writing

$$\phi=\underline{\phi}^T\underline{\alpha}=\underline{\alpha}^T\underline{\phi}\,, \tag{A15}$$

$$\rho=\underline{\rho}^T\underline{\alpha}=\underline{\alpha}^T\underline{\rho}\,, \tag{A16}$$

$$\epsilon=\underline{\epsilon}^T\underline{\alpha}=\underline{\alpha}^T\underline{\epsilon}\,, \tag{A17}$$

leads to the matrix equation

$$(S^*\underline{\epsilon})\underline{\phi}=B\underline{\rho}\,, \tag{A18}$$

or

$$S\underline{\phi}=\underline{b}\,, \tag{A19}$$

where

$$S^*=\int[(\vec{\nabla}\underline{\alpha})\cdot(\vec{\nabla}\underline{\alpha}^T)]\underline{\alpha}^T d\Omega\,, \tag{A20}$$

$$B=\int\underline{\alpha}\,\underline{\alpha}^T d\Omega\,, \tag{A21}$$

and superscript T refers to the transpose of the column vectors. If the basis set is selected to cover only small regions of space in a piecewise-continuous fashion (i.e., a finite element) then the local matrices S and B may be accumulated on an element-by-element basis to form a large, sparse global system matrix. The actual shape functions to be integrated are generated via an isoparametric transformation in order to cover deformed regions of space.[35]

4. The Newton-Raphson algorithm

We now shall relax the restriction requiring the source and medium to be independent of the potential. To solve

$$\underline{R}=S\underline{\phi}-\underline{b}=\underline{0}\,, \tag{A22}$$

the iterative sequence

$$J^n(\underline{\Delta\phi})^{n+1}=\underline{R}^n\,, \tag{A23}$$

where

$$(\underline{\Delta\phi})^{n+1}=\underline{\phi}^n-\underline{\phi}^{n+1}\,, \tag{A24}$$

will converge quadratically for a suitable starting estimate of the potential vector.[36] The Jacobian matrix is given as

$$J_{ij}^n=\frac{\partial R_i^n}{\partial\phi_j^n}=S_{ij}^n+\left[S_{iIJ}^*\left[\frac{\partial\epsilon_j^n}{\partial\phi_j^n}\right]\right]\phi_1^n-B_{ij}\left[\frac{\partial\rho_j^n}{\partial\phi_j^n}\right]\,, \tag{A25}$$

and is reevaluated at each step in the iterative sequence.

Note that as ϵ and ρ are explicitly known functions of potential, the Jacobian is easily calculated. One should also observe that although S is sparse and symmetrical, J is sparse (and of the same topology as S) but asymmetrical. Furthermore, the structure of J does not change as the iterations proceed and, provided J Is nonsingular, the final solution is independent of the Jacobian.

When three equations are involved, the potentials may be combined into a single, complex vector with the resulting matrix equation

$$\begin{bmatrix} \frac{\partial R_i}{\partial \phi_i} & \frac{\partial R_i}{\partial \phi_n} & \frac{\partial R_i}{\partial \phi_p} \\ \frac{\partial R_n}{\partial \phi_i} & \frac{\partial R_n}{\partial \phi_n} & \frac{\partial R_n}{\partial \phi_p} \\ \frac{\partial R_p}{\partial \phi_i} & \frac{\partial R_p}{\partial \phi_n} & \frac{\partial R_p}{\partial \phi_p} \end{bmatrix}^n \begin{bmatrix} \underline{\Delta\phi_i} \\ \underline{\Delta\phi_n} \\ \underline{\Delta\phi_p} \end{bmatrix}^{n+1} = \begin{bmatrix} \underline{R_i} \\ \underline{R_n} \\ \underline{R_p} \end{bmatrix}^n . \tag{A26}$$

As before, the local matrix expressions are accumulated (element-by-element) into a sparse system matrix.

During each iteration of (A26) a large sparse system of linear equations must be solved. The method chosen for this task relies on obtaining a bifactored form of the inverse.[37] The program package ASYMPAK (Ref. 38) incorporates such an algorithm while allowing the user to ignore details of the matrix structure. With this procedure, convergence is usually achieved in three to four iterations for each step of the current-voltage curve being generated.

APPENDIX B: DERIVATION OF γ AND ESTIMATION OF ITS MAGNITUDE FOR PRESENT GRAIN-BOUNDARY SAMPLES

The relationship between dV_{d0}/dT and $d\phi_p/dT$ for a uniform grain boundary is expressed by Eq. (11) as follows:

$$\frac{dV_{d0}}{dT} = -\gamma \frac{d\phi_p}{dT} . \tag{B1}$$

We now derive γ in terms of the interface-state density N_{is} at the grain boundary. With the use of Eq. (16),

$$\frac{dQ_{is}}{dT} = -\frac{d(Q_1+Q_2)}{dT} , \tag{B2}$$

$$qN_{is}\frac{d\phi_b}{dT} \simeq -\frac{d(Q_1+Q_2)}{dV_{d0}}\frac{dV_{d0}}{dT} , \tag{B3}$$

for $V_1=V_2=0$ and $V_{d0} \gg V_T$. Also, from the fact that $\phi_b = V_{d0}+\phi_p$,

$$qN_{is}\left[\frac{d\phi_p}{dT}+\frac{dV_{d0}}{dT}\right] \simeq -\frac{d(Q_1+Q_2)}{dV_{d0}}\frac{dV_{d0}}{dT} \tag{B4}$$

$$\frac{dV_{d0}}{dT} = -\frac{1}{1+\frac{d(Q_1+Q_2)}{dV_{d0}}\frac{1}{qN_{is}}}\frac{d\phi_p}{dT} . \tag{B5}$$

Comparing Eqs. (B5) and (11) we have that

$$\gamma = \frac{1}{1+\frac{d(Q_1+Q_2)}{dV_{d0}}\frac{1}{qN_{is}}} . \tag{B6}$$

In order to evaluate γ for our samples, we employ Eqs. (10) and (11) for Q_1 and Q_2 from which we obtain

$$\frac{d(Q_1+Q_2)}{dV_{d0}} = -[2q\epsilon N_a(V_{d0}-V_T)]^{1/2}2q\epsilon N_a$$

$$= -\left[\frac{2q\epsilon N_a}{V_{d0}-V_T}\right]^{1/2}$$

For example, in our device B-10, $N_a = 3\times10^{21}$ m^{-3}, $\epsilon = 11.8\epsilon_0$, $V_{d0} \simeq 0.32$ V, and $N_{is} \simeq (6-8)\times10^{15}$ m^{-2}eV^{-1} at the equilibrium Fermi-level position ($\simeq E_v + 0.5$ eV) from which we obtain $\gamma \simeq 0.6$.

[1] T. Surek, A. P. Arietedjo, G. C. Cheek, R. W. Hardy, J. B. Milstein, and Y. S. Tsuo, *Proceedings of the 15th IEEE Conference on Photovoltaic Spectroscopy, Kissimmee, Fla., 1981,* edited by C. J. Bishop (Publisher, City, Year), p. 1251.

[2] C. H. Seager, G. E. Pike, and D. S. Ginley, Phys. Rev. Lett. 43, 532 (1979).

[3] G. E. Pike and C. E. Seager, J. Appl. Phys. 50, 3414 (1979).

[4] C. H. Seager and G. E. Pike, Appl. Phys. Lett. 35, 709 (1979).

[5] C. H. Seager, J. Appl. Phys. 52, 3960 (1981).

[6] H. F. Mataré, *Defect Electronics in Semiconductors* (Wiley, New York, 1971).

[7] C. R. Crowell and S. M. Sze, Solid State Electron. 9, 1035 (1966).

[8] B. R. Gossick, Solid State Electron. 6, 445 (1963).

[9] E. H. Rhoderick, J. Phys. D 5, 1920 (1972).

[10] R. Stratton, Proc. Phys. Soc. London Ser. B LXIX, 513 (1956).

[11] D. J. Thomson, S. R. Mejia, and H. C. Card, J. Power Sources 7, 191 (1981).

[12] J. W. Seto, J. Appl. Phys. 46, 5247 (1975).

[13] G. Baccarini, B. Ricco, and G. Spadini, J. Appl. Phys. 49, 5565 (1978).

[14] H. C. Card, J. Appl. Phys. 52, 3671 (1981).

[15] W. E. Taylor, N. H. Odell, and H. Y. Fan, Phys. Rev. 88, 867 (1952).

[16] N. D. Arora, J. R. Hauser, and D. J. Roulston, IEEE Trans. Electron Devices ED-29, 292 (1982).

[17] S. M. Sze, *Physics of Semiconductor Devices,* 2nd Ed. (Wiley, New York, 1981), p. 248.

[18] D. J. Thomson and H. C. Card, J. Appl. Phys. 54, 1976 (1983).

[19] L. Kazmerski, *Polycrystalline and Amorphous Thin Films and Devices* (Academic, New York, 1980).

[20] Y. W. Lam, M. A. Green, and L. W. Davies, Appl. Phys. Lett. 37, 1087 (1980).

[21] H. C. Card and E. S. Yang, IEEE Trans. Electron Devices ED-24, 397 (1977).

[22] P. Panayotatos and H. C. Card, IEEE Electron Devices Lett. EDL-1, 263 (1980).

[23]O. L. Krivanek, S. Isoda, and K. Kobayashi, Philos. Mag. 36, 931 (1977).
[24]M. J. Buerger, *The Precession Method in x-ray Crystallography* (Wiley, New York, 1966).
[25]D. Redfield, Appl. Phys. Lett. 38, 174 (1981).
[26]G. L. Miller, D. V. Lang, and L. C. Kimmerling, Ann. Rev. Mat. Sci. 7, 377 (1977).
[27]C. H. Seager, in *Grain Boundaries in Semiconductors* (North-Holland, New York, 1982), p. 85, and references to their early work within.
[28]J. Werner, W. Jantsch, K. H. Froehner, and H. J. Queisser, Ann. Rev. Sci. Mat., Ref. 26, p. 99 (1982).
[29]M. S. Adler, in *Numerical Analysis of Semiconductor Devices, edited* by B. T. Browne and J. J. Miller (Boole, Dublin, 1979), p. 3.
[30]K. Kani, in *Numerical Analysis of Semiconductor Devices,* Ref. 29, p. 104.
[31]P. E. Cottrell and F. M. Buturla, in *Numerical Analysis of Semiconductor Devices,* Ref. 29, p. 31.
[32]S. G. Mikhlin, *Variational Methods in Mathematical Physics* (Pergamon, Oxford, 1964).
[33]A. Wexler, Report TR80-4, Dept. Electr. Eng., Unversity of Manitoba, Winnipeg, Canada, 1980 (unpublished).
[34]O. C. Zienkiewicz, *The Finite Element Method in Engineering Science* (McGraw-Hill, London, 1971).
[35]A. Wexler, in *International Conference on Finite Elements* in Water Resources Part II, Princeton, New Jersey, edited by W. G. Gray, G. F. Pinder, and C. A. Brebbia (Publisher, City, Year), p. 2.3.
[36]A. Roger, IEEE Trans. AP-29, 232 (1981).
[37]K. Zollenkopf, in *Large Sparse Sets of Linear Equations,* edited by J. K. Reid (Academic, New York, 1971), p. 75.
[38]J. G. Shaw and A. Wexler, Report TR79-4, Dept. of Elect. Eng., University of Manitoba, Winnipeg, Canada (unpublished).

REFERENCES

1. H.K. Gummel, "A Self Consistant Iterative Scheme for One-Dimensional Steady State Transistor Calculations", IEEE Trans. Elec. Dev., ED-11, pp. 455-465, 1964.

2. M.S. Adler, "A Method for Achieving and Choosing Variable Density Grids in Finite Difference Formulations and the Importance of Degeneracy and Band Gap Narrowing in Device Modeling", in Numerical Analysis of Semiconductor Devices. B.T. Browne and J.J. Miller (Eds.), Dublin: Boole Press, pp. 3-30, 1979.

3. V. Arandjelovic, "Accurate Numerical Steady-State Solutions for a Diffused One-Dimensional Junction Diode", Solid-State Electronics, Vol. 13, pp. 865-871, 1970.

4. P.E. Cottrell and E.M. Buturla, "Three-Dimensional Transient Finite Element Analysis of Semiconductor Transport Equations", in Numerical Analysis of Semiconductor Devices and Integrated Circuits. B.T. Browne and J.J. Miller (Eds.), Dublin: Boole Press, pp. 160-165, 1981.

5. G.D. Hachtel, M.H. Mack, R.R. O'Brien, and B. Speelpenning, "Semiconductor Analysis Using Finite Elements -- Part I: Computational Aspects", IBM J. Res. Develop., Vol. 25, No. 4, pp. 232-245, 1981.

6. G.D. Hachtel, M.H. Mack, and R.R. O'Brien, "Semiconductor Analysis Using Finite Elements -- Part II: IGFET and BJT Case Studies", IBM J. Res. Develop., Vol. 25, No. 4, pp. 246-260, 1981.

7. S.G. Mikhlin, Variational Methods in Mathematical Physics. Oxford: Pergamon Press, 1964.

8. A. Wexler, Finite Elements for Technologists. Report TR80-4, Department of Electrical Engineering, University of Manitoba, Winnipeg, Canada, 1980.

9. M. Kurata, Numerical Analysis for Semiconductor Devices. Toronto: Lexington Books, 1982.

10. J.G. Shaw, MANIFEST User's Guide. Report TR82-6, Department of Electrical Engineering, University of Manitoba, Winnipeg, Canada, 1983.

11. J.G. Shaw, MANIFEST Installation Guide. Report TR82-7, Department of Electrical Engineering, University of Manitoba, Winnipeg, Canada, 1983.

12. R.A. Smith, Semiconductors. London: Syndics of the Cambridge University Press, 1964.

13. S.M. Sze, Physics of Semiconductor Devices. New York: Wiley Inter-science, 1969.

14. R.B. Adler, A.C. Smith, and R.L. Longini, Introduction to Semiconductor Physics. New York: Wiley, 1964.

15. J.C. Phillips, Bonds and Bands in Semiconductors. New York: Academic Press, 1973.

16. G. Arfken, Mathematical Methods for Physicists. New York: Academic Press, 1970.

17. J.G. Shaw, A Point-Iterative, Variational Finite-Element Algorithm for Three-Dimensional Vector Fields. Report TR81-6, Department of Electrical Engineering, University of Manitoba, Winnipeg, Canada, 1981.

18. R.F. Harrington, Field Computation by Moment Methods. New York: Macmillian, 1968.

19. O.C. Zienkiewicz, The Finite Element Method in Engineering Science. London: McGraw-Hill, 1971.

20. B. Irons and S. Ahmad, Techniques of Finite Elements. New York: Wiley, 1980.

21. J.R. Whiteman, The Mathematics of Finite Elements and Applications. London: Academic Press, 1973.

22. G.F. Pinder and W.G. Gray, Finite Element Simulation in Surface and Subsurface Hydrology. New York: Academic Press, 1977.

23. P.M. Prenter, Splines and Variational Methods. New York: Wiley, 1975.

24. G.V. Price and A.K. MacPherson, "A Numerical Weather Forecasting Method Using Cubic Splines on a Variable Mesh", Journal of Applied Meteorology, Vol. 12, No. 7, pp. 1102-1113, 1973.

25. A.H. Stroud and D. Secrest, Gaussian Quadrature Formulas. Englewood Cliffs, N.J.: Prentice-Hall, 1966.

26. L.Y. Kantorovitch, "On Newton's method for functional equations", Dokl. Akad. Nauk. SSSR., Vol. 59, pp. 1237-1240., 1948.

27. L. Fox, Numerical Solution of Ordinary and Partial Differential Equations. Oxford: Pergamon Press, 1962.

28. K.J. Bathe and A.P. Cimento, "Some Practical Procedures for the Solution of Nonlinear Finite Element Equations", Computer Methods in Applied Mechanics and Engineering, Vol. 22, pp. 59-85, 1980.

29. R.E. Bellman, Methods of Nonlinear Analysis. New York: Academic Press, Vols. I, II, and III, 1970.

30. Y.B. Yildir and A. Wexler, MANDAP, A FEM/BEM Data Preparation Package - User's Manual. TR82-3, Dept. Electrical Engineering, University of Manitoba, R3T 2N2, 1982.

31. Y.B. Yildir and A. Wexler, MANDAP, A FEM/BEM Data Preparation Package - Program Listings. TR82-3, Dept. Electrical Engineering, University of Manitoba, R3T 2N2, 1982.

32. R. Allen and A. Wexler, CONTOUR User's Manual. TR82-7, Dept. Electrical Engineering, University of Manitoba, R3T 2N2, 1982.

33. B. Carnahan, H.A. Luther, and J.O. Wilkes, Applied Numerical Methods. New York: Wiley, 1969.

34. A.R. Mitchell and R. Wait, The Finite Element Method in Partial Differential Equations. New York: Wiley, 1977.

35. C.I. Voss and G.F. Pinder, Block Iterative Finite Element Preprocessed Scheme for Simulation of Large Non-Linear Problems. Report 77-WR-3, Princeton, N.J.: Princeton University Press, 1977.

36. R.S. Varga, Matrix Iterative Analysis. Englewood Cliffs, N.J.: Prentice-Hall, 1962.

37. K. Zollenkoph, "Bi-Factorisation -- Basic computational algorithm and programming techniques", in Large Sparse Sets of Linear Equations. J.K. Reid (Ed.), New York: Academic Press, pp. 75-96, 1971.

38. J.G. Shaw and A. Wexler, SYMPAK/ASYMPAK -- A Program Package for Solving Large Sparse Systems of Linear Algebraic Equations. TR79-4, Dept. Electrical Engineering, University of Manitoba, R3T 2N2, 1979.

39. D.S. Kershaw, "The Incomplete Cholesky-Conjugate Gradient Method for the Iterative Solution of Systems of Linear Equations", Journal of Computational Physics, Vol. 26, pp. 43-65, 1978.

40. G. Gambolati, "Fast Solution to Finite-Element Flow Equations by Newton Iteration and Modified Conjugate Gradient Method", International Journal for Numerical Methods in Engineering, Vol. 15, pp. 661-675, 1980.

41. J.C. Wu and J.F. Thompson, "Numerical Solutions of Time-Dependent Incompressible Navier-Stokes Equations Using an Integro-Differential Formulation", Computers & Fluids, Vol. 1, pp. 197-215, 1973.

42. C. A. Brebbia (Ed.), New Developments in Boundary Element Methods. Southampton: CML Publishing Limited, 1980.

43. S.E. Laux, "Extraction of Quasi-Static Capacitance from Numerical Device Simulation Data", presented at the Joint SIAM-IEEE Electron Devices Society Conference on Numerical Simulation of VLSI Devices, Boston, Massachusetts, Nov. 2-4, 1982.

44. R. Guerrieri and M. Rudan, "Optimization of the Finite-Element Solution of Poisson's Equation", presented at the Joint SIAM-IEEE Electron Devices Society Conference on Numerical Simulation of VLSI Devices, Boston, Massachusetts, Nov. 2-4, 1982.

45. T.P. Fontana, D.M. MacGregor, and R.P. Lowther, "DEFINES: A Semiconductor Device Finite Element Simulation", presented at the Joint SIAM-IEEE Electron Devices Society Conference on Numerical Simulation of VLSI Devices, Boston, Massachusetts, Nov. 2-4, 1982.

46. W.L. Engl, H.K. Dirks, and B. Meinerzhagen, "Device Modeling", Proceedings of the IEEE, Vol. 17, No. 1, pp. 10-33, 1983.

47. H.P. Strohband, "New results on stability of the BDG-integration method with non-constant stepsize and order", Asilomar Conf. on Circuits, Systems, and Computers, Conf. Rec., pp. 354-358, 1975.

48. A.A. Eltoukhy, Analysis of Small Geometry VLSI Bipolar Transistors Including Polysilicon Emitter Devices. Ph.D. dissertation. University of Waterloo, Ontario, Canada, 1982.

49. S.E. Laux and R.J. Lomax, "Numerical Investigation of Mesh Size Convergence Rate of the Finite Element Method in MESFET Simulation", Solid-State Electronics, Vol. 24, pp. 485-493, 1981.

50. T. Surek, A.P. Arietedjo, G.C. Cheek, R.W. Hardy, J.B. Milstein and Y.S. Tsuo, Proc. 15th IEEE Photovoltaic Spec. Cont., Kissimmee, Fla., May 12-15th pp. 1251-1260, 1981.

51. C.H. Seager, G.E. Pike and D.S. Ginley, Phys. Rev. Lett., 43, 532-535, 1979.

52. G.E. Pike and C.E. Seager, J. Appl. Phys., 50, 3414-3422, 1979.

53. C.H. Seager and G.E. Pike, Appl. Phys. Lett., 35, 709-711, 1979.

54. C.H. Seager, J. Appl. Phys., 52, 3960-3968, 1981.

55. H.F. Matare, Defect Electronics in Semiconductors, John Wiley, New York, 1971.

56. C.R. Crowell and S.M. Sze, Solid St. Electron., 9, 1035, 1966.

57. B.R. Gossick, Solid St. Electron., 6, 445, 963.

58. E.H. Rhoderick, J. Phys. D.: Appl. Phys., 5, 1920, 1972. Also Metal-Semiconductor Contacts, Oxford Press, 1978.

59. R. Stratton, Proc. Phys. Soc., LXIX, 5-B, 513, 1956.

60. E. Palm and F. Van de Wiele, "A Finite Element Approach and Automatic Mesh Generation for the Resolution of Poisson's Equation in Reverse Biased Two-Dimensional Semiconductor Devices", in Numerical Analysis of Semiconductor Devices and Integrated Circuits. B.T. Browne and J.J. Miller (Eds.), Dublin; Boole Press, pp. 259-263, 1981.

61. E.Y. Chan and H.C. Card, unpublished results.

62. H.C. Card, J.G. Shaw, G.C. McGonigal, D.J. Thomson, A.W. deGroot, and K.C. Kao, "Carrier Transport at Grain Boundaries in Silicon", Proc. 16th IEEE Photovoltaic Specialists Conf., San Diego, CA., Sept. 27-30, 1982. In press.

63. G.C. McGonigal, D.J. Thomson, J.G. Shaw and H.C. Card, Electronic Transport at Grain Boundaries in Silicon", Physical Review B. In press.

64. J.G. Shaw and H.C. Card, "A Unified Approach to Numerical Semiconductor Device Analysis", Journal of Computational Physics. In preparation.

65. J.G. Shaw and H.C. Card, "Numerical Simulation of VLSI Devices", 1983 Canadian Conference on Very Large Scale Integration. In preparation.

66. H.C. Card, "The photoconductivity of polycrystalline semiconductors", J. Appl. Phys., 52, 3671-3673, 1981.